Vol. 9 No. 2
October 2025

ISSN 2579-5821
e-ISSN 2579-5546

S3 sinta
Science and Technology Index

Jurnal Geocelebes

Published by:
Geophysics Department
Hasanuddin University
Makassar, Indonesia

JURNAL GEOCELEBES

Geophysics Department | Faculty of Mathematics and Natural Sciences | Hasanuddin University

Volume 9 Number 2, October 2025

P-ISSN: 2579-5821
E-ISSN: 2579-5546

Published by:
Geophysics Department, Math and Natural Science Faculty
Hasanuddin University

JURNAL GEOCELEBES

Volume 9 Number 2, October 2025

ISSN: 2579 – 5821 (Print)
ISSN: 2579 – 5546 (Online)
URL address: http://journal.unhas.ac.id/index.php/geocelebes

Diterbitkan berkala dua kali setahun oleh/ **Published periodically two times annually by**
Dept. Geofisika Universitas Hasanuddin/ **Geophysics Dept., Hasanuddin University**

Dewan Redaksi/ Editor Board

Sekretariat/ Secretariat:
Departemen Geofisika, FMIPA Universitas Hasanuddin
Gedung MIPA, Kampus Unhas Tamalanrea - Jalan Perintis Kemerdekaan, Makassar, Sulawesi Selatan, 90245.
E-mail: geocelebes@sci.unhas.ac.id

Jurnal Geocelebes is a scientific journal published by the Department of Geophysics, Hasanuddin University. This journal is intended as a means of scientific publication in the field of geophysics ranging from theoretical topics to geophysical applications in various fields topics. The articles are original research results, reviews of recent advances in a particular topic, case studies of geophysical applications or reviews of software related to geophysics. Papers should be sent to the editorial website in softcopy using the template provided. Each accepted paper will be reviewed for eligibility through a rigorous reviewing process by the Editorial Board.

Contents

JURNAL GEOCELEBES

Volume 9, Number 2, October 2025

ISSN: 2579 – 5821 (Print)
ISSN: 2579 – 5546 (Online)

URL: http://journal.unhas.ac.id/index.php/geocelebes

Preface

Jurnal Geocelebes managed by the Department of Geophysics, Faculty of Mathematics and Natural Sciences, Hasanuddin University Makassar has entered its eighth year. The Editorial Board expresses gratitude to God Almighty for this achievement and expresses gratitude for the commitment of the Editorial Board, in carrying out this mandate. In particular, the Editorial Board expresses its gratitude and highest appreciation to all authors who have submitted their scientific works and to the Reviewers who have been willing to take the time to provide constructive suggestions and corrections to each article in each issue of the Jurnal Geocelebes.

In the edition of Volume 9 Number 2 October 2025 there are ten articles. The articles published generally discuss the implementation of the role of geosciences, especially geophysics in natural resource exploration and other fields that are in accordance with the focus and scope of the field published by the Jurnal Geocelebes. The language used in this volume is English, which shows that Jurnal Geocelebes deserves to be an international journal in the future. In this month, The Editorial Board still waiting the result of Re-accreditation of SINTA. Jurnal Geocelebes welcomes participation from academics, researchers, industry practitioners, students, and others in the field of geosciences in both theoretical and application perspectives, both related to the subsurface (lithosphere) and above the surface (atmosphere), which of course will go through a series of processes namely submitting, editing, and reviewing.

The Editorial Board of Jurnal Geocelebes is open to suggestions and constructive criticism for future improvements. All suggestions and criticisms can be sent via email geocelebes@sci.unhas.ac.id

Makassar, October 2025

The Editorial Board of Jurnal Geocelebes

ISSN: 2579-5821 (Print)
ISSN: 2579-5546 (Online)
URL address: http://journal.unhas.ac.id/index.php/geocelebes
DOI: 10.70561/geocelebes.v9i2.34767

Jurnal Geocelebes Vol. 9 No. 2, October 2025, 100 – 112

Phase Tensor Analysis and 2D Modeling of Magnetotelluric Method Data in The Nullarbor Area, South Australia

Sarah Manurung, Andri Yadi Paembonan*, Selvi Misnia Irawati

Geophysical Engineering, Faculty of Industrial Technology, Sumatra Institute of Technology, Lampung 35365, Indonesia

*Corresponding author. Email: andri.paembonan@tg.itera.ac.id

Manuscript received: 2 May 2024; Received in revised form: 23 February 2025; Accepted: 18 May 2025

Abstract

Earth's geological structures are generally the result of tectonic processes. This study aims to determine the dimensions and direction of the geoelectric strike based on phase tensor analysis and 2D modeling to determine the subsurface structure in the Nullarbor area, South Australia using the magnetotelluric method. The magnetotelluric method is a passive geophysical technique used to create images of subsurface structures based on variations in rock resistivity. Data was obtained in EDI file mean the data has been processed and convert to apparent resistivity and frequency. Furthermore, data is analysis in the phase tensor process and then identify the Geoelectrical strike direction. Based on the tensor analysis, the results show that the study area has 2D dimensions, and the direction of the geoelectric cross section is from North to South, specifically N5°E. This geoelectric direction corresponds to the regional geological structure. After rotation in this direction, 2D inversion modeling of the MT data shows rock layers consisting of Eucla basins with sediment and volcanics rocks below 10 Ωm and Officer basin contain a sediment rock that has higher resistivity ranging from 10 to about 300 Ωm. Furthermore, the resistive layer with 300 – 2000 Ωm is expected as the upper crust in the central Coompana Province trending granite-rich corridor. This result show that the geological structure and lithology could be identified in this study area by analyzing the phase tensor and from the 2D model.

Keywords: dimensionality; geoelectrical strike; geological structure; inversion; magnetotelluric.

Citation: Manurung, S., Paembonan, A. Y., & Irawati, S. M. (2025). Phase Tensor Analysis and 2D Modeling of Magnetotelluric Method Data in The Nullarbor Area, Southern Australia. *Jurnal Geocelebes*, 9(2): 112–124. doi: 10.70561/geocelebes.v9i2.34767

Introduction

Geological investigations into the Earth's layers reveal structures shaped by tectonic processes within a given region. These phenomena stand out as a critical area of study. It occurs when the deformation of rocks leads to displacements between adjacent rock blocks, offering valuable insights into the dynamic forces that shape our planet. The range of displacements can be very wide, ranging from a few millimeters to tens of kilometers, and are often triggered by the movement of tectonic plates, especially in subduction zones. The geological structures can cause earthquakes that cause significant losses. Therefore, the study of geological structure is important to minimize the impact of earthquake losses. The existence of geological structure such as fault not only has negative impacts, such as the potential for earthquakes that can cause significant losses but also has positive benefits. Faults can increase conductivity creating pathways for mineral fluid flow, which has high economic value (Akbar et al., 2020). This research focused on the Nullarbor Plain region of South Australia, which is known as the largest karst plain in the world. The region has an area of approximately 200,000 km² and is covered by thick layers of limestone (Scheib et al., 2016). Significant transformations occur in this region due to linear cracks caused by thrust faults in the

rock structure (Pawley et al., 2020). The Magnetotelluric method was used in this study to understand the subsurface conditions of the earth (Chang et al., 2023; Lin et al., 2023; Pertiwi et al., 2023). This method utilizes variations in the earth's magnetic field to measure subsurface conductivity (Simpson & Bahr, 2005). Measurements are made in the perpendicular direction on the earth's surface to get an overview of the subsurface structure. This method has the advantage of mapping the resistivity distribution in the subsurface (Barajas-Olalde et al., 2023; Marwan et al., 2022).

Previous research in the Nullarbor region has used various methods, including magnetic (Hu et al., 2019; Pawley et al., 2020), gravity (Heath, 2017; Heath et al., 2018) and seismic methods, to understand the role of fluids in seismic activity and the development of tectonic structures (Yang et al., 2022). However, no studies have used phase tensor analysis. In this study, phase tensor analysis is used to identify the type of dimensionality and direction of geoelectrical strike to determine the direction of structure in the study area (Irawati et al., 2024; Maswah et al., 2021). By combining magnetotelluric data with geological information, this study aims to obtain an accurate 2D subsurface model and interpret the lithology and fault structure in the study area. It is expected that the results of this study will provide a deeper understanding of the geology and potential earthquake risk in the Nullarbor Plain and can contribute to the optimization of mineral resource utilization in the area.

Materials and Methods

Geological setting

Nullarbor is a region located on the coast of the Great Australian Bight in South Australia with the Victorian Desert to its north. The region is the largest expanse of limestone in the world with an area of about 200,000 square kilometers or 77,000 square miles. Based on the Geological Map of Nullarbor sourced from the Geological Map of South Australia in 2020 (Figure 1), the overall geology in the study area is dominated by Tertiary rocks (Geological Survey of Western Australia, 2017; Cowley, 2020). The study is located at the Eucla Basin. Its boundary, which spans 2,000 kilometers from Western Australia to South Australia, are a large offshore, nearshore, and onshore province of marine and coastal sediments up to 300 meters thick (Hou et al., 2022). Sedimentary records from the basin and surrounding paleo valleys offer a more comprehensive picture of the region's geological history than only basin deposits.

Sedimentary rocks in Nullarbor are Miocene and Pliocene age, consisting of limestone and marine fossil limestone (Czi). At the end of the early Miocene, the sea retreated for less than 1 million years and then advanced again in the middle Miocene. Nodular algal limestone was deposited in much the same area as the Abrakurrie limestone forming the mulla mullang member of the Nullarbor limestone. Seawater then encroached further across the valley, depositing thin beds of Nullarbor limestone generally less than 20 meters across the Nullarbor area. The origin of this limestone is attributed to the abundance of foraminifera and the relatively high proportion of aragonite components (Webb & James, 2006).

The middle part of the Coompana Province has a two-layer crust. The upper crust is 14-17 km thick and stretches approximately 140 km westward from the Palinar Shear Zone to the Border Shear Zone. The top crust between the Palinar and Bunburra shear zones is plain and lacks reflectors. It correlates to the northeast trending granite-rich corridor (Pawley et al., 2020).

Magnetotelluric Method

The magnetotelluric method is one of the passive geophysical methods used to create

images of subsurface structures based on variations in rock resistivity (Chang et al., 2023; Lin et al., 2023; Pertiwi et al., 2023). This electromagnetic field originates from a variety of very complex physical processes that result in its frequency spectrum having a very wide range ranging from 10^{-5} Hz to10^{4} Hz (Arisbaya et al., 2023). An understanding of the magnetotelluric (MT) method can be obtained by considering the principle of propagation of incident electromagnetic waves. In a mathematical context, the principle of the magnetotelluric method is explained through Maxwell's equations. The relationship between the orthogonal components of the electric field and the horizontal magnetic field is described using the impedance tensor (Z) (Irawati et al., 2024; Maswah et al., 2021).

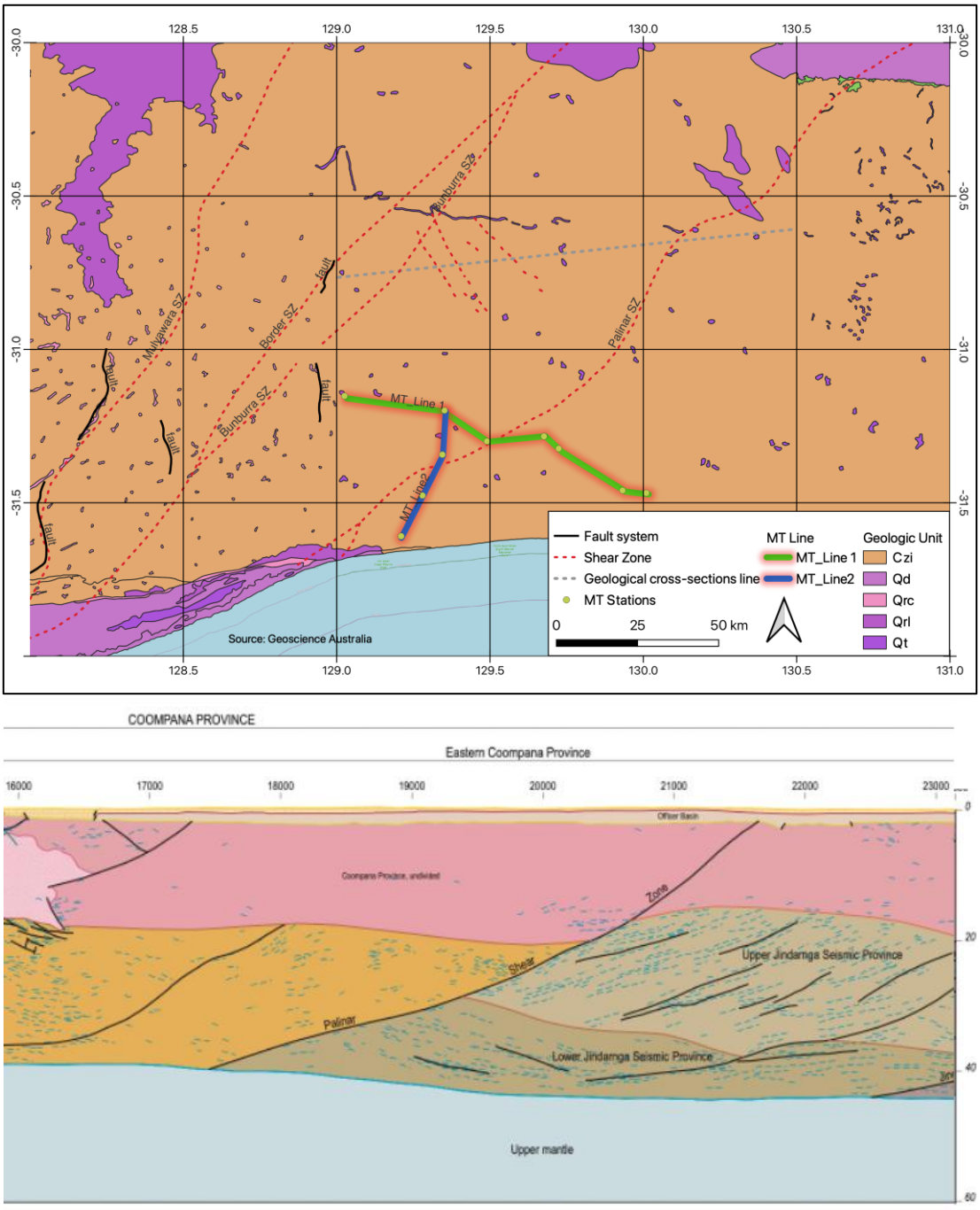

Figure 1. Geologic map (top) showing the fault and fracture zone including magnetotelluric measurements lines at Nullarbor and interpreted geological section (bottom) (Geological Survey of Western Australia, 2017; Cowley, 2020).

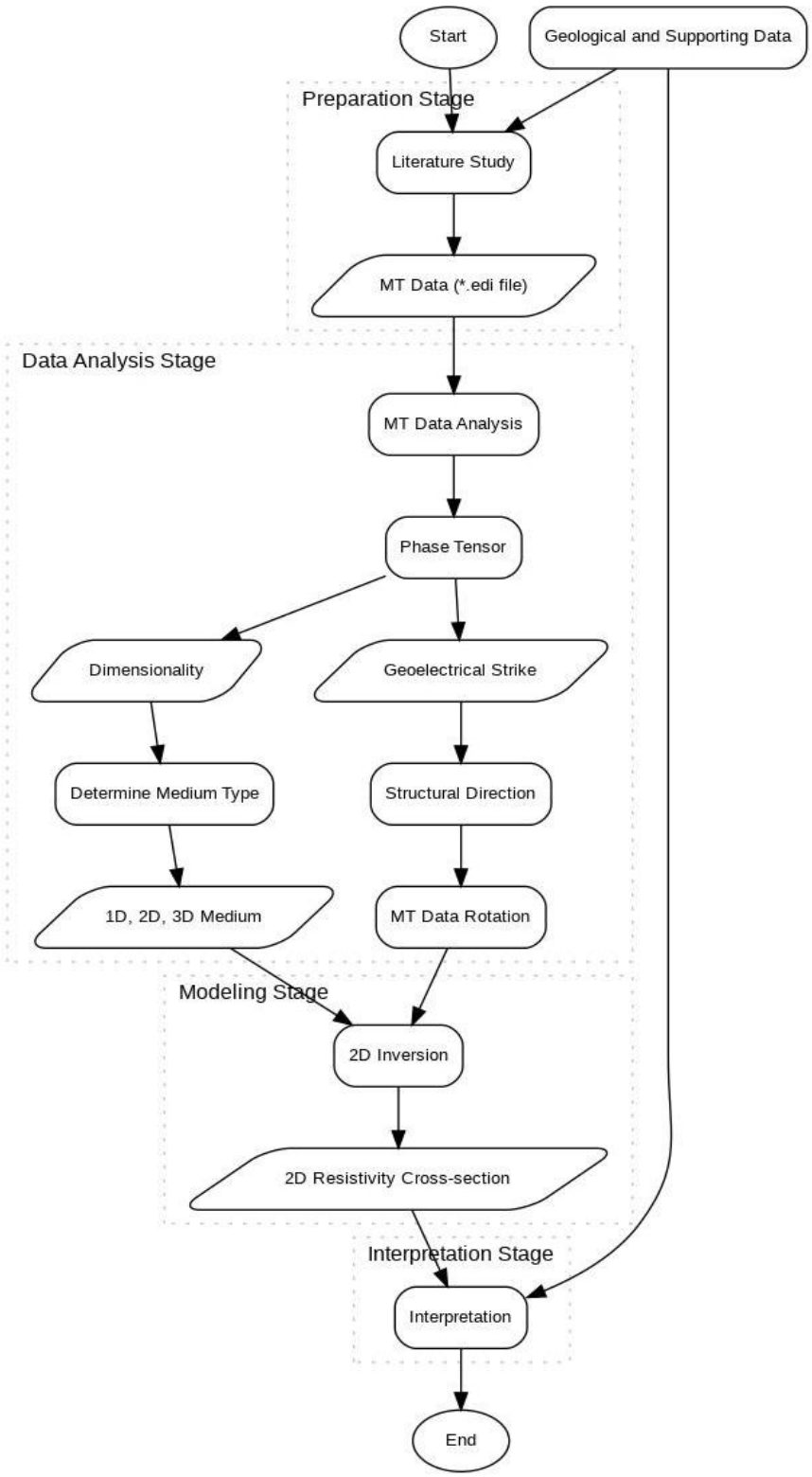

Figure 2. Flow diagram of the MT data processing, analysis, and 2D modeling.

$$E = ZH \quad (1)$$

$$\begin{pmatrix} E_x \\ E_y \end{pmatrix} = \begin{pmatrix} Z_{xx} & Z_{xy} \\ Z_{yx} & Z_{yy} \end{pmatrix} \begin{pmatrix} H_x \\ H_y \end{pmatrix} \quad (2)$$

Where (Z) serves as a transfer function and has the form of a complex number that can also be expressed as apparent and phase resistivity, as described in equations (1) and (2). Therefore, the apparent and phase resistivity can be explained through the following equations:

$$\rho_\alpha = \frac{1}{\omega\mu_0}|Z|^2 \quad (3)$$

$$\phi = \tan^{-1}\left[\frac{lm(Z)}{Re(Z)}\right] \quad (4)$$

According to Bravo-Osuna et al. (2021), the phase (Φ) can be explained as the ratio between the real and imaginary numbers of an impedance tensor complex number. Through the ratio between the real and imaginary numbers, a relationship can be found in the form of a matrix or tensor represented in the following equation:

$$Z = X + iY \quad (5)$$

$$X^{-1}Y = \begin{bmatrix}\phi_{xx} & \phi_{xy}\\ \phi_{yx} & \phi_{yy}\end{bmatrix} \quad (6)$$

Data and Processing Steps

This study utilized secondary data obtained from the acquisition of the Magnetotelluric (MT) method in the Nullarbor region, specifically in Coompana province, conducted by the Geoscience Australia (Jiang et al., 2017). Data consists of 14 measurement points presented in *.edi format where the data have been processed and converted to apparent resistivity and phase (Figure 3). Procedure to process and analyze the data is shown in Figure 2. analysis was conducted to determine the geoelectrical strike and dimensionality of the study area. MT data was analyzed using phase tensor analysis to determine the geoelectrical strike and dimensionality in the study area. The geoelectrical strike analysis process uses the Python programming language on the Google Colab platform with Python code developed by the University of Adelaide (Kirkby et al., 2019). This approach is based on the concept of ellipse theory (Bravo-Osuna et al., 2021) which produces information on the dimensionality and direction of the geoelectrical strike in the study area. The geoelectrical strike analysis was obtained through phase tensor calculations using the MTPy code. The resulting geoelectrical strike directions were then grouped based on low, medium, and high frequency periods, and then represented in the form of a rose diagram. The output of this analysis is an angle which is then used to rotate the MT data. MT modeling is used to describe the subsurface structure in the study area. In this research, the 2D inversion method is used by applying Nonlinear Conjugate Gradient (NLCG) which could simplify an object function (Guo et al., 2020). The modeling results are also associated with the characteristics of the research area. At this stage, modeling of Transverse Electric (TE) mode and Transverse Magnetic (TM) mode is also conducted. The interpretation process involves analyzing the specific gravity through a 2D inversion process by considering the phase tensor. Furthermore, the results of this analysis were correlated with relevant geological data in the study area (Figure 4).

Results and Discussion

MT data analysis is the first step before starting the modeling process. In this research begins with phase tensor analysis, where in dimensionality it is necessary to overlay the ellipse with the geologic sheet and review the Geoelectrical strike by plotting the rose diagram (Figure 5). In this case to determine the direction of the structure and conductivity of the subsurface medium used for MT data rotation to obtain accurate 2D inversion modeling. The period ranges (low, medium, and high).

The phase tensor analysis in Figure 3(a) shows the phase tensor overlay map at a low period of 0.01 s with skew angle values associated with shallow depths because the resulting skew angle values are dominantly close to zero (where the maximum axis is equal to the minimum axis ($\Phi_{max} = \Phi_{min}$)), dominated by white circles, representing a type of 1D dimensionality. Figure 3(b) displays the phase tensor overlay map at a medium period of 1s with skew angle values associated with medium depth

because the resulting skew angle value is dominantly -3°< β < 3° where the maximum axis is not equal to the minimum axis ($\Phi_{max} \neq \Phi_{min}$), dominated by elliptical shapes colored faint red and faint blue, representing the type of 2D dimensionality. Figure 3(c) displays the phase tensor overlay map at a medium period of 100s with skew angle values associated with deep depths because the resulting skew angle values are dominant at -3°< β < 3° where the maximum axis is not equal to the minimum axis ($\Phi_{max} \neq \Phi_{min}$), dominated by elliptical shapes that are colored faint red and faint blue, representing a type of 2D dimensionality. Therefore, over all this MT data has 2D dimensionality.

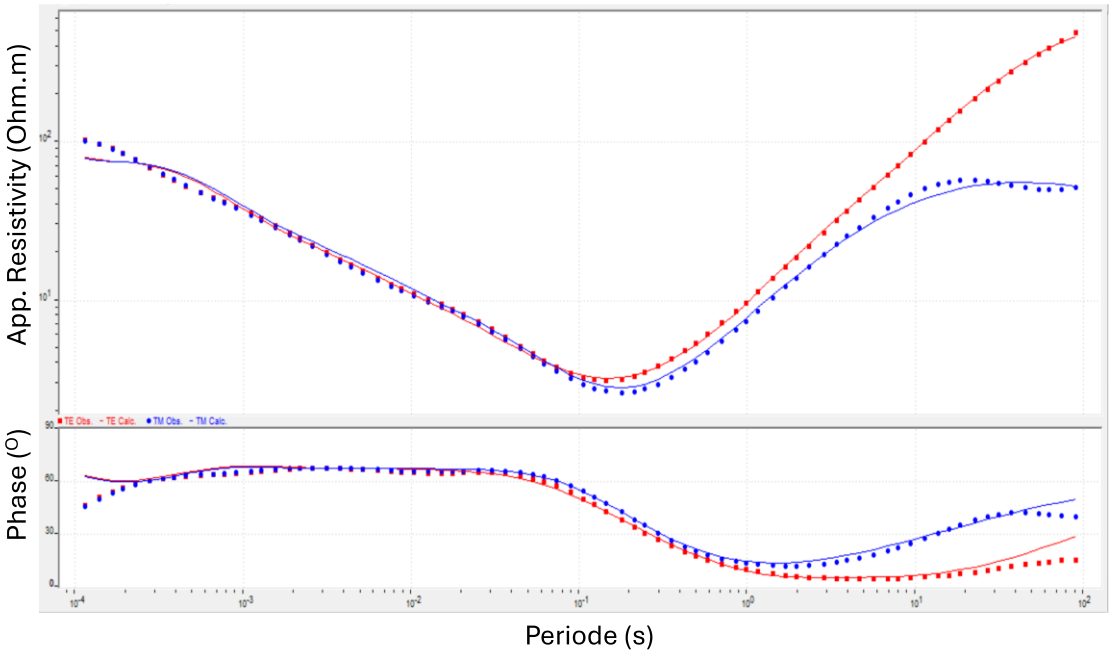

Figure 3. Sample of MT data from the study area, showing both TE (read) and TM (Blue) mode in apparent resistivity (above) and phase (below).

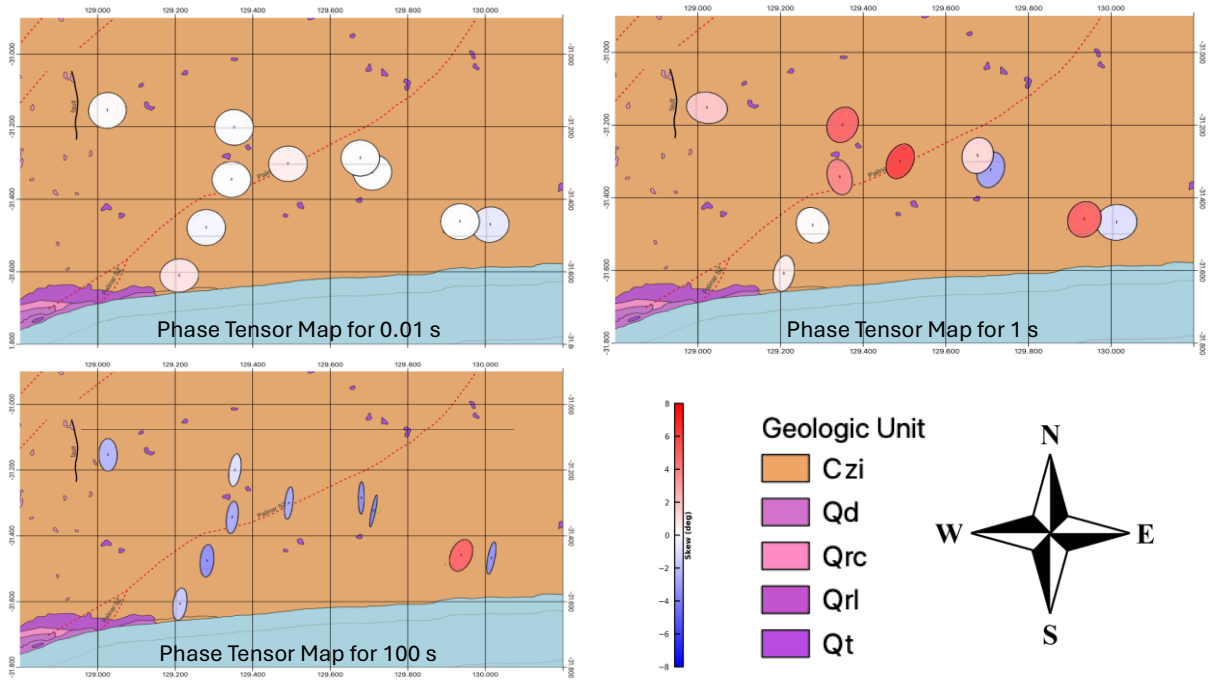

Figure 4. Phase tensor maps of (a) low period (0.01 s), (b) medium period (1 s), and (c) high period (100 s).

In knowing the geoelectric strike direction of the research area that produces the direction of the structure can be visualized with a rose diagram. Geoelectric strike direction in the low period (0.001 - 0.01 s) shows rose diagram Figure 5(a) from phase tensor analysis has an orientation of N75°E. In the medium period (0.1 - 1 s) Figure 5(b) has an orientation of N15°E and N5°E and in the high period (10 - 100 s) has the same orientation of N5°E in Figure 5(c).

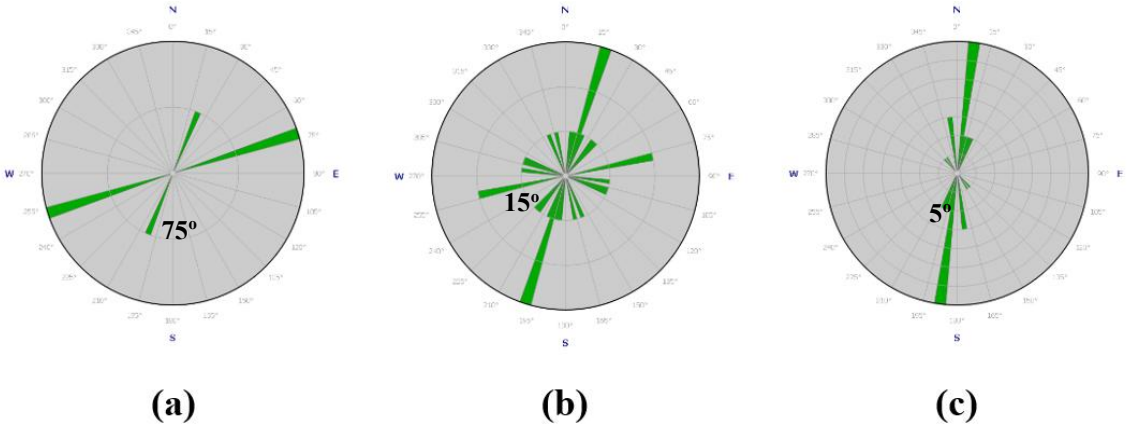

Figure 5. Rose diagram of phase tensor analysis of (A) low period, (B) medium period, and (C) high period.

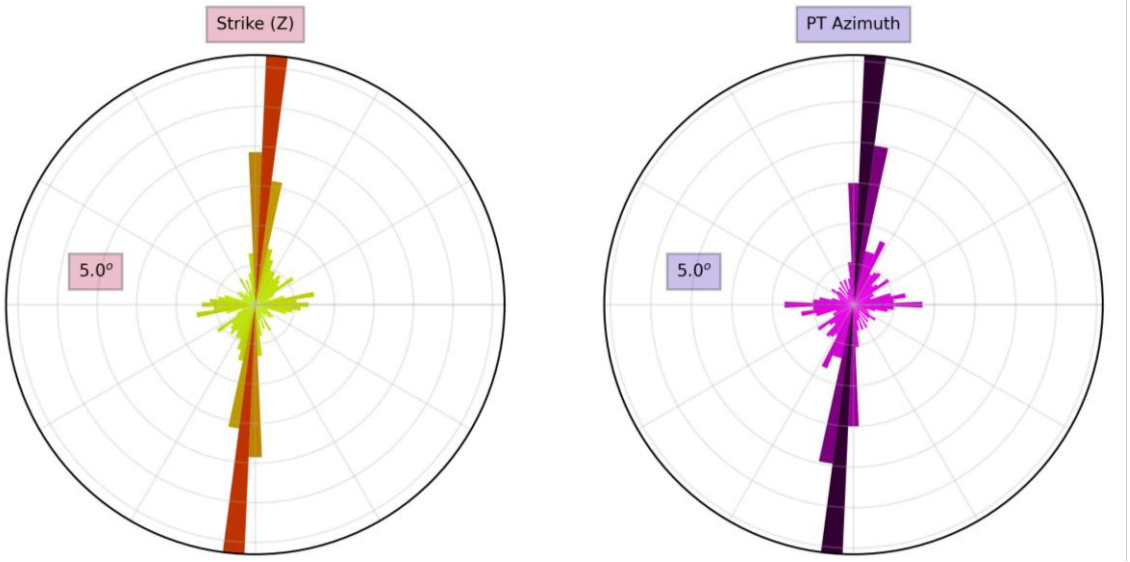

Figure 6. Rose diagrams all periods showing the direction in 5ºNS from both strike(left) and phase tensor (right) analysis.

The orientation of the direction found in the high period is N5°E and in all periods also has a dominant orientation of N5°E (Figure 6). Compared to the orientation of the direction of the geological structure in the research area, it is the same as the geoelectrical strike results using a phase tensor of N5°E. The orientation obtained through geoelectrical strike analysis was used to rotate the MT data. A rotation of N5°E was performed to align the data with the regional strike direction before proceeding to the modeling stage. Rotation is necessary in 2D modeling due to the dominance of dimensionality data in this study area by 2D. It aims to ensure the assumption of an infinite elongated structure is met. Thus, the measured geoelectrical strike direction can be aligned with the measurement line because the measurement direction is not always the same as the direction in the modeling.

Based on the phase tensor analysis of all period ranges, it is known that the dominant direction in the MT data of the Nullarbor

area obtained is N5°E and then used to rotate the MT data. Determination of the geoelectric strike direction must have relevance to the geology of the study area, because phase tensor analysis has an ambiguity of 90°. Geoelectric analysis also serves to draw line directions. After the data is rotated and the line is drawn, a 2D inversion is then performed with the Nonlinear Conjugate Gradient (NLCG) approach. This inversion uses a differential function at the minimum function which aims to minimize outliers to produce an optimum model. In this inversion modeling, a combination of TE and TM mode inversion is used. Utilization of TE mode produces good vertical detail (depth) but is less than optimal in displaying lateral layers of the earth. Conversely, TM mode provides good lateral detail but less vertically (depth). Therefore, combining these two modes is necessary to obtain good overall model results both in terms of vertical (depth) and lateral. 2D inversion modeling uses 3 passes where each pass has the same homogeneous initial model with a resistivity of 100 m and has the same iteration treatment of 60 times.

Figure 6 is the result of 2D inversion modeling on line 1 which consists of 7 MT measurement points which are D13, D1, D11, D10, D6, D3, and D9 with a northwest-southeast line direction. In this case using inversion weighting parameters alpha 4, beta 3 and tau 3 produces an RMS error of 1.79%. The 2D model has a depth of 10 km with a line length of 100 km. The resistivity distribution of the model is ranging from 1 to 2000 Ωm. Resistivity values as in Table 1 based on the results of previous research by Jiang et al (2017), Geological Survey of Western Australia (2017), and Pawley et al. (2020). in the South Australia. The resistivity value of Eucla basins consisting of sediment and volcanics rocks below 10 Ωm. Officer basin contain a sediment rock has higher resistivity ranging from 10 to about 300 Ωm. Furthermore, the resistive layer with 300 - 2000 Ωm is expected as the upper crust in the central Coompana Province trending granite-rich corridor.

The existence of geologic structure located in the Nullarbor, especially on line 1, can be suspected using resistivity contrast in 2D inversion modeling. By understanding the different resistivity patterns, especially the contrast between the rocks affected by the structure such as fault or shear zone and the surrounding rocks, we can obtain an indication of the presence and location of the structure. Figure 6 shows the 2D model of line 1, with basin sediment extended to approximately 6 km depth, and bedrock (granite) at >1000 m depth.

Table 1. Rock resistivity in previous studies and drilling results (Geological Survey of Western Australia, 2017).

Lithology	Resistivity (Ωm)
Eucla and Bright Basins consisting of sediment and Vulcanic rocks including Tun formation (Czi)	<10
Office Basin, Sedimentary rock	10-300
Coompana province, undivided (Basement Granite)	300-2000

The geological structures in the Nullarbor area were formed through tectonic activity, sedimentation, and climatic influences. The craton that forms the core of the Nullarbor region is characteristically characterized by a cold and thick lithosphere, providing high rigidity against tectonic deformation. However, neotectonic evidence indicates fault, shear, and fold activity within it, particularly evident in the carbonate rocks (limestones) that form the surface layers of the Nullarbor Plain. The result from the resistivity model line 1 (Figure 6) showing the low resistivity anomaly below 300 Ohm.m in the basement rock, that indicates the shear zone. This could be a part of the Palimar SZ that found in the section of the seismic interpretation in the north.

Figure 7 display 2D modeling on track 2 which consists of 4 MT points which are

D1, D12, D08 and D7 with the direction of the northeast - southwest. In this case using inversion weighting parameters alpha 4, beta 2 and tau 0.3 produces an RMS error of 1.50%. The 2D inversion results have a depth of 10 km with an area of 50 km. The 2D inversion results seen in Figure 7 produce a resistivity distribution in the cross section ranging from a range of 1 - 2000 m.

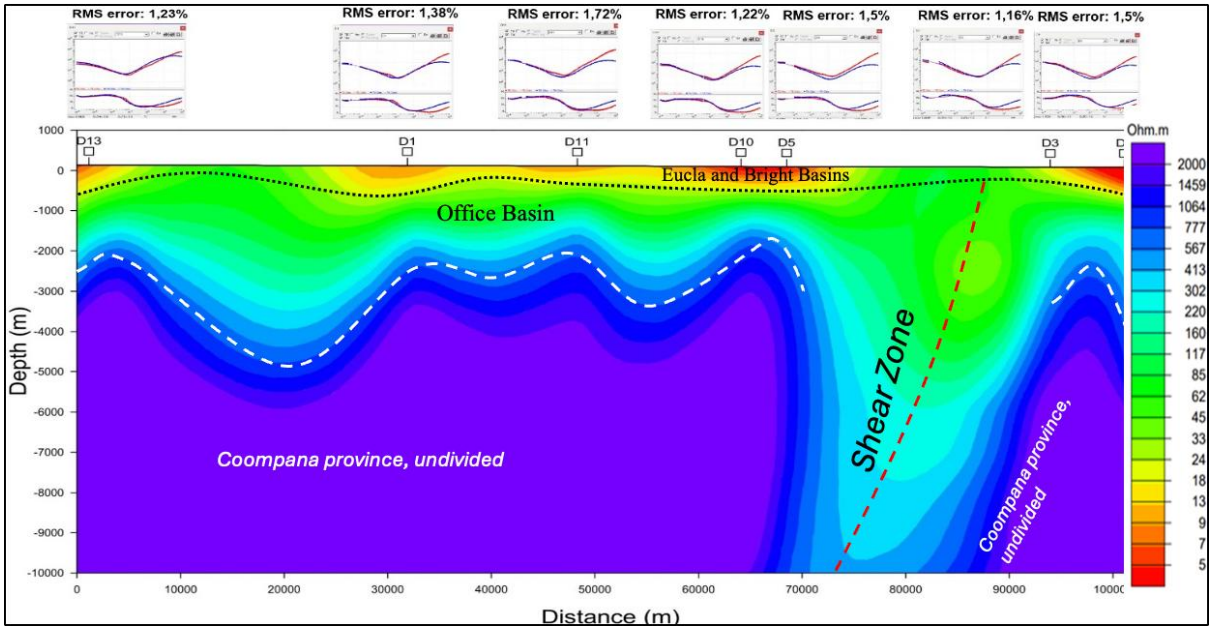

Figure 6. 2D inversion line 1 at Nullarbor.

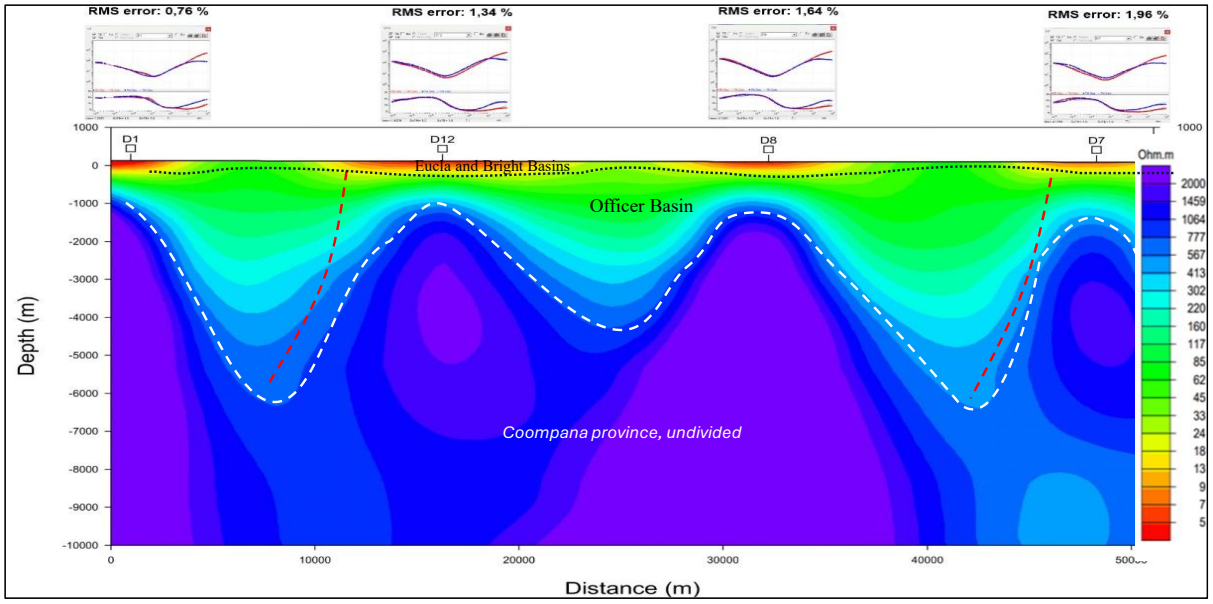

Figure 7. 2D inversion line 2 at Nullarbor.

The 2D resistivity model in line 2 also shows the low to intermediate resistivity uptown 6000 m and bedrock (basement) is identified as intrusive rock, granite, at >1000 m. In line 2, geological structures in the form of suspected shear zone with a maximum depth of 6000 m. The Eucla and Bright Basins consisting of sediment and Vulcanic rocks including Tun formation (Czi) are identified at varying depths ranging from surface to several hundred meters. Sedimentary rock, Claystone, are identified to be at varying depths ranging from 500 m to approximately 6000 m.

Bedrock (basement) is identified as intrusive rock, which is granite is at varying depths with a maximum depth range of > 1000 m. In addition, a line 3 (not include in this research) has similar lithology (shown in crossline, Figure 8).

Figure 8 is a visualization of crossline modeling for all lines, where crosslines are created with the aim of seeing the continuity of resistivity in each subsurface model for each line.

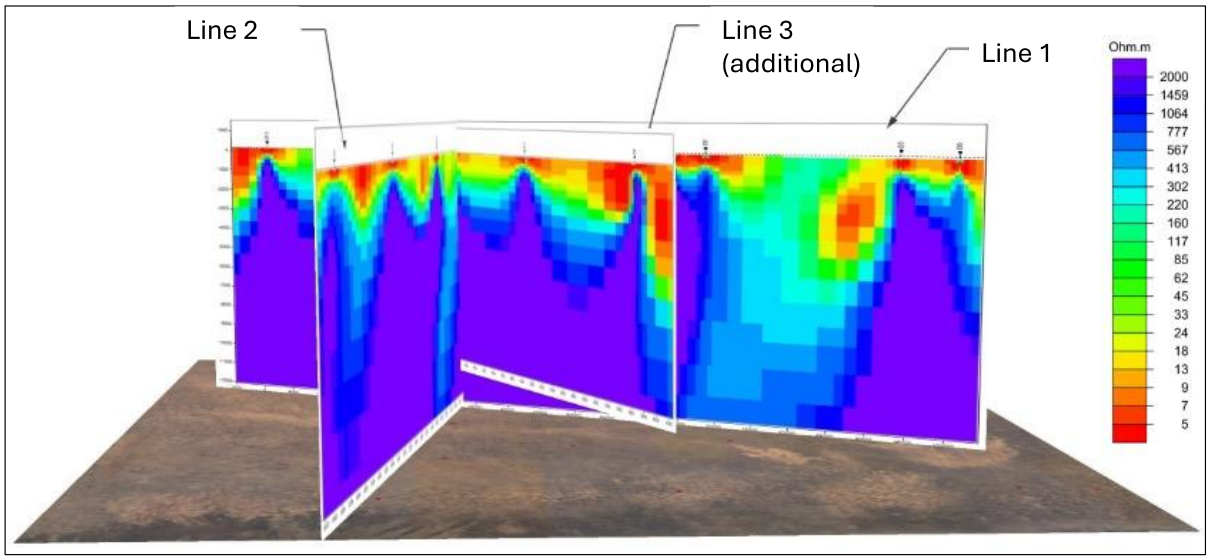

Figure 8. Crossline visualization of all lines.

In the first layer, the most conductive layer is interpreted as limestone, the second layer as claystone, and the basement is the most resistive layer interpreted as granite. Based on the correlation between previous research and the crossline line model, a geological structure in the form of a shear zone with a maximum depth of up to 6 km was identified. The existence of this SZ is believed to be the cause of the earthquake and has the potential to form other structural geological features. Based on the correlation between the geologic map and the crossline model of the line, one main structure of Miocene to Pliocene age in the Quaternary period was identified (Yang et al., 2022). The crossline in Figure shows the continuation of the geological structure at the intersection at point D1 and reflects the consistency of the rock layers and the continuity of the lithologic types of all the passes.

The existence of this geological structure is confirmed based on previous research by Yang et al. (2022) who interpreted that there are geological structures in Nullarbor. According to Yang et al. (2022) there are geological structures in the form of thrust faults and folds that have poor resolution because the MT method has a low resolution of 10^{-5} to 10^{4}. Earthquakes that occur repeatedly on the same surface on a fault can extend the fault through lateral propagation and accumulate displacements that can be measured through fault or fold analysis. In Australia, about 2900 individual surface traces combine into about 350 tectonic surface features (faults and folds) mostly caused by thrust fault displacement (Sellmann et al., 2022).

Conclusion

Based on the results of this study, it can be concluded that the phase tensor analysis states that the dimensional structure in the study area has 1D characteristics at shallow depth, 2D at medium depth, and 2D at deep depth. In the study area, 2D data is dominant at intermediate depths with the N5^{o}E displayed in geoelectric direction.

This geoelectric direction is used to rotate the MT data and minimize errors in 2D inversion modeling. The MT data shows rock layers consisting of the Eucla Basin, which is composed of sedimentary and volcanic rocks, has a resistivity value below 10 Ωm. In contrast, the Officer Basin, which contains sedimentary rock, exhibits higher resistivity values ranging from 10 to approximately 300 Ωm. Additionally, a highly resistive layer with values between 300 and 2000 Ωm is believed to represent the upper crust in the central Coompana Province, particularly along a corridor rich in granite. The 2D inversion cross section shows a resistivity contrast that is identified as a geological structure in form of shear zone with a depth until 6000 m depth, confirming the presence of significant geological structures. The study demonstrates the efficacy of combining phase tensor analysis and 2D MT inversion for delineating subsurface lithology and structure in the region.

Acknowledgements

Thanks to Geoscience Australia data for the open access data, so the authors can use it in this research. We also express our gratitude to who contributed to this research.

Author Contribution

Sarah Manurung conceptualized the research, data processing and analysis, and write the manuscript and. Andri Yadi Paembonan supervised the research, provided critical guidance throughout the research process, and contributed to the interpretation of the results. Selvi Misnia Irawati provided expertise in data analysis, contributed to data interpretation, and provided valuable insights during manuscript preparation. All authors contributed to the writing and revision of the manuscript.

Conflict of Interest

The authors declare no conflict of interest.

References

Akbar, S., Setyawan, A., Yulianto, T., Baroek, M. C., & Ramadhan, I. (2020). Analisis Dimensionalitas Data Magnetotellurik Lapangan Panas Bumi "SA" Berdasarkan Metode Tensor Fase. *Berkala Fisika*, 23(2), 49–55. https://ejournal.undip.ac.id/index.php/berkala_fisika/article/view/30623

Arisbaya, I., Wijanarko, E., Warsa, W., Sumintadireja, P., Sudrajat, Y., Handayani, L., Mukti, M. M., & Grandis, H. (2023). Magnetotellurics (MT) and gravity study of a possible active fault in southern Garut, West Java, Indonesia. *International Journal of Geophysics*, 4482074. https://doi.org/10.1155/2023/4482074

Barajas-Olalde, C., Adams, D. C., Curcio, A., Davydycheva, S., Klapperich, R. J., Martinez, Y., Paembonan, A. Y., Peck, W. D., Strack, K., & Soupios, P. (2023). Application of electromagnetic methods for reservoir monitoring with emphasis on carbon capture, utilization, and storage. *Minerals*, 13(10), 1308; https://doi.org/10.3390/min13101308

Bravo-Osuna, A. G., Gómez-Treviño, E., Cortés-Arroyo, O. J., Delgadillo-Jauregui, N. F., & Arellano-Castro, R. F. (2021). Reframing the magnetotelluric phase tensor for monitoring applications: improved accuracy and precision in strike determinations. *Earth Planets Space*, 73, 34. https://doi.org/10.1186/s40623-021-01354-y

Chang, P.-Y., Amania, H. H., Fikri, A., Puntu, J. M., Lin, D.-J., Kuo, C.-H., Wang, C.-Y., & Chang, W.-Y.

(2023). Probing shallow subsurface structures in the arc-continent collision suture zone near Hualien in Eastern Taiwan with magnetotelluric methods. *Geoscience Letters*, 10(1). 29. https://doi.org/10.1186/s40562-023-00283-w

Cowley, W. (2020). *Geological Map South Australia.* Department for Energy and Mining.

Geological Survey of Western Australia. (2017). *Geological interpretation of the Madura and Coompana Provinces along the Eucla-Gawler seismic and magnetotelluric line 13GA-EG1*. Geological Survey of Western Australia.

Guo, R., Li, M., Yang, F., Xu, S., & Abubakar, A. (2020). Application of supervised descent method for 2D magnetotelluric data inversion. *Geophysics*, 85(4), WA53–WA65. https://doi.org/10.1190/geo2019-0409.1

Heath, P., Gouthas, G., Irvine, J., Krapf, C., & Dutch, R. (2018). Microgravity surveys on the Nullarbor. *ASEG Extended Abstracts*, 2018(1), 1–7. https://doi.org/10.1071/ASEG2018abM3_2H

Heath, P. (2017). Quantifying the differences between gravity reduction techniques. *Exploration Geophysics*, 49(5), 735–743. https://doi.org/10.1071/eg17094

Hou, B., Keeling, J., Reid, A., Petts, A., & Stoian, L. (2022). *Eucla Basin and peripheral paleovalleys, Report Book 2022/00011*. Adelaide: Department for Energy and Mining, South Australia

Hu, P., Heslop, D., Rossel, R. A. V., Roberts, A. P., & Zhao, X. (2019). Continental-scale magnetic properties of surficial Australian soils. *Earth-Science Reviews*, 203, 103028. https://doi.org/10.1016/j.earscirev.2019.103028

Irawati, S. M., Paembonan, A. Y., & Fernanda, L. (2024). Aplikasi Tensor Fase Data Magnetotellurik untuk Pemodelan Panas Bumi The Geysers, California dan Dikorelasikan dengan Data Gaya Berat. *Jurnal Geosains Dan Teknologi*, 6(3), 186–202. https://doi.org/10.14710/jgt.6.3.2023.186-202

Jiang, W., McAlpine, S., Duan, J., Dutch, R., & Pawley, M. (2017). *Cover Thickness Estimates in the Coompana Province, South Australia.* Canberra: Commonwealth of Australia (Geoscience Australia)

Kirkby, A. L., Zhang, F., Peacock, J., Hassan, R., & Duan, J. (2019). The MTPy software package for magnetotelluric data analysis and visualisation. *The Journal of Open-Source Software*, 4(37), 1358. https://doi.org/10.21105/joss.01358

Lin, W., Yang, B., Han, B., & Hu, X. (2023). A Review of Subsurface Electrical Conductivity Anomalies in Magnetotelluric Imaging. *Sensors*, 23(4), 1803. https://doi.org/10.3390/s23041803

Marwan, M., Yanis, M., Zahratunnisa, Z., Idroes, R., Nugraha, G. S., Dharma, D. B., Susilo, A., Saputra, D., Suriadi, S., & Paembonan, A. Y. (2022). Geothermal reservoir depth of Seulawah Agam Volcano estimated from 1D Magnetotelluric. *Journal of Applied Engineering Science*, 20(3), 754–764. http://dx.doi.org/10.5937/jaes0-36077

Maswah, F., Suryantini, S., Srigutomo, W., Fajri, R. J., Pratama, A. B., & Pratomo, P. M. (2021). Magnetotelluric data analysis using phase tensor and tipper strike to determine geoelectrical strike in "DKH" geothermal field. *IOP Conference Series Earth and Environmental Science*, 732(1),

012014. https://doi.org/10.1088/1755-1315/732/1/012014

Pawley, M. J., Dutch, R. A., & Wise, T. W. (2020). The relationship between crustal architecture, deformation, and magmatism in the Coompana Province, Australia. *Tectonics*, 39(12), e2019TC005593. https://doi.org/10.1029/2019TC005593

Pertiwi, T. B., Daud, Y., & Fahmi, F. (2023). Investigation of geological structure using magnetotelluric and gravity data optimization on non-volcanic geothermal, Bora, Centre of Sulawesi. *Journal of Geoscience, Engineering, Environment, and Technology*, 8(2), 103–111. https://doi.org/10.25299/jgeet.2023.8.02-2.13876

Scheib, A., Morris, P., Murdie, R., & Piane, C. D. (2016). A passive seismic approach to estimating the thickness of sedimentary cover on the Nullarbor Plain. *Western Australia. Australian Journal of Earth Sciences*, 63(5), 583–598. https://doi.org/10.1080/08120099.2016.1233455

Sellmann, S., Quigley, M., Duffy, B., Yang, H., & Clark, D. (2022). Fault geometry and slip rates from the Nullarbor and Roe Plains of south-central Australia: Insights into the spatial and temporal characteristics of intraplate seismicity. *Earth Surface Processes and Landforms*, 48(2), 350–370. https://doi.org/10.1002/esp.5490

Webb, J. A., & James, J. M. (2006). *Karst evolution of the Nullarbor Plain, Australia.* Geological Society of America. https://doi.org/10.1130/2006.2404(07)

Yang, H., Sellmann, S., & Quigley, M. (2022). Fluid-Enhanced Neotectonic Faulting in the Cratonic Lithosphere of the Nullarbor Plain in South-Central Australia. *Geophysical Research Letters*, 49(4), e2022GL099155. https://doi.org/10.1029/2022GL099155

ISSN: 2579-5821 (Print)
ISSN: 2579-5546 (Online)
URL address: http://journal.unhas.ac.id/index.php/geocelebes
DOI: 10.70561/geocelebes.v9i2.42903

Jurnal Geocelebes Vol. 9 No. 2, October 2025, 113 – 125

Analysis of Pollutant Distribution Due to Forest Fires in Ketapang Regency in 2015 Using The WRF-Chem Model

Elyda Yani[1], Andi Ihwan[1]*, Randy Ardianto[2], Riza Adriat[1], Muhammad Ishak Jumarang[1]

[1]Department of Physics, Faculty of Mathematics and Natural Sciences, Tanjungpura University, Jl. Prof. H Hadari Nawawi, Pontianak 78124, West Kalimantan, Indonesia.
[2]Pontianak Maritime Meteorological Station, Dwikora Port Complex, Pontianak Sea Port Road, Pontianak 78112, West Kalimantan, Indonesia.

*Corresponding author. Email: andihwan@physics.untan.ac.id

Manuscript received: 14 January 2025; Received in revised form: 28 May 2025; Accepted: 2 June 2025

Abstract

A forest fire occurred on September 9, 2015, resulting in 616 hotspots distributed across several regencies in West Kalimantan, 442 of which were in Ketapang Regency. This study aims to analyze the spatial and temporal distribution of pollutants caused by forest fires in Ketapang Regency in 2015 using the Weather Research and Forecasting with Chemistry (WRF-Chem) model. The data used to run the model includes the Final Global Data Assimilation System (FNL) dataset, the Emission Database for Global Atmospheric Research (EDGAR), and The Fire Inventory from NCAR (FINN), which serve as input and emission source data. The highest concentrations of pollutants, which are $PM_{2.5}$ and PM_{10} at 30 μg/m³ each and CO at 342.9 μg/m³, were observed in the southern part of Kalimantan, which is the main source of the forest fires. These pollutants subsequently dispersed toward the northern part of Kalimantan. During the fire events, pollutants were transported to the upper atmosphere from morning to noon but accumulated near the surface at night. This pattern was influenced by meteorological conditions, including wind speed and direction, surface pressure, and air temperature. During forest fires, pollutants are emitted into the atmosphere from morning to afternoon, and accumulate near the surface during the night. This pattern was influenced by meteorological factors, including wind speed and direction, surface pressure, and air temperature.

Keywords: CO; forest fire; $PM_{2.5}$; PM_{10}; WRF-Chem.

Citation: Yani, E., Ihwan, A., Ardianto, R., Adriat, R., & Jumarang, M. I. (2025). Analysis of Pollutant Distribution Due to Forest Fires in Ketapang Regency in 2015 Using The WRF-Chem Model. *Jurnal Geocelebes*, 9(2):113–125, doi: 10.70561/geocelebes.v9i2.42903

Introduction

Indonesia has experienced significant deforestation due to forest fires, with forest loss reaching 1.1 million hectares annually (2% of the total area), out of a total forested area of 130 million hectares (Darmawan, 2020). One of the major consequences of forest fires in Indonesia is air pollution. Air pollution predominantly arises from human activities, including transportation, forest fires, industrial processes, waste decomposition and burning, as well as other household activities (Manisalidis et al., 2020; Siddiqua et al., 2022). Substances contributing to air pollution include carbon monoxide (CO) and particulate matter (PM) (Siegmund et al., 2024; Tang et al., 2022). PM refers to a type of air pollutant composed of a mixture of various elements such as sulfates, ammonia, organic matter, nitrates, sea salt, dust, water, and other compounds (Dahari et al., 2021).

The 2015 forest fires were the largest in the past 20 years in Sumatra and Kalimantan. That year witnessed a significant increase in hotspots compared to the previous year, resulting in widespread haze (Nurhayati et al., 2021, Yin et al., 2020; Ihwan et al., 2024). These fires burned approximately 2.6 million hectares of land and garnered

international attention due to severe smoke impacts, which disrupted public health and daily activities. According to Terra Aqua satellite imagery, around 70,000 hotspots were recorded in 2015. Ketapang District, located in the southern part of West Kalimantan Province, was among the areas most affected by the fires that year (Miettinen et al., 2017). Forest and land fires in Ketapang Regency in 2013, 2015, and 2017 affected an area of 368.28 hectares, with 141 hotspots predominantly located in mixed dryland agriculture, swamp scrub, and scrubland areas (Jusman et al., 2023; Yananto et al., 2017). Based on MODIS satellite monitoring by BMKG (Indonesian Agency for Meteorological, Climatological and Geophysics), on Wednesday, September 9, 2015, at 05:00 WIB (West Indonesia Time), 616 hotspots were recorded across several districts in West Kalimantan. Ketapang Regency recorded the highest number, with 442 hotspots—a sharp increase from 73 hotspots reported in the previous update at 16:00 WIB on September 8, 2015.

One approach to predicting and analyzing pollution emissions during forest fires is the use of the Weather Research and Forecasting with Chemistry (WRF-Chem) model. WRF-Chem is a weather research and forecasting model integrated with chemical processes. Developed by NOAA/ESRL and DOE/PNNL, this model is designed to assess air quality at relatively small scales. WRF-Chem provides detailed descriptions of the emission, mixing, transport, and chemical transformation of gases and aerosols influenced by meteorological factors (NOAA, 2022). It is also capable of analyzing the distribution of air pollutants such as carbon monoxide and particulate matter (Tampubolon & Boedisantoso, 2016). Several previous studies have employed the WRF-Chem model, including those by (Darmanto & Sofyan, 2012; Sicard et al., 2021; Ghude et al., 2020).

The phenomenon of pollutant distribution caused by forest fires in West Kalimantan in 2015 presents an interesting subject for study. Due to the scarcity of air quality data in Indonesia and limitations in direct observation. To address this gap, we employ the Weather Research and Forecasting model coupled with Chemistry (WRF-Chem) to simulate the emission, transport, and deposition of CO, PM_{10} , and $PM_{2.5}$ during the peak fire period in September 2015. The WRF-Chem model is well-suited for such applications as it integrates meteorological and chemical processes in a fully coupled framework, allowing for the dynamic interaction between atmospheric conditions and chemical constituents (Grell et al., 2005; Spiridonov et al., 2019; Georgiou et al., 2022; Agarwal et al., 2024). This study provides a high-resolution analysis of CO, PM_{10}, and $PM_{2.5}$ distributions during the 2015 Ketapang fires, emphasizing of pollutant dispersion and accumulation processes. By focusing on regional-scale impacts and transboundary transport, which are crucial for air quality management during future forest fire crises.

Materials and Methods

Conducting Data Collection

Data collection was carried out in 2015. The required data includes the Final Global Data Assimilation System (FNL) data for the period from September 7, 2015 at 00:00 UTC to September 11, 2015 at 00:00 UTC, with a spatial resolution of 0.25° x 0.25°, which can be downloaded from https://rda.ucar.edu/datasets/ds083.3/dataaccess/. Additionally, global air emission concentration data from the Emission Database for Global Atmospheric Research (EDGAR) for 2015, with a resolution of 0.1° x 0.1°, can be obtained from https://edgar.jrc.ec.europa.eu/emissions_data_and_maps. The Fire Inventory from NCAR (FINN) version 2 provides annual global daily emission estimates for major gases and aerosols, with a spatial resolution

of 0.1° x 0.1°, available for download at https://rda.ucar.edu/datasets/ds312.9/dataaccess/.

Running the WRF-Chem Model

1. Pre-processing
The simulation focused on the western region of Kalimantan (Figure 1). The simulation period was set based on the peak of forest fire events occurring from 8 to 10 September 2015.

Meteorological data were obtained from FNL provided by NCEP and processed using the WRF Preprocessing System (WPS) through three stages: geogrid, ungrib, and metgrid, to generate meteorological input data consistent with the simulation domain.
The emission data used included anthropogenic emissions of CO, PM_{10}, and $PM_{2.5}$ from EDGAR, as well as biomass burning emissions from FINN (Callewaert et al., 2023). These datasets were first converted to NetCDF format and adjusted both vertically (injection height) and spatially. Subsequently, both datasets were integrated into the WRF-Chem simulation domain.

2. Processing
The WRF-Chem simulation was conducted using the following physical parameterization schemes: microphysics using WRF Single-Moment 3, and cumulus parameterization using the Grell-Dévényi ensemble (Grell & Dévényi, 2002). The chemical schemes included MOZCART for gas-phase chemistry and GOCART for aerosols.

3. Post-processing
The model output is visualized using the NCAR Command Language (NCL) software.

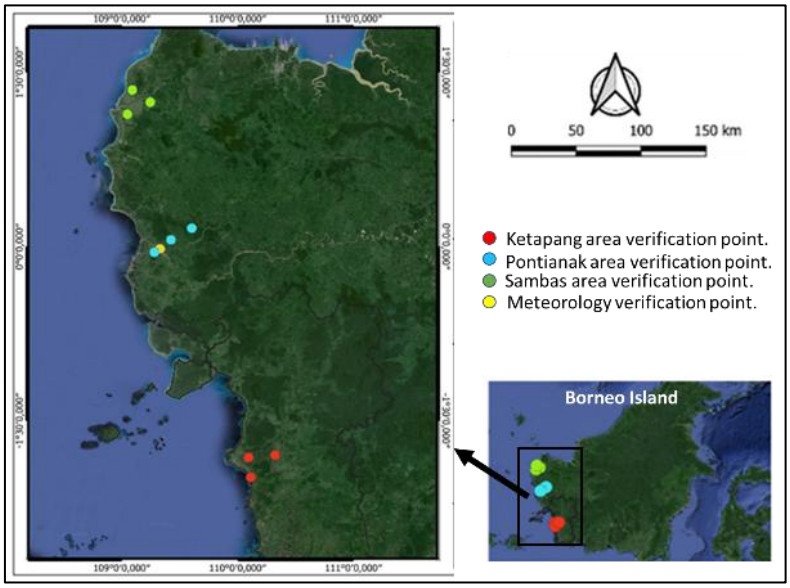

Figure 1. Research location.

Data Analysis

At this stage, various parameters, including wind speed and direction, $PM_{2.5}$, PM_{10}, and CO, are analyzed to understand how weather parameters influenced the spatial and temporal distribution of pollutants during the forest and land fires in Ketapang Regency in 2015.

The sampling method in this study involved selecting three representative regions: Ketapang, Pontianak, and Sambas for the WRF-Chem model simulation results. In each region, three observation points were evenly distributed to collect data on air pollution distribution. The average value from the three observation points was used to represent the air quality data for each

respective region (Figure 1). These results were used to examine the temporal dynamics during the simulation period.

The average concentrations of CO, PM_{10}, and $PM_{2.5}$ were then compared to the classification of the Air Pollutant Standard Index (ISPU) as stated in the Regulation of the Minister of Environment and Forestry of the Republic of Indonesia Number P.14/MENLHK/SETJEN/KUM.1/7/2020 (Table 1).

Table 1. The classification of the Air Pollutant Standard Index (Minister of Environment and Forestry of the Republic of Indonesia, 2020).

ISPU Category	$PM_{2.5}$ concentration ($\mu g/m^3$)	PM_{10} concentration ($\mu g/m^3$)	CO concentration ($\mu g/m^3$)
Good	15.5	50	4000
Moderate	55.4	150	8000
Unhealthy	150.4	350	15000
Very unhealthy	250.4	420	30000
Dangerous	500	500	45000

Results and Discussion

Wind Speed and Direction

The WRF-Chem model output illustrates wind direction conditions from September 8 to September 10, 2015, predominantly blowing from the southeast toward the north. Figure 2 shows wind speed in the West Kalimantan region, with the highest speeds occurring between 07:00 WIB and 13:00 WIB, ranging from 5 m/s to 10 m/s. The increase in particulate matter was closely linked to meteorological factors, including the dispersion and diffusion of pollutants caused by changes in meteorological conditions (Yang et al., 2020a). Wind plays a key role in spreading pollutants out of areas with high concentrations and reducing pollutant levels in other regions (Yang et al., 2020b).

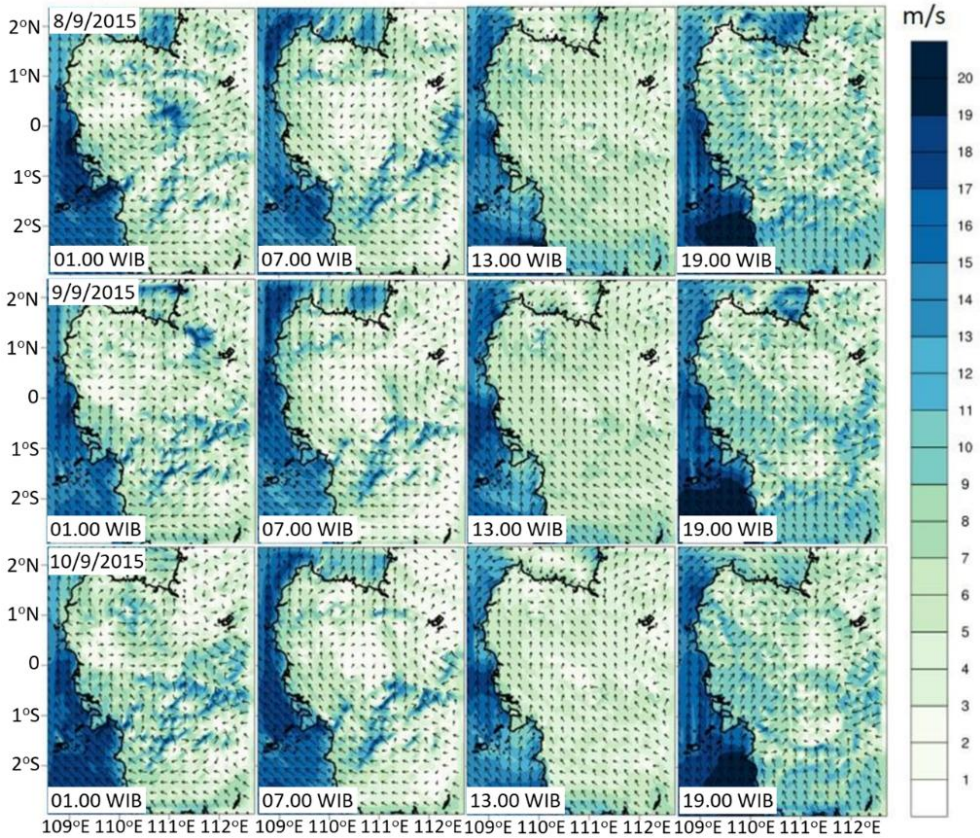

Figure 2. Map of Wind speed and direction in West Kalimantan on 08-10 September 2015.

Figure 3 shows the wind direction and speed at coordinates 0.02º S – 109.33º E from September 7, 2015, to September 11, 2015. The dominant wind direction from the model output (Figure 3a) is from the south-southeast toward the north, consistent with the wind direction from the observation data (Figure 3b), which predominantly moves northward. This indicates that during the forest fire event, the air mass carrying pollutants was transported toward the northern region.

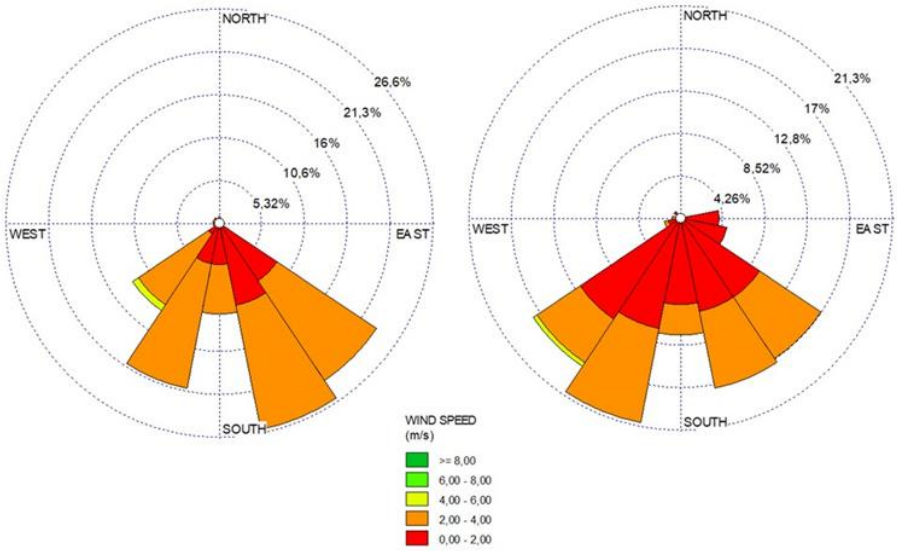

Figure 3. Wind speed and direction at coordinates 0.02º S – 109.33º E (a) wind-rose from model output (b) wind-rose from observation data.

Particulate Matter ($PM_{2.5}$)

The model output shows the distribution of $PM_{2.5}$ pollutants in West Kalimantan, with Ketapang Regency having the highest number of hotspots. $PM_{2.5}$ spread northward, following the southeast wind direction. Figure 4 shows $PM_{2.5}$ concentrations from September 8 to September 10, 2015. In the southern part of West Kalimantan, particularly Ketapang Regency, $PM_{2.5}$ concentrations increased due to forest fires.

$PM_{2.5}$ concentrations ranged from 10 µg/m³ to 15 µg/m³ between 19:00 WIB and 01:00 WIB. At 07:00 WIB, $PM_{2.5}$ concentrations began to disperse, following the wind toward Pontianak City and Sambas Regency. By 13:00 WIB, pollutants spread rapidly toward the northern border of neighboring countries. Figure 10 shows that from 01:00 WIB on September 8 to 23:00 WIB on September 10, 2015, Ketapang Regency, Pontianak City, and Sambas Regency were key sampling points for $PM_{2.5}$ concentrations. The highest concentrations, recorded at 19:00 WIB, ranged from 10 µg/m³ to 12 µg/m³. $PM_{2.5}$ concentrations consistently decreased between 07:00 WIB and 16:00 WIB, with values ranging from 1 µg/m³ to 2 µg/m³.

The meteorological pattern for $PM_{2.5}$ is similar to that for CO and PM_{10}. Wind from the southeast caused pollutants to spread northward. Strong winds facilitated wider dispersion, while weak winds led to localized buildup. Low-pressure systems, occurring between 12:00 WIB and 16:00 WIB, helped reduce $PM_{2.5}$ concentrations near the surface by promoting air mixing and rising. In contrast, low temperatures between 19:00 WIB and 07:00 WIB trapped $PM_{2.5}$ near the surface, resulting in higher concentrations.

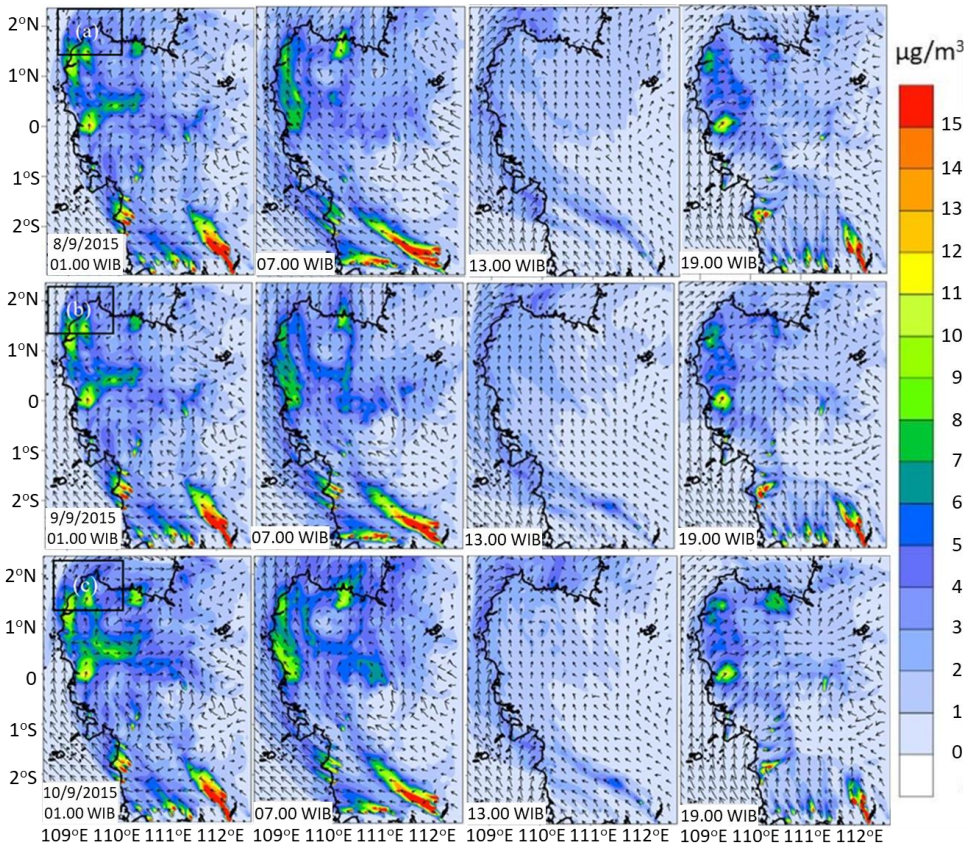

Figure 4. Map of $PM_{2.5}$ distribution in West Kalimantan on 08-10 September 2015.

Figure 5 illustrates a graph showing $PM_{2.5}$ concentrations recorded between September 8, 2015, at 01:00 WIB, and September 10, 2015, at 23:00 WIB in Ketapang Regency, Pontianak City, and Sambas Regency. Ketapang Regency is recognized as the main source of $PM_{2.5}$ emissions. Figure 5 indicates that $PM_{2.5}$ levels in these three regions reached their highest point at 19:00 WIB, with concentrations between 10 µg/m³ and 12 µg/m³. In contrast, concentrations dropped during the period from 07:00 WIB to 16:00 WIB, ranging from 1 µg/m³ to 2 µg/m³. This decline in $PM_{2.5}$ concentration during the morning and midday hours is linked to meteorological conditions, including increased wind speed and rising temperatures due to solar radiation.

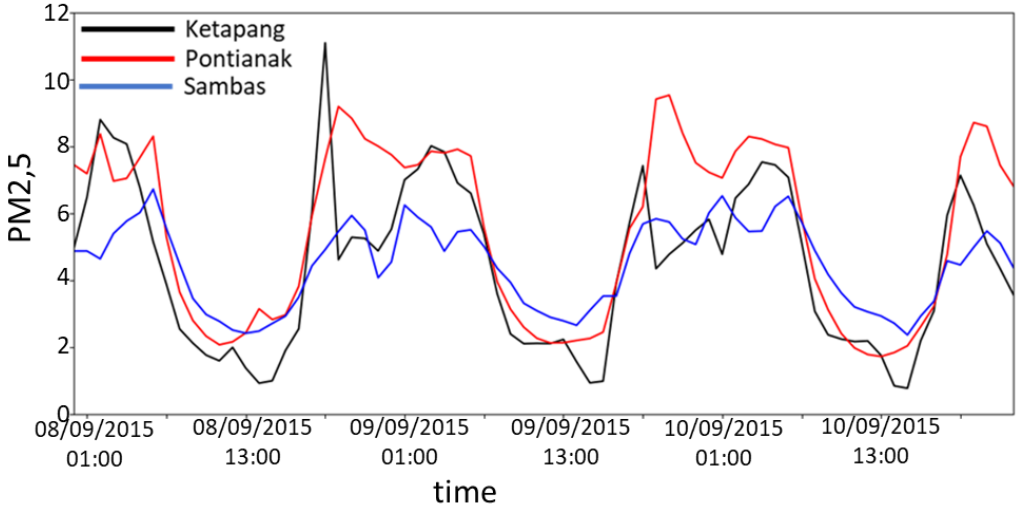

Figure 5. Time series graph of $PM_{2.5}$ per 3 hours in Ketapang Regency, Pontianak City, and Sambas Regency from September 8, 2015 at 01.00 WIB to September 10, 2015 at 23.00 WIB.

Particulate Matter (PM_{10})

The model output shows the distribution of PM_{10} pollutants in West Kalimantan, with the largest number of hotspots located in Ketapang Regency. PM_{10} spread northward, following the wind direction from the southeast. Figure 6 shows that the highest PM_{10} concentrations ranged from 10 µg/m³ to 15 µg/m³, indicating significant air pollution caused by forest fires between September 8 and September 10, 2015. Over the three-day period, a consistent pattern emerged, where PM_{10} concentrations were highest between 19:00 WIB and 01:00 WIB. At 07:00 WIB, PM_{10} concentrations began to disperse as pollutants were carried away by wind toward northern areas, such as Sambas Regency and the neighboring country border. By 13:00 WIB, pollutants spread significantly, reducing concentrations at the source due to rising air temperatures. High temperatures made PM_{10} particles less dense, facilitating their dispersion and lowering pollutant concentrations.

Figure 7. presents a graph illustrating PM_{10} concentrations from September 8, 2015, at 01:00 WIB to September 10, 2015, at 23:00 WIB in Ketapang Regency, Pontianak City, and Sambas Regency. PM_{10} concentrations in these three areas varied over time. The levels peaked at 19:00 WIB, reaching a maximum of 14 µg/m³. Conversely, they decreased between 07:00 WIB and 16:00 WIB, ranging from 1 µg/m³ to 3 µg/m³.

The findings indicate that pollutant concentrations in Pontianak are higher than those in Ketapang and Sambas (Figure 7). The elevated levels of pollutants in Pontianak are attributed to a combination of emission sources, including anthropogenic activities such as transportation and industry (characteristic of a developing urban area) and transboundary pollution originating from forest and land fires in the Ketapang region.

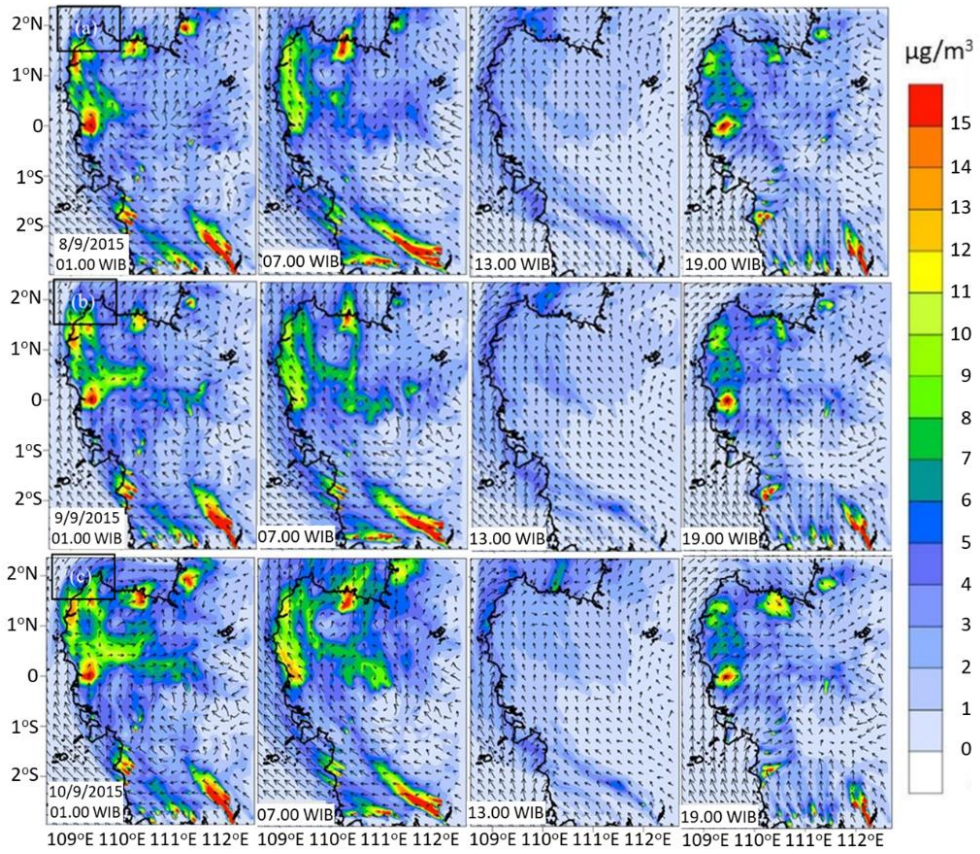

Figure 6. Map of PM_{10} distribution in West Kalimantan on 08-10 September 2015.

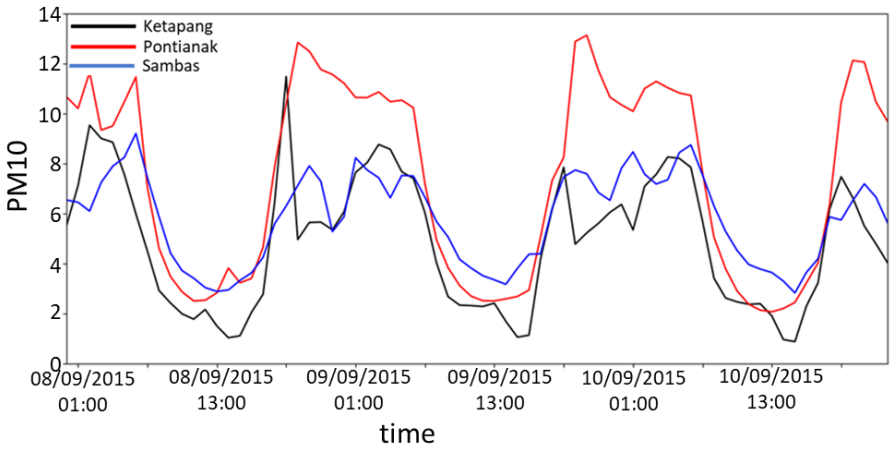

Figure 7. Time series graph of PM_{10} per 3 hours in Ketapang Regency, Pontianak City, and Sambas Regency from September 8, 2015 at 01.00 WIB to September 10, 2015 at 23.00 WIB.

Carbon Monoxide (CO)

Carbon monoxide (CO), a common emission from forest fires, contributes to climate change by affecting the concentration of greenhouse gases in the atmosphere, making it a serious environmental issue (Volkova et al., 2019; Touma et al., 2021). The WRF-Chem model output illustrates the spatial distribution of CO pollutants in the West Kalimantan region from September 8 to September 10, 2015, between 01:00 WIB and 23:00 WIB (Figure 8). In Ketapang, the distribution of hotspots was relatively high compared to other regions in West Kalimantan Province, resulting in high CO concentrations from 19:00 WIB to 01:00 WIB. This occurred because pollutants accumulated near the fire source at night when air temperatures were relatively low, and wind speeds were calmer. At 07:00 WIB, CO concentrations began to disperse as pollutants were carried away by wind toward northern areas, such as Pontianak City and Sambas Regency. By 13:00 WIB, CO concentrations decreased rapidly as high air temperatures caused pollutants to become dry and light, allowing them to spread easily with moving air masses toward the borders of neighboring countries.

In this study, wind speed and direction played a crucial role in pollutant dispersion. Wind from the southeast caused pollutants originating from Ketapang Regency to spread northward across Kalimantan. Strong winds facilitated wider dispersion of CO, whereas weak winds led to localized concentration buildup. Surface pressure influenced pollutant concentrations at the emission source, with low-pressure systems occurring between 12:00 WIB and 16:00 WIB, associated with rising and mixing air, which helped reduce CO concentrations near the surface. Meanwhile, low temperatures between 19:00 WIB and 07:00 WIB trapped CO near the surface, resulting in higher concentrations.

The results indicate that between 01:00 WIB on September 8, 2015, and 19:00 WIB on September 10, 2015, Ketapang Regency, Pontianak City, and Sambas Regency were the areas with the highest CO concentrations. Ketapang Regency, being the primary source of the pollutant, recorded the highest CO concentration of 205.7 $\mu g/m^3$ at 19:00 WIB (Figure 9). CO concentrations consistently decreased between 07:00 WIB and 16:00 WIB, with values ranging from 102.9 $\mu g/m^3$. This decrease occurs because, from morning to midday, rising temperatures and stronger wind speeds facilitate the dispersion of pollutants over a wider area.

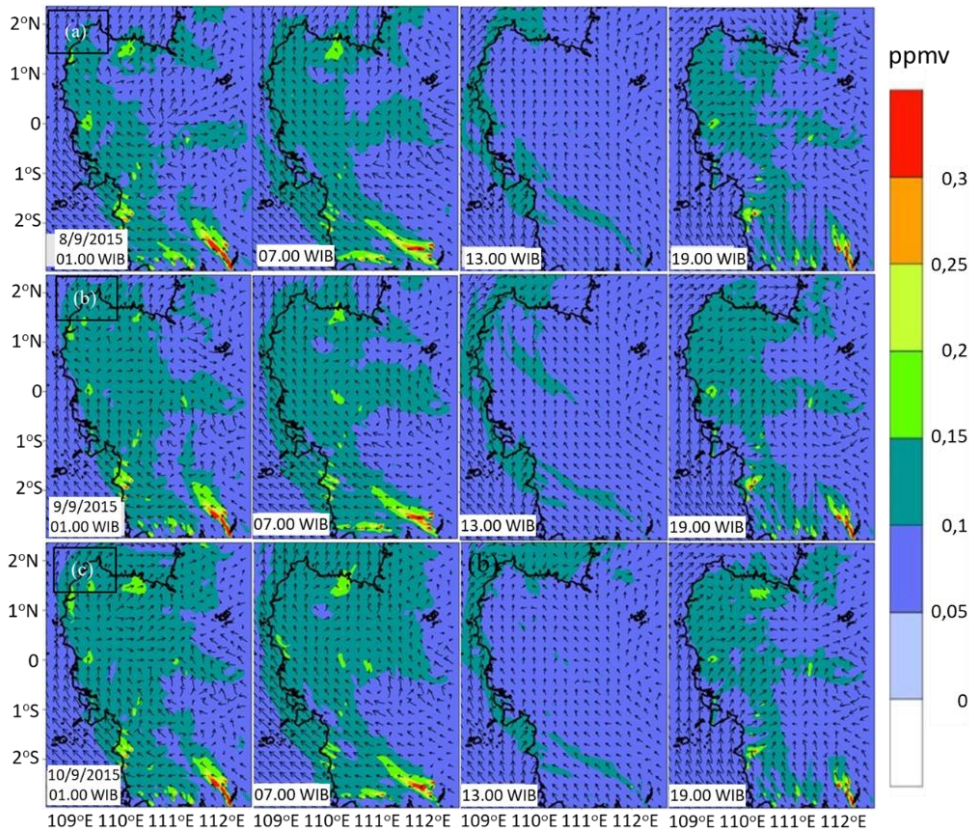

Figure 8. Map of CO distribution in West Kalimantan on 08-10 September 2015.

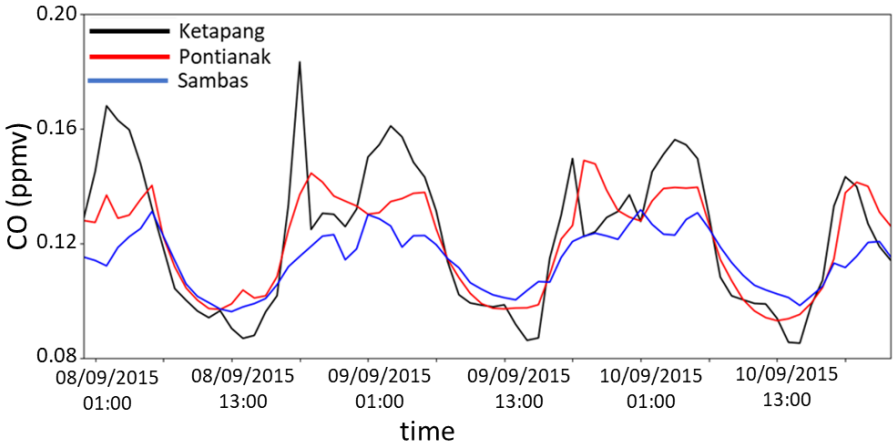

Figure 9. Time series graph of CO per 3 hours in Ketapang Regency, Pontianak City, and Sambas Regency from September 8, 2015 at 01.00 WIB to September 10, 2015 at 23.00 WIB.

Meteorological parameters significantly influence the distribution of pollutants in the atmosphere, including PM_{10}, $PM_{2.5}$, and CO (Zhang et al., 2015; Jin et al., 2021). During forest and land fires, wind direction from the southeast transported pollutants from Ketapang Regency toward the northern part of Kalimantan. Previous research similarly found that wind speed and direction can disperse pollutants over a wider area, whereas weak winds tend to cause localized accumulation of pollutants (Fedoniuk et al., 2020; Yuval et al., 2020).

Surface pressure also affects pollutant concentrations at the emission source. In this study, low-pressure systems observed between 12:00 and 16:00 WIB were associated with rising and mixing air, which helped reduce pollutant concentrations near the surface. Conversely, low air temperatures recorded

between 19:00 and 07:00 WIB trapped pollutants near the surface, resulting in higher concentrations during these hours. Previous research supports these findings, indicating that high pollutant concentrations at night are due to stable atmospheric conditions, low temperatures, and calmer winds (Li et al., 2020).

The WRF-Chem model was able to represent the distribution of pollutants (PM_{10}, $PM_{2.5}$, and CO), which was influenced by meteorological factors, particularly wind direction. The simulation results indicated that wind transported pollutants from the main source in Ketapang Regency toward northern Kalimantan. A limitation of this study is that, although the model effectively represents the spatial distribution of pollutants, the concentrations of the three pollutants remain relatively low and are still classified as "good" according to the Air Pollutant Standard Index (ISPU) (Table 1). This finding contrasts with the results of previous research by Yin et al. (2020), which reported that haze from forest fires in Kalimantan had a significant negative impact on air quality.

The distribution of pollutants during forest fires poses a significant threat to human health, highlighting the need for further investigation to better understand its implications and develop effective mitigation strategies.

Conclusion

The WRF-Chem model accurately simulates meteorological parameters and effectively models the distribution of pollutants during forest fires in Ketapang. The simulation shows that pollutants spread northward to areas such as Pontianak City and Sambas Regency, as well as to neighboring countries, driven by air masses moving from the southeast to the north.

The WRF-Chem model simulation results, the temporal patterns of pollutant concentrations, including CO, PM_{10}, and $PM_{2.5}$, indicate high pollutant concentrations from night to early morning (between 19:00 and 03:00). This is influenced by meteorological factors such as low wind speed, high surface pressure, and low temperature, which inhibit the dispersion of pollutants. In contrast, during the daytime (between 07:00 and 16:00), high wind speed, low surface pressure, and elevated temperatures facilitate the dispersion of pollutants over a wider area, following the wind direction.

Acknowledgements

The authors would like to express their gratitude to the Pontianak Maritime Meteorological Station for its support in providing observational data (wind data), which were used as validation data for the model output in this study.

Author Contribution

AI: Conceptualization, Methodology, Data Interpretation, Writing—Reviewing and Editing, Supervision. EY: Data Collection, Statistical Analysis, Writing—Original Draft Preparation. RA (Randi Ardianto): Methodology, Statistical Analysis, Visualization, Validation. RA (Riza Adriat): Data Interpretation, Validation. MIJ: Methodology, Data Interpretation, Visualization.

Conflict of Interest

The authors declare that they have no conflict of interest regarding the publication of this paper.

References

Agarwal, P., Stevenson, D. S., & Heal, M. R. (2024). Evaluation of WRF-Chem-simulated meteorology and aerosols over northern India during the severe pollution episode of 2016.

Atmospheric Chemistry and Physics, 24(4), 2239–2266. https://doi.org/10.5194/acp-24-2239-2024

Callewaert, S., Zhou, M., Langerock, B., Wang, P., Wang, T., Mahieu, E., & De Mazière, M. (2023). A WRF-Chem study on the variability of CO_2, CH_4 and CO concentrations at Xianghe, China supported by ground-based observations and TROPOMI, *EGUsphere.* https://doi.org/10.5194/egusphere-2023-2103

Darmawan, D. H. A. (2020). Fuelling the fires: practical steps towards wildfires in Indonesia. *IOP Conference Series: Earth and Environmental Science*, 504(1), 012021. https://doi.org/10.1088/1755-315/504/1/012021

Darmanto, N. S., & Sofyan, A. (2012). Analisis distribusi pencemar udara NO2, SO2, CO dan O2 di Jakarta dengan WRF-CHEM. *Jurnal Teknik Lingkungan,* 18(1), 54–64. http://dx.doi.org/10.5614/jtl.2012.18.1.6

Dahari, N., Muda, K., Latif, M. T., & Hussein, N. (2021). Studies of Atmospheric PM2.5 and its Inorganic Water Soluble Ions and Trace Elements around Southeast Asia: a Review. *Asia-Pacific Journal of Atmospheric Sciences*, 57, 361–385. https://doi.org/10.1007/s13143-019-00132-x

EDGAR. (2024). *Emissions Data and Maps*. https://edgar.jrc.ec.europa.eu/emissions_data_and_maps

Fedoniuk, R. H., Fedoniuk, T. P., Zimaroieva, A. A., Pazych, V. M., & Zubova, O. V. (2020). Impact of air born technogenic pollution on agricultural soils depending on prevailing winds in Polissya region (NW Ukraine). *Ecological Questions*, 31(1), 69–85. https://doi.org/10.12775/EQ.2020.007

Georgiou, G. K., Christoudias, T., Proestos, Y., Kushta, J., Pikridas, M., Sciare, J., Savvides, C., & Lelieveld, J. (2022). Evaluation of WRF-Chem model (v3.9.1.1) real-time air quality forecasts over the Eastern Mediterranean. *Geoscientific Model Development*, 15(10), 4129–4146. https://doi.org/10.5194/gmd-15-4129-2022

Ghude, S. D., Kumar, R., Jena, C., Debnath, S., Kulkarni, R. G., Alessandrini, S., Biswas, M., Kulkrani, S., Pithani, P., Kelkar, S., Sajjan, V., Chate, D., Soni, V., Singh, S., Nanjundiah, R. S., & Rajeevan, M. (2020). Evaluation of PM2.5 forecast using chemical data assimilation in the WRF-CHEM model: A novel initiative under the ministry of earth sciences air quality early warning system for Delhi, India. *Current Science*, 118(11), 1803–1815. https://doi.org/10.18520/cs/v118/i11/1803-1815

Grell, G. A., & Dévényi, D. (2002). A generalized approach to parameterizing convection combining ensemble and data assimilation techniques. *Geophysical Research Letters*, 29(14), 1693. http://dx.doi.org/10.1029/2002gl015311

Grell, G. A., Peckham, S. E., Schmitz, R., McKeen, S. A., Frost, G., Skamarock, W. C., & Eder, B. (2005). Fully coupled "online" chemistry within the WRF model. *Atmospheric Environment*, 39(37), 6957–6975. https://doi.org/10.1016/j.atmosenv.2005.04.027

Ihwan, A., Tsabita, T. K., & Adriat, R. (2024). Analisis Kekeringan Meteorologi Di Wilayah Iklim Hutan Hujan Tropis Pada Saat El-Niño Kuat Tahun 2015. *Jurnal Agrotek Tropika*, 12(2), 310–317. http://dx.doi.org/10.23960/jat.v12i2.7514

Jin, X., Cai, X., Yu, M., Wang, X., Song, Y., Kang, L., Zhang, H., & Zhu, T.

(2021). Mesoscale structure of the atmospheric boundary layer and its impact on regional air pollution: A case study. *Atmospheric Environment,* 258, 118511. https://doi.org/10.1016/j.atmosenv.2021.118511

Jusman, R. A., Fikriyah, V. N., Jumadi, J., & Saputra, A. (2023). Analysis of land fire vulnerability using remote sensing in Ketapang Regency, West Kalimantan, Indonesia. *AIP Conference Proceedings*, 2727(1), 050007. https://doi.org/10.1063/5.0141541

Li, B., Shi, X.-F., Liu, Y.-P., Lu, L., Wang, G.-L., Thapa, S., Sun, X.-Z., Fu, D.-L., Wang, K., & Qi, H. (2020). Long-term characteristics of criteria air pollutants in megacities of Harbin-Changchun megalopolis, Northeast China: Spatiotemporal variations, source analysis, and meteorological effects. *Environmental Pollution*, 267, 115441. https://doi.org/10.1016/j.envpol.2020.115441

Manisalidis, I., Stavropoulou, E., Stavropoulos, A., & Bezirtzoglou, E. (2020). Environmental and health impacts of air pollution: a review. *Frontiers in public health*, 8, 14. https://doi.org/10.3389/fpubh.2020.00014

Minister of Environment and Forestry of the Republic of Indonesia. (2020). *Indeks Standar Pencemar Udara (ISPU) sebagai Informasi Mutu Udara Ambien di Indonesia Tahun 2020*. https://ditppu.menlhk.go.id/portal/uploads/news/1600940556_P_14_2020_ISPU_menlhk_07302020074834.pdf

Miettinen, J., Shi, C., & Liew, S. C. (2017). Fire distribution in Peninsular Malaysia, Sumatra and Borneo in 2015 with special emphasis on peatland fires. *Environmental management*, 60, 747–757. https://doi.org/10.1007/s00267-017-0911-7

National Centers for Environmental Prediction/ National Weather Service/ NOAA/ U.S. Department of Commerce. (2015). *NCEP GDAS/FNL 0.25 Degree Global Tropospheric Analyses and Forecast Grids*. https://rda.ucar.edu/datasets/d083003/dataaccess/

NOAA. (2022). *WRF-Chem Version 4.4 User's Guide*. https://etrp.wmo.int/pluginfile.php/87070/mod_resource/content/1/Users_guide.WRF-Chemv4.4.pdf

Nurhayati, A. D., Saharjo, B. H., Sundawati, L., Syartinilia, S., & Cochrane, M. A. (2021). Forest and peatland fire dynamics in South Sumatra Province. *Forest and Society*, 5(2), 591–603. https://doi.org/10.24259/fs.v5i2.14435

Sicard, P., Crippa, P., De Marco, A., Castruccio, S., Giani, P., Cuesta, J., Paoletti, E., Feng, Z., & Anav, A. (2021). High spatial resolution WRF-Chem model over Asia: Physics and chemistry evaluation. *Atmospheric Environment*, 244, 118004. https://doi.org/10.1016/j.atmosenv.2020.118004

Siddiqua, A., Hahladakis, J. N., & Al-Attiya, W. A. K. A. (2022). An overview of the environmental pollution and health effects associated with waste landfilling and open dumping. *Environmental Science and Pollution Research*, 29(39), 58514–58536. https://doi.org/10.1007/s11356-022-21578-z

Siegmund, T., Gollmer, C., Horstmann, N., & Kaltschmitt, M. (2024). Carbon monoxide (CO) and particulate matter (PM) emissions during the combustion of wood pellets in a small-scale combustion unit–Influence of aluminum-(silicate-) based fuel additivation. *Fuel Processing*

Technology, 262, 108111. https://doi.org/10.1016/j.fuproc.2024.108111

Spiridonov, V., Jakimovski, B., Spiridonova, I., & Pereira, G. (2019). Development of air quality forecasting system in Macedonia, based on WRF-Chem model. *Air Quality, Atmosphere & Health*, 12, 825–836. https://doi.org/10.1007/s11869-019-00698-5

Tampubolon, A. P. C., & Boedisantoso, R. (2016). Analisis persebaran polutan karbon monoksida dan partikulat dari kebakaran hutan di Sumatera Selatan. *Jurnal Teknik ITS*, 5(2), C160–C165. http://dx.doi.org/10.12962/j23373539.v5i2.18955

Tang, R., Zhao, J., Liu, Y., Huang, X., Zhang, Y., Zhou, D., Ding, A., Nielsen, C. P., & Wang, H. (2022). Air quality and health co-benefits of China's carbon dioxide emissions peaking before 2030. *Nature communications*, 13(1), 1008. https://doi.org/10.1038/s41467-022-28672-3

Touma, D., Stevenson, S., Lehner, F., & Coats, S. (2021). Human-driven greenhouse gas and aerosol emissions cause distinct regional impacts on extreme fire weather. *Nature communications*, 12(1), 212. https://doi.org/10.1038/s41467-020-20570-w

Volkova, L., Roxburgh, S. H., Surawski, N. C., Meyer, C. P., & Weston, C. J. (2019). Improving reporting of national greenhouse gas emissions from forest fires for emission reduction benefits: an example from Australia. *Environmental Science & Policy*, 94, 49-62. https://doi.org/10.1016/j.envsci.2018.12.023

Wiedinmyer, C., & Emmons, L. (2022). *Fire Inventory from NCAR version 2 Fire Emission*. https://rda.ucar.edu/datasets/d312009/dataaccess/#

Yananto, A., Prayoga, M. B. R., & Harsoyo, B. (2017). Forest and Land Fire Danger Mapping Based on Land Physical Parameters in Sumatera and Kalimantan Region of Indonesia. *Journal of Applied Geospatial Information*, 1(2), 75–81. https://doi.org/10.30871/jagi.v1i2.521

Yang, T., Wang, Y., Wu, Y., Zhai, J., Cong, L., Yan, G., Zhang, Z., & Li, C. (2020). Effect of the wetland environment on particulate matter and dry deposition. *Environmental technology*, 41(8), 1054–1064. https://doi.org/10.1080/09593330.2018.1520307

Yang, J., Shi, B., Shi, Y., Marvin, S., Zheng, Y., & Xia, G. (2020). Air pollution dispersal in high density urban areas: Research on the triadic relation of wind, air pollution, and urban form. *Sustainable Cities and Society*, 54, 101941. https://doi.org/10.1016/j.scs.2019.101941

Yin, S., Wang, X., Guo, M., Santoso, H., & Guan, H. (2020). The abnormal change of air quality and air pollutants induced by the forest fire in Sumatra and Borneo in 2015. *Atmospheric research,* 243, 105027. https://doi.org/10.1016/j.atmosres.2020.105027

Yuval, Y., Tritscher, T., Raz, R., Levi, Y., Levy, I., & Broday, D. M. (2020). Emissions vs. turbulence and atmospheric stability: A study of their relative importance in determining air pollutant concentrations. *Science of the Total Environment*, 733, 139300. https://doi.org/10.1016/j.scitotenv.2020.139300

Zhang, H., Wang, Y., Hu, J., Ying, Q., & Hu, X.-M. (2015). Relationships between meteorological parameters and criteria air pollutants in three megacities in China. *Environmental research*, 140, 242–254. https://doi.org/10.1016/j.envres.2015.04.004

ISSN: 2579-5821 (Print)
ISSN: 2579-5546 (Online)
URL address: http://journal.unhas.ac.id/index.php/geocelebes
DOI: 10.70561/geocelebes.v9i2.43009

Jurnal Geocelebes Vol. 9 No. 2, October 2025, 126 – 138

Relocation of the Hypocenter of an Earthquake with the Double Difference Method in the Mentawai

Siti Hannifah Maulani[1*], Refrizon[1,2], Rida Samdara[1], Lori Agung Satria[3], Suaidi Ahadi[3]

[1]Department of Physics, Faculty of Mathematics and Natural Sciences, Bengkulu University, 38371 Bengkulu, Indonesia.
[2]Department of Geophysics, Faculty of Mathematics and Natural Sciences, Bengkulu University, 38371 Bengkulu, Indonesia.
[3]Meteorology, Climatology, and Geophysics Agency, Sta. Geophysics Class I Padang Panjang, 27118 Padang Panjang, Indonesia.

*Corresponding author. Email: hannifah66@gmail.com

Manuscript received: 23 January 2025; Received in revised form: 16 May 2025; Accepted: 18 May 2025

Abstract

This research aimed to accurately relocate the hypocenter of earthquakes in the Mentawai region to enhance precision in hypocenter determination. The arrival time data used were secondary data recorded in the seiscomp4 software at BMKG Class I Padang Panjang. The dataset comprised 66,979 arrival time data point form 2,380 earthquakes that occurred between September 2023 and September 2024. The Double-difference method, utilizing the Crust 2.0 velocity models, was employed for the relocation process. This method evaluated two hypocenters using a single recording station, provided that the distance between the hypocenters was less than the distance to the recording station. The HypoDD program was used for data processing. The relocation results indicated that the hypocenter had shifted and exhibited an increasing tendency toward cluster formation. The hypocenter depth was adjusted from an initial average of approximately 41.05 km to 51.05 km. This shift suggested am improvement in the quality of residual distribution. The enhancement of earthquake hypocenter resolution supported disaster mitigation by accelerating early warnings, improving construction safety in earthquake-prone areas, and optimizing emergency response. The relocation results in the Mentawai region identified 89 earthquake hypocenter points out of the 94 points recorded before relocation.

Keywords: double difference; HypoDD; residual histogram.

Citation: Maulani, S. H., Refrizon, R., Samdara, R., Satria, L. A., & Ahadi, S. (2026). Relocation of The Hypocenter of an Earthquake with the Double Difference Method in the Mentawai. Jurnal Geocelebes, 9(2): 126–138, doi: 10.70561/geocelebes.v9i2.43009

Introduction

The Mentawai region is highly seismically active and prone to earthquakes due to the subduction of the Indo-Australian tectonic plate beneath Sumatera. This Subduction progresses at an estimated rate of 45 mm per year, affecting the mentawai Islands. These islands, situated off the west coast of Sumatera, lie at the intersection of the Sumatran Fault and the Sumatran Subduction Zone (Naim, 2018).

The Tuba Ridge (TR) is formed by the convergence of the Mentawai Fault (MF) and the West Andaman Fault (WAF) in the northern Sumatra forearc area. The kinematics of this zone are characterized by backthrust and strike-slip movements (Marzuki et al., 2022). TR is defined as an anticline that induces uplift and progradation, resulting from deformation in the restraining bend. South of Sumatra, the WAF marks the boundary between the arc besin and the primary accretionary complex (Le Béon & Lu, 2023).

The MF serves as the boundary between the acctionary prism and the forearc basin, acting as a backthrust in southern Sumatra.

The extension of this fault into the arc has led to the formation of the MF zone, with recent structural developments concentrated in the eastern region. The extent of the Mentawai Fault in this area remains uncertain. The anticline structure delineates the boundary between two geological zones. An accretionary prism was identified as being indented in the Sunda Strait region and parts of the southern Java Islands (Pusgen, 2017).

An earthquake is a natural disaster that occurs suddenly and rapidly, causing devastation to various entities on Earth, including individuals, property, and artifacts (Wijaya, 2024). An earthquake as a ground perturbation resulting from the rapid release of energy. Which propagates outward form the epicenter in all directions (Kammer et al., 2024). Indonesia, located at the convergence of three tectonic plates, frequently experiences earthquake due to the resultant volcanic and seismic activity, significantly influencing their distribution. The impact of an earthquake, including fatalities, is influenced by social factors such as population density, the timing of the event, and community preparedness. Despite advancements, the ability to accurately forecast earthquake impacts remain limited. Earthquake are classified into three categories based on hypocenter depth. Shallow earthquakes occur at depths of less than 60 kilometers from the Earth's surface. Moderate earthquake has hypocenter ranging from 60 to 300 kilometers while deep earthquakes are those with hypocenters exceeding 300 kilometers (Bulo, 2020).

Tectonic earthquakes are significant due to their destructive consequences. Understanding the frequency, energy output, and impact of tectonic earthquakes in relation to tectonic plates is essential. Displacements along fault planes caused by tectonic earthquake typically range from 0.2 to 0.8 meters (Gomberg & Ludwig, 2017). The epicenters of tectonic earthquake are generally located along faults and subduction zones, where frequent movements occur. Shallow earthquake epicenters are often found in regions where magma migration leads to the gradual thinning of the oceanic plate and the formation of faults. This phenomenon, known as seafloor spreading, contributes to the generation of the shallow earthquakes. Additionally, a submarine fault traversing the central mountains of Sumatra further influences tectonic activity in the region. A multitude of faults emerge from the subduction zones formed by the interaction of two tectonic plates (Gomberg & Ludwig, 2017).

Earthquake sources are classified into three categories. The first category consists of subduction earthquake sources, which are defined as zones of seismic activity located near the boundary where an oceanic plate descends beneath a continental plate. The second category includes fault earthquakes, which originate from the movement of superficial faults or fissures. Finally, the third category, known as background earthquake sources, refers to earthquake that occur in a target location despite the absence of identifiable seismogenic data (Kumala, 2016).

The precise determination of earthquake hypocenter relocation is essential for global and local seismicity analysis, fault zone identification, microfracture distribution and orientation, and velocity structure analysis. A seismic relocation method is necessary to ascertain a more precise hypocenter location. The Double Difference method is a method for relocating the hypocenter of an earthquake. Earthquakes can be relocated simultaneously via the Double Difference method. This method links earthquakes to achieve a more accurate hypocenter location by utilizing the differences in their travel periods (Apdila, 2015).

Identifying the hypocenter of an earthquake, a crucial earthquake parameter, plays a significant role in seismology. The accurate determination of earthquake hypocenter locations is essential for comprehensive tectonic structure studies, particularly in detecting fault zones and subduction zone patterns. Several factors influence the accuracy of predicting earthquake hypocenter sites, including seismic station network layout, earthquake data distribution, arrival time readings, and velocity structure models (Dewi, 2018).

The benefits of hypocenter relocation include :
1. Reducing disaster risks and impacts
By determining the accurate location of the hypocenter, authorities can provide faster and more precise warnings to the public, thereby minimizing the risk of damage and casualties.
2. Safer construction planning
Accurate hypocenter data enables better and safer infrastructure development, particularly in earthquake-prone areas.
3. More efficient emergency response
Emergency response teams can promptly reach the most affected areas, improving the effectiveness of relief efforts (Ramdhan et al., 2023).

Parameters of the earthquake hypocenter released by BMKG (Meteorological Agency Climatology and Geophysics) are still lacking optimal in terms of accuracy because it is more focuses on the speed of information for tsunami early warning for the community (Sabonbali, 2020).

This investigation was conducted in the Mentawai region, located between the coordinates 0.7235°N to 3.9263°S and 97.3142°E to 100.98°E. The study examines disparities in earthquake hypocenter depths in the Mentawai region before and after relocation, along with a comparative analysis of hypocenter positions pre- and post –relocation. The objective is to apply the twofold difference approach to accurately relocate the hypocenter in the mentawai region, evaluate he changes in hypocenter locations due to relocation, and determine the average depth of earthquakes in area.

Materials and Methods

The principal location of the study was the Mentawai region in western Sumatera, Indonesia. is the Mentawai region in western Sumatra, Indonesia. The investigations utilized arrival time data of seismic waves from seismic stations near Mentawai. Data from both P (primary) and S (secondary) waves were utilized. The double difference (DD) method was employed to ascertain the migration of the hypocenter using arrival time from September 2023 to September 2024. The Position of the earthquake hypocenter was refined using the Double Difference (DD) method.

The initial data used in this study were obtained from BMKG Padang Panjang (PGR-VI), comprising a total of 2,380 records from all observation areas. However, for the Mentawai region, only 94 data points were selected as the initial dataset. After the relocation process using the Double Difference method, the final dataset for the Mentawai region was reduced to 89 data points. This reduction resulted from a data filtering process aimed at enhancing the accuracy of the relocation results.

The hypoDD program was utilized to relocate the seismic hypocenter. Waldhauser & Ellsworth (2000) introduced this method, derived from the Geiger method, which utilizes residual transit time data from each pair of hypocenters to the earthquake recording station. It is suggested that the distance between the two hypocenters should be shorter than the distance from a hypocenter to the earthquake recording station. Thus, the objective is to compare the two hypocenters with the station. This is accomplished by

modeling the waves from the two hypocenters as propagating through the same ray path or medium. Errors can be minimized by determining the new hypocenter's location based on the differential travel time between the two hypocenters (Serhalawan, 2018).

Determining the location of the hypocenter of an earthquake hypocenter has been widely conducted and developed using various approaches and methods. One of these is the Double Difference method (Baskoro et al., 2024). This method is a technique for hypocenter relocation derived from the Geiger approach, utilizing travel time residuals from two adjacent earthquake hypocenters to each seismograph station (Dewi, 2018).

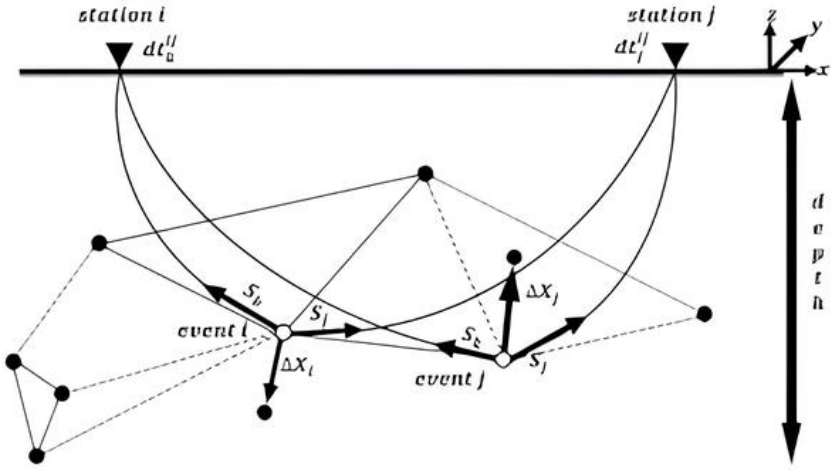

Figure 1. Illustration of the double difference methods (Waldhauser & Ellsworth, 2000).

Figure 1 illustrates the Double Difference algorithm. The white circles, recorded at stations k and l with a travel time differential (dt_k^{ij}) and its slowness vector s, represent the hypocenters of adjacent earthquake events. These events are analyzed using cross-correlation data (solid lines) or earthquake catalogs (dashed lines) for events i and j. The ray path remains consistent as the two events are significantly closer to the earthquake recording station than to each other. Δx_i and Δx_j denote the relocation vector (Powell & Lamontagne, 2017). The velocity model plays a crucial role in determining hypocenter relocation. If the velocity model does not align with geological conditions, the relocation results may not accurately reflect tectonic conditions. The velocity model itself is influenced by the geological structure of a region. According to Powell & Lamontagne (2017), in identifying the precise position of an earthquake hypocenter, the velocity model is a key priority. Hypocenter determination often relies on global velocity models, which can produce significant residuals. One of the primary requirements for obtaining accurate earthquake locations is the availability of a high-precision seismic wave velocity model at a local or regional scale. Based on the relationship between earthquake positions, velocity models, and complex geological conditions (Tumangkeng, 2020), the Crust 2.0 model (Zheng et al., 2022) at depths of 0–80 km in the Mentawai Islands region serves as the reference model for the P-wave velocity used in this study. Table 1 displays the values for each layer of the crust 2.0 model.

Table 1. Model for the P-wave velocity (Zheng et al., 2022).

Depth (km)	Velocity (km/s)
0.00	1.45
3.00	1.65
8.30	5.80
10.00	6.80
18.00	8.35
80.00	8.45

The difference in travel time between two seismic events, as expressed in the following equation, is referred to as the residual time between observation and calculation (Jannah, 2016).

$$d_k^{ij} = (t_k^i - t_k^j) - (t_k^i - t_k^j)^{cal} \quad (1)$$

Where:
i and j = two contiguous hypocenters.
k and l = recorded both earthquake events.
d_k^{ij} = residual travel time between earthquake pairs I and J at station K.
t_k^i = travel time of earthquake I recorded by station K.
t_k^j = travel time of earthquake J recorded by station K.
t^{obs} = Recorded travel time of observation (as noted by the receiving station).
t^{cal} = calculated trip time (derived from computations based on ray tracing in accordance with the employed velocity model).

The phase with the observed arrival time can be determined using either the relative travel time difference through cross-adjustment or the absolute travel time, as indicated by Equation (1) (Jannah, 2016). The differential variation between events I and J for each parameter is used to calculate the residual travel time between two seismic events. Equation (1) can be expressed as follows (Jannah, 2016):

$$\Delta d = \left(\frac{\partial t_k^i}{\partial m}\right)\Delta m^i - \left(\frac{\partial t_k^i}{\partial m}\right)\Delta m^j \quad (2)$$

Upon deconstructing the parameters for modifying the hypocenter model (Δm), Equation 2 can be articulated as follows (Powell & Lamontagne, 2017):

$$\Delta d = \frac{\partial t_k^i}{\partial x}\Delta x^i + \frac{\partial t_k^i}{\partial y}\Delta y^i + \frac{\partial t_k^i}{\partial z}\Delta z^i + \Delta t_0^i - \frac{\partial t_k^j}{\partial x}\Delta x^j + \frac{\partial t_k^j}{\partial y}\Delta y^j + \frac{\partial t_k^j}{\partial z}\Delta z^j + \Delta t_0^j \quad (3)$$

Equation (3) is applicable to an earthquake cluster (Powell & Lamontagne, 2017). The recorded number of n earthquakes at station k is arranged into a matrix according to Equation (2). The matrix equation for each station can be expressed as follows (Powell & Lamontagne, 2017):

$$WGm = Wd \quad (4)$$

Where:
W = A diagonal matrix used to weight each equation (containing values of 0 and 1).
G = A matrix of partial derivatives of travel time with respect to hypocenter parameters (M × 4N).
m = A vector representing relative position changes between hypocenter pairs concerning the predicted hypocenter's relative position $[dx, dy, dz]^T$ within a single cluster (2N × 1).
d = Residual travel time data for all hypocenter pairs (M × 1).
M = The number of double-difference observations.
N = quantity number of hypocenters.

G represents the travel time in relation to the partial derivative residual matrix of hypocenter parameters, with dimensions M × 4N. N denotes the number of hypocenters within a cluster, while M refers to the number of equations derived from each hypocenter pair within that cluster. d represents the residual double difference of all hypocenter pairs, whereas m is the vector of relative position changes between hypocenter pairs and the estimated (initial) hypocenter locations $[dx, dy, dz, dt]^T$ within a single cluster.

Each equation is assigned a weight using a diagonal matrix, W, to account for variations in the signal-to-noise ratio for each event at every station. The W matrix assigns weights based on the quality of event selection (Mahendra et al., 2016). Iterative calculations are conducted to refine the hypocenter position until the

residual travel time between computed and observed data approaches zero.

Results and Discussion

This investigation was conducted in the Mentawai region, located between the coordinates 0.7235°N to 3.9263°S and 97.3142°E to 100.98°E. A total of 2,380 earthquake events recorded between September 2023 and September 2024 served as the initial input for the hypocenter relocation methodology. After applying the Ph2Dt filtering tool, 94 earthquake events were selected. The HypoDD program further refined this selection, identifying 89 earthquake events based on hypocenter displacement distribution.

Figure 2 illustrates the cross-section. The red color (Before) and yellow color (After) cross-section before and after relocation, respectively. While the overall cross-section remains similar before and after relocation, the depth of earthquake sources generally shows a shallower trend after relocation. Earthquakes occurring at depths of 0 to 60 kilometers tend to form clusters. According to Raharjo et al (2023), the activity of the Sumatran fault has triggered shallow earthquakes at depths of around 40 km, observed at 300 kilometers. Additionally, the data indicate the presence of a subduction zone at a depth of approximately 150 km directly beneath the Sumatran fault, also identified from 300 km.

This study identifies a cluster of earthquakes distributed at depths below 60 km, primarily occurring along the Mentawai fault. Furthermore, the subduction zone is characterized by a high frequency of earthquakes. Before relocation, approximately 82 shallow earthquakes, 9 medium-depth earthquakes, and 2 deep earthquakes were recorded. After relocation, the distribution changed to 72 shallow earthquakes, 18 medium-depth earthquakes, and 4 deep earthquakes. The correlation between earthquake origins and depth was derived from the analysis of cross-section maps shown in Figures 5 and 6.

The parameters obtained from data processing differ from the original dataset, illustrating variations in longitude and latitude when applying the double-difference method. These adjustments indicate that the relocation process aligns with the expected relocation requirements. Before relocation, the average hypocenter depth was approximately 41.05 km, which increased to around 51.05 km after relocation.

In a geotechnical context, relocation often affects the depth of soil layers or subsurface structures. Before relocation, the soil and geological strata beneath the original area were relatively stable, having undergone natural compression over time. However, post-relocation, changes in structural load and alterations in soil pressure distribution may influence the depth of existing soil layers (Feng, 2024).

Depth alterations may also result from load redistribution, leading to increased pressure on deeper soil strata or shifts within soil layers. In some cases, the thickness of a soil layer may increase due to the compaction of deeper soil or the displacement of previously shallower layers.

Figure 4 presents the seismicity map of the Mentawai region after relocation, based on processing results. The earthquakes primarily consist of shallow seismic events occurring at depths between 0 and 60 km, with a few moderate-depth earthquakes. Compared to Figure 3, which displays the original hypocenter locations, several notable changes are evident. Both the hypocenter and epicenter of the earthquakes have shifted. Following the relocation, many epicenter distributions now form clusters that appear closer to the Mentawai fault.

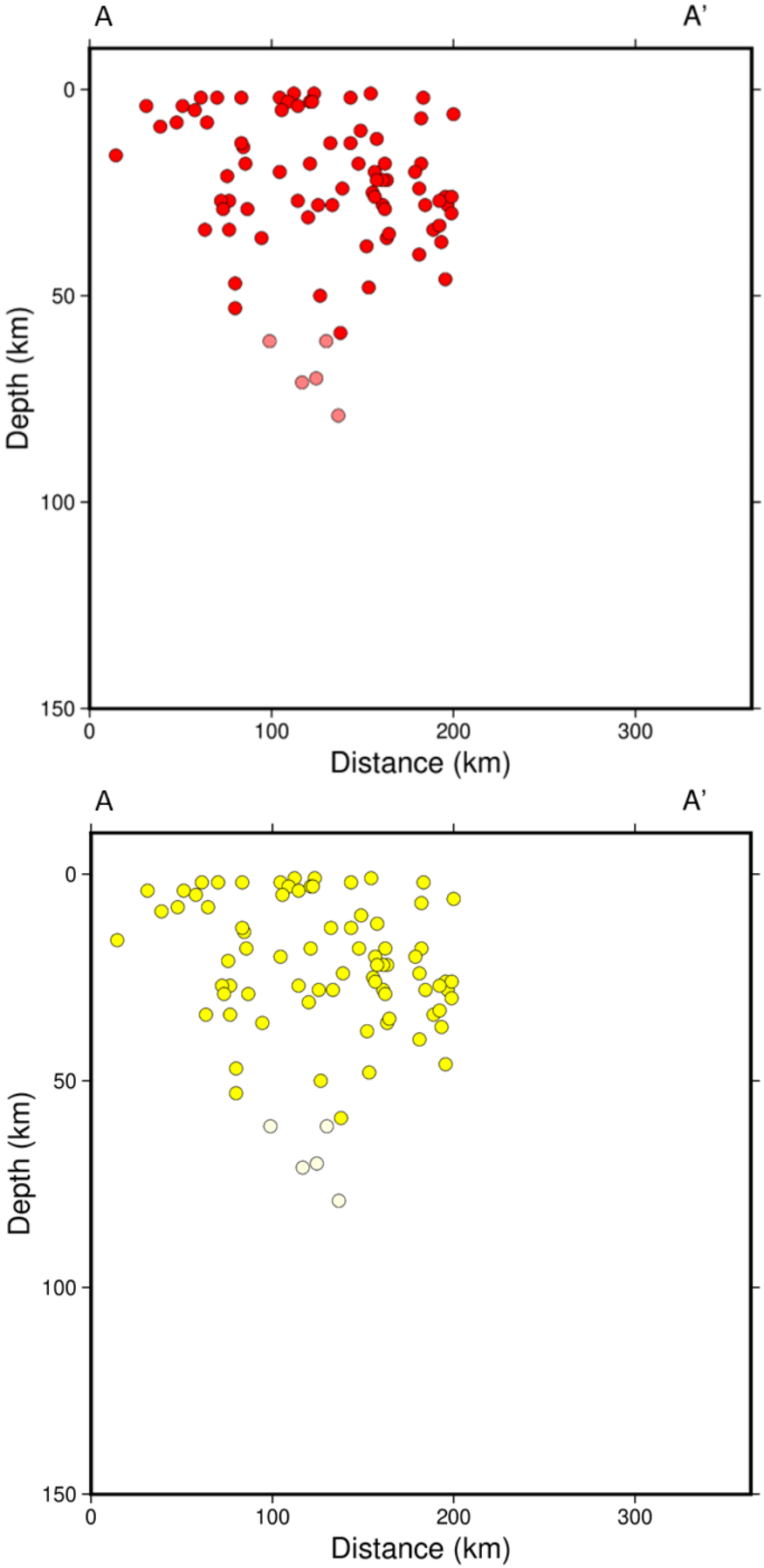

Figure 2. Cross-Section Before (red) and After (yellow) Relocation.

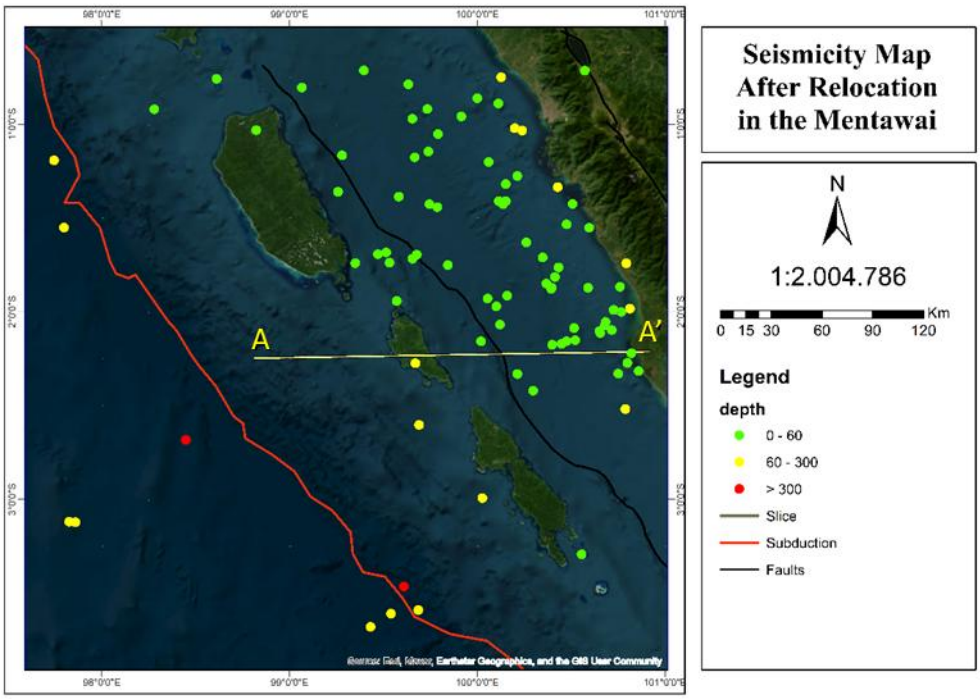

Figure 3. Seismicity map after relocation.

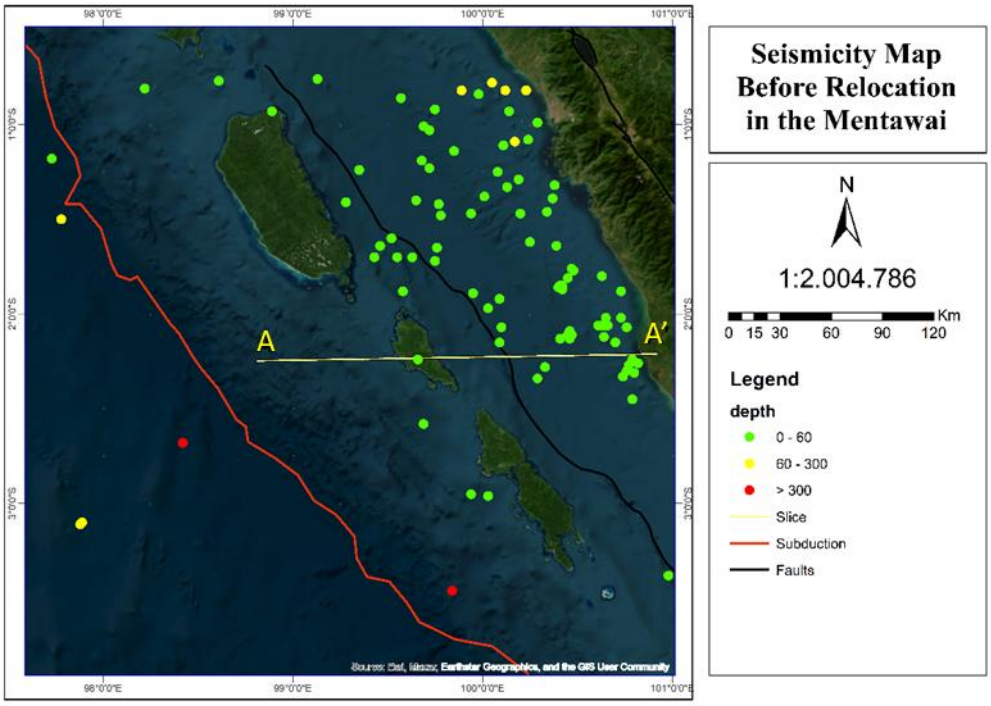

Figure 4. Seismicity map before relocation.

Un-relocated data refers to events or event pairs that do not meet the predefined criteria. These criteria are applied during the processing of earthquake occurrences using the Ph2dt program. The author sets the following parameters: minimum picking weight (MINWGHT) = 0, maximum distance between earthquake pairs and stations (MAXDIST) = 450 km, maximum distance between earthquake pairs (MAXSEP) = 210 km, maximum number of neighbors (MAXNGH) = 8, minimum number of links for a neighbor (MINLNK) = 2, minimum number of links for an earthquake pair (MINOBS) = 2, and maximum number of links for an

earthquake pair (MAXOBS) = 20. Additionally, iterative adjustments to the earthquake hypocenter during relocation may lead to further modifications.

The relocation process led to a reduction in the number of data points from 94 to 89. This reduction was due to a data filtering process that prioritized quality and accuracy in the analysis. Data that did not meet the quality criteria during the relocation process were automatically eliminated to prevent biased analytical outcomes.

The relocation data reveal distinct clusters, suggesting a significant level of seismic activity along the Mentawai fault. It is hypothesized that minor faults are triggered by earthquakes occurring along the main Mentawai fault, particularly in areas with high seismic density. According to Lange et al (2018), the Mentawai fault, the Andaman fault, and several smaller faults exhibit notable activity within the region between the subduction zone and the Sumatran fault zone.

Constructing a histogram of the residual travel time after relocation enables an evaluation of the accuracy of the Double Difference method applied in the relocation process. The research findings are categorized based on quality (Q), as outlined by Utama & Garini (2022), and can be defined in Table 2.

Table 2. Hypocenter RMS Quality

Q (quality)	*RMS*
A	*<0.15*
B	*<0.30*
C	*<0.50*
D	*others*

The RMS parameters in Figure 7 shows that, compared to the pre-relocation RMS value, the post-relocation RMS value is decreasing (approaching zero). In this study, RMS represents residual error or inaccuracy measured in seconds. Therefore, when converted into hypocenter quality (Q), the data results can be considered to meet a relatively high standard. The primary objective of the Double Difference approach, applied to two consecutive earthquake events recorded by the same seismic stations, is to minimize residual discrepancies between calculated and observed travel times (Dahlia, 2022). The results of the earthquake hypocenter relocation using the Double Difference method are considered satisfactory, as the computation yields an average RMS value of 0.665.

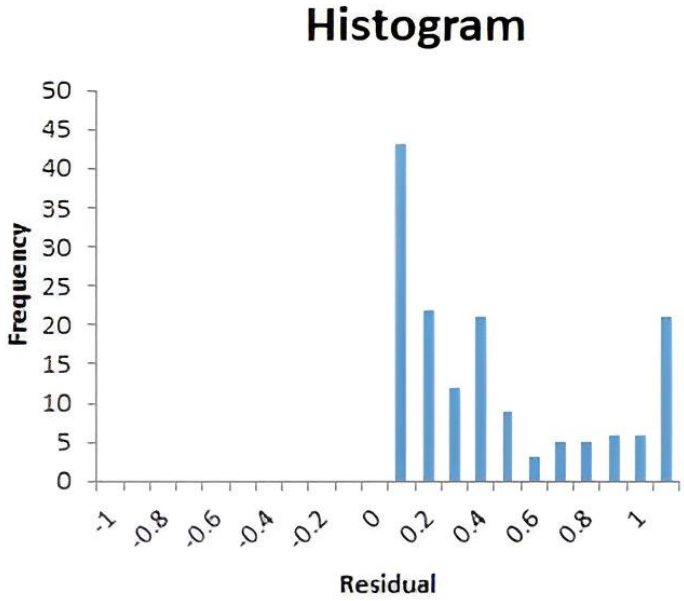

Figure 5. Histogram of travel time residual.

Conclusion

The distribution of seismic hypocenters before and after relocation exhibited several changes. Prior to relocation, data from 94 earthquake events were collected, whereas post-relocation, 89 events were identified using the hypoDD software. The relocation process adjusted both the hypocenters and epicenters, revealing a clustering of events primarily along minor faults, particularly around the Mentawai fault.

The average depth of seismic events before relocation was 41.05 km, whereas after relocation, it increased to 51.05 km. Based on this depth, it can be inferred that most of the earthquakes remain classified as shallow.

Acknowledgements

The authors wish to express their profound appreciation to the editors, reviewers, and manuscript evaluators for their invaluable feedback and support in refining this work. Gratitude is also extended to the technical personnel and colleagues at the Department of Physics and Geophysics, Faculty of Mathematics and Natural Sciences, University of Bengkulu, for their assistance in equipment preparation and data analysis. Furthermore, the authors deeply appreciate the contributions of those involved in the survey and data collection, which were essential for the subsequent analysis of hypocenter displacement of earthquakes in the Mentawai region using the double difference approach.

Author Contribution

Siti Hannifah Maulani: Formulated the research concepts, designed the methodology, and conducted data analysis using the double difference method with HypoDD.

Refrizon: Provided expertise in geophysical analysis and contributed to the interpretation of results.

Rida Samdara: Managed the technical aspects of equipment setup and reviewed and revised the manuscript for intellectual content.

Lori Agug Satria: Supervised the research process, assisted with data processing, and edited the publication for intellectual clarity.

Suaidi Ahadi: Provided research resources and assisted in data compilation.

Conflict of Interest

The authors declare no conflicts of interest regarding this study. There are no personal or financial affiliations that could influence the findings and conclusions of this research. All authors have conducted this study independently.

References

Apdila, A., & Sunardi, B. (2015). Aplikasi Metode Double Difference Untuk Relokasi Hiposenter Gempabumi Halmahera 15 November 2014 dan Susulannya. *Proseding Seminar Nasional Fisika dan Aplikasinya,* FB-37 – FB-46.

Baskoro, W. T., Kasmawan, G., Yuliara, M., Putra, K., & Sismanto, D. (2024). Double-Difference Method for Relocating the Hypocenter of Aftershock Earthquakes in Seririt Singaraja. *Asian Journal of Research and Reviews in Physics*, 8(1), 33–40. https://doi.org/10.9734/ajr2p/2024/v8i1156

Bulo, D., Djayus, D., Supriyanto, S., & Hendrawanto, B. (2020). Penelitian Titik Epicenter dan Hypocenter Serta

Parameter Magnitude Gempabumi Berdasarkan Data Seismogram. *Geosains Kutai Basin*, 3(1), 1–8. https://jurnal.fmipa.unmul.ac.id/index.php/geofis/article/view/597

Dahlia, B., Natijo, N., Dewi, I. K., Kurniawan, S. E., & Yogaswara, S. (2022). Relokasi Hiposenter Gempabumi Dengan Menggunakan Metode Double Difference Serta Implikasinya Terhadap Seismotektonik Di Wilayah Sumatera Barat. *Jurnal Teknik Kebumian*, 7(2), 18–25. https://online-journal.unja.ac.id/jtk/article/view/23092

Dari, A. W., Syafriani, S., & Sabarani, A. Z. (2016). Relokasi Hiposenter Gempabumi Sumatera Barat Menggunakan Metode Double Difference (DD). *Pillar Of Physics*, 8(l), 17–24. https://ejournal.unp.ac.id/students/index.php/fis/article/view/2486

Dewi, F. C., Karyanto, K., Rustadi, R., & Wibowo, A. (2018). Relokasi Hiosenter Gempabumi Wilayah Sumatera Bagian Selatan Menggunakan Metode Double Difference (HypoDD). *Jurnal Geofisika Eksplorasi*, 3(2), 65–76. https://journal.eng.unila.ac.id/index.php/geo/article/view/1041

Feng, J., Dong, X., Luo, R., Wang, L., Wang, L., &; Mei, G. (2024). One-dimensional consolidation analysis of layered foundations with continuous drainage boundaries considering soil structure and physical properties. *Frontiers in Earth Science*, 12, 1493821. https://doi.org/10.3389/feart.2024.1493821

Gomberg, J. S., & Ludwig, K. A. (2017). *Reducing risk where tectonic plates collide*. U.S. Geological Survey Fact Sheet 2017–3024. https://doi.org/10.3133/fs20173024

Jannah, L. N., Anggono, T., & Toni, Y. M. T. (2016). Aplikasi Metode Double Difference Dalam Relokasi Hiposenter Untuk Menggambarkan Zona Transisi Antara Busur Banda dan Busur Sunda. *Youngster Physics Journal*, 5(3) 113–122. https://ejournal3.undip.ac.id/index.php/bfd/article/view/12760

Kammer, D. S., McLaskey, G. C., Abercrombie, R. E., Ampuero, J. P., Cattania, C., Cocco, M., Dal Zilio, L., Dresen, G., Gabriel, A.-A., Ke, C., Marone, C., Selvadurai, P. A., & Tinti, E. (2024). Energy dissipation in earthquakes. *ArXiv*. https://doi.org/10.48550/arxiv.2403.06916

Kumala, S. A., & Wahyudi, W. (2016). Analisis Nilai PGA (Peak Ground Acceleration) Untuk Seluruh Wilayah Kabupaten dan Kota Di Jawa Timur). *Inersia : Jurnal Teknik Sipil Dan Arsitektur*, 12(1), 37–43. https://doi.org/10.21831/inersia.v12i1.10348

Lange, D., Tilmann, F., Henstock, T. J., Rietbrock, A., Natawidjaja, D. H., & Kopp, H. (2018). Structure of the central Sumatran subduction zone revealed by local earthquake travel-time tomography using an amphibious network. *Solid Earth*, 9(4), 1035–1049. https://doi.org/10.5194/SE-9-1035-2018

Le Béon, M., Shih, J.-W., Chen, C.-C., Huang, W.-J., Tseng, Y.-C., Chiu, Y.-W., Liu, Y.-C., Hsieh, M.-L., Lu, C.-H., & Pathier, E. (2023). Active anticline and backthrust override a geological thrust: evidence from present and Holocene deformation rates within the foothills of southwestern Taiwan. *EGU General Assembly 2023*, Vienna, Austria, 24–28 Apr 2023, EGU23-15525.

https://doi.org/10.5194/egusphere-egu23-15525, 2023

Mahendra, R., Supriyanto, R., & Rudyanto, A. (2016). Relokasi dan Klasifikasi Gempabumi untuk Database Strong Ground Motion di Wilayah Jawa Timur. *Jurnal Meteorologi, klimatologi dan Geofisika*, 3(3), 46–51. https://jurnal.stmkg.ac.id/index.php/jmkg/article/view/15

Marzuki, M., Ramadhan, R., Friska, V., Primadona, H., Ramadhan, R. A., Monica, F., Arisa, D., & Namigo, E. L. (2022). Dynamics of West Coast of Sumatra and Island Arc Mentawai during the Coseismic Phase of the Mentawai Mw7.8 25 October 2010 Earthquake. *Journal of Physics: Conference Series*, 2309(1), 012030. https://doi.org/10.1088/1742-6596/2309/1/012030

Naim, M. I., Supriyadi, S., & Linuwih, S. (2018). Analisis Seismisitas dari Kepulauan Mentawai Pada Periode 2010-2016. *Indonesian Journal of Applied Physic*, 8(1), 6–12. https://doi.org/10.13057/ijap.v8i1.15274

Powell, C. A., & Lamontagne, M. (2017). Velocity Models and Hypocenter Relocations for the Charlevoix Seismic Zone. *Journal of Geophysical Research Solid Earth*, 122, 6685–6702. https://doi.org/10.1002/2017JB014191

Ramdhan, M., Priyobudi, P., Mursitantyo, A., Palgunadi, K. H., Panjaitan, A. L., & Jatnika, J. (2023). Hypocenter relocation of the Mw 5.9 eastern Manggarai earthquake 2022 and its aftershocks based on BMKG seismic network. IOP Conference Series: Earth and Environmental Science, 1227(1), 012042. https://doi.org/10.1088/1755-1315/1227/1/012042

Sabonbali, S.C, Taunaumang, H., Dungus, F, Zulkifli, M., & Sriyanto, S. P. D. (2020). Relokasi Hiposenter Menggunakan Metode Modidied Joint Hypocenter Determination (Studikasus Gempabumi Laut Maluku Tanggal 15 November 2019). *Charm Sains: Jurnal Pendidikan Fisika*, 1(3), 132–138. https://eurekaunima.com/index.php/jpfunima/article/view/50

Serhalawan, Y. R. (2018). *Petunjuk Teknis Relokasi Hiposenter Gempabumi Menggunakan Program Hypocenter Double Difference (HypoDD) Berdasarkan Data Katalog/ Buletin Gempabumi*. Stasiun Geofisika Sorong, Badan Klimatologi, Meteorologi, dan Geofisika. https://www.scribd.com/document/419507411/Petunjuk-Teknis-Hypodd-Serhalawan-2018

Syafriani, S., Raharjo, F. D., Ahadi, S., & Ramdhan, M. (2023). Study of Seismicity Based on the Results of Hypocenter Relocation Using Double Difference (HypoDD) Method in West Sumatera and Its Surrounding. *Jurnal Penelitian Pendidikan IPA (JPPIPA)*, 9(7), 5150–5156. https://doi.org/10.29303/jppipa.v9i7.3792

Tumangkeng, C. S., Wenas, D. R., & Umboh, S. I. (2020). Model Kecepatan 1d Gelombang P Dan Relokasi Hiposenter Wilayah Sulawesi Utara Dan Sekitarnya Menggunakan Metode Couple Velocity-Hypocenter. *Charm Sains: Jurnal Pendidikan Fisika*, 1(2), 1–7. https://eurekaunima.com/index.php/jpfunima/article/view/9

Utama, W., & Garini, S. A. (2022). Hypocenter Determination and Estimation 1-D Velocity Models Using Coupled Velocity-Hypocenter Method. *International Journal on Advanced Science, Engineering and Information Technology*, 12(3), 892–898.

https://doi.org/10.18517/ijaseit.12.3.12488

Waldhauser, F., & Ellsworth, W. L. (2000). A Double-Difference Earthquake Location Algorithm: Method and Application to the Northern Hayward Fault, California. *Bulletin of the Seismological Society of America*, 90(6), 1353–1368. https://doi.org/10.1785/0120000006

Wijaya, D. K., Widjaya, R., Kurniawan, A., & Diana, D. (2024). Using Time Series Analysis to Predict Earthquake. *2024 International Conference on Artificial Intelligence, Blockchain, Cloud Computing, and Data Analytics (ICoABCD), Indonesia*, 25–30. https://doi.org/10.1109/icoabcd63526.2024.10704296

Zheng, H., Li, T., He, R., Yu, H., Yang, H., Wen, Y., Wang, P., Liu, F., & Sun, D. (2022), P-wave Velocity Structure of Crustal and Upper Mantle beneath South China and its Tectonic Implications. *Acta Geologica Sinica - English Edition*, 96(2), 621–630. https://doi.org/10.1111/1755-6724.14854

ISSN: 2579-5821 (Print)
ISSN: 2579-5546 (Online)
URL address: http://journal.unhas.ac.id/index.php/geocelebes
DOI: 10.70561/geocelebes.v9i2.44633

Jurnal Geocelebes Vol. 9 No. 2, October 2025, 139 – 156

Spatial Analysis of the Seismic Gap Zone Based on Multiparameter Seismotectonics in Southern East Java as an Indicator of Megathrust Earthquake Potential

Diva Maharani Putri[1]*, Nanda Maharani[2], Ilham[3], Riska Yulinda[3]

[1]Geophysics Department, Padjadjaran University, Bandung, 40132, Indonesia.
[2]Physics Department, Brawijaya University, Malang, 65145, Indonesia.
[3]Malang Geophysical Station, Agency for Meteorology, Climatology and Geophysics (BMKG), Malang, 65165, Indonesia.

*Corresponding author. Email: diva21001@mail.unpad.ac.id

Manuscript received: 7 June 2025; Received in revised form: 18 August 2025; Accepted: 2 September 2025

Abstract

The southern region of East Java is located above an active subduction zone, where the Indo-Australian Plate is subducting beneath the Eurasian Plate. This tectonic condition makes the region potentially susceptible to large-scale megathrust earthquakes. This study aims to characterize the suspected seismic gap segments in the southern subduction zone of East Java, with a primary focus on the area between Pacitan and Lumajang. The approach used is based on high-resolution seismotectonic spatial analysis, combining three main parameters: seismicity distribution, earthquake return period estimates, and a-values and b-values as indicators of tectonic activity and stress condition. The analyzed data covers a long period of time, from 1910 to 2025, and was compiled by the BMKG and USGS catalogs. The results of the analysis show that the Pacitan-Lumajang segment experiences a lack of earthquake activity in the plate interface, although this area is tectonically active. In addition, this segment has a very long return period (> 500 years for M_w7 and > 4,000 years for M_w8), accompanied by low a-value and b-value, indicating low earthquake frequency and high stress accumulation. These findings indicate that the segment is a locked zone that has the potential to release large amounts of energy in the future. The results of this study provide an initial contribution in understanding the spatial distribution of seismic activity in the southern region of East Java, and can be used as supporting considerations in initial disaster risk assessments, especially in densely populated coastal areas.

Keywords: Earthquake return period; locked segment; subduction; tectonic stress.

Citation: Putri, D. M., Maharani, N., Ilham, I., & Yulinda, R. (2025 Spatial Analysis of the Seismic Gap Zone Based on Multiparameter Seismotectonics in Southern East Java as an Indicator of Megathrust Earthquake Potential. *Jurnal Geocelebes*, 9(2):139–156, doi: 10.70561/geocelebes.v9i2.44633

Introduction

Java Island is one of the regions with complex tectonic conditions in Indonesia. This is due to its location above the convergence zone between the Indo-Australian Plate and the Eurasian Plate, which forms an active subduction zone along the southern coast of Java. This zone is known as a source of major earthquakes, including megathrust earthquakes that have the potential to trigger tsunamis (Hutchings & Mooney, 2021; Rakuasa & Pakniany, 2024). In recent decades, tectonic activity in this zone has continued to be a concern due to its potential to trigger large-scale disasters. Several studies (Rakuasa & Pakniany, 2024; Widiyantoro et al., 2020; Xie et al., 2023) indicate that the southern Java megathrust zone has the potential for large-magnitude earthquakes. Widiyantoro et al. (2020) conducted tsunami modeling based on GPS data inversion results. One of the scenarios used modeled the megathrust segment south of Central to East Java, with an estimated magnitude reaching M_w8.8. The modeling results indicate that this scenario could generate a tsunami with a

maximum run-up height of up to 12 meters along the coast of East Java. The high concentration of the population, national economic centers, and strategic infrastructure on the island of Java makes the potential for a major earthquake a serious threat, not only in geological terms but also from a social and economic perspective.

Tectonically, the subduction zone in the south of Java Island is classified as very active (Hutchings & Mooney, 2021). However, several segments in this zone show very minimal seismic activity over a long period. This phenomenon of no earthquake activity is known as a seismic gap, which is a segment at the plate interface that, although located in an active tectonic area, does not show significant release of seismic energy (Xia et al., 2021). This condition indicates the presence of an interlocking process on the subduction plane, which inhibits the slow release of slip. However, the subduction force between the plates continues, causing stress accumulation, which in the long term has the potential to be released suddenly in the form of a large earthquake (Wetzler et al., 2017; Haerudin et al., 2019).

Efforts to identify the existence of a seismic gap in the southern region of East Java have been carried out by Putra et al. (2019), who used seismicity data from the Agency for Meteorology, Climatology and Geophysics (BMKG) for the period 2006–2018. Their study results show that the segment between Pacitan and Lumajang has a low level of seismicity, especially in the plate interface area. This finding is supported by the study of Widiyantoro et al. (2020), which utilized GPS data from 37 observation stations spread across Central Java and East Java. They succeeded in mapping the slip deficit zone, which is the difference between the rate of tectonic plate movement and the actual slip rate on the fault at the plate interface. The results of geodetic data inversion show a high slip deficit rate in the southern East Java during the 2008–2014 observation period, namely 20–40 mm/yr. This area is then interpreted as a locked segment that has not fully released tectonic energy.

Study by Pasari et al. (2021) examined the earthquake potential in Java Island through an earthquake nowcasting approach, which is based on the statistical analysis of seismicity data from the period 1963–2021. This study showed that on February 18, 2021, Malang and Blitar, East Java, had an Earthquake Potential Score (EPS) of more than 90% for $M \geq 6.5$ earthquakes. Although this score is not a precise prediction of earthquake occurrence time, the value indicates significant tectonic stress accumulation. This study also reinforces the idea of the existence of a locked segment in the subduction interface. This zone is considered a seismic gap and is a seismogenic zone that can consistently generate large earthquakes within the subduction zone.

The existence of a seismic gap identified by Putra et al. (2019), along with the slip deficit zone mapped by Widiyantoro et al. (2020) on the same segment, and further reinforced by the findings of Pasari et al. (2021), collectively strengthens the suspicion that the Pacitan–Lumajang region is an area with high megathrust earthquake potential. However, previous studies have not integrated high-resolution seismotectonic spatial parameters and generally only use limited data up to 2021. This limitation has the potential to cause locked segment mapping to be less than optimal because it ignores the recent earthquake activity, which is important in estimating earthquake risk more accurately.

To strengthen our understanding of the seismic potential in this segment, this study integrates three main approaches: seismicity analysis, earthquake return period estimation, and seismotectonic evaluation through a- and b-value. This

study aims to characterize the suspected seismic gap zone in the southern subduction zone of East Java, to obtain an overview of the potential accumulation of unreleased seismic energy. The method used is based on a spatial approach with a high-resolution grid that has not been widely applied in this region. In addition, the use of a long-term earthquake catalog (1910–2025) allows for the development of a more representative regional seismic model. Through this approach, the study is expected to provide an initial contribution in mapping the potential seismic hazards in the southern region of East Java.

Tectonic Setting of Java Island

Java Island, which is part of the Sunda Arc, formed in response to the interaction between the Indo-Australian Plate and the Eurasian Plate as depicted in Figure 1 (Gunawan et al., 2017; Godang et al., 2024). Tectonically, this region is located in an active convergent boundary zone, where the Indo-Australian Plate subducts north-northeastward beneath the Eurasian Plate at an average subduction rate of about 6–7 cm per year based on GPS observations and tectonic modeling (Gunawan & Widiyantoro, 2019; Widiyantoro et al., 2020). This subduction forms a system consisting of several main components: trench, forearc basin, volcanic arc, and backarc basin (Sribudiyani et al., 2003; Gunawan & Widiyantoro, 2019).

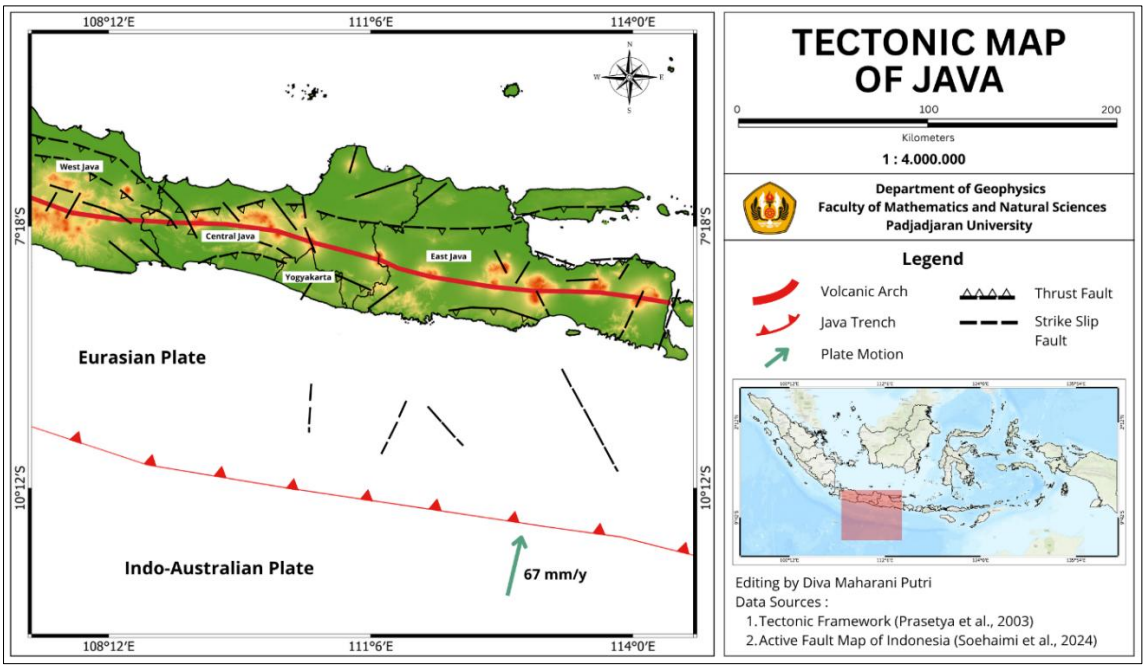

Figure 1. Regional tectonic map of Java Island showing active faults (Soehaimi et al., 2021), main tectonic plate boundaries (Indo-Australia and Eurasia), the direction and plate motion of Java subduction, the position of the Java Trench, and the morphology of the tectonic arc (modified from Sribudiyani et al., 2003).

In the southern part of Java Island lies the Java Trench, which represents the surface expression of an active subduction zone, appearing as a linear depression on the seafloor (Godang et al., 2024). Based on the Slab2.0 model, the subducting slab's dip steepens northward, reaching depths of more than 600 km beneath the Java Sea (Hayes et al., 2018). Around this trench zone, numerous normal faults are found, formed due to the bending of the subducting oceanic plate (Patria & Aulia, 2020). In East Java, the dominant structures are normal faults, such as the Pasuruan, Probolinggo, and Baluran Faults. Meanwhile, Central to East Java is more dominated by reverse faults, including the

Kendeng Fault Zone and the Semarang Fault (PuSGeN, 2022).

Between the Java Trench and the volcanic arc, there is a geological feature known as a forearc basin (Mukti, 2018; Noda, 2016). The Western and Eastern Java arcs are classified as compressional accretionary, where the presence of the forearc basin is closely related to the accretionary body surrounding the trench. The accretionary body in a subduction zone is formed through the accumulation of sediments dragged from the subducting plate. The sedimentary layers at the seaward edge of this forearc basin show a landward dip and undergo structural folding (Noda, 2016).

Marine seismic studies in the East Java forearc structure, particularly around the 1994 (M_w7.8) tsunami earthquake rupture zone offshore Banyuwangi, have identified splay faults branching from the landward flank of a subducting seamount beneath the forearc basin (Xia et al., 2021). These faults accommodate deformation in the overriding plate, triggered by compressional forces and the subduction motion of the oceanic plate (van Zelst et al., 2022; Xia et al., 2021).

Splay faults can trigger significant displacement on the seafloor or land surface. This displacement not only causes direct earthquake shaking but can also generate complex and intense seismic waves, as seen in cases like the 2018 Palu, Sulawesi, and 2016 Kaikoura, New Zealand earthquakes (Hollingsworth et al., 2017; Xia et al., 2021). In subduction zones, splay faults are also frequently associated with megathrust earthquakes, such as the 2004 Sumatra earthquake (van Zelst et al., 2022).

A volcanic arc is a chain of volcanoes that forms as a result of tectonic plate subduction. According to data from the Ministry of Energy and Mineral Resources (2025), there are 35 active volcanoes distributed along Java Island. When an oceanic plate subducts beneath a continental plate, it reaches depths where high pressure and temperature cause dehydration of the subducting plate. The water released from the plate then migrates into the overlying mantle wedge, thereby lowering the melting point of the mantle rocks and leading to magma generation (Dong et al., 2024; Widagdo et al., 2018). Morphologically, volcanic arcs are generally arranged in a linear pattern and are parallel to the subduction trench (Adam et al., 2022).

A backarc basin is a sedimentary basin that forms on the overriding plate, located behind a volcanic arc and away from the subduction trench. These basins form due to extensional forces in the Earth's crust, which can be triggered by the thermal influence of magmatic activity within the volcanic arc. This heat weakens the backarc crust, making it more susceptible to stretching. This stretching process leads to crustal thinning and subsidence, which then forms a basin that is subsequently filled with sedimentary material over time (Aribowo et al., 2022; Artemieva, 2023; Lupi et al., 2022). Although generally formed in an extensional tectonic context, some backarc basins in Java show secondary compressional phase, resulting in the formation of active thrust faults. These fault structures have the potential to be sources of seismic activity. One example is the Java Backarc Thrust in northwest Java, which has been identified as seismogenic, generating earthquakes (Aribowo et al., 2022).

Java Island, from a seismotectonic perspective, is divided into two main settings: the highly active arc seismotectonic settings in the western part and the active arc seismotectonic settings covering the West Java to East Java region (Godang et al., 2024). This tectonic setting is associated with a variety of seismic activities, ranging from megathrust

earthquakes at the interface to intraplate slab earthquakes and upper crustal earthquakes due to internal slab deformation and lithospheric fragmentation (Zhou & Xia, 2020).

Data and Methods

Data

This study focuses on the southern Java East subduction zone, covering geographic coordinates between 7.87° S to 11.63° S, and 110.52° E to 115.00° E. The data used are secondary data from two sources, both are open-access and available to the public. First, the hypocenter data from the BMKG amount to 6,927 events recorded during the period 2022–2024. This data includes information on the epicenter, depth, magnitude, and origin time. The geometry of the subduction slab refers to the Slab 2.0 model developed by Hayes et al. (2018). BMKG data and the subduction slab model are used for seismicity mapping and cross-section. The second source comes from the United States Geological Survey (USGS), covering 1,930 earthquake data with a magnitude M_w>3.2 during the period 1910–2025. This data is used for statistical analysis purposes, including the estimation of earthquake return period, as well as the calculation of a-value and b-value parameters based on the frequency-magnitude distribution. The earthquake catalog used includes records of earthquakes from subduction zones, fault zones, and from scattered earthquake activity without any connection to clearly mapped faults (background seismicity) (Bazrafshan et al., 2024).

a- and b-value

Earthquakes are complex phenomena that cluster in space and time (Hisyam et al., 2024; Zaliapin & Ben-Zion, 2020). To avoid bias in seismic catalogs, a declustering process is necessary to separate dependent earthquakes (foreshocks and aftershocks) from independent earthquakes (mainshocks) (Maiti & Kim, 2025; Zaliapin & Ben-Zion, 2020). In this study, declustering was applied using the empirical Gardner & Knopoff (1974) method, which utilizes a magnitude-based spatio-temporal window approach. This method aims to produce an earthquake catalog that approximates stationary Poisson behavior for more representative seismotectonic statistical analysis (Gardner & Knopoff, 1974; Zaliapin & Ben-Zion, 2020).

The analysis of seismotectonic parameters is conducted based on the Gutenberg–Richter relation, which describes how the number of earthquakes decreases with the increase in the magnitude of the earthquakes. This relationship is expressed in Equation (1), where N is the number of events with a magnitude $\geq M$, and the terms a and b are seismic and tectonic parameters (Gutenberg & Richter, 1944)

$$\log N = a - bM \quad (1)$$

The analysis was conducted using the Maximum Likelihood Estimation (MLE) method as formulated by Utsu (1966), which is statistically considered more stable than the linear regression method. To improve spatial resolution, the analysis was conducted using a spatial grid of size 0.1° × 0.1° with minimum events are 50 events. In each grid, the a-value and b-value are calculated using Equation (2) (Utsu, 1966) and (3) (Pakiding et al., 2025; Rehman & Zhang, 2024).

$$b = \frac{\log e}{\bar{M} - M_0} \quad (2)$$

$$a = \log N + \log(b \ln 10) + M_0 b \quad (3)$$

With $\bar{M}$ being the average magnitude and $\log e$ being 0.4343 (da Costa et al., 2024; Pakiding et al., 2025). M_0 being Magnitude of Completeness (M_c), which in this study is valued at 4.9. This value was obtained through the MLE method (Utsu, 1966) based on the Frequency-Magnitude Distribution (FMD) of the declustered

earthquake catalog (Figure 2). This value was chosen because it represents the threshold where the magnitude distribution begins to follow a linear pattern. Thus, the m_c value indicates the minimum limit for well-documented data (Rehman & Zhang, 2024). An accurate m_c estimation is crucial for the application of Equation (1). An m_c that is too high will significantly reduce the number of data samples, whereas an m_c that is too low can potentially yield biased a- and b-values (da Costa et al., 2024).

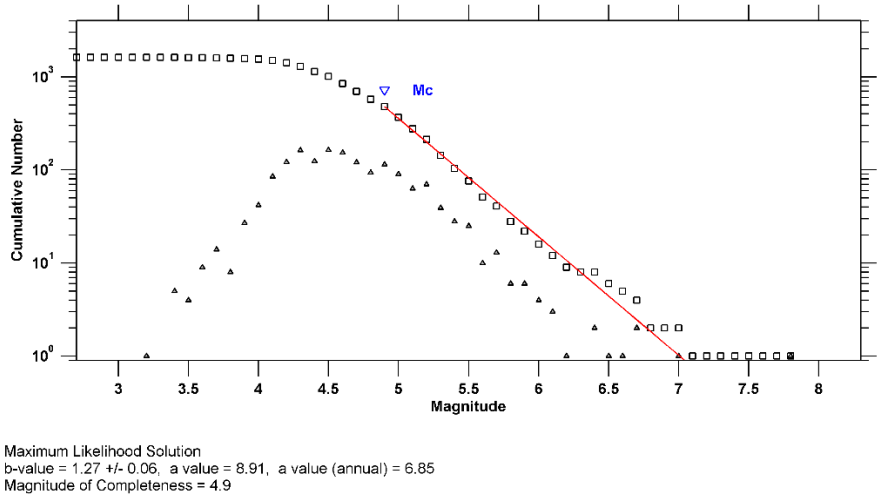

Figure 2. Frequency-Magnitude Distribution (FMD) based on the USGS Catalog 1910-2025.

Earthquake Return Period

The estimation of earthquake return periods in this study was conducted based on statistical analysis for three magnitude categories, which are M_w6, M_w7, and M_w8. This estimation aims to identify how often earthquakes of such magnitudes occur spatially in the research area. The return period (θ) for each grid cell is calculated using Equation (4) (Munandar & Sulsaladin, 2022; Rehman & Zhang, 2024; Siregar et al., 2023).

$$\theta = \frac{1}{N_1\,(M \geq M_0)} \qquad (4)$$

Where $N_1\,(M \geq M_0)$ is a seismicity index that reflects how often earthquakes with a magnitude of $M \geq M_0$ occur in the region during the observation period.

Software

Data analysis and visualization in this study were conducted using several main software packages tailored to the needs of each stage. ZMAP version 6 (Wyss et al., 2001), based on MATLAB version 7.8 (Pratap, 2010), was used for the calculation and spatial visualization of seismotectonic parameters a-value and b-value, as well as earthquake return periods. ZMAP supports the use of the MLE method in calculating seismic statistical parameters (Ernandi & Madlazim, 2020; Hisyam et al., 2024; Rehman & Zhang, 2024). Spatial visualization of hypocenters was performed using Generic Mapping Tools (GMT) version 6 (Wessel et al., 2019), which allows for the creation of cross-sections based on slab model references. This visualization was combined with QuantumGIS version 3.43 (Menke, 2022), which functions in geospatial data processing, such as overlaying seismicity data, geological structures, and administrative boundaries. All visualization processes are based on geographic coordinates referring to the World Geodetic System 1984 (WGS84) reference system. Additionally, Microsoft Excel was used as a tool for data alignment, format conversion, and earthquake catalog filtering.

Results and Discussion

Seismicity Distribution

The seismicity map of the southern region of East Java during the period 2022-2024, as shown in Figure 3, indicates the spatial distribution of earthquake epicenters forming a linear pattern-oriented West-East and aligned with the subduction zone, rather than local faults. This linear pattern represents the continuity of seismic activity that geometrically follows the direction of plate subduction, extending parallel to the Java Trench. However, the seismicity map shows a seismic anomaly, which is a zone of less seismic activity in the southern sea region from Pacitan to Lumajang, indicated by the dashed line on the map as a seismic gap zone. This area is spatially located directly above the projection of the Indo-Australian Plate slab that subducts beneath the Eurasian Plate, but it does not show significant energy release in the form of earthquakes over a long period based on BMKG catalog data. This pattern indicates the presence of a seismic gap due to the less earthquake activity during the observation period (Rakuasa & Pakniany, 2024; Megawati et al., 2024).

The indication of a seismic gap zone in southern East Java is supported by a study by Hutchings & Mooney (2021), which used the USGS earthquake catalog for events with magnitudes > M4.6 during the 2000–2020 period. Based on cross-section analysis, this study indicates that the southern region of East Java lies above a seismic gap zone that extends laterally for ~400 km. This confirms that the region has the potential for earthquakes originating from the megathrust zone and also from processes within the mantle due to the complex subduction structure beneath it.

Further analysis was conducted through three cross-sections, which are cross-section A–A′, B–B′, and C–C′, to provide an overview of the vertical distribution of the hypocenter, as shown in Figure 3 (b–d). This cross-section shows the distribution of hypocenters relative to the position of the slab modeled based on the geometric curve. The distribution of hypocenters shows a consistent tilt towards the north, corresponding to the subduction of the Indo-Australian plate. In cross-sections A-A' and B-B', it is evident that very few earthquakes occur precisely at the plate interface. Most earthquakes are distributed above the slab, specifically in the Eurasian Plate (overriding plate) with a depth range of 20–60 km or within the slab at depths > 60 km, which are referred to as intraslab earthquakes (Xie et al., 2023; Wickham-Piotrowski et al., 2024). The earthquakes that occur in the overriding plate are likely shallow crustal earthquakes related to the structural adjustment of the lithosphere due to the pressure from the subduction of the plate or local fault activity that forms above the interface. On the other hand, intraslab earthquakes indicate tectonic activity occurring within the slab body due to internal deformation during subduction (Haerudin et al., 2019).

The B–B’ cross-section, which traverses the Pacitan-Lumajang region as a suspected seismic gap zone, shows relatively less seismic activity and is not distributed along the plate interface. The less seismic activity strengthens the hypothesis that the B-B' profile crosses a seismic gap zone that is currently locked. These results are in line with the research by Muttaqy et al. (2022), which identified a seismic gap in the southern region of East Java, covering the southern coast up to the trench. This is supported by the results of tomography and slip deficit modeling, which indicate that this area is part of a locked slab segment with the potential for megathrust (Muttaqy et al., 2022).

Unlike the B-B' cross-section, which shows a lack of seismic activity at the plate interface, the C-C' cross-section, which covers the southern Banyuwangi region, shows relatively higher seismic activity

with hypocenters at depths of 10-100 km, and some earthquakes occur right at the plate interface at depths of 30-60 km. This distribution represents the slab's response to the convergence forces that have been partially released seismically. This supports the differences in tectonic behavior between megathrust segments (Bilek & Lay, 2018). Such segmentation patterns are a common feature in subduction zones, where slip behavior is not uniform across segments, and locked segments are the primary candidates for megathrust earthquake sources (Wetzler et al., 2017; Muttaqy et al., 2022).

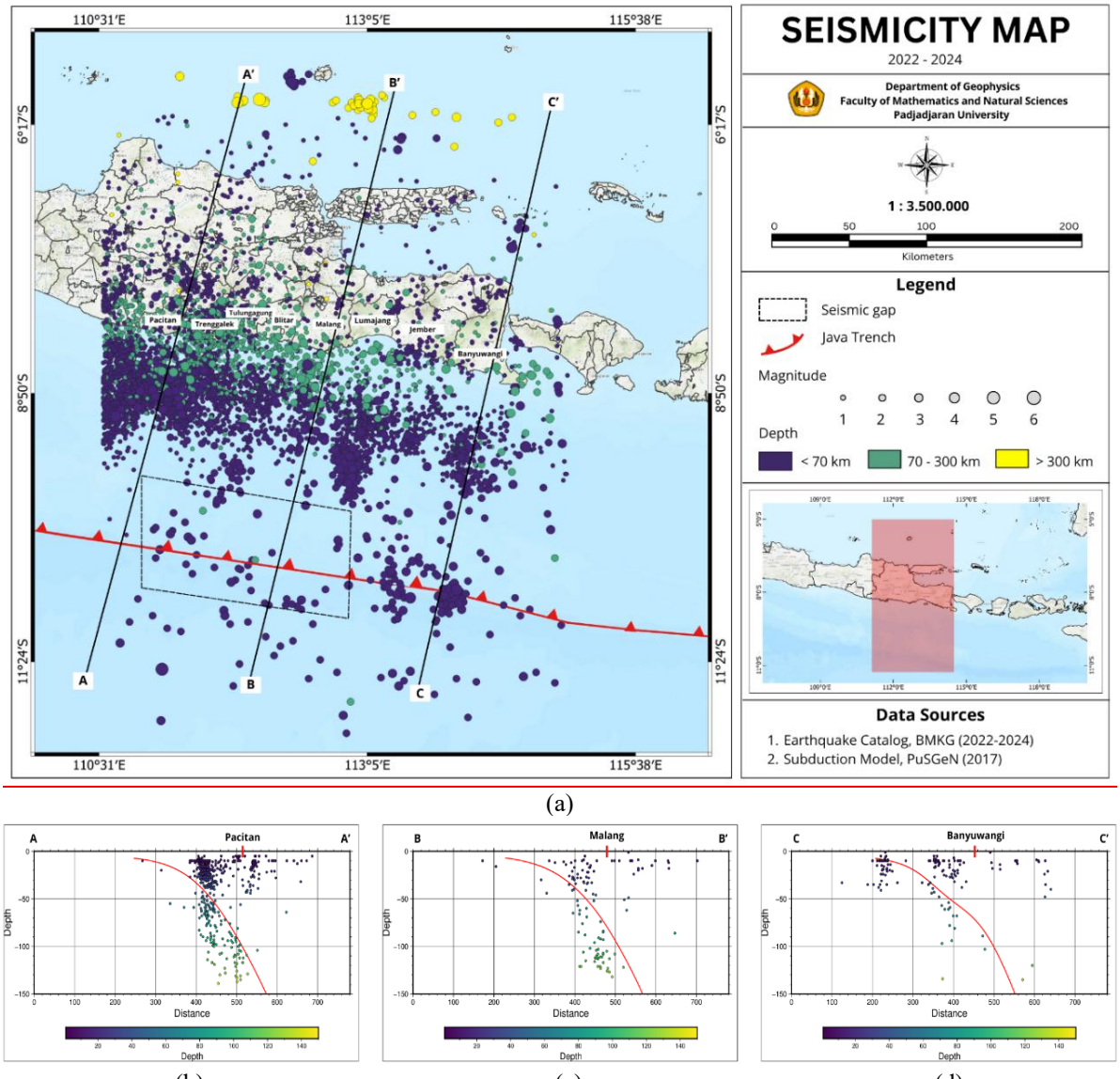

(a)

(b) (c) (d)

Figure 3. Seismicity map of the southern East Java region (2022–2024). The distribution of earthquake epicenters forms a linear pattern parallel to the Java Trench (red line), representing subduction activity. Three lines (A-A', B-B', and C-C') indicate the location of vertical cross-sections shown in Figure 3. The dashed line indicates the seismic gap zone of Pacitan–Lumajang, which has less earthquake activity. Three lines indicate the location of vertical cross-section (b) A–A′, (c) B–B′, and (d) C–C′, which show the distribution of hypocenters relative to the subducting plate.

Earthquake Return Period

The estimation of the earthquake return period is conducted for earthquakes with magnitudes M_w6, M_w7, and M_w8 based on the earthquake catalog. This parameter is very important in understanding the dynamics of seismic energy release in

subduction zones. In general, the results of return period mapping show that the greater the magnitude of the earthquake analyzed, the longer the estimated return period. The return period of earthquakes does not provide a precise time prediction, but rather offers a long-term probability (Sandhu et al., 2022). In the context of the megathrust zone, the longer the return period, the greater the likelihood that the segment has not released energy for a long time, thus storing significant potential (Rehman & Zhang, 2024).

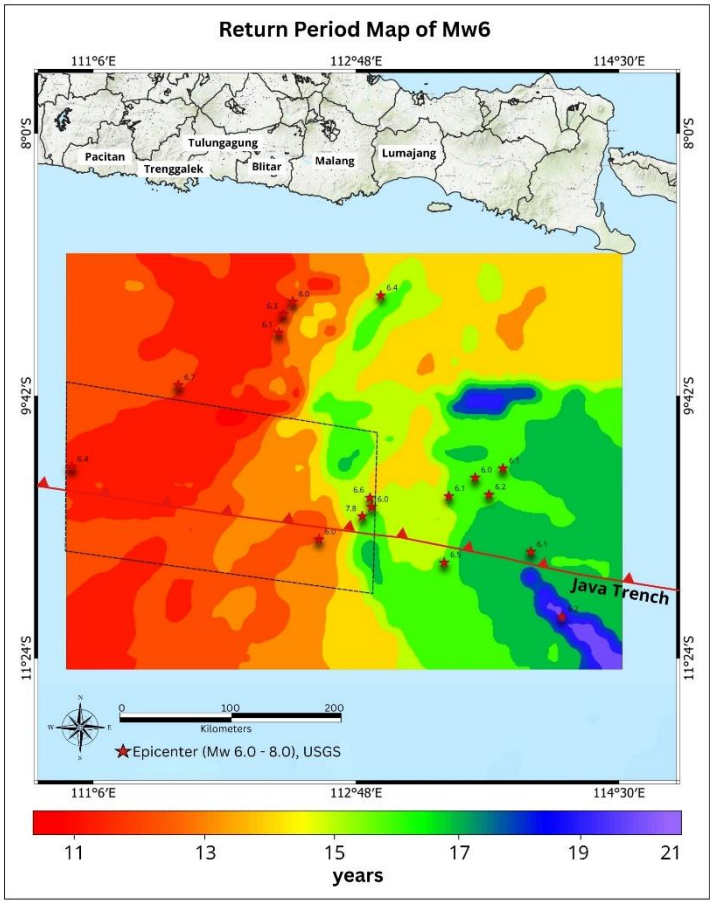

Figure 4. Spatial map of earthquake return period estimates for M_w6.

Figure 4 shows that most of the southern East Java subduction zone exhibits a short return period for M_w6 earthquakes, ranging from 11 to 21 years. This indicates that M_w6 earthquakes occur quite frequently in this zone due to the gradual release of energy. However, in the Pacitan–Lumajang segment, although the return period for M_w6 is in 10–15 years, the hypocenter location is outside the plate interface, tending to be in the overriding plate (Figure 3). According to Wickham-Piotrowski et al. (2024), earthquakes outside the plate interface generally reflect the release of energy due to crustal deformation against tectonic forces from the subduction slab. Therefore, although it appears statistically active, this segment has not yet experienced a major energy release.

The return period map of M_w7 earthquakes in Figure 5 shows that the Pacitan–Lumajang segment has a return period between 260 to >500 years, which is considered long on the major earthquakes scale. The long return period indicates that it is very rare for M_w7 earthquakes to occur in that zone during the observation period. This condition describes a slip deficit and the accumulation of stress that has not yet been released at the plate interface (Widiyantoro et al., 2020).

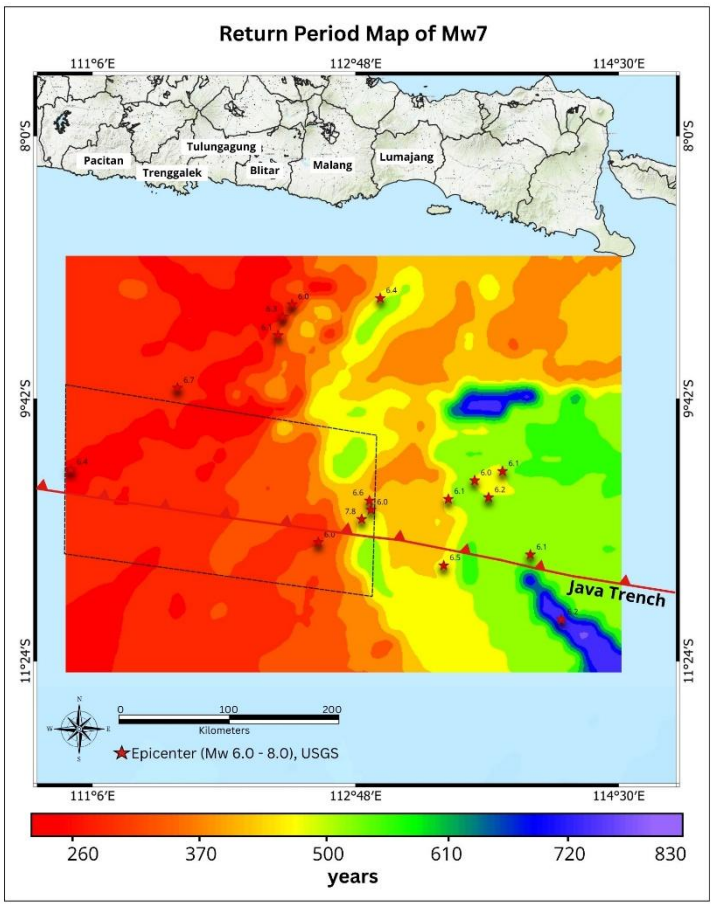

Figure 5. Spatial map of earthquake return period estimates for M_w7.

The return period map for M_w8 earthquakes (Figure 6) shows that the Pacitan–Lumajang zone is estimated to have a return period ranging from 4,000 to <16,000 years. This area is marked from red to yellow. The long return period indicates that no M_w8 earthquake events were recorded in the region during the observation period (1910-2025). According to Scholl et al. (2015), $M_w \geq 8$ earthquakes are rare but destructive events, usually occurring in highly locked subduction zones with minimal seismic history. This characteristic corresponds to the Pacitan-Lumajang zone observed on this map. This is a common characteristic of megathrust zones that have the potential to produce "great megathrust earthquakes" such as those in Chile (1960, M9.5), Alaska (1964, M9.2), and Sumatra (2004, M9.1), which originate from subduction zones with similar characteristics (Scholl et al., 2015).

The long return period for these large earthquakes is consistent with the elastic rebound theory, which posits that plate movements undergo a phase of energy accumulation over a prolonged period and are released during a major earthquake (Lowrie, 2007). Additionally, this phenomenon is also supported by the Gutenberg-Richter Law in the frequency-magnitude relationship, which states that the frequency of earthquakes is inversely proportional to their magnitude. Thus, large earthquakes occur less frequently compared to small earthquakes (Aslamia & Supardi, 2022).

Seismotectonic Parameters a-value and b-value

The statistical parameters a-value and b-value based on the Gutenberg–Richter law are often used to interpret seismotectonic conditions. In several studies that have been conducted (Aslamia & Supardi, 2022;

Ernandi & Madlazim, 2020; Pakiding et al., 2025), both values are analyzed together because they can indicate the potential for significant earthquakes in a given area. a-value is a seismicity constant that describes the number of earthquake occurrences within a certain period, without considering the magnitude (Suwandi et al., 2017). Meanwhile, the b-value reflects the frequency distribution between large and small earthquakes. According to Pakiding et al. (2025), b-value is also related to tectonic conditions, as it reflects the magnitude of differential stress and the brittleness of rocks. A low b-value usually indicates high stress accumulation in relatively homogeneous and brittle zones (Taroni et al., 2021).

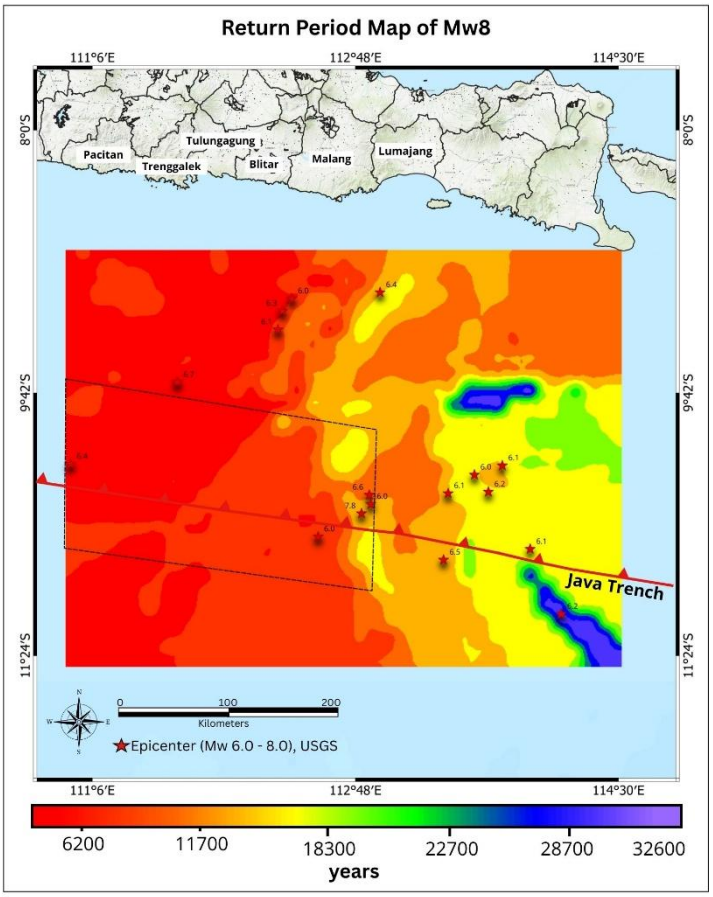

Figure 6. Spatial map of earthquake return period estimates for M_w8.

Based on the spatial distribution map of a-value and b-value produced, it appears that the Pacitan-Lumajang segment has a similar pattern, both being relatively lower compared to the surrounding segments. Regions with low a-values and low b-values are generally associated with locked megathrust zones, that is, zones where accumulated stress has not been released (Pakiding et al., 2025; Sandhu et al., 2022).

In Figure 7, the a-value in this segment mostly falls within the range of <9.5, with some areas reaching a minimum value close to 9. The low a-value reflects the generally low level of seismic activity in the area, as shown in the seismicity map (Figure 2) and the seismic cross-section B–B′ (Figure 3 (b)). The spatial decrease in a-value can also indicate the presence of a "seismic quiescence" zone, which is often associated with areas storing high stress (Katsumata & Nakatani, 2021).

Similarly, the b-value shown in Figure 8, the Pacitan-Lumajang segment is in the low range, which is <1.4, even reaching a minimum value of ~1.2 in several areas.

This characteristic is consistent with the area of minimal earthquake activity at the plate interface, as shown in the previous seismic cross-section results. This interpretation strengthens the suspicion that the segment is a locked segment with a high potential for the accumulation of unreleased seismic energy.

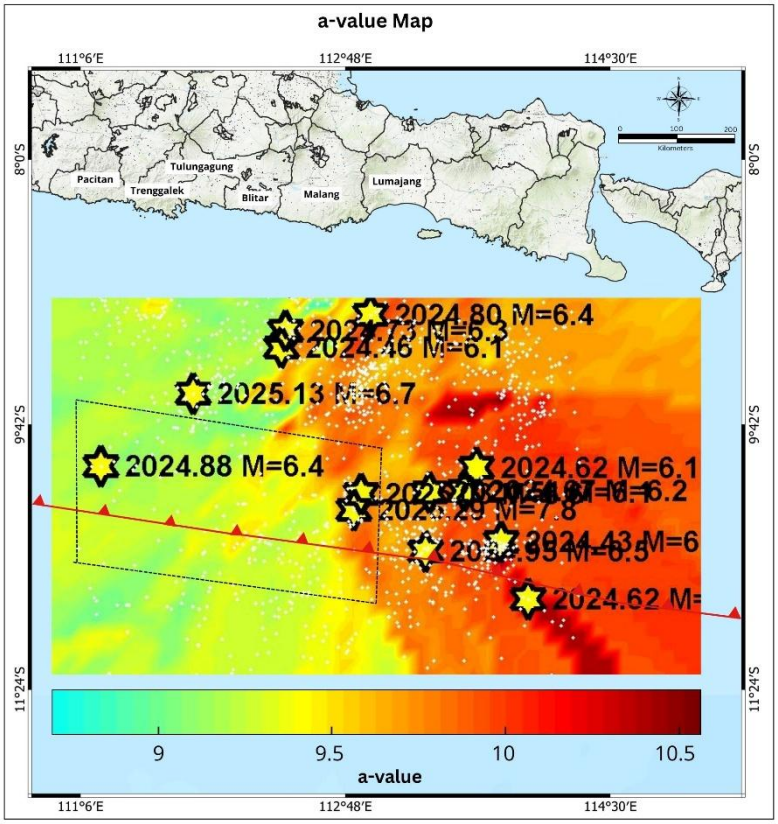

Figure 7. Spatial map of a-value reflecting the earthquake frequency in the research area.

These results are consistent with the study by Hisyam et al. (2024), which asserts that in East Java, the majority of significant earthquakes from 2002 to 2022 were preceded by a temporal decrease in b-value. The study also identified that the major earthquake on April 10, 2021 (M_w6.1) in Malang occurred in an area with a low b-value (~0.9), indicating that zones with low b-values are closely associated with the locations of major earthquakes. The low b-value in the Pacitan–Lumajang segment represents the potential for a major earthquake due to the high level of stress accumulation at the plate interface. Patterns like this are often associated with locked megathrust zones, as recorded in the Nankai, Chile, and Sumatra zones before major events (da Costa et al., 2024).

The correlation results between spatial parameters indicate that the Pacitan–Lumajang segment exhibits consistent seismotectonic characteristics, consistent with those of the seismic gap zone. The distribution of seismicity (Figure 2 and 3) shows that seismic activity in this region is very low, especially at depths of less than 70 km. Furthermore, the return period estimation map (Figure 4–6) reinforces this indication, dominated by shades of red to green in this zone. The long return period of major earthquakes, more than 200 years for M_w7 and more than 4,000 years for M_w8, indicates that significant seismic energy release has not occurred for a long time. This condition is further reinforced by the relatively low a-value distribution (<9.5), as well as the low b-value (<1.4), even approaching 1.2 at some points. The

combination of these two parameters indicates a low frequency of earthquake occurrences and a high accumulation of stress in the zone.

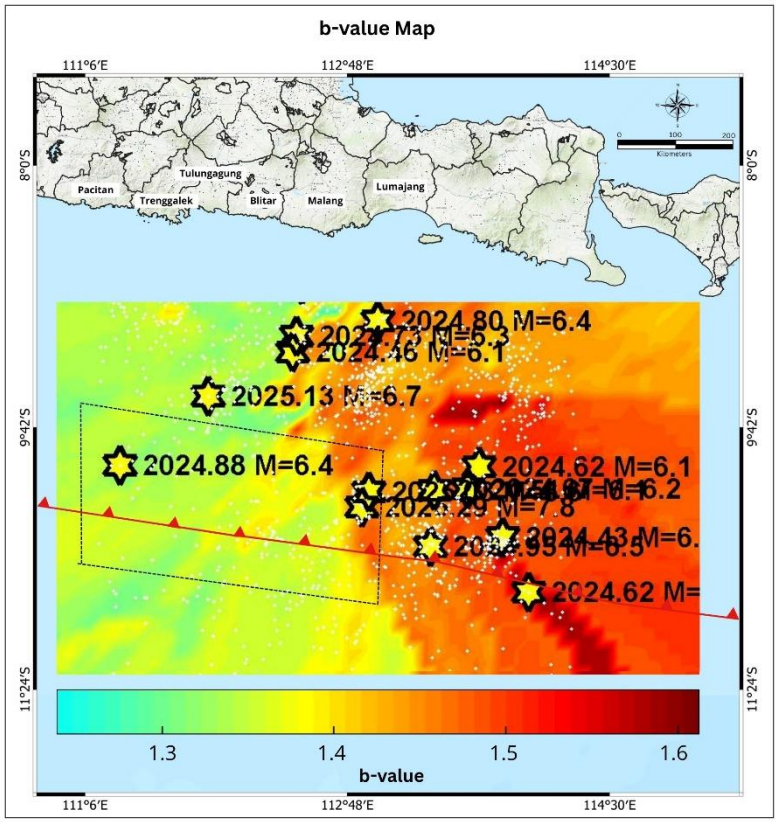

Figure 8. Spatial map of b-value reflecting the tectonic conditions in the research area.

The results of this study are consistent with Widiyantoro et al. (2020), which identified a slip deficit of 20–40 mm/year in a suspected seismic gap zone off the southern coast of East Java during the 2008–2014 geodetic observation period. This slip deficit serves as an indicator of a locked segment, which is likely experiencing significant accumulation of tectonic stress that has yet to be released. According to the study, if this segment were to release its stored energy suddenly, it could generate an earthquake with a potential magnitude of M_w8.8.

The integration of the three parameters, which include low seismicity, long return periods, and relatively low a-value and b-value, supports the interpretation that the Pacitan–Lumajang segment is a seismic gap zone. Suppose a megathrust earthquake occurs in this segment, the southern coastal areas of East Java, including Pacitan, Trenggalek, Tulungagung, Blitar, Malang, and Lumajang, are at risk of experiencing significant impacts on infrastructure and population.

Conclusion

This research successfully characterized spatially the Pacitan-Lumajang segment in the southern subduction zone of East Java, which is suspected to be a seismic gap zone. The integration of three main approaches, which are seismicity analysis, return period estimation, and evaluation of seismotectonic parameters such as a-value and b-value, results in a consistent spatial picture. The seismicity distribution map and cross-section show less earthquake activity on the interface, a long return period for major earthquakes, which is >200 years for M_w7 and >4,000 years for M_w8, as well as relatively low a-value and b-value. The high-resolution spatial

approach used, along with the integration of long-term data (1910–2025), significantly contributes to mapping the seismic potential in greater detail. Although this study is limited to instrumental earthquake data, the results of this study are expected to provide an initial contribution to mapping the spatial distribution of seismic activity and serve as initial considerations in megathrust and tsunami disaster risk assessments in the southern coastal areas of Java.

Acknowledgements

The authors would like to thank the Meteorological, Climatological, and Geophysical Agency (BMKG) and the United States Geological Survey (USGS) for providing earthquake data used in this study.

Technical support from BMKG facilities was also essential in preparing and validating the seismological analysis. This study did not receive specific external funding.

Author Contribution

Diva Maharani Putri contributed to the study through Conceptualization, Formal Analysis, Investigation, and Writing – original draft. Nanda Maharani was responsible for Data curation and Visualization. Ilham and Riska Yulinda contributed to Validation, Supervision, and Writing – review & editing.

Conflict of Interest

The authors declare no conflict of interest.

References

Adam, C., Vidal, V., Grosse, P., & Ichihara, M. (2022). Correlations Between Subduction of Linear Oceanic Features and Arc Volcanism Volume Around the Pacific Basin. *Geochemistry, Geophysics, Geosystems,* 23(12), e2022GC10553. https://doi.org/10.1029/2022GC010553

Aribowo, S., Husson, L., Natawidjaja, D. H., Authemayou, C., Daryono, M. R., Puji, A. R., Valla, P. G., Pamumpuni, A., Wardhana, D. D., de Gelder, G., Djarwadi, D., & Lorcery, M. (2022). Active Back-Arc Thrust in North West Java, Indonesia. *Tectonics*, 41(7), e2021TC007120. https://doi.org/10.1029/2021TC007120

Artemieva, I. M. (2023). Back-arc basins: A global view from geophysical synthesis and analysis. *Earth-Science Reviews*, 236, 104242. https://doi.org/10.1016/j.earscirev.2022.104242

Aslamia, H., & Supardi, Z. A. I. (2022). Analisis Parameter a-Value dan b-Value sebagai Mitigasi Bencana Gempa Bumi di Nusa Tenggara Timur. *Jambura Physics Journal*, 4(1), 14–27. https://doi.org/10.34312/jpj.v4i1.13815

Bazrafshan, A., Khaji, N., & Paolucci, R. (2024). On the effect of background seismicity in physics-based earthquake simulations. *Journal of Asian Earth Sciences*, 274, 106261. https://doi.org/10.1016/j.jseaes.2024.106261

Bilek, S. L., & Lay, T. (2018). Subduction zone megathrust earthquakes. *Geosphere*, 14(4), 1468–1500. https://doi.org/10.1130/GES01608.1

da Costa, J., Maryanto, S., Juwono, A. M., Pires, J., Almeida, G. P. d. S., & da Costa, L. T. (2024). Preliminary Study of a-value and b-value of Earthquake at Timor Leste Period 1975 – 2022. 10(SpecialIssue), 711–718. https://jppipa.unram.ac.id/index.php/jppipa/article/view/8578

Dong, M., Hao, T., Xu, L., Zhang, J., Zhang, J., Lü, C. C., & He, Q. (2024). Subduction without volcanic arc magma: Insights from two young

subduction zones in the western Pacific. *Tectonophysics*, 874, 230231. https://doi.org/10.1016/j.tecto.2024.230231

Ernandi, F. N., & Madlazim, M. (2020). Analisis Variasi a-Value dan b-Value dengan Menggunakan Software Zmap V.6 sebagai Indikator Potensi Gempa Bumi di Wilayah Nusa Tenggara Barat. *Jurnal Inovasi Fisika Indonesia*, 9(3), 24–30. https://doi.org/10.26740/ifi.v9n3.p24-30

Gardner, J. K., & Knopoff, L. (1974). Is the sequence of earthquakes in Southern California, with aftershocks removed, Poissonian?. *Bulletin of the Seismological Society of America*, 64(5), 1363–1367. https://doi.org/10.1785/BSSA0640051363

Godang, S., Saputro, S. P., & Li, H. (2024). The slab failure in Central Java (Indonesia): New insight into its tectonic setting and origin. *Solid Earth Sciences*, 9(3), 100199. https://doi.org/10.1016/j.sesci.2024.100199

Gunawan, E., Meilano, I., Hanifa, N. R., & Widiyantoro, S. (2017). Effect of coseismic and postseismic deformation on homogeneous and layered half-space and spherical analysis: Model simulation of the 2006 Java, Indonesia, tsunami earthquake. *Journal of Applied Geodesy*, 11(4), 207–214. https://doi.org/10.1515/jag-2017-0009

Gunawan, E., & Widiyantoro, S. (2019). Active tectonic deformation in Java, Indonesia inferred from a GPS-derived strain rate. *Journal of Geodynamics*, 123, 49–54. https://doi.org/10.1016/j.jog.2019.01.004

Gutenberg, B., & Richter, C. F. (1944). Frequency of Earthquakes in California. *Bulletin of the Seismological Society of America*, 34(4), 185–188. https://doi.org/10.1785/BSSA0340040185

Haerudin, N., Alami, F., & Rustadi, R. (2019). *Mikroseismik, Mikrotremor dan Microearthquake dalam Ilmu Kebumian*. Pusaka Media

Hayes, G. P., Moore, G. L., Portner, D. E., Hearne, M., Flamme, H., Furtney, M., & Smoczyk, G. M. (2018). Slab2, a comprehensive subduction zone geometry model. *Science*, 362(6410), 58–61. https://doi.org/10.1126/science.aat4723

Hisyam, F., Susilo, A., Anshori, M., & Hasan, M. F. R. (2024). Spatio-Temporal Variation Seismicity Pattern in East Java Between 2002 and 2022 Based on the b-value and Seismic Quiescence z-value. *Trends in Sciences*, 21(4), 7608. https://doi.org/10.48048/tis.2024.7608

Hollingsworth, J., Ye, L., & Avouac, J.-P. (2017). Dynamically triggered slip on a splay fault in the M_w 7.8, 2016 Kaikoura (New Zealand) earthquake. *Geophysical Research Letters*, 44(8), 3517–3525. https://doi.org/10.1002/2016GL072228

Hutchings, S. J., & Mooney, W. D. (2021). The Seismicity of Indonesia and Tectonic Implications. *Geochemistry, Geophysics, Geosystems*, 22(9), e2021GC009812. https://doi.org/10.1029/2021GC009812

Katsumata, K., & Nakatani, M. (2021). Testing the seismic quiescence hypothesis through retrospective trials of alarm-based earthquake prediction in the Kurile–Japan subduction zone. *Earth, Planets and Space*, 73, 100. https://doi.org/10.1186/s40623-021-01418-z

Lowrie, W. (2007). *Fundamental of Geophysics* (Second). Cambridge University Press.

https://doi.org/10.1017/CBO9780511807107 I

Lupi, M., De Gori, P., Valoroso, L., Baccheschi, P., Minetto, R., & Mazzini, A. (2022). Northward migration of the Javanese volcanic arc along thrust faults. *Earth and Planetary Science Letters*, 577, 117258. https://doi.org/10.1016/j.epsl.2021.117258

Maiti, S. K., & Kim, B. (2025). An Updated, Homogeneous, and Declustered Earthquake Catalog for South Korea and Neighboring Regions. *Natural Hazards and Earth System Sciences [preprint]*, 1–34. https://nhess.copernicus.org/preprints/nhess-2024-197/

Megawati, M., Ma, K.-F., Chen, P.-F., Sianipar, D., & Hsieh, M.-C. (2024). Source characterization of Intermediate-Depth earthquakes in southern Java, Indonesia. *Journal of Asian Earth Sciences*, *264*(128), 106040. https://doi.org/10.1016/j.jseaes.2024.106040

Menke, K. (2022). *Discover QGIS 3.x* (2nd Editio). Locate Press.

Ministry of Energy and Mineral Resources. (2025). *MAGMA Indonesia*. https://magma.esdm.go.id/

Mukti, M. M. (2018). Structural complexity in the boundary of forearc basin – accretionary wedge in the northwesternmost Sunda active margin. *Bulletin of the Marine Geology*, 33(1), 1–14. https://doi.org/10.32693/bomg.33.1.2018.536

Munandar, R. A., & Sulsaladin, R. (2022). Karakteristik Tektonik dan Periode Ulang Gempabumi pada Sesar Cimandiri Jawa Barat. *Buletin Metorologi, Klimatologi, Dan Geofisika*, 2(4), 42–51. https://balai2bmkg.id/index.php/buletin_mkg/article/view/30

Muttaqy, F., Nugraha, A. D., Mori, J., Puspito, N. T., Supendi, P., & Rohadi, S. (2022). Seismic Imaging of Lithospheric Structure Beneath Central-East Java Region, Indonesia: Relation to Recent Earthquakes. *Frontiers in Earth Science*, 10, 756806. https://doi.org/10.3389/feart.2022.756806

Noda, A. (2016). Forearc basins: Types, geometries, and relationships to subduction zone dynamics. *Bulletin of the Geological Society of America*, 128(5–6), 879–895. https://doi.org/10.1130/B31345.1

Pakiding, A., Maulana, A., & Azikin, B. (2025). Analysis of a-Value and b-value parameters for earthquake disaster mitigation around the Saddang Fault. *IOP Conference Series: Earth and Environmental Science*, 1462(1), 012041. https://doi.org/10.1088/1755-1315/1462/1/012041

Pasari, S., Simanjuntak, A. V. H., Mehta, A., Neha, N, & Sharma, Y. (2021). The Current State of Earthquake Potential on Java Island, Indonesia. *Pure and Applied Geophysics*, 178(8), 2789–2806. https://doi.org/10.1007/s00024-021-02781-4

Patria, A., & Aulia, A. N. (2020). Structural And Earthquake Evaluations Along Java Subduction Zone, Indonesia. *RISET Geologi Dan Pertambangan*, 30(1), 65–79. https://jrisetgeotam.brin.go.id/index.php/jrisgeotam/article/view/1072

Pratap, R. (2010). *Getting Started with MATLAB A Quick Introduction for Scientists and Engineers*.

Pusat Studi Gema Nasional (PuSGeN). (2022). *Peta Deagregasi Bahaya Gempa Indonesia*. https://sitaba.pu.go.id/user/file/2024_12_19_02_22_36.909104_file.pdf

Putra, F. P., Apriliani, E., & Handoko, E. Y. (2019). Estimation the Height of Tsunami Waves in the Southern Island

of Java Using Ensemble Kalman Filter Method. *Proceedings of the International Conference on Electrical Engineering and Informatics*, 477–482. https://doi.org/10.1109/ICEEI47359.2019.8988859

Rakuasa, H., & Pakniany, Y. (2024). *Assessing the Probability of Megathrust Earthquakes in Indonesia : A Review of Seismic Hazard Assessment and Mitigation Strategies*. *Journal of Loomingulisus Ja Innovatsioon*, 1(3), 98–116. https://journal.ypidathu.or.id/index.php/innovatsioon/article/view/1275

Rehman, A., & Zhang, H. (2024). Seismicity and return period investigation of destructive earthquake in Makran subduction zone. *Discover Geoscience*, 2, 40. https://doi.org/10.1007/s44288-024-00047-9

Sandhu, M., Yadav, R. B. S., Kumar, R., Baruah, S., Singh, A. P., Mishra, M., & Yadav, J. S. (2022). Spatial variability of earthquake hazard parameters, return periods and probabilities of earthquake occurrences in the eastern Himalayan seismic belt. *Physics and Chemistry of the Earth Parts A/B/C*, 127, 103194. https://doi.org/10.1016/j.pce.2022.103194

Scholl, D. W., Kirby, S. H., von Huene, R., Ryan, H., Wells, R. E., & Geist, E. L. (2015). Great (≥Mw8.0) megathrust earthquakes and the subduction of excess sediment and bathymetrically smooth seafloor. *Geosphere*, 11(2), 236–265. https://doi.org/10.1130/GES01079.1

Siregar, U. K., Sirait, R., & Lubis, L. H. (2023). Identifikasi Tingkat Kerapuhan Batuan (b-Value) dengan Menggunakan Metode Likelihood di Wilayah Sumatera Utara Periode 1990-2021. *Jurnal Kumparan Fisika*, 6(1), 37–46. https://doi.org/10.33369/jkf.6.1.37-46

Sribudiyani, S., Prasetya, I., Muchsin, N., Sapiie, B., Ryacudu, R., Asikin, S., Kunto, T., Harsolumakso, A. H., Astono, P., & Yulianto, I. (2003). The collision of east java microplate and its implication for hydrocarbon occurences in the east Java basin. *Proceesdings, Indonesian Petroleum Association, Twenty-Ninth Annual Convention & Exhibition October 2003*. https://www.researchgate.net/publication/285848798

Soehaimi, A., Sopyan, Y., Ma'mur, M., & Agustin, F. (2021). *Active Fault Map of Indonesia (Peta Patahan Aktif Indonesia)*. Directorate of Settlement and Housing Engineering Development Directorate General of Human Settlements Ministry of Public Works and Public Housing. https://geologi.esdm.go.id/geomap/pages/preview/peta-patahan-aktif-indonesia.

Suwandi, E. A., Sari, I. L., & Waslaluddin, W. (2017). Analisis Percepatan Tanah Maksimum, Intensitas Maksimum Dan Periode Ulang Gempa Untuk Menentukan Tingkat Kerentanan Seismik di Jawa Barat (Periode Data Gempa Tahun 1974-2016). *Wahana Fisika*, 2(2), 78–96. https://doi.org/10.17509/wafi.v2i2.9371

Taroni, M., Vocalelli, G., & De Polis, A. (2021). Gutenberg–Richter B-Value Time Series Forecasting: A Weighted Likelihood Approach. *Forecasting*, *3*(3), 561–569. https://doi.org/10.3390/forecast3030035

Utsu, T. (1966). A Statistical Significance Test of the Difference in b-value Between Two Earthquake Group. *Journal of Physics of The Earth*, 14(2), 37–40. https://doi.org/10.4294/jpe1952.14.37

van Zelst, I., Rannabauer, L., Gabriel, A. -A., & van Dinther, Y. (2022). Earthquake Rupture on Multiple Splay

Faults and Its Effect on Tsunamis. *Journal of Geophysical Research: Solid Earth*, 127(8), e2022JB024300. https://doi.org/10.1029/2022JB024300

Wessel, P., Luis, J. F., Uieda, L., Scharroo, R., Wobbe, F., Smith, W. H. F., & Tian, D. (2019). The Generic Mapping Tools Version 6. *Geochemistry, Geophysics, Geosystems*, 20(11), 5556–5564. https://doi.org/10.1029/2019GC008515

Wetzler, N., Lay, T., Brodsky, E. E., & Kanamori, H. (2017). Rupture-Depth-Varying Seismicity Patterns for Major and Great (Mw ≥ 7.0) Megathrust Earthquakes. *Geophysical Research Letters*, 44(19), 9663–9671. https://doi.org/10.1002/2017GL074573

Wickham-Piotrowski, A., Font, Y., Regnier, M., Delouis, B., Nocquet, J. M., De Barros, L., Durand, V., Bletery, Q., & Segovia, M. (2024). Intraslab seismicity migration simultaneously with an interface slow slip event along the Ecuadorian subduction zone. *Tectonophysics*, 883, 230365. https://doi.org/10.1016/j.tecto.2024.230365

Widagdo, A., Pramumijoyo, S., & Harijoko, A. (2018). Morphotectono-volcanic of Tertiary volcanic rock in Kulon Progo mountains area, Yogyakarta-Indonesia. *IOP Conference Series: Earth and Environmental Science*, 212(1), 012051. https://doi.org/10.1088/1755-1315/212/1/012051

Widiyantoro, S., Gunawan, E., Muhari, A., Rawlinson, N., Mori, J., Hanifa, N. R., Susilo, S., Supendi, P., Shiddiqi, H. A., Nugraha, A. D., & Putra, H. E. (2020). Implications for megathrust earthquakes and tsunamis from seismic gaps south of Java Indonesia. *Scientific Reports*, 10, 1–11. https://doi.org/10.1038/s41598-020-72142-z

Wyss, M., Wiemer, S., & Zúñiga, R. (2001). *ZMAP A Tool For Analyses of Seismicity Patterns Typical Applications and Uses : A Cookbook*.

Xia, Y., Geersen, J., Klaeschen, D., Ma, B., Lange, D., Riedel, M., Schnabel, M., & Kopp, H. (2021). Marine forearc structure of eastern Java and its role in the 1994 Java tsunami earthquake. *Solid Earth*, 12(11), 2467–2477. https://doi.org/10.5194/se-12-2467-2021

Xie, F., Wang, Z., Zhao, D., Gao, R., & Chen, X. (2023). Seismic imaging of the Java subduction zone: New insight into arc volcanism and seismogenesis. *Tectonophysics*, 854, 229810. https://doi.org/10.1016/j.tecto.2023.229810

Zaliapin, I., & Ben-Zion, Y. (2020). Earthquake Declustering Using the Nearest-Neighbor Approach in Space-Time-Magnitude Domain. *Journal of Geophysical Research: Solid Earth*, 125(4), e2018JB017120. https://doi.org/10.1029/2018JB017120

Zhou, P., & Xia, S. (2020). Effects of the heterogeneous subducting plate on seismicity: Constraints from b-values in the Andaman–Sumatra–Java subduction zone. *Physics of the Earth and Planetary Interiors*, 304, 106499. https://doi.org/10.1016/j.pepi.2020.106499

ISSN: 2579-5821 (Print)
ISSN: 2579-5546 (Online)
URL address: http://journal.unhas.ac.id/index.php/geocelebes
DOI: 10.70561/geocelebes.v9i2.43347

Jurnal Geocelebes Vol. 9 No. 2, October 2025, 157 – 170

HVSR Microtremor Analysis to Assess Subsurface Fault Characteristics and Geothermal Potential in Kepahiang

Muhammad Rifqi Rabbani, Arif Ismul Hadi, Budi Harlianto, Muchammad Farid, Hana Raihana, Arya Putra Anggi

Faculty of Mathematics and Natural Sciences, Universitas Bengkulu, Bengkulu 38371, Indonesia.

*Corresponding author. Email: ismulhadi@unib.ac.id

Manuscript received: 27 February 2025; Received in revised form: 5 May 2025; Accepted: 8 September 2025

Abstract

Kepahiang, Bengkulu, is an area with considerable geothermal potential, especially in the Air Sempiang and Babakan Bogor areas. This study aims to analyze subsurface fault characteristics and assess geothermal potential using the Horizontal-to-Vertical Spectral Ratio (HVSR) microtremor method. This passive seismic method is used to determine key geophysical parameters, including dominant frequency (f_0), amplification factor (A_0), shear wave velocity (v_s), and primary wave velocity (v_p), which are essential for characterizing subsurface geological structures and identifying geothermal reservoir zones. The results show that dominant frequency values in Kepahiang range from 1.24 Hz to 20.45 Hz, while the amplification factor varies between 1.29 and 7.22. v_s values range from 121.61 m/s to 3251.79 m/s, and v_p values range from 214.91 m/s to 6469.79 m/s. These findings suggest that the surface layer consists mainly of alluvium and hard sandy gravel, with thicknesses varying between 10 and 50 meters. The 3D subsurface model constructed from the data indicates the presence of fault-controlled geothermal manifestations, mainly influenced by the Babakan Bogor Fault and Bogor Fault. These faults facilitate the upward migration of geothermal fluids, forming surface manifestations such as hot springs, fumaroles, and altered rocks. The geothermal system in the study area is classified as a low-temperature geothermal system, mainly caused by residual magmatic heat from Kaba Mountain and Bukit Hitam Crater. This research provides important insights for geothermal energy exploration and geotourism development in Kepahiang. These findings serve as a scientific basis for future geothermal resource assessment, land use planning, and sustainable energy utilization.

Keywords: Air Sempiang; Fault; Geothermal; Microseismic.

Citation: Rabbani, M. R., Hadi, A. I., Harlianto, B., Farid, M., Raihana, H., & Anggi, A. P. (2025). HVSR Microtremor Analysis to Assess Subsurface Fault Characteristics and Geothermal Potential in Kepahiang. *Jurnal Geocelebes*, 9(2): 157–170, doi: 10.70561/geocelebes.v9i2.43347

Introduction

Indonesia is included in the “ring of fire”, where three plates meet, the Pacific, Eurasian and Indo-Australian tectonic plates. Being right below the equator between two continents and two large oceans makes for a wealth of potential natural resources such as geothermal energy (Fransiska, 2019). Indonesia's geothermal potential is currently very large, which is 40% of the total potential in the world that has been explored around 276 geothermal areas spread across 26 provinces with a total energy of 28.99 GW, but the energy developed only reaches 196 MW, or about 4% of the total energy potential. Geothermal energy is one type of renewable energy that is owned by Indonesia in a very large amount of potential (Bilondatu et al., 2021). The Kepahiang geothermal area is located in the Kepahiang and Rejang Lebong regencies, Bengkulu Province which is a high volcanic area and is on the subduction line in the magmatic arc area located in the west of Sumatra Island. Geologically, the study area generally has andesite-basaltic rock types that are closely related to magmatic

activity in the hill Barisan range. The formation of rock formations in the Bukit Kaba area is influenced by tectonic activity in the direction of the Sumatra fault pattern which is southwest to northeast. Hot fluids in the Kepahiang geothermal system are bicarbonate and sulfate types in the immature water zone (Raharjo et al., 2022).

At the research location not only has geothermal potential, this location can also be made as a place that has the potential as geotourism which is quite supportive because of the hot springs in the research area. Indrayati & Setyaningsih (2017) defines geotourism as sustainable tourism with a primary focus on the evolution of the earth and its geological features that promotes environmental and cultural understanding, appreciation and conservation, and benefits local communities (Andriany et al., 2016). The scope of geotourism spans the scale of geological and geomorphological features, from mountains and coasts to smaller scales, such as the built environment and geological outcrops. It can occur in a variety of locations from natural areas to urban environments and includes geoparks and geosites, as well as buildings and monuments with geological associations. Geotourism is related to ecotourism, cultural tourism and adventure tourism but is not the same as these three types of tourism. Geotourism focuses on creating products to introduce and protect geological heritage, as well as building a community (Indrayati & Setyaningsih, 2017).

Parameters that determine the prospect area in the geothermal field are characterized by the presence of manifestations in the form of hot springs, geothermal manifestations appear due to the propagation of heat from the subsurface or the presence of fractures that can flow fluid to the surface (Ratag et al., 2022). Based on Ramadhan & Massinai (2022), the higher the surface temperature, the more likely the area has geothermal potential. The recorded surface temperature can be interpreted as the outer temperature of the object. In areas with low to moderate vegetation, the surface temperature is the temperature of the outermost layer of the soil surface, while areas with high levels of vegetation such as forests can be interpreted as the surface temperature of plants.

One of the areas that has the potential for hot springs is Babakan Bogor and Air Sempiang Village, Kepahiang Regency, Bengkulu Province. The existence of secondary permeability in the form of the Musi fault, more precisely the Bogor fault, affects the existence of geothermal manifestations in the study area. Subsurface faults are difficult to identify, one of the geophysical methods that are good enough to map subsurface conditions to determine the structure of layers and faults. This method is also a good indicator to identify fault-related structures. These faults control the hot fluids in the reservoir to flow to the surface in the form of hot springs, rock alteration, and emerging fumaroles. The Kepahiang geothermal prospect area is located 90 km northeast of Bengkulu city, which is in Bengkulu Province. The area is located on a subduction line in the western part of the Sumatra magmatic arc in the tectonic setting of western Indonesia. The volcanic activity that developed in the ring of fire of Sumatra Island, especially Mount Kaba, is responsible for the existence of geothermal systems in this area (Fahmi et al., 2015).

Previous research on hot springs in Kepahiang Regency has also been conducted by Simbolon et al. (2020). Indications of geothermal systems in this area are characterized by the appearance of manifestations such as hot water with the highest temperature of 94°C, neutral pH, solfatara and fumaroles with temperatures up to 360ºC and rock alteration around Air Sempiang, Kaba peak, and hot springs in the Sempiang and Babakan Bogor areas. Faults that were not visible in the initial

seismic data can be more clearly identified in the vertical and horizontal cross sections. To show the discontinuities more clearly on the seismic cross section, this attribute combines more than two seismic traces to highlight the seismic lateral changes caused by the different geological conditions (Darma & Pujiastuti, 2021). Geological data of the Kepahiang geothermal area shows the presence of impermeable rocks with a high content of montmorillonite and kaolinite clay minerals in the alteration area around the Air Sempiang manifestation. The alteration rocks formed are argillic to advanced argillic types. The alteration appears in pyroclastic flows and lava products of the mountain. However, research in the research area focuses on Kepahiang Regency, whereas many more specific geothermal manifestations are thought to originate from Kaba Hill (Ramadhan & Massinai, 2022).

In geothermal reservoirs, hydrothermal distribution is significant. One geophysical method that is quite good at mapping subsurface conditions to determine geothermal distribution is the passive seismic method, which is microseismic (Rasimeng et al., 2024). This method aims to study the variation of secondary wave specific gravity through rock inversion in the subsurface of the earth, so as to produce a one-dimensional profile of the subsurface and is used to describe the variation of specific gravity values with depth in a multi-layered subsurface resistivity structure, this research is expected to model in 1 dimension and map the distribution of geothermal manifestations due to faults with data processing using Geopsy and HV-Inv software. This software is used because the software is freely accessible, and the data processing process does not take a long time (Purnomo, 2019).

The emergence of geothermal heat is influenced by the existence of faults that act as pathways for hot fluids from the earth to the surface. These faults are formed due to the movement of tectonic plates that cause cracks or fractures in the earth's crust, allowing heat and geothermal fluids to move upwards. This research aims to identify faults that function as the main conduit for hot fluids, which contribute to the emergence of geothermal manifestations in Air Sempiang. Focus on geothermal distribution is also needed if the government wants to develop regional geotourism, therefore, further research is needed to see the geothermal distribution and determine the type of rock in Babakan Bogor Village, Kepahiang Regency, Bengkulu Province. This study is also expected to provide recommendations for strategic steps that can be taken by the Indonesian government as a solution to geothermal energy exploration activities, based on previous efforts made by the government.

Geology Setting

Kepahiang Regency is located in the border area of the magmatic arc and the continental plate with the oceanic plate which resulted in the emergence of several geothermal manifestations on the surface in the form of solfatara, fumarole, and alteration rocks so that it becomes a geothermal energy prospect (Sihombing et al., 2024). The rock formation of the Kepahiang area is dominated by volcanic rocks so that the Kepahiang district is found in many igneous rocks because of its close proximity to volcanoes such as Kaba hill and foothills of Kaba (Firdasari, 2018). At the location of this study, geothermal manifestations in the Babakan Bogor and Air Sempiang areas that appear hot water manifestations are indicated due to the Babakan Bogor Fault and the Bogor Fault, causing geothermal manifestations in Air Sempiang (Fahmi et al., 2015). According to the geological information can be seen in the geology in Figure 1. In the alteration area around the Air Sempiang manifestation, there are rocks that have impermeable properties with a high content of montmorillonite and kaolinite type clay

minerals, according to the geological data of the Kepahiang geothermal area. The alteration rocks are argillic to advanced argillic types. These host rocks are located in the area of the Sempiang fault structure that runs almost north south, where pyroclastic flows and lava products of Mount Kaba show alteration. In addition to the alteration data, the massive and not yet strongly domed Kaba product lavas are an additional potential for the cap rock (Raharjo et al., 2022). At the research location, the rock formation is dominated by the volcanic Kaba rock type.

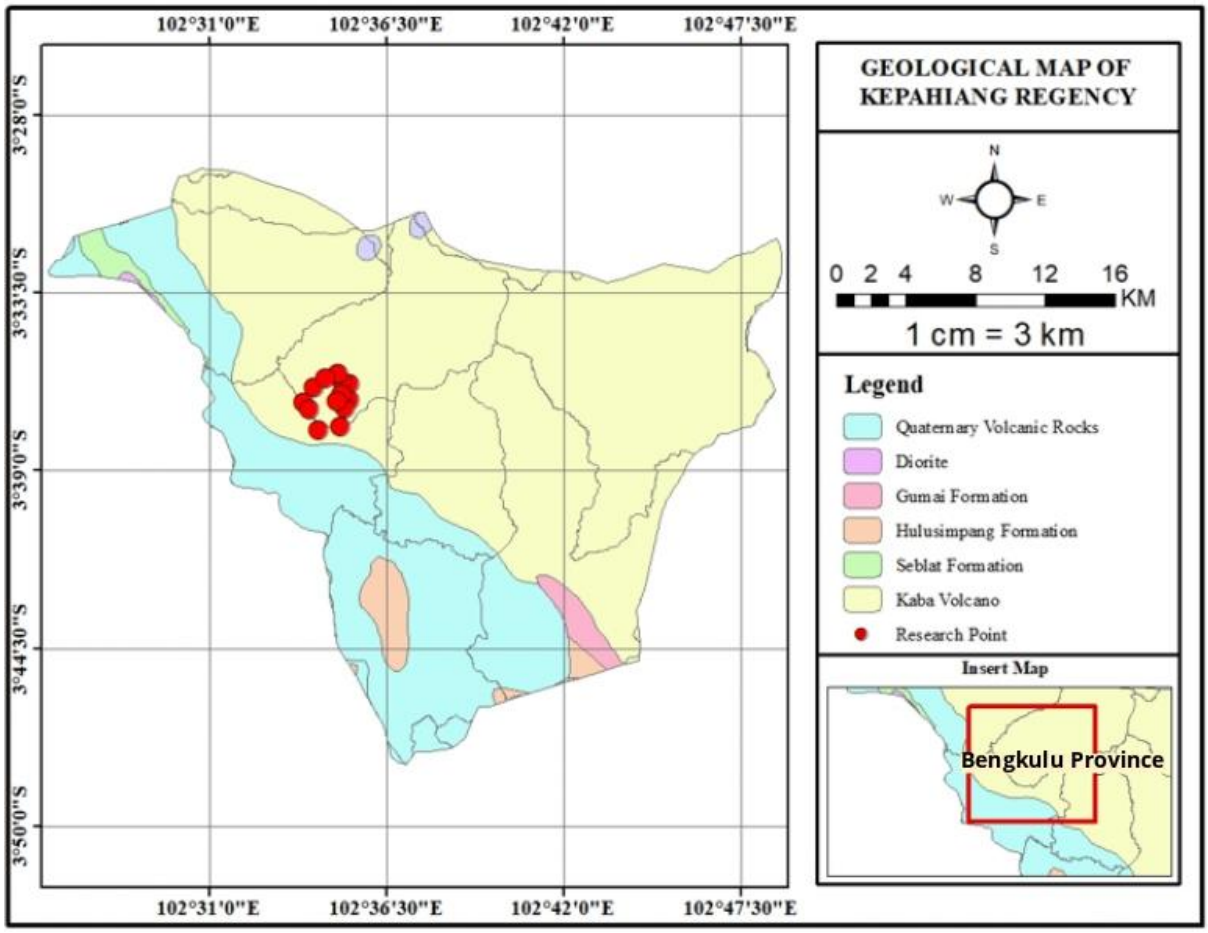

Figure 1. Geological map of Kepahiang regency.

The geology of Kepahiang hot springs clearly shows the presence of impermeable rocks with high concentrations of montmorillonite and kaolinite mineral types around the alteration zone at Air Sempiang. The altered rocks are mainly argillic to argillic rocks. This alteration is the result of pyroclastic flows and lava from Mount Kaba. These host rocks are located in the zone of the north-south trending Sempiang fault structure. The young, massive lava products of Kaba that have not been widely exposed are also classified as host rocks (Sihombing & Rustadi, 2018).

Materials and Methods

This research will be conducted in Kepahiang Regency, Bengkulu Province. In this study, 90 measurement points will be carried out which can be seen in Figure 2.

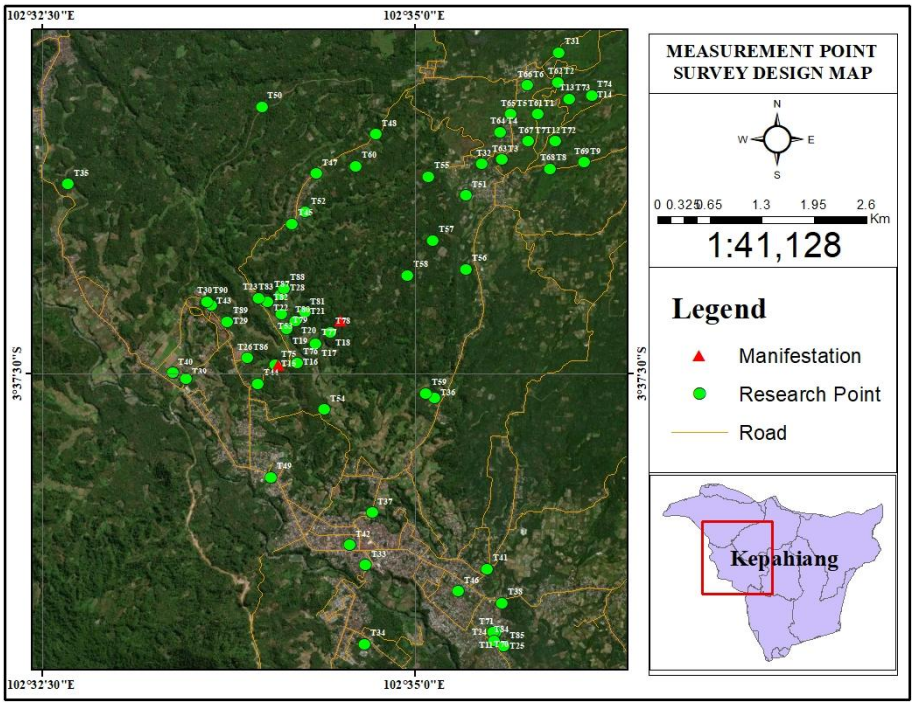

Figure 2. Map of research point location.

This research uses the microtremor method which measures very small and continuous ground vibrations sourced from various kinds of vibrations such as traffic, wind, human activity and others (Arifin et al., 2014). Research using microtremors can determine the characteristics of the soil layer based on the parameters of its dominant period and its wave amplification factor (amplification). Microtremor has a higher frequency. Microtremor recording is array based F-K method, Spacial Auto Correlation and Refraction (SPAC) microtremor and HVSR/ Nakamura methods (Arintalofa et al., 2020). Microtremor data that has obtained frequency curves and amplification values along with examples of HVSR curves as for the equation in obtaining HVSR results as follows (Arintalofa et al., 2020):

$$HVSR(f) = \frac{\sqrt{H_x^2(f)+H_y^2(f)}}{2 \cdot V(f)} \quad (1)$$

$Hx(f), Hy(f) Hy(f)$: spectral amplitude of horizontal component of microtremor at frequency ff

$V(f)$: spectral amplitude of the vertical component.

$HVSR(f)$: the value of spectral ratio at frequency ff from data processing with Geopsy software (Arintalofa et al., 2020) as shown below (Figure 3).

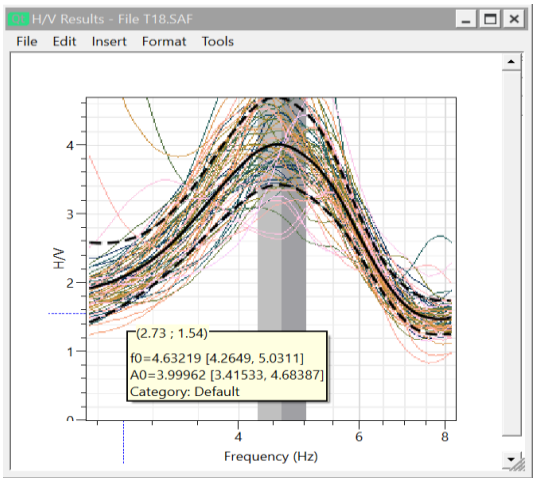

Figure 3. H/V curve graph processed using Geopsy software.

Then entered into the Hv-Inv software in the form of processed data results. The Hv-Inv application is a MATLAB-based computer application developed by Garcia-Jerez et al. (2016), which is used to analyze and model subsurface structures using the Monte Carlo (MC) principle, then analyzed using Monte Carlo simulation to get the most suitable curve. The curve is said to be

suitable if the misfit value obtained is small and the H/V graph coincides. In the data processing with HV-Inv, the parameters of thickness, shear wave velocity, and rock density were obtained The Site Effect (TSITE) on the surface of a sediment layer, usually described as by comparing the amplification factors of horizontal and vertical motion at the sedimentary soil surface (Setyowati et al., 2024).

$$T_{SITE} = \frac{T_H}{T_V} \quad (2)$$

$$T_H = \frac{S_{HS}}{S_{HB}} \quad (3)$$

where SHS represents the spectrum of the horizontal motion component at the surface, and SHB represents the spectrum of the horizontal motion component at the bottom of the soil layer (Setyowati et al., 2024). Data collection in the field needs to do a literature study and also look for information related to geological data at the research site or with regard to previous research that has been done as supporting research data and make a survey design as an initial benchmark before taking field data. This microtremor data collection is based on the Site Effects Assessment Using Ambient Using Ambient Excitations (SESAME) standard. According to Bard et al. (2004), The length of the data recording process in the field will be able to provide good results if the dominant frequency (f_0) at the data collection site obtains fairly low results. So that in the field data collection, 30 minutes of data is taken for each location (Hadi et al., 2021). Microtremor is passive seismic that uses a three-component seismometer to observe spectral anomalies. The seismometer used in this research has a fairly high sensitivity, so it is very important to avoid disturbances (noise) that will be able to damage the data during recording. Before collecting data, make sure the data collection location is not close to plant roots and other disturbances that can make the data less accurate and need to pay attention to the surrounding soil must be flat (Diah et al., 2024).

Data processing is done by inputting microtremor recording data on imported signals. The data obtained is in the form of data that shows frequency, therefore it is necessary to convert the field data from the time domain to the frequency domain, then a cutting process is carried out which aims to cut noise data, after the cutting process, the data is processed with Geopsy software, to obtain HVSR curve modeling. HVSR is a geophysical method that can solve the problem of identifying the response of subsurface layers. This data processing method can produce the dominant frequency value (f_0), H/V curve, period, and peak amplification value (A_0). Furthermore, the inversion process using HV-Inv software aims to obtain the value of secondary wave velocity (v_s), primary wave velocity (v_p), and depth value (A_0) (Nurwidyanto et al., 2023). So that it can be used to identify subsurface structures in geothermal prospect areas in Kepahiang Regency.

Results and Discussion

Based on Table 1 below, which explains the range of v_s and v_p values based on depth values that apply in all locations, so this can be a reference in research locations that are dominated by volcanic rocks.

Table 1. Classification of velocity **(v_s)** and (v_p) values by depth in all areas with volcanic rocks (Kamil, 2020).

Depth (km)	v_p (km/s)	v_s (km/s)
2.0	5.80	3.46
20.0	5.80	3.46
27.0	6.50	3.85
35.0	6.50	3.85
56.0	8.04	4.48
77.0	8.04	4.49
>77.0	8.05	4.50

Dominant Frequency Value (f_0)

The f_0 value obtained from the processing results using geopsy software can be seen in Figure 4 and Table 2.

Table 2. Rock classification value based on dominant frequency value (f_0) (Yogaswara & Kuncahyani, 2024).

Soil classification		Frequency Natural (*Hz*)	Kanai classification	Description	Measurement Point	Color
Type	Type					
IV	I	6.667-20	Tertiary or older rocks. Consists of Hard sandy rocks, gravel and others.	The thickness of surface sediments is very thin, dominated by hard rocks.	1,2,3,4,6,7,8,9,11, 14,16,17,23,25,26, 30,31,33,34,35,38, 41,46,50,51,52,53, 54,55,56,57,58,59, 60,61,64,65,67,75, 80,81,8286,87,88,	
III	II	4.0-6.667	Tertiary or older rocks. Consists of Hard sandy rocks, gravel and others.	Surface sediment thickness falls into the medium category 5-10 m	13,18,20,21,22,28, 43,44,45,48,49,66, 72,74,77,79,83,85 89	
II	III	2.5-4.0	Alluvial rocks, with a thickness of more than 5m. Consists of sandy hard clay, loam and others.	The thickness of surface sediments is categorized as thick, about 10-30m.	10,19,24,27,29,32,36, 37,39,40,42,47,69,71, 76,78,84,90	
I	IV	< 2.5	Alluvial rocks, formed from sedimentation of deta, top soil, mud and others. Depth ≥ 30m.	Surface sediment thickness is very thick	5,12,15,62,68,70,73,	

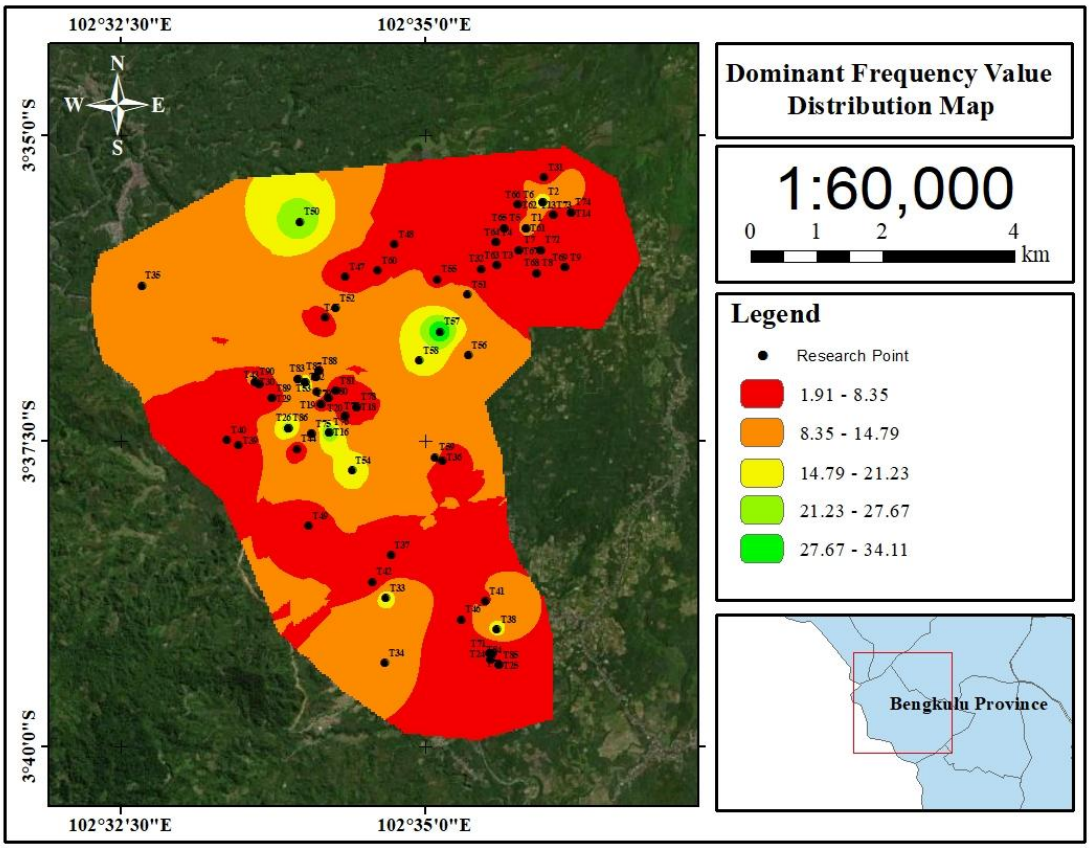

Figure 4. Rock classification value based on dominant frequency value (f_0).

Referring to the dominant frequency classification table and also the distribution map (f_0), it can be interpreted that the dominant frequency value with a large value can be said to be a fairly dense rock type while the dominant frequency value with a small value is assumed to have a fairly thick sediment layer or soft rocks such as alluvial rock types, at the research location is dominated by rocks that have a thin sediment thickness, usually consisting of igneous rocks in the form of volcanic rocks and granite. So, it can be concluded that the research location has a dense rock type because the research location is near the volcano zone.

The A_0 designation indicates the amplification of seismic waves resulting from significant differences between geological layers. Table 3 presents a classification based on the magnitude of the amplification values, as illustrated in Figure 5. The amplification value distribution map in Figure 4 shows that the Air Sempiang area, the amplitude values range from 1.29 to 7.22 times. According to Setianegara et al. (2023), amplification values are categorized into four risk levels, namely low risk ($0 < A_0 < 3$ times), medium risk ($3 < A < 6$ times), medium risk ($3 < A_0 < 6$ times), high risk ($6 < A_0 < 9$ times), and very high risk ($A_0 > 9$ times) (Risa et al., 2023).

Amplification Value (A_0)

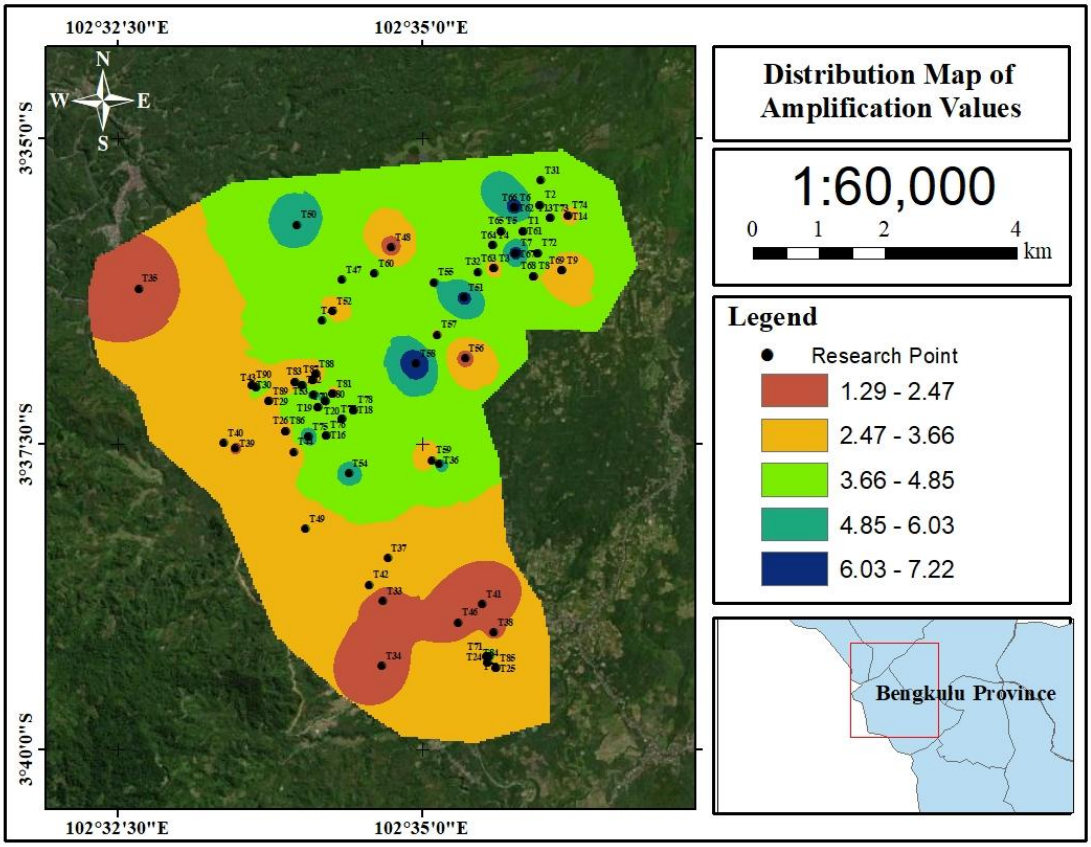

Figure 5. Distribution map of amplification values.

Based on the observations from the research table and the map of the distribution of amplification values, it can be concluded that the amplification value is inversely proportional to the dominant frequency value, so that the amplification value with a large value indicates soft rock, while the location dominated by a small amplification value is a hard rock type.

Table 3. Rock classification value based on amplification values (A_0) (Yogaswara & Kuncahyani, 2024).

Zone	Classified	Amplification Value	Measurement Point	Color
1	Low	$A_0 < 3$	4, 9, 11,12, 14, 17, 21, 24, 25, 26, 28,29, 30, 33, 34, 35, 38, 39, 40, 41, 42, 44, 46, 48, 49, 52, 56, 59, 63, 70, 73, 83, 86, 87	
2	Medium	$3 < A_0 < 6$	1, 2, 3, 5, 6, 8, 10, 13, 15, 16, 18, 19, 20, 23, 27, 31, 32, 36, 37, 43,45,47, 50, 53,54,55,57,60,61,62,64,65,67,68,69,7172, 75, 76, 77, 78, 79, 81, 82, 84, 85, 88,89,90	
3	High	$6 < A_0 < 9$	7,22,51,58,66,74,80,	
4	Very High	$A_0 > 9$	-	-

S-wave Velocity (v_s)

Softer rock materials have relatively lower values compared to harder rock materials. This is due to the fact that the shear wave velocity is directly proportional to the density of the rock. A reduction in the density of the rock in question will result in a reduction in the wave velocity value of the rock. Therefore, the v_s value is a convenient method used by researchers to interpret subsurface lithology and classify rock types based on the v_p value (Arisona et al., 2023).

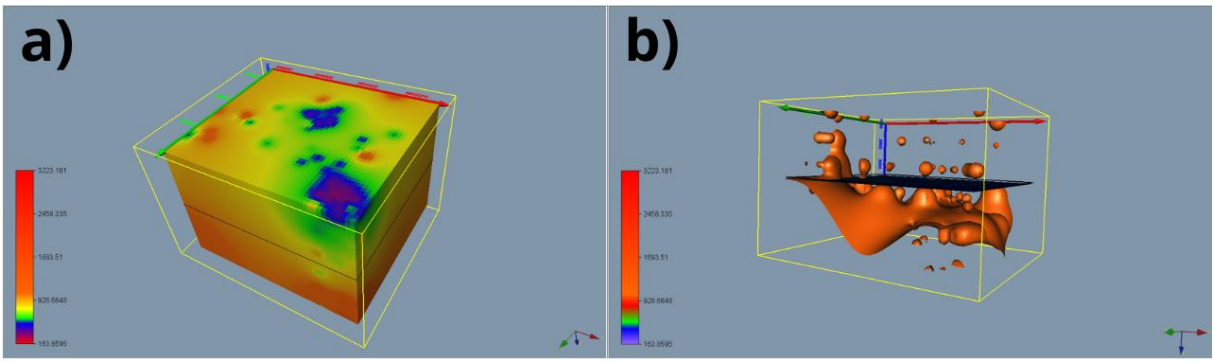

Figure 6. a) Three-dimensional modeling of (v_s) value solid rock. b) volumetric modeling of (v_s) value assumed to be solid.

Table 4. Site classification based on v_s value according to SNI (Arisona et al., 2023)

Site Classification	Shear Wave Velocity v_s (m/s)
Hard Rocks (SA)	$v_s > 1500$
Rocks (SB)	$750 < v_s < 1500$
Very dense soil and soft rock (SC)	$350 < v_s < 750$
Medium soil (SD)	$175 < v_s < 350$
Soft Soil (SE)	$v_s < 175$

It can be assumed that the large v_s value is a compact rock type with a v_s value of 1600 ≥ 3251.79 m/s which can be seen in the rock classification table based on the value based on Table 4 (Wibowo & Huda, 2020). This result is the range of values obtained from the research results, because the value range is in accordance with the research location which is dominated by volcanic rocks with a large enough v_s value. Based on rock type with v_s value classification as shown in Table 5 below.

Table 5 . Classification of v_s values by mineral type at the study site.

Material and Source	v_s (m/s)
Granite	3040
Granodiorite, Weston, Mass	3100-3200
Dunite	3790-4370
Limestone	2880-3030
Clay	500

So that the model in Figure 6 can be seen in the research location is still dominated by compact rocks.

P-wave Velocity (v_p)

P-wave propagation in the subsurface occurs through elastic media such as rock, liquid, or gas. High density values and high P-wave velocities indicate that P-waves have a high frequency. This indicates that the propagating P-waves are only affected by the variation of minerals in the subsurface (Hutami et al., 2020). The 3 (three) dimensional conceptual modeling shown in Figure 7 shows the relationship between the subsurface conditions of the study area and the occurrence of hot springs which have a layer of soil rock shown by the value of v_p ranges from 214.91 - 679.7 m/s, the v_p value between 703 − 1113.6 m/s indicates the material is alluvium, the v_p value ranges from 1120.34 – 2512.48 m/s indicates the clay layer, the v_p value is between 2517 – 3390.49 m/s in the form of sandstone layer, and the basalt material layer is indicated by the v_p value of 3393.38 – 5649.86 m/s. The clay layer is indicated as a clay cap that is impermeable so that it can withstand the flow of geothermal fluid so as not to come out to the surface, while the sand layer is thought to be a permeable layer which is where the fluid is stored (reservoir) which then through the fracture fracture zone will migrate out to the surface due to the fault Babakan Bogor and Bogor The geothermal system in the study area is classified as a low-temperature geothermal system, mainly caused by residual magmatic heat from Mount Kaba and Hitam hill crater. This research provides important insights for geothermal energy exploration and geotourism development in Kepahiang (Arintalofa et al., 2020). Classification of v_p values by mineral type can be seen in Table 6 below.

Table 6. Classification of v_p values by mineral at the study site.

Material and Source	v_p (m/s)
Granite	5640–5880
Granodiorite, Weston, Mass	4780–6400
Dunite	7400–8600
Limestone	4200–6060
Clay	1100–1800

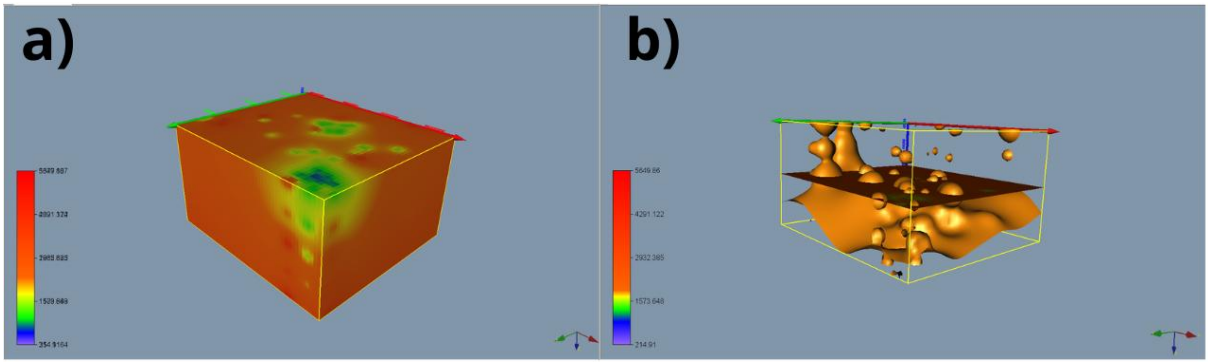

Figure 7 a) Three-dimensional modeling of the value (v_p) which is assumed to be a fault. b) volumetric modeling of the value (v_p).

Conclusion

The estimated dominant frequency parameter value (f_0) ranges from 1.24 Hz to 20.45 Hz, with an amplification value (A_0) of 1.29 to 7.22. These values are used in a statistical model to estimate the thickness of the sediment layer. The results of numerical inversion show that the shear wave velocity (v_s) ranges from 121.61 m/s to 3251.79 m/s. High v_s values indicate the presence of hard rocks below the surface, while low values indicate soft rocks. The primary wave velocity (v_p) ranges from 214.91 m/s to 6469.79 m/s. The results of 3D modeling show the vertical and horizontal distribution of v_s, which clarifies the zone of lithological change and the potential for

geothermal reservoir boundaries. In the geological model identified the presence of a fault indicated by a fracture zone, which has the potential to be a path for the rise of hydrothermal fluids. The manifestation of the Air Sempiang hot springs is strongly suspected to originate from a fracture system controlled by the meeting of two main fault zones, which are the Bogor Fault and the Babakan Bogor Fault. The existence of this fault creates geological conditions that support the formation of geothermal reservoirs, both vertically (depth of the hot zone) and horizontally (lateral spread of faults and fractures). Geothermal manifestations in Air Sempiang are the result of geothermal activity triggered by active fault fractures, and the zone between the Bogor Fault and the Babakan Bogor Fault which is a potential geothermal location.

Acknowledgements

We would like to thank all those who have contributed to this research, which is fully supported by the Geophysics Department of Bengkulu University, especially to the supervisors who have helped in the data processing until the interpretation stage. We would also like to thank the people of Kepahiang, especially in the Air Sempiang area, Bengkulu City, who have received us well and kindly during the research.

Author Contribution

In compiling this research journal, each author is divided into several job desks. Conceptualization: Muhammad Rifqi Rabbani (MRR) contributed to the research through data **curation and investigation**, as well as preparing the original draft of the manuscript. Arif Ismul Hadi (AIH) was responsible for **formal analysis and validation of the results**, and also contributed to reviewing and editing the manuscript. Budi Harlianto (BH) supported the work by assisting in **validation and writing – review & editing**. Muchammad Farid (MF) contributed to the **validation of data processing outcomes**. Hana Raihana (HR) assisted in **writing – review and editing**, particularly through proofreading the manuscript. Arya Putra Anggi (APA) played a role in **investigation**, specifically by assisting with the **data acquisition process**.

Conflict of Interest

The authors declare that there is no conflict of interest related to this research. There is no involvement of third parties, either directly or indirectly, in the financing, implementation, analysis, or writing of this article. The entire research process was conducted independently and objectively, without any pressure or influence from any institution, organisation, or individual that could affect the results and interpretation of the data.

References

Andriany, S. S., Fatimah, M. R., & Hardiyono, A. (2016). Geowisata Geopark Ciletuh: Geotrek Mengelilingi Keindahan Mega Amfiteater Ciletuh (the Magical of Ciletuh Amphitheater). *Bulletin of Scientific Contribution*, 14(1), 75–88. https://jurnal.unpad.ac.id/bsc/article/view/9796

Arifin, S. S., Mulyatno, B. S., Marjiyono, M., & Setianegara, R. (2014). Penentuan Zona Rawan Guncangan Bencana Gempa Bumi Berdasarkan Analisis Nilai Amplifikasi HVSR Mikrotremor dan Analisis Periode Fundamental Daerah Liwa dan Sekitarnya. *Jurnal Geofisika Eksplorasi*, *2*(1), 30–40. https://journal.eng.unila.ac.id/index.php/geo/article/view/217/211

Arintalofa, V., Yulianto, G., & Harmoko, U. (2020). Analisa Mikrotremor Menggunakan Metode HVSR untuk Mengetahui Karakteristik Bawah Permukaan Manifestasi Panas Bumi Diwak dan Derekan Berdasarkan Nilai Vp. *Jurnal Energi Baru Dan*

Terbarukan, 1(2), 54–61. https://doi.org/10.14710/jebt.2020.9276

Arisona, A., Manginsih, S. L., Praja, N. K., Hasria, H., & Azhar, A. (2023). Pemetaan Lapisan Tanah Menggunakan Data Mikrotremor HVSR dan Dampaknya Terhadap Daya Dukung Tanah di Kawasan Kota Kendari. *Jurnal Geologi Dan Sumberdaya Mineral*, 24(1), 51–58. https://doi.org/10.33332/jgsm.geologi.v24i1.724

Bard, P., Duval, A., Koehler, A., & Rao, S. (2004). SESAME European research project. *SESAME: Site EffectS Assessment Using Ambient Excitations*, *D23.12*(December), 62 pp.

Bilondatu, A., Londa, T., & Bujung, C. (2021). Distribusi Suhu Bawah Permukaan Manifestasi Panas Bumi Untuk Analisis Gradien Suhu Di Bukit Kasih Kanonang. *Jurnal FisTa : Fisika Dan Terapannya*, 2(2), 61–65. https://doi.org/10.53682/fista.v2i2.130

Darma, Y., & Pujiastuti, D. (2021). Analisis Multi-Atribut Dan Jaringan Syaraf Tiruan Dengan Optimasi Filter Untuk Deteksi Patahan Pada Penampang Seismik Lapangan Penobscot Kanada. *Jurnal Fisika Unand*, *10*(3), 364–370. https://jfu.fmipa.unand.ac.id/index.php/jfu/article/view/708

Diah, C. A., Setiawan, B., & Putra, H. S. (2024). Penentuan zona prospek hidrokarbon menggunakan metode passive seismic pada daerah Kecamatan Langsa Baro, Kota Langsa. *Acta Geoscience, Energy, and Mining*, 3(1), 21–25. https://jurnal.usk.ac.id/JAG/article/view/36741

Fahmi, F., Daud, Y., Suwardi, B. N., Zarkasyi, A., Sugiyanto, A., & Suhanto, E. (2015). 3-D Inversion of Magnetotelluric Data in Kepahiang Geothermal System, Bengkulu. *Proceedings Indonesia International Geothermal Convention & Exhibition 2015*, 3–8. https://www.newquest-geotechnology.com/pdf.php?file=download/paper/20150807.pdf

Firdasari, A. (2018). *Geologi dan Karakteristik Petrografi Batuan Vulkanik Formasi Hulusimpang Daerah Temdak dan Sekitarnya, Kabupaten Kepahiang, Provinsi Bengkulu*. Universitas Sriwijaya.

Fransiska, L. (2019). Peran Perguruan Tinggi Dalam Penanggulangan Bencana Di Indonesia. *Journal Pendekatan Multidisiplin Ilmu Dalam Manajemen Bencana*, *Volume 1,* 5. https://prosiding.respati.ac.id/index.php/PSN/article/view/47

García-Jerez, A., Piña-Flores, J., Sánchez-Sesma, F. J., Luzón, F., & Perton, M. (2016). A Computer Code For Forward Calculation And Inversion Of The H/V Spectral Ratio Under The Diffuse Field Assumption. *Computers and Geosciences*, 97, 67–78. https://doi.org/10.1016/j.cageo.2016.06.016

Hadi, A. I., Refrizon, R., Halauddin, H., Lidiawati, L., & Edo, P. (2021). Interpretasi Tingkat Kekerasan Batuan Bawah Permukaan di Daerah Rawan Gempa Bumi Kota Bengkulu. *Indonesian Journal of Applied Physics*, 11(1), 11–24. https://doi.org/10.13057/ijap.v11i1.46525

Hutami, H. Y., Fitriyani, F., Priniarti, T. L., & Handoyo, H. (2020). Analisis Model Kecepatan Gelombang-P pada Coal-Seam Gas Studi Kasus Cekungan Sumatera Selatan, Indonesia. *JGE (Jurnal Geofisika Eksplorasi)*, 6(2), 113–120. https://doi.org/10.23960/jge.v6i2.74.

Indrayati, A., & Setyaningsih, W. (2017). Mengungkap Potensi Kabupaten Rembang Sebagai Geowisata Dan Laboratoriun Lapangan Geografi. *Jurnal Geografi : Media Informasi Pengembangan Dan Profesi Kegeografian*, 14(1), 1–17.

https://journal.unnes.ac.id/nju/JG/article/view/9773

Kamil, I. (2020). *Pemodelan Struktur Kecepatan Seismik Gelombang P (Vp), Kecepatan Seismik Gelombang S (Vs) Dan Vp/Vs Pada Daerah Vulkanik Kabupaten Tanggamus Berdasarkan Tomografi Seismik Menggunakan Data Microearthquake (Meq) Desember 1992 – Februari 1993*. Institut Teknologi Sumatera.

Nurwidyanto, M. I., Zainuri, M., Wirasatrya, A., & Yuliyanto, G. (2023). Struktur Bawah Permukaan Pantai Semarang berdasarkan Metode HVSR. *Indonesian Journal of Applied Physics*, 13(1), 117–127. https://doi.org/10.13057/ijap.v13i1.66864

Ratag, A. S., Bujung, C. A. N., Tumimomor, F., & Polii, J. (2022). Analisis Tipe Fluida Mata Air Panas Berdasarkan Diagram Cl-SO_4-HCO_3 di Desa Pinaesaan Kabupaten Minahasa Selatan. *Jurnal FisTa: Fisika dan Terapannya*, 3(2), 1–7. http://dx.doi.org/10.53682/fista.v3i2.206

Purnomo, S. S. (2019). *Analisis Struktur Bawah Permukaan Kota Surakarta Bagian Timur Berdasarkan Nilai Kecepatan Gelombang Geser dengan Metode Ellipticity Curve*. Universitas Sebelas Maret.

Raharjo, S. A., Saputra, A. V., & Rahadinata, T. (2022). Identifikasi Struktur Geologi Bawah Permukaan Berdasarkan Pemodelan 3D Data Gravitasi (Studi Kasus Daerah Potensi Panas Bumi Kepahiang). *Jurnal Teras Fisika*, *5*(2), 28–35. https://doi.org/10.20884/1.jtf.2022.5.2.7248

Ramadhan, M. I., & Massinai, M. A. (2022). Analysis of Subsurface Layers using the Multichannel Analysis of Surface Waves Method in Manimbahoi, Gowa Regency. *Jurnal Geocelebes*, 6(2), 126–134. https://doi.org/10.20956/geocelebes.v6i2.22025

Rasimeng, S., Pratama, T. P. E., & Wibowo, R. C. (2024). Structural Geology Identification based on Derivative Analysis Gravity Data in Tangkuban Perahu Mountain. *Journal of Engineering and Scientific Research*, 6(1), 7–15. https://doi.org/10.23960/jesr.v6i1.163

Risa, I. N., Maison, M., & Dewi, I. K. (2023). Analisis Kerentanan Tanah Berdasarkan Pengukuran Mikrotremor Di Desa Jati Mulyo, Tanjung Jabung Timur. *JGE (Jurnal Geofisika Eksplorasi)*, 9(1), 18–31. https://doi.org/10.23960/jge.v9i1.236

Setianegara, R., Muslim, D., Ismawan, I., & Marjiyono, M. (2023). Potensi Penguatan Gelombang Gempabumi oleh Sedimen Permukaan Berdasarkan Analisis Mikrotremor: Studi Kasus di Cekungan Bandung Bagian Selatan. *Jurnal Geologi dan Sumberdaya Mineral*, 24(2), 107–115. https://doi.org/10.33332/jgsm.geologi.v24i2.749

Setyowati, Y., Farid, M., Hadi, A. I., Helinnes, P., Refrizon, R., Hardiansyah, D., Gumanty, U., Raihana, H., Al-Ansory, A. R., Syah, M. T. (2024). Subsurface Sediment Layer Analysis at the Dendam Tak Sudah Lake Flyover Construction Site in Bengkulu City Using the HV-Inv Method. *Jurnal Ilmu Fisika | Universitas Andalas*, 16(2), 187–197. https://doi.org/10.25077/jif.16.2.187-197.2024

Sihombing, P. A., Hadi, A. I., Refrizon, R., & Zakariya, H. (2024). Identification of the distribution of geothermal reservoirs around Kepahiang Bengkulu Province using GGMPlus gravity data anomalies by the 2D inversion method. *Journal of Aceh Physics Society*, 13(1), 1–8. https://doi.org/10.24815/jacps.v13i1.37642

Sihombing, R. B., & Rustadi, R. (2018). Pemodelan dan Analisa Struktur

Bawah Permukaan Daerah Prospek Panasbumi Kepahiang Berdasarkan Metode Metode Gayaberat. *Jurnal Geofisika Eksplorasi*, 4(2), 159–172. https://doi.org/10.23960/jge.v4i2.14.

Simbolon, P., Refrizon, R., & Sugianto, N. (2020). Peta Sebaran Intensitas Anomali Magnetik Di Daerah Prospek Geothermal Kepahiang Berdasarkan Survei Metode Geomagnet. *Newton-Maxwell Journal of Physics*, *1*(1), 7–12. https://doi.org/10.33369/nmj.v1i1.14290

Wibowo, N. B., & Huda, I. (2020). Analysis of Amplification, Seismic Vulnerability Index And Soil Clasification Based On Vs30 In Yogyakarta. *Buletin Meteorologi, Klimatologi, Dan Geofisika*, 1(2), 21–31.

Yogaswara, A. R. D., & Kuncahyani, A. (2024). Analisis Mikrotremor Berbasis Metode HVSR Untuk Mengetahui Indeks Kerentanan Seismik Di Wilayah Kabupaten Kulonprogo. *Jurnal Stasiun Geofisika Sleman*, 2(1), 14–20. https://jurnal.stageofsleman.id/index.php/jsgs/article/view/14

ISSN: 2579-5821 (Print)
ISSN: 2579-5546 (Online)
URL address: http://journal.unhas.ac.id/index.php/geocelebes
DOI: 10.70561/geocelebes.v9i2.45404

Jurnal Geocelebes Vol. 9 No. 2, October 2025, 171 – 188

Assessment of Ground Deformation and Landslide Susceptibility Using InSAR and Hypsometric Data in Jayapura City, Papua

Nur Ayu Anas[1,5*], Harsan Ingot Hasudungan[2], Rahmat Indrajati[1,5], Marcelino N. Yonas[3,5], Harnanti Y. Hutami[4]

[1]Geological Engineering Study Program, Faculty of Engineering, Cenderawasih University, Jayapura, Papua, 99351, Indonesia.
[2]Civil Engineering Study Program, Faculty of Engineering, Cenderawasih University, Jayapura, Papua, 99351, Indonesia.
[3]Mineral Engineering Study Program, Faculty of Engineering, Cenderawasih University, Jayapura, Papua, 99351, Indonesia.
[4]Geophysical Engineering Department, Faculty of Industry and Technology, Institut Teknologi Sumatera, Lampung, 35365, Indonesia.
[5]Papua Regional Chapter of the Indonesian Association of Geologists (IAGI), Jayapura, Papua, 99351, Indonesia.

*Corresponding author. Email: ayuanas741@gmail.com

Manuscript received: 5 July 2025; Received in revised form: 18 September 2025; Accepted: 4 October 2025

Abstract

Ground deformation and landslides are major geohazards affecting Jayapura City, Papua, due to its active tectonic setting and steep topography. This study aims to assess the correlation between surface deformation and landslide susceptibility using a combination of Interferometric Synthetic Aperture Radar (InSAR) and hypsometric analysis. Sentinel-1A SAR data from ascending and descending tracks, combined with DEMNAS elevation data, were used to detect deformation patterns and evaluate geomorphological maturity through hypsometric parameters. The results reveal significant deformation patterns, including subsidence up to –0.77 m and uplift up to +0.25 m, predominantly concentrated in sub-watersheds Sw2, Sw3, and Sw4. Hypsometric analysis indicates that most sub-watersheds are in the mature geomorphological stage (HI between 0.476 and 0.495), except Sw14, which is classified as young (HI = 0.501). Validation with the landslide inventory further confirms this correlation: 75% of documented landslides occurred in areas of high deformation, while 25% were associated with moderate deformation, and none in low or stable zones. These findings provide essential insights for disaster risk reduction, highlighting priority areas for slope stabilization, land-use management, and early warning systems.

Keywords: Deformation; Hypsometric; Landslide Susceptibility; SAR Interferometry.

Citation: Anas, N. A., Hasudungan, H. I., Indrajati, R., Yonas, M. N., & Hutami, Y. H. (2025). Assessment of Ground Deformation and Landslide Susceptibility Using InSAR and Hypsometric Data in Jayapura City, Papua. *Jurnal Geocelebes*, 9(2): 171–188, doi: 10.70561/geocelebes.v9i2.45404

Introduction

Ground deformation and landslides are critical geotechnical and environmental hazards in regions with steep topography, high rainfall, and active tectonic processes. Jayapura City (Figure 1), one of the major urban centers in Papua, is located within a complex morphological zone featuring significant slope gradients and unstable geological conditions (Abrauw, 2017). Several major landslide events in the past decade have caused severe impacts on infrastructure, residential areas, and public safety.

Conventional monitoring methods, such as field surveys and geological mapping, are limited in spatial coverage and frequency. The development of remote sensing, particularly Interferometric Synthetic Aperture Radar (InSAR), enables the

detection of ground deformation with high spatial and temporal resolution. The integration of InSAR and hypsometric integral (HI) provides an effective framework for assessing slope instability and tectonic activity. InSAR has been used for landslide detection and monitoring across diverse settings (Fan et al., 2024; Guvel et al., 2023; Sorkhabi et al., 2023; Mondini et al., 2019), with further applications in wide-area mapping, precursor recognition, hazard assessment, and probabilistic modeling (Ahmad et al., 2024; Cai et al., 2023; Dai et al., 2022; Gao et al., 2025; Hu et al., 2025; Strząbała et al., 2024). Additional studies highlight its role in risk reduction, multi-sensor integration, slope deformation monitoring, and high-altitude environments (Bianchini et al., 2021; Casagli et al., 2023; Dong et al., 2025; Guo & Martínez-Graña, 2024; Lin et al., 2025; Novellino et al., 2021; Piroton et al., 2020; Yao et al., 2023; Yu et al., 2024; Zhang et al., 2024). In parallel, HI has proven valuable for linking tectonic activity and landslide susceptibility through basin morphology, DEM sensitivity, and hydrological influences (Arabameri et al., 2019; Chatterjee et al., 2024; Diercks et al., 2023; Gu et al., 2021; Gururani et al., 2023; Hang et al., 2025; Kothyari et al., 2024; Li et al., 2021; Liem et al., 2016; Makrari et al., 2022; Nikoonejad et al., 2015; Ntokos, 2025; Othman et al., 2018; Patel et al., 2024; Taloor et al., 2019; Zhang et al., 2024).

Although numerous studies have successfully applied InSAR and hypsometric analysis separately to assess ground deformation, slope instability, and tectonic activity in various regions worldwide, their combined application remains underexplored. This is particularly true in tropical, tectonically active regions with complex geomorphological settings such as Jayapura City, where integrating both approaches could significantly enhance the accuracy of landslide susceptibility assessment.

Therefore, this study aims to assess ground deformation and landslide susceptibility in Jayapura City by combining InSAR and hypsometric analysis. The findings are expected to advance landslide hazard mapping methodologies and provide scientific support for disaster risk reduction and urban planning.

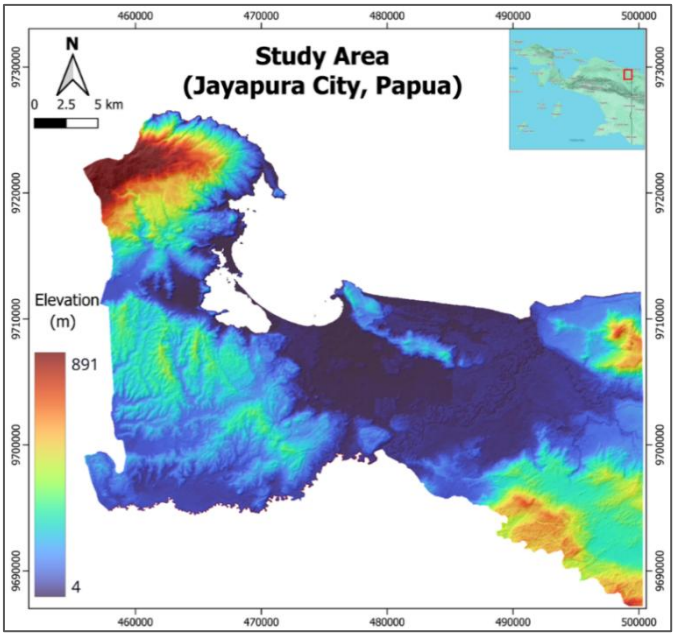

Figure 1. The study area is in Jayapura City, Papua Province, Indonesia, within the coordinate range of 460000–500000 East and 9690000–9730000 North (UTM Zone 54S). The location is presented using an elevation map to illustrate the geographical extent of the study area.

Materials and Methods

In this study, both primary and secondary datasets were utilized. The primary data consist of Sentinel-1A imagery and the Indonesian National Digital Elevation Model or DEMNAS (Badan Informasi Geospasial, 2018). The secondary data includes landslide inventory, earthquake epicenter records, and the geological map of Jayapura City. The selection of these datasets was based on their respective analytical purposes, where Sentinel-1A imagery was employed for ground deformation analysis, while DEMNAS was used for hypsometric analysis. Furthermore, the secondary data were incorporated to strengthen the spatial analysis and to validate the results obtained from the primary data processing. The specifications of the Sentinel-1A imagery used in this study are presented in Table 1.

Table 1. Sentinel-1A imagery used in this study (Alaska Satellite Facility Distributed Active Archive Center (ASF DAAC), 2025; European Space Agency, 2014).

No.	ID Scene	Acquisition	Polarization	Orbit	Abs Orbit	Spatial Resolution	Swath Width
1	S1A_IW_SLC__1SDV_20240128T085635_20240128T085701_052304_0652F0_F557	28 January 2024	VV+VH	Ascending	52304	5 x 20 m	250 km
2	S1A_IW_SLC__1SDV_20240714T085634_20240714T085700_054754_06AAC1_B8A5	14 July 2024	VV+VH	Ascending	54754	5 x 20 m	250 km
3	S1A_IW_SLC__1SDV_20250111T202114_20250111T202143_057401_0710D8_51CC	11 January 2025	VV+VH	Descending	57401	5 x 20 m	250 km
4	S1A_IW_SLC__1SDV_20250417T202112_20250417T202142_058801_07491E_079F	17 April 2025	VV+VH	Descending	58801	5 x 20 m	250 km

The InSAR processing was carried out using the SNAP 9.0 software package provided by the European Space Agency, with SNAPHU applied for phase unwrapping. Interferograms were generated from Sentinel-1A SAR data using a coherence threshold of 0.3, ensuring reliable phase stability in both vegetated and urbanized areas. For topographic phase removal and hypsometric analysis, the DEMNAS with a spatial resolution of 8.1 m was employed. A sensitivity check was also conducted by resampling DEMNAS to 15 m, which indicated no significant changes in the hypsometric integral values, thereby confirming the robustness of the results.

The selection of Sentinel-1 imagery from 2024 and 2025 was based on the need to capture the most recent ground deformation conditions in Jayapura City. Utilizing this recent temporal range allows researchers to monitor geological dynamics in real-time or near real-time, particularly concerning tectonic activity and geotechnical hazards such as landslides and land subsidence. The period from 2024 to 2025 was specifically chosen to capture ongoing change trends, ensuring that the analysis results are highly relevant to current field conditions. Moreover, this timeframe encompasses critical phases that are likely to reflect environmental responses to increased

seismic activity and geological stress in the region.

In this study, the InSAR and hypsometric methods were applied as effective tools for analyzing landslide susceptibility, particularly in tectonically active regions like Jayapura, Papua. The workflow of the applied methodology is illustrated in Figure 2.

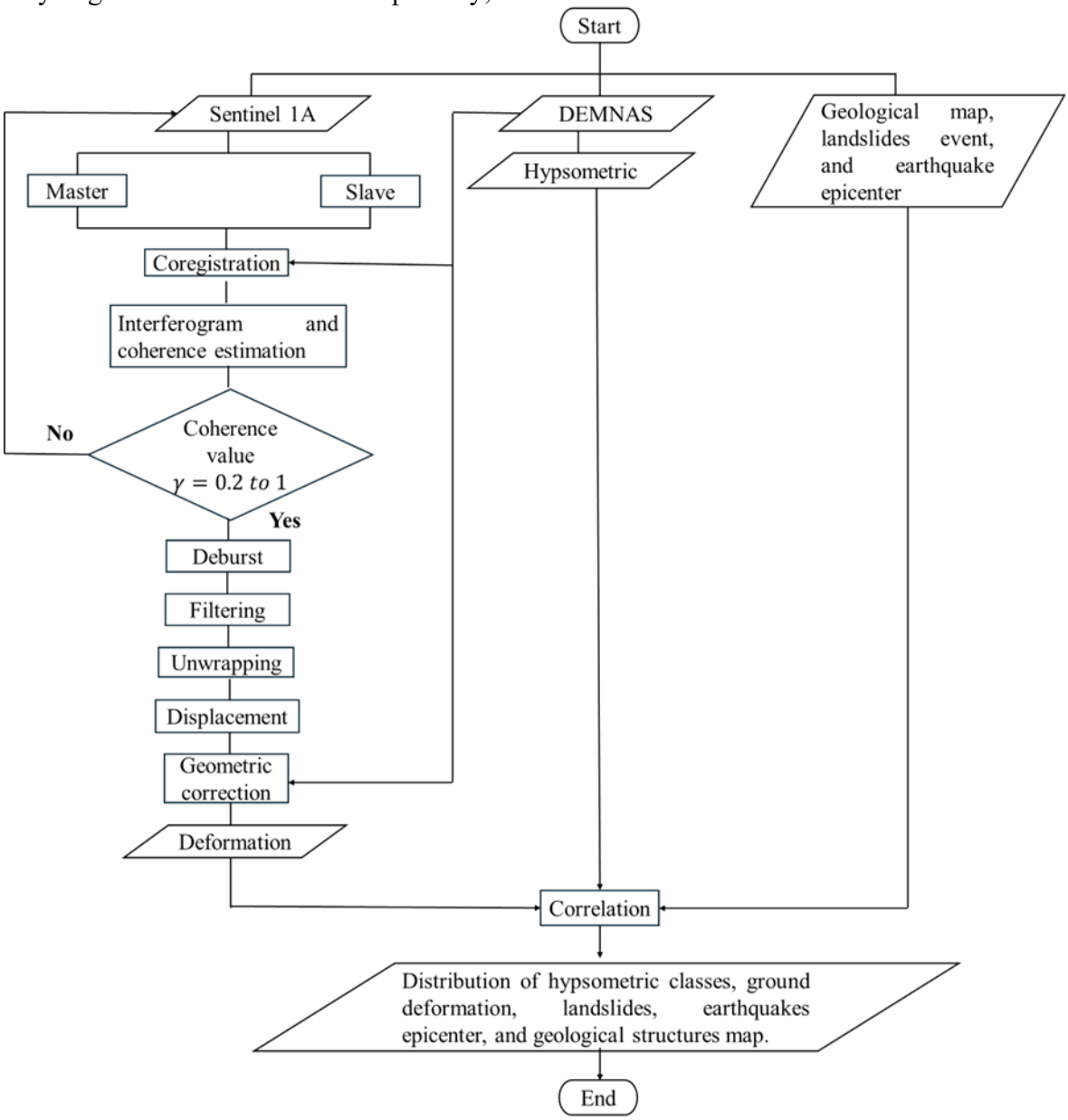

Figure 2. Research flowchart.

The Figure 2 illustrates the workflow for obtaining ground deformation values using the InSAR method. InSAR enables accurate measurements of surface deformation over large spatial scales by comparing the phase differences of radar signals acquired from two separate observations (Brengman & Barnhart, 2021; Saepuloh, 2021; Shan et al., 2024).

$$\Delta d = \frac{\lambda}{4\pi} \times \Delta\varphi \quad (1)$$

where:

Δd : surface deformation along the Line of Sight (LOS) direction (in meters)

λ : radar wavelength (for Sentinel-1A C-band, $\lambda \approx 5.6$ cm or 0.056 meters)

$\Delta\varphi$: interferometric phase difference (in radians)

4π : conversion factor from phase to displacement.

Equation (1) expresses how surface deformation along the radar line of sight (LOS) is derived from the interferometric phase difference. The displacement d is directly proportional to the phase change $\Delta\varphi$, which results from comparing two SAR acquisitions over the same area at different times. Because the radar phase is cyclic between 0 and 2π, and one full cycle corresponds to half of the radar wavelength (λ/2), the conversion factor 4π appears in the denominator. Thus, a larger phase shift indicates a larger surface displacement, while the radar wavelength λ controls the sensitivity of the measurement shorter wavelengths allow the detection of smaller ground movements.

Then the hypsometric method refers to the measurement of elevation distribution within a given area, allowing researchers to evaluate the morphology and geological development that may contribute to slope stability. This approach aligns with previous studies conducted by Aristizábal & Korup (2025). As illustrated in Figure 3, hypsometric integral (HI) values equal to or greater than 0.5 are characterized by convex-shaped curves, representing the young stage, which reflects a high level of tectonic activity. Meanwhile, HI values ranging from 0.4 to less than 0.5 indicate the intermediate (mature) stage, typically represented by straight curves or a slight combination of convex and concave forms, suggesting that tectonic activity is still present but at a moderate level. In contrast, HI values below 0.4 are associated with concave-shaped curves, corresponding to the old stage, which indicates relatively inactive tectonic conditions (Khattab et al., 2023; Liem et al., 2016; Mulyasari et al., 2017; Rabii et al., 2017).

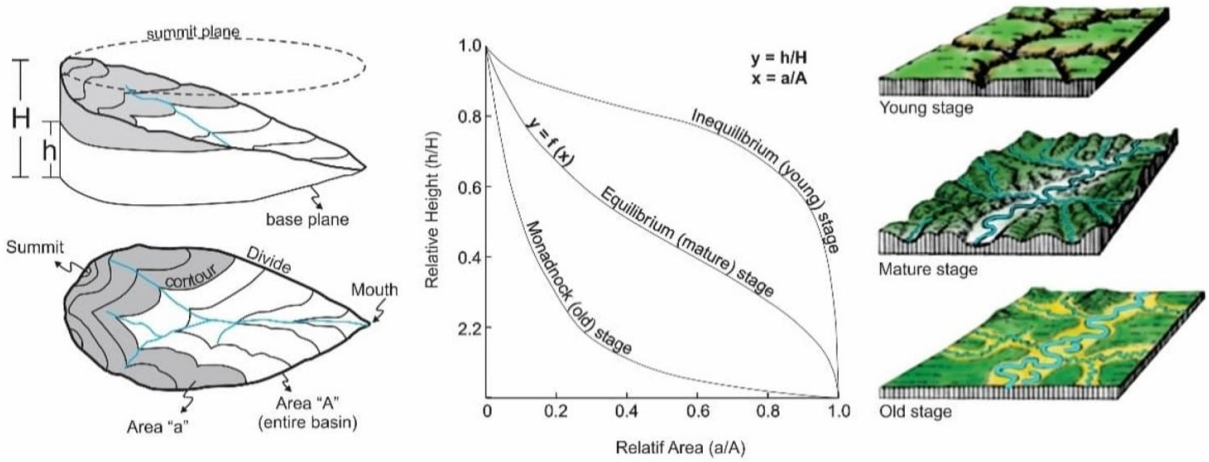

Figure 3. Schematic illustration of hypsometric analysis parameters and geomorphological stages.

In Figure 3, the schematic of hypsometric analysis parameters for a watershed (left) illustrates the relationship between relative elevation (h/H) and relative area (a/A). The hypsometric curve diagram (center), based on the concepts of (Keller & Pinter, 2002) depicts three primary patterns associated with geomorphological development stages: (1) a convex curve indicates a young stage with minimal erosion; (2) a nearly straight or slightly concave-convex curve represents the mature stage, reflecting more balanced erosion processes; and (3) a concave curve corresponds to the old stage, indicating a landscape that has been significantly worn down by long-term erosion. The right side presents illustrations of geomorphological conditions associated with each developmental stage.

The hypsometric curve is expressed in terms of the hypsometric integral (HI), which quantifies the area beneath the curve as a measure of the proportion of the basin volume that remains uneroded (Schumm, 1956). The calculation of HI follows the formula introduced by (Romero, 2024):

$$HI = \frac{\bar{h} - h_{min}}{h_{max} - h_{min}} \quad (2)$$

where:

HI : hypsometric integral
$\bar{h}$: represents the mean elevation of the geomorphic unit
h_{min} : the minimum elevation within the studied area
h_{max} : the maximum elevation within the studied area

When combined, the InSAR and hypsometric methods not only provide a comprehensive understanding of the geological and topographical conditions of the area but also enable early detection and effective management of landslide risks.

Results and Discussion

The results of this study consist of surface deformation values and hypsometric data. The surface deformation values were obtained using Sentinel-1A imagery from both ascending and descending tracks, with different acquisition time pairs as shown in Figure 4. The processed interferograms and deformation maps were utilized to detect ground movements occurring throughout the Jayapura City area, which was divided into 16 sub-watersheds (Sw1 to Sw16). This subdivision aims to facilitate spatial analysis of the deformation distribution patterns.

The results indicate that surface deformation in Jayapura City, identified through InSAR analysis using Sentinel-1A data from both ascending and descending tracks, reveals significant deformation patterns such as subsidence and uplift distributed across several sub-watersheds. Based on the ascending interferogram generated from the image pair dated January 28 to July 14, 2024, a phase change ranging from -3.12 to +3.11 radians was detected, with the densest fringe concentrations observed in Sw2, Sw3, and Sw4. The deformation map from the ascending track indicates a maximum ground subsidence of up to -0.77 m, predominantly occurring in Sw2, Sw3, and Sw4, and partially in Sw9, Sw10, Sw11, and Sw14. Meanwhile, other sub-watersheds such as Sw1, Sw5, Sw6, Sw7, Sw8, Sw12, Sw13, Sw15, and Sw16 generally show minor to insignificant deformation, indicating stable conditions.

The results from the descending track using the image pair acquired between January 11 and April 17, 2025, show a pattern consistent with that of the ascending track. The maximum uplift was recorded at +0.25 m in Sw4, with moderate uplift deformation occurring in Sw2, Sw3, Sw9, Sw10, Sw11, and Sw14, ranging from +0.072 to +0.25 m. Other areas generally exhibited insignificant deformation. The consistency of the results from both tracks strengthens the accuracy and validity of the deformation interpretation, spatially confirming that the zones with the highest deformation are concentrated in the northern part of Jayapura City, particularly within Sw2 to Sw4.

In addition to the deformation analysis, the hypsometric results (Figure 5) indicate that most sub-watersheds in Jayapura City are in the mature geomorphological stage, characterized by hypsometric integral (HI) values ranging from 0.476 to 0.495. This condition reflects that the landscape in these areas has undergone significant erosion processes while still retaining considerable relief and slope steepness. This suggests that despite prolonged erosion, slope instability potential persists due to the presence of rugged topography in several locations. Interestingly, Sw14 is the only sub-watershed classified as being in the young geomorphological stage, with a

HI value of 0.501. This indicates that Sw14 exhibits a younger morphological condition, characterized by steep topography, high relief, and a relatively low degree of erosional development compared to other sub-watersheds. However, despite its classification as geomorphologically young and the detection of localized deformation within this sub-watershed, Sw14 is not associated with fault zones or landslide occurrences during the observation period. This suggests that the instability potential in this area is primarily driven by geomorphological factors rather than tectonic activity.

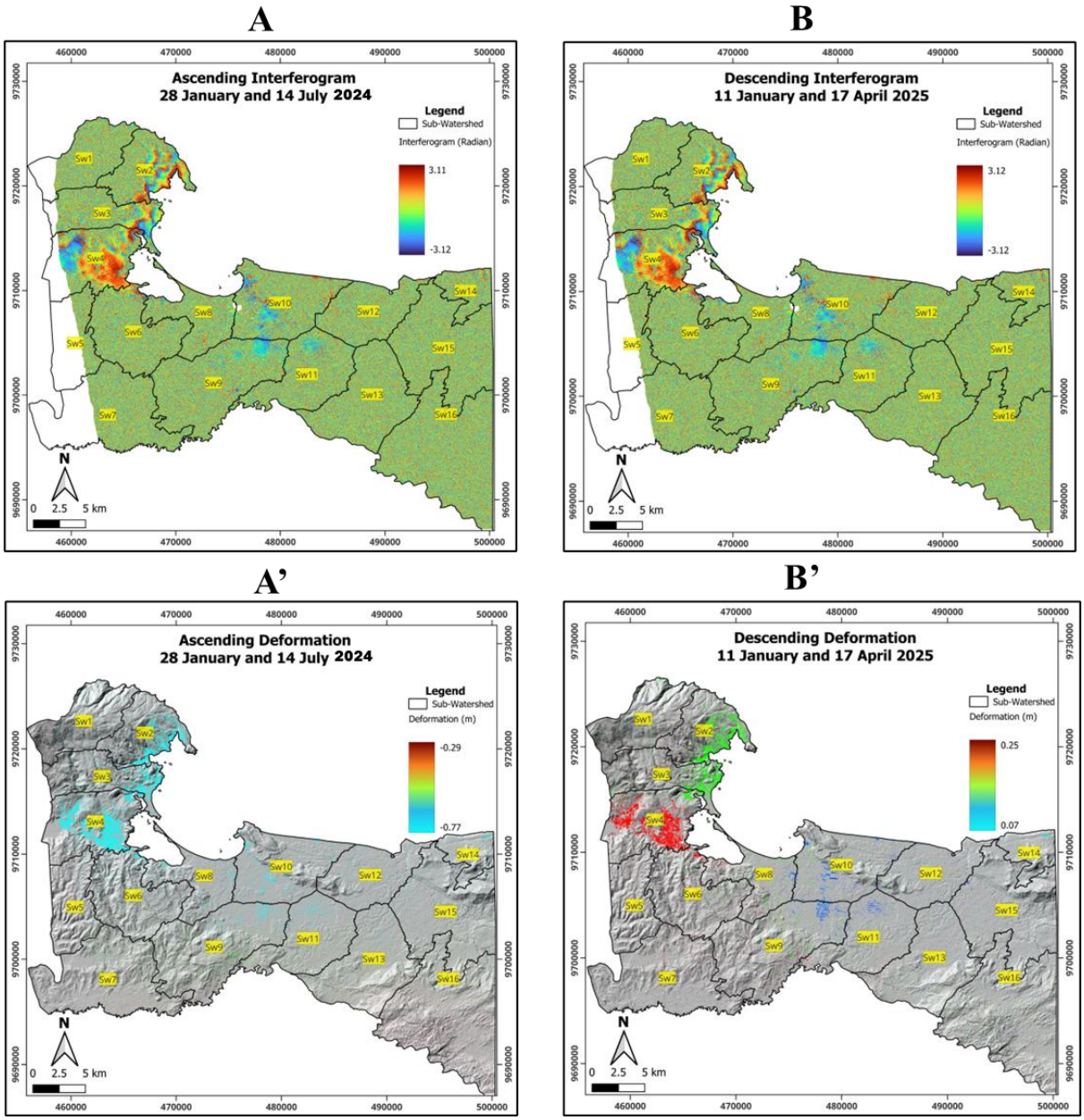

Figure 4. Surface deformation analysis in Jayapura City using Sentinel-1A SAR data: (A) interferogram from ascending pair (28 January–14 July 2024); (A′) deformation map from ascending track; (B) interferogram from descending pair (11 January–17 April 2025); (B′) deformation map from descending track.

The correlation between surface deformation, hypsometry, geological structures, earthquake epicenter distribution from 2002 to 2025, and landslide occurrences in Jayapura City reveals a strong interconnection (Figure 6). The presence of a thrust fault trending northwest–southeast (NW–SE) within the

metamorphic rocks of the Cycloops Schist Complex (pTmc), which represent a metamorphic facies zone, serves as the primary control of the deformation observed in Sw3 and Sw4. The hard but brittle nature of the metamorphic rocks in this zone acts as a medium for the accumulation and release of compressive stress, which actively triggers vertical deformation. In addition to thrust faulting, patterns of lateral deformation and uplift are also controlled by normal faults dominantly trending north-northwest–south-southeast (NNW–SSE) and west-southwest–east-northeast (WSW–ENE), as well as strike-slip faults trending WSW–ENE, which are distributed across several sub-watersheds, particularly from Sw2 to Sw9 and Sw12. The occurrence of faults along the boundary between the Ultramafic Rock Formation (Um), composed of harzburgite, serpentinite, pyroxenite, and dunite, and the Nubai Formation (Tomn), dominated by limestone interbedded with biomicrite, marl, fine-grained sandstone, and tuffaceous greywacke, further emphasizes the structural complexity of Jayapura, where strong lithological contrasts promote deformation concentration (Welikanna & Jin, 2023).

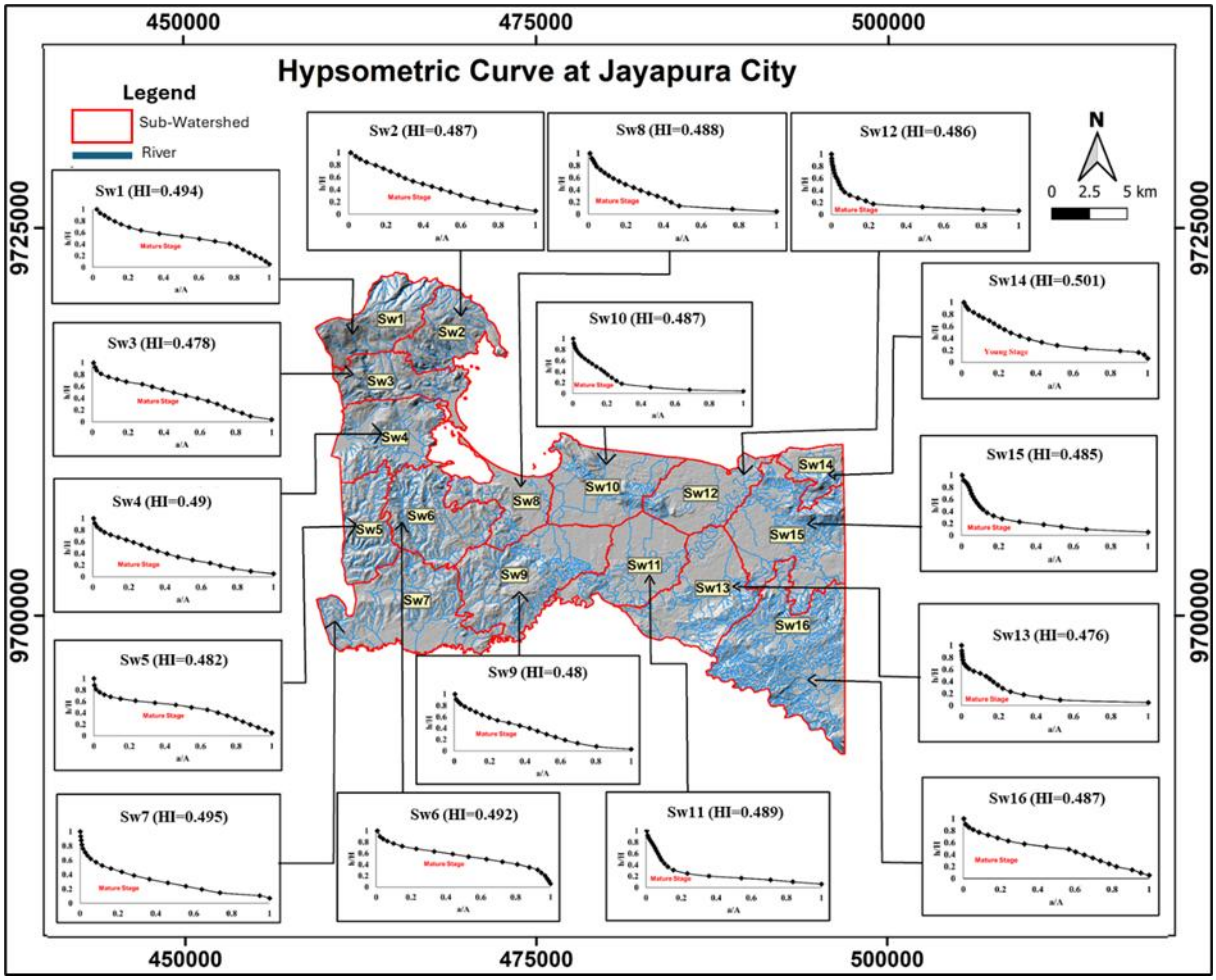

Figure 5. Hypsometric curves of 16 sub-watersheds (Sub-DAS) in Jayapura City. The hypsometric integral (HI) values are used to assess the geomorphological development stage of each sub-watershed.

This tectonic complexity does not act in isolation but interacts strongly with the lithological framework of Jayapura. The convergence of multiple weak sedimentary formations further amplifies the impact of fault activity, making the area more prone to both vertical and lateral deformation. The Makats Formation (Tmm) consists of greywacke, siltstone, shale, marl, conglomerate, interbedded limestone, tuff,

and volcanic breccia. Meanwhile, the Jayapura Formation (Qpj) comprises coral-algal limestone, calcirudite, calcarenite, marl, and reef-structured limestone (Suwarna & Noya, 1995). The combination of lithologies from the Makats, Nubai, and Jayapura Formations, which are dominated by weak sedimentary rocks with low cohesion, makes the area highly susceptible to both vertical (subsidence and uplift) and lateral deformation. This inherent lithological weakness, when combined with active fault movements, leads to significant stress accumulation and deformation across multiple sub-watersheds.

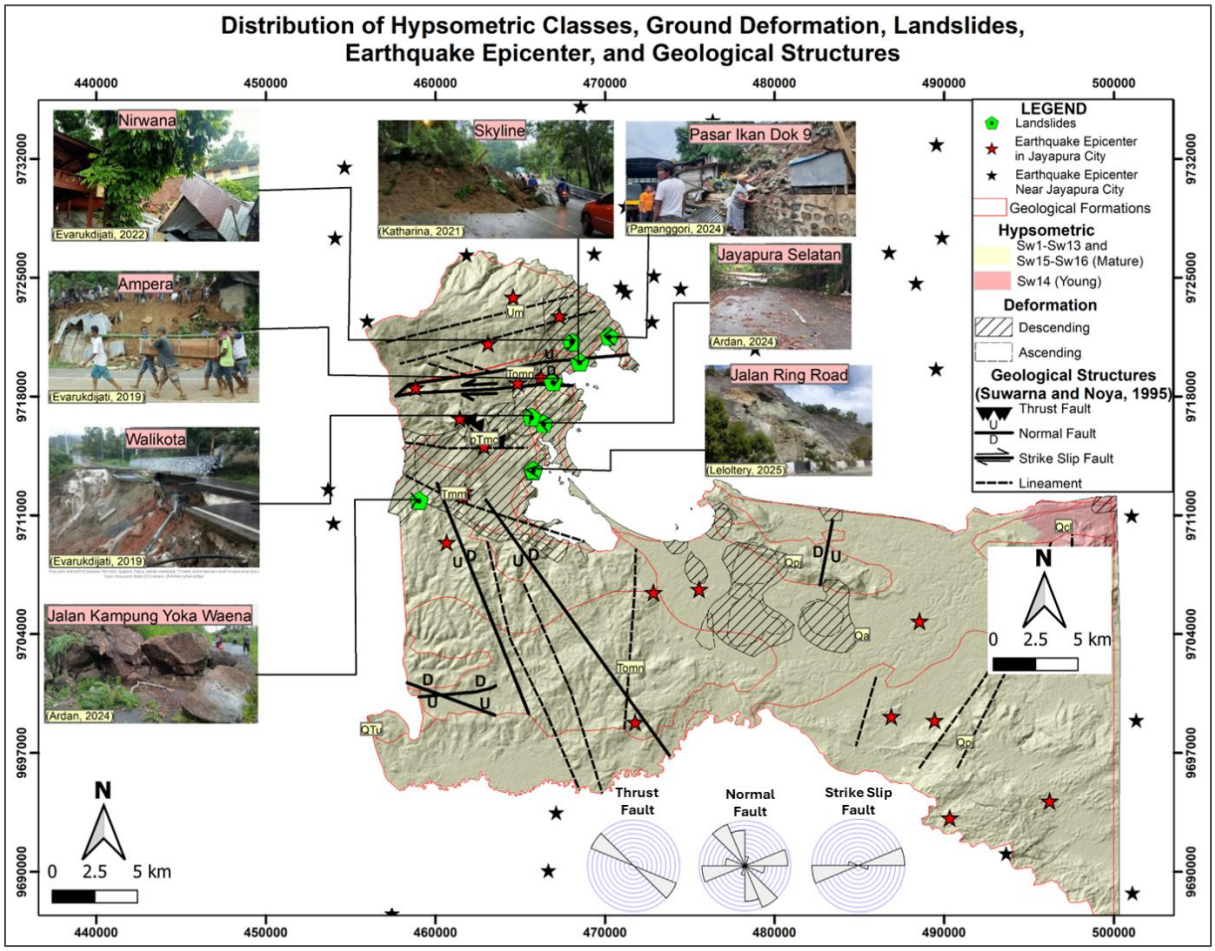

Figure 6. Distribution of deformation, hypsometry, landslides, earthquake epicenters, geological structures, and lithological formations in Jayapura City.

In addition, the spatial distribution of earthquake epicenters from 2002 to 2025 shows a proximity to several documented landslide locations, particularly in Sw2, Sw3, and Sw4 (Figure 6). This spatial relationship suggests that seismic activity may act as a triggering factor that accelerates slope failure in areas already weakened by active deformation and fragile lithologies. The potential activity of these faults leads to stress accumulation that promotes deformation in soils and rocks with inherently weak mechanical properties. InSAR effectively captures deformation in these areas due to a combination of fault block movements, the presence of fractures or shear zones, and the reduction in rock strength caused by weathering or subsurface moisture changes (Alonso-Díaz et al., 2023; Farolfi et al., 2019). In addition to tectonic factors, the presence of lithologies such as marl, shale, and conglomerate—materials that are highly compressible and plastically deformable (Staniewicz & Chen, 2024) further amplifies the surface deformation

response, which is clearly recorded in the InSAR results. Conversely, the deformation detected in Sw10 and Sw11, which are underlain by the Qa Formation consisting of alluvium and coastal deposits, is unrelated to tectonic activity. Instead, it is attributed to non-tectonic factors, particularly rapid land-use changes associated with intensive urban development, which appear as deformation signals in the InSAR analysis.

Table 2 . Deformation classification and landslide occurrences in sub-watersheds of Jayapura city.

No.	Sub-watershed	Sub-watershed Area (ha)	Deformation Area (ha)	Percentage of Deformation Area (%)	Deformation Classification	Total landslide Events 2019-2025	Location
1	Sw1	4149.23	-	-	No deformation	-	-
2	Sw2	3628.46	2317.19	63.86	High	4	Kawasan Ampera, Nirwana, Pasar Ikan Dok 9, and Skyline
3	Sw3	3643.76	1459.32	40.05	Moderate	2	Kantor Distrik Jayapura Selatan and Kantor Walikota
4	Sw4	4897	4128.59	84.31	High	2	Kampung Yoka Waena and Jalan Ringroad
5	Sw5	3482.58	7.67	0.22	No deformation	-	-
6	Sw6	5307.22	438.88	8.27	Low	-	-
7	Sw7	7671.4	-	-	No deformation	-	-
8	Sw8	3431.34	280.38	8.17	Low	-	-
9	Sw9	7738.04	930.15	12.02	Low	-	-
10	Sw10	5597.85	1551.6	27.72	Moderate	-	-
11	Sw11	4995.9	899.73	18.01	Low	-	-
12	Sw12	4255.3	84.02	1.97	Low	-	-
13	Sw13	6323.65	-	-	No deformation	-	-
14	Sw14	1806.58	126.39	6.99	Low	-	-
15	Sw15	7838.1	-	-	No deformation	-	-
16	Sw16	10029.7	-	-	No deformation	-	-

Table 3. Landslide distribution by deformation class.

Deformation Classification	Landslide Events	Percentage (%)
High	6	75.0
Moderate	2	25.0
Low	0	0.0
No deformation	0	0.0

The occurrence of landslides along several locations, including Jalan Kampung Yoka Waena, the area surrounding the Walikota's Office, Ampera, Nirwana, Jalan Skyline, Pasar Ikan Dok 9, Jayapura Selatan, and Jalan Ringroad (Ardan, 2024; Evarukdijati, 2019a, 2019b, 2022; Katharina, 2021; Leloltery, 2025; Pamanggori, 2024), further supports the observation that landslide events are predominantly concentrated in areas experiencing a combination of active deformation and mature hypsometric conditions, particularly in Sw2, Sw3, and Sw4. To strengthen this correlation, a quantitative validation was conducted by comparing deformation zones with the landslide inventory from 2019 – 2025. For this purpose, it is developed our own deformation classification system based on

the proportion of affected area within each sub-watershed, which are: No deformation (0%), Low deformation (1–25%), Moderate deformation (26–50%), and High deformation (51–100%).

The results are summarized in Table 2 and Table 3, which demonstrates that sub-watersheds Sw2, Sw3, and Sw4, categorized as high to moderate deformation zones (40–84% coverage), correspond with many documented landslide events. In contrast, areas with low or no deformation show either minor or no landslide occurrences. This quantitative validation is consistent with the geological and geomorphological evidence, as ongoing deformation in these areas likely increases slope stress and instability.

In these areas, ongoing deformation likely increases slope stress, which is further exacerbated by the presence of weak lithologies such as marl, clay, brecciated ultramafic rocks, and weathered serpentinite. These conditions render the slopes highly unstable and susceptible to landslides, especially when triggered by extreme rainfall or seismic activity. Conversely, although Sw14 exhibits steep morphology, a high HI value, and detectable deformation, no landslide events have been identified in this area. This indicates that the hazard potential in Sw14 is more latent and primarily associated with long-term geomorphological processes rather than active tectonic deformation.

In order to strengthen the interpretation, landslide events recorded between 2019 and 2025 were analyzed in relation to the deformation classification. The number of landslide events was compared across different deformation classes, as summarized in Table 3.

Validation of the deformation zones using the landslide inventory data indicates a strong spatial correlation. Out of a total of eight recorded landslide events, six events (75%) occurred within areas classified as High deformation, while two events (25%) were in the Moderate deformation zones. No landslides were observed in areas categorized as Low deformation or No deformation. These results demonstrate that the deformation zones mapped from InSAR analysis correspond well with the actual landslide occurrences, particularly within the high deformation areas.

This consistency is in line with previous studies support the findings of this research by emphasizing the strong relationship between ground deformation and landslide susceptibility. Miao et al., (2023) and Wu et al., (2024) highlighted that areas experiencing significant deformation are more prone to slope failures, and that incorporating InSAR data substantially improves landslide risk evaluation. Dai et al., (2022), Lau et al., (2024), and Ran et al., (2023) further demonstrated that advanced InSAR techniques such as SBAS and PS-InSAR are highly effective in detecting subtle ground movements, particularly in mountainous terrains. In addition, hypsometric analysis has been widely used to link geomorphic evolution with landslide potential, where youthful basins with higher hypsometric integral values tend to show greater instability (Vijith et al., 2017). The integration of InSAR-derived deformation with hypsometric parameters has therefore been recognized as a robust framework for improving landslide susceptibility assessments (Gera & Agegnehu, 2021; Ramzan et al., 2022).

Overall, this study highlights that landslide susceptibility in Jayapura City is governed by the interaction of two main factors: ongoing tectonic activity, particularly along thrust, normal, and strike-slip fault zones in Sw2, Sw3, and Sw4; and non-tectonic factors such as extensive land-use changes (Juna, 2025), especially in Sw10 and Sw11. These findings have significant implications for urban planning and disaster mitigation strategies in Jayapura

City. Areas characterized by active uplift, subsidence, mature hypsometric conditions, and weak lithologies should be prioritized in mitigation programs, including slope reinforcement, land-use regulation, and the implementation of early warning systems. Additionally, although areas like Sw14 currently show no recorded landslides, they should remain under close observation due to their steep geomorphological characteristics and latent instability potential, which may be exacerbated by ongoing denudation processes and increased human activities in the future.

Despite the comprehensive spatial analysis presented in this study, there are several limitations that should be acknowledged. The assessment relies solely on InSAR-derived deformation and hypsometric data, without incorporating other critical factors such as soil mechanical properties, rainfall intensity, and subsurface conditions. Therefore, the deformation patterns and slope instability identified represent preliminary indicators based on geomorphological and tectonic parameters rather than a complete landslide hazard assessment.

Conclusion

This study demonstrates that landslide susceptibility in Jayapura City is primarily governed by the interaction between tectonic deformation and geomorphological factors. InSAR analysis reveals significant uplift and subsidence concentrated in sub-watersheds Sw2, Sw3, and Sw4, which also correspond to areas with documented landslide events. The hypsometric assessment further highlights the role of mature to old geomorphic stages in amplifying slope instability. The integration of InSAR-derived deformation and hypsometric parameters thus provides an effective framework for identifying high-risk zones, with practical implications for slope reinforcement, land-use planning, and the development of early warning systems to reduce disaster risk in Jayapura City.

Despite these findings, several limitations should be acknowledged. The accuracy of InSAR analysis is influenced by atmospheric noise, temporal and spatial decorrelation, and the resolution of DEM data used for phase removal. Moreover, the study did not incorporate other key factors such as rainfall intensity, soil mechanical properties, and groundwater conditions, which are critical for comprehensive landslide hazard assessment. Therefore, the results should be considered preliminary indicators of slope instability. Future research combining multi-sensor SAR time-series, hydrological records, and geotechnical field validation will be essential to refine hazard mapping and support more robust disaster mitigation strategies in Jayapura City.

Acknowledgements

The authors gratefully acknowledge the Lembaga Penelitian dan Pengabdian kepada Masyarakat (LPPM) Universitas Cenderawasih for providing financial support for this research.

Author Contribution

All authors contributed substantially to this research. NAA contributed to the conceptualization, methodology, and writing original draft. HIH was responsible for investigation (landslide analysis) and visualization. RI and MNY conducted structural and tectonic analysis. HYH was responsible for integration of datasets. All authors contributed to writing, review, editing, and approved the final manuscript.

Conflict of Interest

The authors declare that there are no known financial or personal conflicts of interest

that could have appeared to influence the work reported in this paper.

References

Abrauw, R. D. (2017). Wilayah rawan longsor di Kota Jayapura. *Jurnal Geografi Lingkungan Tropik*, 1(1), 2. https://doi.org/10.7454/jglitrop.v1i1.4

Ahmad, M. S., Lisa, M., & Khan, S. (2024). Assessment and mapping of landslides in steep mountainous terrain using PS-InSAR: A case study of Karimabad Valley in Chitral. *Kuwait Journal of Science*, 51(1), 100137. https://doi.org/10.1016/j.kjs.2023.09.007

Alaska Satellite Facility Distributed Active Archive Center (ASF DAAC). (2025). *Sentinel-1 data search and download portal*. University of Alaska Fairbanks. https://search.asf.alaska.edu/

Alonso-Díaz, A., Casado-Rabasco, J., Solla, M., & Lagüela, S. (2023). Using InSAR and GPR Techniques to Detect Subsidence: Application to the Coastal Area of "A Xunqueira" (NW Spain). *Remote Sensing*, 15(15), 3729. https://doi.org/10.3390/rs15153729

Arabameri, A., Pradhan, B., Rezaei, K., & Lee, C.-W. (2019). Assessment of landslide susceptibility using statistical- and artificial intelligence-based FR-RF integrated model and multiresolution DEMs. *Remote Sensing*, 11(9), 999. https://doi.org/10.3390/rs11090999

Ardan. (2024). *Jayapura Hujan Deras, Akibatkan Longsor dan Banjir*. Radio Republik Indonesia Jayapura (RRI). https://www.rri.co.id/daerah/1199068/jayapura-hujan-deras-akibatkan-longsor-dan-banjir

Aristizábal, E., & Korup, O. (2025). Linking Landslide Patterns to Transient Landscapes in the Northern Colombian Andes. *Journal of Geophysical Research: Earth Surface*, 130(3), e2024JF008027. https://doi.org/10.1029/2024JF008027

Badan Informasi Geospasial. (2018). *DEMNAS*. Bada Informasi Geospasial. https://tanahair.indonesia.go.id/portal-web/unduh/demnas

Bianchini, S., Solari, L., Bertolo, D., Thuegaz, P., & Catani, F. (2021). Integration of satellite interferometric data in civil protection strategies for landslide studies at a regional scale. *Remote Sensing*, 13(10), 1881. https://doi.org/10.3390/rs13101881

Brengman, C. M. J., & Barnhart, W. D. (2021). Identification of Surface Deformation in InSAR Using Machine Learning. *Geochemistry, Geophysics, Geosystems*, 22(3), 1–15. https://doi.org/10.1029/2020GC009204

Cai, J., Zhang, L., Dong, J., Guo, J., Wang, Y., & Liao, M. (2023). Automatic identification of active landslides over wide areas from time-series InSAR measurements using Faster RCNN. *International Journal of Applied Earth Observation and Geoinformation*, 124(November), 103516. https://doi.org/10.1016/j.jag.2023.103516

Casagli, N., Intrieri, E., Tofani, V., Gigli, G., & Raspini, F. (2023). Landslide detection, monitoring and prediction with remote-sensing techniques. *Nature Reviews Earth and Environment*, 4(1), 51–64. https://doi.org/10.1038/s43017-022-00373-x

Chatterjee, S., Ansari, K., Biswas, M., Mukherjee, S., & Kavitha, B. (2024). Morphometry and active tectonics of the Konkan coast, western India. *Evolving Earth*, 2(January), 100041. https://doi.org/10.1016/j.eve.2024.100041

Dai, K., Deng, J., Xu, Q., Li, Z., Shi, X., Hancock, C., Wen, N., Zhang, L., & Zhuo, G. (2022). Interpretation and

sensitivity analysis of the InSAR line of sight displacements in landslide measurements. *GIScience and Remote Sensing*, 59(1), 1226–1242. https://doi.org/10.1080/15481603.2022.2100054

Diercks, M.-L., Grützner, C., Welte, J., & Ustaszewski, K. (2023). Challenges of geomorphologic analysis of active tectonics in a slowly deforming karst landscape (W Slovenia and NE Italy). *Geomorphology*, 440(November), 108894. https://doi.org/10.1016/j.geomorph.2023.108894

Dong, J., Guo, Y., Mei, Y., & Gao, K. (2025). Deformation monitoring and safety stability evaluation study of high-altitude limestone dumps. *PLoS ONE*, 20(2 February), 1–27. https://doi.org/10.1371/journal.pone.0318589

European Space Agency. (2014). *Sentinel-1 SAR data*. Copernicus Open Access Hub. https://sentinels.copernicus.eu/web/sentinel/missions/sentinel-1

Evarukdijati. (2019a). *Banjir dan Tanah Longsor melanda kota jayapura*. Antara News. https://papua.antaranews.com/berita/475037/banjir-dan-tanah-longsor-melanda-kota-jayapura

Evarukdijati. (2019b). *Longsor di Kawasan Ampera Kota Jayapura, empat orang meninggal*. https://www.antaranews.com/berita/811167/longsor-di-kawasan-ampera-kota-jayapura-empat-orang-meninggal

Evarukdijati. (2022). *Tanah longsor menyebabkan tujuh orang meninggal di Kota Jayapura*. Antara News.

Fan, B., Luo, G., Hellwich, O., Shi, X., Yuan, X., Ma, X., Shang, M., & Wang, Y. (2024). Monitoring Creeping Landslides with InSAR in a Loess-covered Mountainous Area in the Ili Valley, Central Asia. *PFG - Journal of Photogrammetry, Remote Sensing and Geoinformation Science*, 92(3), 235–251. https://doi.org/10.1007/s41064-024-00292-0

Farolfi, G., Del Soldato, M., Bianchini, S., & Casagli, N. (2019). A procedure to use GNSS data to calibrate satellite PSI data for the study of subsidence:an example from the north-western Adriatic coast (Italy). *European Journal of Remote Sensing*, 52(sup4), 54–63. https://doi.org/10.1080/22797254.2019.1663710

Gao, X., Wang, B., Dai, W., & Liu, Y. (2025). A landslide susceptibility assessment method using SBAS-InSAR to optimize Bayesian network. *Frontiers in Environmental Science*, 13(February), 1–25. https://doi.org/10.3389/fenvs.2025.1522949

Gera, S., & Agegnehu, N. (2021). Landslide Susceptible Mapping using InSAR and GIS Techniques: A Case Study at Debresina Area, Ethiopia. *Journal of Geology and Geophysics*, 10(3), 988. https://www.longdom.org/open-access-pdfs/landslide-susceptible-mapping-using-insar-and-gis-techniques-overview-of-debresina-area-ethiopia.pdf

Gu, Z.-K., Yao, X., Yao, C.-C., & Li, C.-G. (2021). Mapping of geomorphic dynamic parameters for analysis of landslide hazards: A case of Yangbi river basin on the upper Lancang-Mekong of China. *Journal of Mountain Science*, 18(9), 2402–2411. https://doi.org/10.1007/s11629-021-6795-2

Guo, H., & Martínez-Graña, A. M. (2024). Susceptibility of Landslide Debris Flow in Yanghe Township Based on Multi-Source Remote Sensing Information Extraction Technology (Sichuan, China). *Land*, 13(2), 206. https://doi.org/10.3390/land13020206

Gururani, K., Kothyari, G. C., & Kotlia, B.

S. (2023). Morphotectonic assessment of the Gaula river basin, Kumaun lesser Himalaya, Uttarakhand. *Quaternary Science Advances*, 12(October), 100115. https://doi.org/10.1016/j.qsa.2023.100115

Guvel, Ş. P., Akgul, M. A., & Akkoyunlu, M. F. (2023). Monitoring and Evaluation of 2015 Devrek Zonguldak Landslide within the scope of Flood Risk Assessment by Landsat-8 Satellite Data. *Doğal Afetler ve Çevre Dergisi*, 9(1), 81–89. https://doi.org/10.21324/dacd.1152670

Hang, P. T. T., Shakirov, R., Thom, B. V., Dung, L. V., Syrbu, N., Hieu, T. T., Anh, P. T. N., Yen, T. H., Maltseva, E., Kholmogorov, A., Tuyen, N. H., & An, V. H. (2025). Assessment of the Tectonic Activity of the Muong La–Bac Yen–Cho Bo Fault (Northwest Vietnam) by Analysis of Geomorphological Indices. *GeoHazards*, 6(2), 16. https://doi.org/10.3390/geohazards6020016

Hu, X., Sun, Z., Wang, Z., Huang, X., Zhou, M., He, S., Xiao, H., Liu, D., Yang, Y., & Xu, W. (2025). InSAR-based deep learning prediction model for multi-type landslides displacement and failure time in Zigui, Three Gorges Area, China. *Landslides,* (2025). https://doi.org/10.1007/s10346-025-02613-9

Juna. (2025). *900 Unit Perumahan Grand Royal Residen II akan Dibangun di Holtekamp*. Cenderawasih Pos. https://cenderawasihpos.jawapos.com/ekonomi-bisnis/04/02/2025/900-unit-perumahan-grand-royal-residen-ii-akan-dibangun-di-holtekamp/%0A

Katharina. (2021). *Jayapura Rawan Longsor, Warga Harus Waspada*. Kumparan. https://kumparan.com/bumi-papua/jayapura-rawan-longsor-warga-harus-waspada-1vE0VmMh3zo/full

Keller, E. A., & Pinter, N. (2002). Active Tectonics Earthquakes, Uplift, and Landscape. In *Prentice Hall earth science series* (second edi). Prentice Hall. https://doi.org/10.2113/gseegeosci.iii.3.463

Khattab, M. I., Abotalib, A. Z., Othman, A., & Selim, M. K. (2023). Evaluation of multiple digital elevation models for hypsometric analysis in the watersheds affected by the opening of the Red Sea. *The Egyptian Journal of Remote Sensing and Space Science*, 26(4), 1020–1035. https://doi.org/10.1016/j.ejrs.2023.11.011

Kothyari, H. C., Kothyari, G. C., Joshi, R. C., Gururani, K., Nandy, S., & Patidar, A. K. (2024). Assessment of fluvial response to landslide susceptibility and transient response of tectonically active upper Alaknanda River basin of Uttarakhand Himalaya, India. *Quaternary Science Advances*, 15(September), 100221. https://doi.org/10.1016/j.qsa.2024.100221

Lau, R., Seguí, C., Waterman, T., Chaney, N., & Veveakis, M. (2024). InSAR-informed in situ monitoring for deep-seated landslides: insights from El Forn (Andorra). *Natural Hazards and Earth System Sciences*, 24(10), 3651–3661. https://doi.org/10.5194/nhess-24-3651-2024

Leloltery, A. (2025). *BPBD Papua: Longsor Jalan Ring Road Kota Jayapura Perlu Penanganan Serius*. Antara News. https://papua.antaranews.com/berita/735782/bpbd-papua-longsor-jalan-ring-road-kota-jayapura-perlu-penanganan-serius

Li, C., Yi, B., Gao, P., Li, H., Sun, J., Chen, X., & Zhong, C. (2021). Valuable clues for dcnn-based landslide detection from a comparative

assessment in the wenchuan earthquake area. *Sensors*, 21(15), 5191. https://doi.org/10.3390/s21155191

Liem, N. V., Dat, N. P., Dieu, B. T., Phai, V. V., Trinh, P. T., Vinh, H. Q., & Phong, T. V. (2016). Assessment of Geomorphic Processes and Active Tectonics in Con Voi Mountain Range Area (Northern Vietnam) Using the Hypsometric Curve Analysis Method. *Vietnam Journal of Earth Sciences*, 38(2), 202–216. https://doi.org/10.15625/0866-7187/38/2/8602

Lin, N., Ding, K., Tan, L., Li, B., Yang, K., Wang, C., Wang, B., Li, N., & Yang, R. (2025). Dynamic landslide susceptibility mapping on time-series InSAR and explainable machine learning: a case study at Wushan in the Three Gorges Reservoir area, China. *Advances in Space Research*, 75(12), 8439–8465. https://doi.org/10.1016/j.asr.2025.03.067

Makrari, S., Sharma, G., Taloor, A. K., Singh, M. S., Sarma, K. K., & Aggarwal, S. P. (2022). Assessment of the geomorphic indices in relation to tectonics along selected sectors of Borpani River Basin, Assam using Cartosat DEM data. *Geosystems and Geoenvironment*, 1(3), 100068. https://doi.org/10.1016/j.geogeo.2022.100068

Miao, F., Ruan, Q., Wu, Y., Qian, Z., Kong, Z., & Qin, Z. (2023). Landslide Dynamic Susceptibility Mapping Base on Machine Learning and the PS-InSAR Coupling Model. *Remote Sensing*, 15(22), 5427. https://doi.org/10.3390/rs15225427

Mondini, A. C., Santangelo, M., Rocchetti, M., Rossetto, E., Manconi, A., & Monserrat, O. (2019). Sentinel-1 SAR amplitude imagery for rapid landslide detection. *Remote Sensing*, 11(7), 0760. https://doi.org/10.3390/rs11070760

Mulyasari, R., Brahmantyo, B., & Supartoyo. (2017). Morphometric analysis of relative tectonic activity in the Baturagung Mountain, Central Java, Indonesia. *IOP Conference Series: Earth and Environmental Science*, 71(1), 012006. https://doi.org/10.1088/1755-1315/71/1/012006

Nikoonejad, A., Pourkermani, M., Asadi, A., & Almasian, M. (2015). Hypsometric Properties of South Zagros Fold-Thrust Belt Basins: A Case Study in Namdan Basin in SW Iran. *Open Journal of Geology*, 5(10), 701–717. https://doi.org/10.4236/ojg.2015.510062

Novellino, A., Cesarano, M., Cappelletti, P., Di Martire, D., Di Napoli, M., Ramondini, M., Sowter, A., & Calcaterra, D. (2021). Slow-moving landslide risk assessment combining Machine Learning and InSAR techniques. *Catena*, 203(August), 105317. https://doi.org/10.1016/j.catena.2021.105317

Ntokos, D. (2025). Unveiling tectonic activity through lithological-erosional interplay with the Tectonic Processes Index Tδ. *Journal of Asian Earth Sciences*, 291(September), 106680. https://doi.org/10.1016/j.jseaes.2025.106680

Othman, A. A., Gloaguen, R., Andreani, L., & Rahnama, M. (2018). Improving landslide susceptibility mapping using morphometric features in the Mawat area, Kurdistan Region, NE Iraq: Comparison of different statistical models. *Geomorphology*, 319, 147–160. https://doi.org/10.1016/j.geomorph.2018.07.018

Pamanggori. (2024). *Longsor menimpa Pasar Ikan Dok 9 Namun Tidak Ada Korban Jiwa*. Noken Live. https://www.nokenlive.com/2024/12/18/longsor-menimpa-pasar-ikan-dok-

9-namun-tidak-ada-korban-jiwa/

Patel, D. K., Thakur, T. K., Saini, S., Patel, A., Bhatt, S. C., Kumar, A., Kumar, R., & Husain, F. M. (2024). Morphometric indices assessment: Implications for active tectonics in the upper Narmada Basin, central India. *Physics and Chemistry of the Earth*, 136(December), 103746. https://doi.org/10.1016/j.pce.2024.103746

Piroton, V., Schlögel, R., Barbier, C., & Havenith, H.-B. (2020). Monitoring the recent activity of landslides in the Mailuu-Suu valley (Kyrgyzstan) using radar and optical remote sensing techniques. *Geosciences*, 10(5), 164. https://doi.org/10.3390/geosciences10050164

Rabii, F., Achour, H., Rebai, N., & Jallouli, C. (2017). Hypsometric integral for the identification of neotectonic and lithology differences in low tectonically active area (Utica-Mateur region, north-eastern Tunisia). *Geocarto International*, 32(11), 1229–1242. https://doi.org/10.1080/10106049.2016.1195890

Ramzan, U., Fan, H., Aeman, H., Ali, M., & Al-qaness, M. A. A. (2022). Combined analysis of PS-InSAR and hypsometry integral (HI) for comparing seismic vulnerability and assessment of various regions of Pakistan. *Scientific Reports*, 12, 22423. https://doi.org/10.1038/s41598-022-26159-1

Ran, P., Li, S., Zhuo, G., Wang, X., Meng, M., Liu, L., Chen, Y., Huang, H., Ye, Y., & Lei, X. (2023). Early Identification and Influencing Factors Analysis of Active Landslides in Mountainous Areas of Southwest China Using SBAS−InSAR. *Sustainability (Switzerland)*, 15(5), 4366. https://doi.org/10.3390/su15054366

Romero, R. V. (2024). Application of Geographic Information System (GIS) for Hypsometric Analysis of a Bicol River Basin Area. *Engineering and Technology Journal*, 09(08), 4787–4794. https://doi.org/10.47191/etj/v9i08.25

Saepuloh, A. (2021). *Prinsip dan aplikasi penginderaan jauh geologi gunungapi*. ITB Press.

Schumm, S. A. (1956). Geological Society of America Bulletin Evolution Of Drainage Systems And Slopes In Badlands At Perth Amboy , New Jersey. *Bulletin of the Geological Society of America*, 67(5), 597–646. https://doi.org/10.1130/0016-7606(1956)67

Shan, Y., Xu, Z., Zhou, S., Lu, H., Yu, W., Li, Z., Cao, X., Li, P., & Li, W. (2024). Landslide Hazard Assessment Combined with InSAR Deformation: A Case Study in the Zagunao River Basin, Sichuan Province, Southwestern China. *Remote Sensing*, 16(1), 99. https://doi.org/10.3390/rs16010099

Sorkhabi, O. M., Khajehzadeh, M., & Keawsawasvong, S. (2023). Landslides monitoring with SBAS-InSAR and GNSS. *Physics and Chemistry of the Earth*, 132(December), 103486. https://doi.org/10.1016/j.pce.2023.103486

Staniewicz, S., & Chen, J. (2024). Automatic Detection of InSAR Surface Deformation Signals in the Presence of Severe Tropospheric Noise, *TechRxiv*, 1–12. https://doi.org/10.36227/techrxiv.20128406.v2

Strząbała, K., Ćwiąkała, P., & Puniach, E. (2024). Identification of Landslide Precursors for Early Warning of Hazards with Remote Sensing. *Remote Sensing*, 16(15), 2781. https://doi.org/10.3390/rs16152781

Suwarna, N., & Noya, Y. (1995). *Peta geologi lembar Jayapura (Pegunungan Cycloops), Irian Jaya*.

Pusat Penelitian dan Pengembangan Geologi (P3G). Bandung.

Vijith, H., Prasannakumar, V., & Pratheesh, P. (2017). Landform evaluation through hypsometric characterisation: An example from a selected river basin in Southern Western Ghats, India. *Environmental Research, Engineering and Management*, 73(4), 41–57. https://doi.org/10.5755/j01.erem.73.4.19553

Welikanna, D., & Jin, S. (2023). Investigating ground deformation due to a series of collapse earthquakes by means of the ps-insar technique and sentinel 1 data in kandy, sri lanka. *Journal of Applied Remote Sensing*, 17(1), 014507. https://doi.org/10.1117/1.jrs.17.014507

Wu, X., Qi, X., Peng, B., & Wang, J. (2024). Optimized Landslide Susceptibility Mapping and Modelling Using the SBAS-InSAR Coupling Model. *Remote Sensing*, 16(16). https://doi.org/10.3390/rs16162873

Yao, Z., Chen, M., Zhan, J., Zhuang, J., Sun, Y., Yu, Q., & Yu, Z. (2023). Refined Landslide Susceptibility Mapping by Integrating the SHAP-CatBoost Model and InSAR Observations: A Case Study of Lishui, Southern China. *Applied Sciences*, 13(23), 12817. https://doi.org/10.3390/app132312817

Yu, W., Li, W., Wu, Z., Lu, H., Xu, Z., Wang, D., Dong, X., & Li, P. (2024). Integrated Remote Sensing Investigation of Suspected Landslides: A Case Study of the Genie Slope on the Tibetan Plateau, China. *Remote Sensing*, 16(13), 2412. https://doi.org/10.3390/rs16132412

Zhang, X., Gan, S., Yuan, X., Zong, H., Wu, X., & Shao, Y. (2024). Early Identification and Characteristics of Potential Landslides in Xiaojiang Basin, Yunnan Province, China Using Interferometric Synthetic Aperture Radar Technology. *Sustainability (Switzerland)*, 16(11), 4649. https://doi.org/10.3390/su16114649

ISSN: 2579-5821 (Print)
ISSN: 2579-5546 (Online)
URL address: http://journal.unhas.ac.id/index.php/geocelebes
DOI: 10.70561/geocelebes.v9i2.46445

Jurnal Geocelebes Vol. 9 No. 2, October 2025, 189 – 212

Comparative Analysis of SARIMA, FFNN, and Hybrid Models for Sea Surface Temperature Prediction at Enggano Island (2018–2024)

Raditya Janaloka Natisharevi, Jose Rizal*, Firdaus, Pepi Novianti, Wina Ayu Lestari

Department of Statistics, Faculty of Mathematics and Natural Science, University of Bengkulu, Bengkulu 38371, Indonesia

*Corresponding author. Email: jrizal04@unib.ac.id

Manuscript received: 21 August 2025; Received in revised form: 13 October 2025; Accepted: 15 October 2025

Abstract

Sea Surface Temperature (SST) is a key oceanographic variable that influences fish distribution and the livelihoods of coastal communities. On Enggano Island, where most residents rely on fishing, SST is critical for identifying optimal fishing grounds due to limited accessibility and high operational costs. Accurate modeling and forecasting of SST are therefore essential for effective fisheries management and sustainable resource use. This study analyzes and predicts monthly SST patterns in Enggano Island using Seasonal Autoregressive Integrated Moving Average (SARIMA), Feed Forward Neural Network (FFNN), and Hybrid SARIMA-FFNN models. SARIMA effectively captures linear trends and seasonal variations but struggles with nonlinear dynamics and requires statistical assumptions. Conversely, FFNN models nonlinear relationships without such assumptions but is less efficient in representing linear and seasonal structures. The hybrid SARIMA-FFNN combines the strengths of both approaches, integrating linear-seasonal accuracy with nonlinear adaptability. Monthly SST data from January 2018 to December 2024, covering northern, eastern, southern, and western regions of Enggano Island, were analyzed. Results show that all models achieved high predictive accuracy, with MAPE values below 10%. Based on RMSE, FFNN outperformed the other models across all regions (north: 1.173, east: 0.999, south: 1.245, west: 1.049), confirming FFNN as the most accurate model for SST prediction. Predicted SST values across the four regions exhibited only minor differences, offering fishermen flexibility in selecting fishing grounds. Sustainable fishing strategies should also consider species-specific temperature preferences and other ecological factors influencing fish distribution.

Keywords: Enggano Island; FFNN; Hybrid SARIMA-FFNN; SARIMA; Sea Surface Temperature.

Citation: Natisharevi, R. J., Rizal, J., Firdaus, F., Novianti, P., & Lestari, W. A. (2025). Comparative Analysis of SARIMA, FFNN, and Hybrid Models for Sea Surface Temperature Prediction at Enggano Island (2018–2024). *Jurnal Geocelebes*, 9(2):189–212, doi: 10.70561/geocelebes.v9i2.46445

Introduction

Oceanography is the scientific discipline that studies various dynamic and physical processes in seawater (Kambey et al., 2023). One of the important variables in oceanography is sea surface temperature (SST), which influences fish distribution (Rifai, 2023). This factor is particularly crucial for the residents of Enggano Island, the majority of whom work as fishermen (Silsia et al., 2019). Enggano Island is one of the outermost islands in Bengkulu Province, relatively remote with very limited access, requiring approximately 12 hours of sea travel to reach (Sari, 2020). Such limited accessibility affects the high price of fuel oil, which serves as the primary energy source for fishing vessels, since fuel is supplied in small quantities from Bengkulu City via sea transportation (Silsia et al., 2019). This situation poses a challenge for Enggano fishermen, who generally rely only on experience in determining fishing locations. As a result, fishermen often set sail without certainty regarding optimal fishing grounds, which may lead to increased operational costs or low catch yields (Baharudin et al., 2022). One solution to the problem of fishing ground determination is predicting

SST, with the expectation that it can provide insights into optimal fishing locations (Shabrina et al., 2017).

SST exhibits seasonal patterns influenced by meteorological conditions (Hastuti et al., 2024). Therefore, one of the appropriate models to apply is the Seasonal Autoregressive Integrated Moving Average (SARIMA). This model represents that the current observation is affected by previous observations and prediction errors in both regular and seasonal periods. However, SARIMA has certain limitations, particularly the statistical assumptions that must be satisfied, such as data stationarity and the white noise assumption. In addition, SARIMA is unable to capture nonlinear patterns in the data (Susila et al., 2023). These limitations can be addressed through the application of Neural Networks (NN).

NN do not require statistical assumptions in modeling and are capable of learning nonlinear patterns in data through their network structures and activation functions (Zhang, 2003). NN are artificial representations of the human brain that continuously attempt to simulate the learning mechanisms of the human mind (Septiana & Bangun, 2023). Various network architectures exist within Neural Networks, one of which is the Feed Forward Neural Network (FFNN). The principle of FFNN is to transmit information forward from the input layer to the hidden layer and then to the output layer, without the presence of loops (Aminy & Walid, 2022). Although the flow of information is unidirectional, the weights in FFNN are updated using the backpropagation algorithm to produce more accurate predictions. Nevertheless, FFNN tends to be less effective in capturing linear and seasonal structures in time series data (Fadhlia et al., 2024).

Considering these complementary strengths and weaknesses, the Hybrid SARIMA-FFNN model integrates both approaches to leverage their advantages. In this framework, the residuals from the SARIMA model, which represent the nonlinear components, are used as inputs for the FFNN to capture nonlinear dynamics. The outputs from the FFNN are then combined with the SARIMA predictions to produce the final forecast, thereby enhancing accuracy in complex time series such as SST (Fadhlia et al., 2024). Since SST can exhibit linear patterns, nonlinear dynamics, or a combination of both due to interactions between seasonal cycles, ocean currents, and meteorological factors, it is important to systematically compare SARIMA, FFNN, and hybrid approaches to determine which method is most suitable for different data characteristics, avoiding models that are either too simple or unnecessarily complex.

Several studies have been conducted on the modeling and prediction of sea surface temperature (SST). Syahrin et al. (2024) utilized the NeuralProphet model to forecast SST. However, this model does not specifically accommodate the seasonal patterns present in SST data. Meanwhile, Hisyam et al. (2025) applied the SARIMA approach to predict SST, which is effective in representing seasonal components. Nevertheless, this model is less capable of capturing nonlinear patterns that may arise in SST data. Based on these studies, it is evident that each model has its strengths and limitations. Consequently, a research gap remains in the development of methods that can integrate the advantages of both approaches for SST forecasting. In addition, studies on SST prediction in Bengkulu Province, particularly in Enggano Island, are still very limited.

Therefore, this study aims to address the existing research gap by modeling sea surface temperature (SST) in Enggano Island using SARIMA, FFNN, and Hybrid SARIMA-FFNN approaches. In addition to developing these models, the study also seeks to evaluate the performance of all three approaches, with the expectation of providing new insights into the most

effective model for supporting improved SST prediction accuracy.

Materials and Methods

Data Type and Sources

This study utilized secondary data, which was obtained from Giovanni, a free web-based system from NASA accessible at https://giovanni.gsfc.nasa.gov/giovanni. The data used was monthly SST observations, recorded from January 2018 to December 2024. The collected data was of the time series area average type with several specifications. The SST data was specifically taken at nighttime to avoid measurement bias caused by the reflection of solar radiation. This choice is also relevant as it aligns with the common practice of local fishermen, who typically go out to sea at night to maximize their catch. Furthermore, a 4 km spatial resolution was used to obtain a more detailed and accurate view of the research area, and an 11-micron spectral resolution was chosen because it represents the most reliable wavelength for measuring SST. This data covers four distinct observation locations: the northern, southern, western, and eastern parts of Enggano Island. An illustration of these observation areas is presented in Figure 1.

Figure 1. Illustration of observation area.

Figure 1 illustrates the observation area. The specific details of the observation locations are provided by the following coordinates:

1. East: 05º11'S – 05º32'S and 101º50'E – 102º05'E.
2. North: 05º11'S – 05º17'S and 101º59'E – 102º29'E.
3. West: 05º11'S – 05º32'S and 102º23'E – 102º29'E.
4. South: 05º29'S – 05º35'S and 101º59'E – 102º29'E.

For modeling purposes, the data were partitioned into 72 data points were used for training, and the remaining 12 points were used for testing. This partition preserves the full annual cycle in the training data, which is important for capturing seasonal patterns in SST. The selection of the 72:12 split was guided by preliminary spectral analysis, ensuring that the strongest seasonal components were retained in the training set while allowing for reliable out-of-sample evaluation.

Data Cleaning

Data cleaning is the process of identifying and correcting incorrect data (Azmi et al., 2023). In this study, the data cleaning process focuses on addressing the issue of

missing values. Since this research utilizes time series data, which requires complete and sequential observations for proper analysis (Wei, 2006), data imputation is considered the most appropriate approach.

If missing data are found at the beginning or end of the dataset, imputation will be carried out using linear extrapolation according to Equation 1 (Pangruruk & Barus, 2022).

$$Z_t = \begin{cases} Z_{t1} + \frac{Z_{t2}-Z_{t1}}{t_2-t_1}(t-t_1), \text{for } t < t_1 \\ Z_{t2} + \frac{Z_{t2}-Z_{t1}}{t_2-t_1}(t-t_2), \text{for } t < t_2 \end{cases} \quad (1)$$

Meanwhile, if missing data occur between two observation points, imputation will be performed using linear interpolation according to Equation 2 (Pangruruk & Barus, 2022).

$$Z_t = Z_{t1} + \frac{Z_{t2} - Z_{t1}}{t_2 - t_1}(t - t_1) \quad (2)$$

where Z_{t1} represents the second-to-last known value and Z_{t2} represents the last known value.

Seasonal Pattern Testing

Seasonal patterns can be identified using spectral regression. Spectral regression is a technique useful for detecting hidden periodicities in data (Wei, 2006). The first step in this testing involves representing the data using a Fourier equation, as shown in Equation 3 (Wei, 2006).

$$Z_t = \sum_{m=0}^{[\frac{n}{2}]} (a_m \cos \omega_m t + b_m \sin \omega_m t) \quad (3)$$

where $m = 0,1, \dots, [\frac{n}{2}]$ represents the frequency components of ω_m dan $\omega_m = \frac{2\pi m}{n}$ denotes the Fourier frequency.

Next, the Fourier coefficients are calculated using Equations 4 to 6 (Wei, 2006).

1. For $m = 0$ dan $m = \frac{n}{2}$ if n even

$$a_m = \frac{1}{n}\sum_{t=1}^{n} Z_t \cos \omega_m t \quad (4)$$

2. For $m = 1,2, \dots, \left[\frac{n-1}{2}\right]$

$$a_m = \frac{2}{n}\sum_{t=1}^{n} Z_t \cos \omega_m t \quad (5)$$

$$b_m = \frac{2}{n}\sum_{t=1}^{n} Z_t \sin \omega_m t \quad (6)$$

Next, the ordinate values are calculated using Equation 7.

$$I(\omega_m) = \begin{cases} na_0^2, m = 0, \\ \frac{n}{2}(a_m^2 + b_m^2), m = 1, \dots, \left[\frac{n-1}{2}\right], \\ na_{n/2}^2, m = \frac{n}{2} \text{ when } n \text{ even.} \end{cases} \quad (7)$$

After obtaining the ordinate values that reflect the strength of the seasonal components, the highest ordinate value is then tested using a hypothesis test. The hypotheses are:
$H_0: a_m = b_m = 0$ (not influenced by seasonal components)
$H_1: a_m \neq 0$ atau $b_m \neq 0$ (influenced by seasonal components).

The test statistic is calculated using Equation 8 (Wei, 2006).

$$T = \frac{I^{(m)}(\omega_{(m)})}{\Sigma_{m=1}^{[\frac{n}{2}]} I(\omega_m)}. \quad (8)$$

If the value of $T > g_\alpha$, then H_0 is rejected, it means that seasonal components influence the data.

Data Stationarity

A process $\{Z_t\}$ is said to be stationary if it satisfies the following conditions (Wei, 2006):

1. $E(Z_t) = \mu$, constant for all t.
2. $Var(Z_t) = E(Z_t - \mu)^2 = \sigma^2$, constant for all t.
3. $Cov(Z_t, Z_{t-k}) = \gamma_{t,t-k} = \gamma_k$, constant for all t.

Data are considered to meet the stationarity criteria if both the variance and mean remain constant over time. The assumption of stationarity in variance is considered satisfied if the value of λ is equal to or close

to one. If this assumption is not met, it can be addressed using the Box-Cox transformation, as shown in Equation 9 (Cryer & Chan, 2008).

$$Z_t(\lambda) = \begin{cases} \dfrac{Z_t^{\lambda} - 1}{\lambda}, (\lambda \neq 0) \\ ln\, Z_t, (\lambda = 0). \end{cases} \quad (9)$$

The stationarity assumption of the mean can be tested using the Augmented Dickey-Fuller (ADF) test, with $H_0 : \psi = 0$ (The data are non-stationary in mean) dan $H_1 : \psi < 0$ (The data are stationary in mean). The test statistic used is as follows (Cryer & Chan, 2008):

$$\tau = \frac{\hat{\psi}}{SE(\hat{\psi})}. \quad (10)$$

If the test statistic value is obtained $\tau < DF_{(\alpha)}$ or $P_{value}(\tau) < \alpha$, then H_0 is rejected. Here, the value of τ is obtained from the calculation in Equation 10, and $DF_{(\alpha)}$ represents the critical value taken from the Dickey-Fuller distribution table at the chosen significance level. Rejection of H_0 indicates that the tested data are stationary in mean. If the data do not yet satisfy mean stationarity, it can be addressed using differencing, either non-seasonal ($\Delta^d Z_t = (1-B)^d Z_t$) or seasonal ($\Delta^s Z_t = (1-B)^s Z_t$).

Autocorrelation Function (ACF)

The ACF is a function used to describe the correlation between Z_t and Z_{t+k} separated by a lag of k time units. The ACF estimation is expressed in Equation 11 (Wei, 2006).

$$\hat{\rho}_k = \frac{\hat{\gamma}_k}{\hat{\gamma}_0} = \frac{\Sigma_{t=1}^{n-k}(z_t - \bar{z})(z_{t+k} - \bar{z})}{\Sigma_{t=1}^{n}(z_t - \bar{z})^2} \quad (11)$$

Partial Autocorrelation Function (PACF)

The PACF is a function used to measure the direct strength of the relationship between Z_t and Z_{t+k}, assuming that the effects of the intervening lags $1, 2, 3, \ldots, k-1$ are removed. The PACF can be estimated using Equation 12 (Wei, 2006).

$$\hat{\phi}_{k,k} = \frac{\hat{\rho}_k - \Sigma_{j=1}^{k-1}\hat{\phi}_{k-1,j}\,\hat{\rho}_{k-j}}{1 - \Sigma_{j=1}^{k-1}\hat{\phi}_{k-1,j}\,\hat{\rho}_j} \quad (12)$$

Seasonal Autoregressive Integrated Moving Average (SARIMA)

SARIMA is a model that represents the dependence of the current observation on both previous observations and predictions, as well as on observations from previous seasonal periods. Mathematically, the SARIMA model is expressed in Equation 13 (Wei, 2006).

$$\phi_p(B)\Phi_P(B^S)(1-B)^d\,(1-B^S)^D\,Z_t = \theta_q(B)\,\Theta_Q(B^S)\,e_t \quad (13)$$

SARIMA Steps

SARIMA modeling can be carried out through several steps, as follows:

1. Model identification

ACF and PACF plots, which exhibit characteristics as shown in Table 1, can identify the SARIMA model.

Table 1. Characteristics of ACF & PACF plots (Wei, 2006).

Model	ACF	PACF
AR(p)	Decays exponentially	Cuts off after lag p
MA(q)	Cuts off after lag q	Decays exponentially
AR(P)^S	Decays exponentially at lag lag kS	Cuts off after lag PS
MA(Q)^S	Cuts off after lag QS	Decays exponentially at lag lag kS

2. Parameter estimation method

The parameters of the SARIMA model can be estimated using the Maximum Likelihood Estimation (MLE) approach. MLE is a method of estimation based on the distribution that maximizes the likelihood function.

The general steps in parameter estimation using MLE include identifying the probability density function (PDF) of the data, constructing the likelihood function, transforming it into the log-likelihood, taking the first derivatives to find the parameter values that maximize the log-likelihood, and verifying that these estimates indeed correspond to a maximum by examining the second derivatives.

3. Parameter significance

The significance of the SARIMA model parameters can be tested using the hypothesis test. The hypotheses are:
$H_0: \beta_i = 0$ (significant parameters)
$H_1: \beta_i \neq 0$ (insignificant parameters).

The test statistic as shown in Equation 14 (Wei, 2006).

$$Z = \frac{\hat{\beta}_i}{SE(\hat{\beta}_i)}. \quad (14)$$

If the test statistic value is obtained $|Z| > Z_{\frac{a}{2}}$ or $P_{value}(Z) < \alpha$, this indicates that the parameter is significant.

4. Model diagnostics

The process of verifying that the model is correctly specified is called model diagnostics. Model diagnostics consist of two testing stages: testing the assumption of autocorrelation in the errors and testing the normality of the errors (Wei, 2006). The assumption of autocorrelation in the errors is tested using the Ljung-Box test, with the test statistic $Q = n(n+2)\sum_{k=1}^{K} \frac{\hat{\rho}_k^2}{n-k}$. The normality assumption of the errors is tested using the Kolmogorov-Smirnov (KS) test, with the test statistic defined as $D_{KS} = \sup|F_n(x) - F_0(x)|$. Both assumptions, autocorrelation and normality of the residuals, are considered satisfied if the test statistic value is greater than the critical value, or if the $P_{value} < \alpha$. Meeting these assumptions indicates that the model is correctly specified and suitable for prediction purposes.

5. Selection of the optimal SARIMA model

According to Cryer & Chan (2008), models developed using the Box-Jenkins approach, such as SARIMA, can be compared and evaluated to select the optimal model from several candidate models. In this study, the optimal SARIMA model was chosen based on the lowest values of the Akaike Information Criterion (AIC) and Bayesian Information Criterion (BIC). The AIC and BIC values can be calculated using Equations 15 and 16 (Zhang & Meng, 2023).

$$\text{AIC} = -2\ln(L) + 2I. \quad (15)$$
$$\text{BIC} = -2\ln(L) + I\ln(n). \quad (16)$$

where I denotes the number of parameters in the model and L refers to the maximum value of the likelihood function.

Data Preprocessing

This process represents the initial stage used for network training in the FFNN model. Its purpose is to select the input values to be used, where the input values consist of past observations (Zhang, 2003). In the input layer of the FFNN, the input neurons are derived from a set of variables constructed from the time series data. The following function expresses these variables (Zhang, 2003):

$$Z_t = (X_1, X_2, \ldots, X_I) \quad (17)$$

where $X_i = Z_{t-i}$, $i = 1,2,\ldots,I$, and $t = 1,2,\ldots,n$. This means that each input neuron X_i represents the value of the time series Z at lag i. In other words, the FFNN uses the past I observations of the series as input to predict the current value Z_t.

Data Normalization

Data normalization is the process of rescaling data prior to the learning process, aimed at ensuring that the data can be processed in accordance with the applied activation function (Permana & Salisah, 2022). In this study, min-max scaling normalization was employed, as shown in Equation 18 (Izonin et al., 2022).

$$Z_t' = \frac{Z_t - Z_{min}}{Z_{\max} - Z_{min}}(D - C) + C \quad (18)$$

where D represents the upper range and C represents the lower range of the desired output.

Activation Function

The activation function determines each neuron's output. It operates by transforming the total input received by a neuron into an output that is forwarded to the subsequent neuron. This study employed the binary sigmoid activation function, as it is easily differentiable and does not decrease monotonically. The binary sigmoid activation function is mathematically expressed as shown in Equation 19 (Kurniasari et al., 2023).

$$f(x) = \frac{1}{1 + e^{-x'}} \quad (19)$$

where

$$f'(x) = f(x)\,(1 - f(x)) \quad (20)$$

Equation 20 is the derivative of Equation 19, which will be used to calculate error information in the backpropagation algorithm.

Learning Rate

The training parameter used to control the speed of weight updates in the network is called the learning rate. There is no strict rule for determining the learning rate value; however, it must lie between 0 and 1. A higher learning rate accelerates the training process, but it may also reduce the accuracy of the network's results (Kurniasari et al., 2023).

Weight Initialization

The strength of connections is determined by values called weights. At the initial stage of training, weights are first initialized with small random numbers. Weight initialization in neural networks does not follow a fixed rule, and various methods can be applied. However, based on general heuristics, biases can be initialized to 0, and weights can be generated from a uniform distribution $U\left[-\frac{1}{\sqrt{n}}, \frac{1}{\sqrt{n}}\right]$, where n is the number of neurons in the previous layer (Glorot & Bengio, 2010). After initializing the weights and biases, the network undergoes training, during which the weights are updated to obtain optimal values and produce accurate outputs.

Feed Forward Neural Network (FFNN)

The FFNN is a network architecture capable of handling nonlinear patterns. It consists of three main layers: the input layer, the hidden layer, and the output layer (Ichwan & Alfarisyi, 2024). The input layer feeds data into the network, the hidden layer processes data from the input layer, and the output layer generates outputs based on the provided inputs. Figure 2 illustrates the architecture of the FFNN.

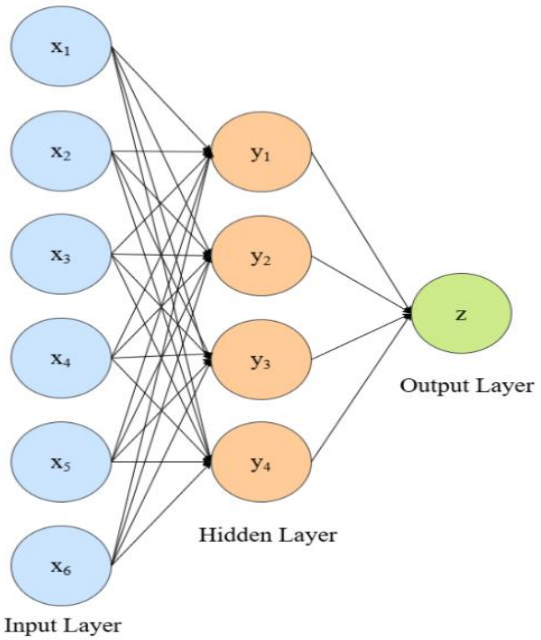

Figure 2. FFNN architecture (Modified from Alrowais et al., 2023).

The principle of the FFNN shown in Figure 2 is the forward flow of information from the input layer to the hidden layer and then to the output layer, without any loops (Aminy & Walid, 2022). The blue circles representing the input neurons process the preprocessed data. This information is then passed to the hidden layer, where the orange circles (hidden neurons) process it through a combination of

weights and activation functions. The output layer, which consists of green neurons, then shows the final output or prediction based on the network's processing. Although the information flows only forward, the weights in the FFNN are updated using the backpropagation algorithm to produce more accurate predictions.

Backpropagation

Backpropagation functions to adjust the weights of all neurons. The process involves several stages: feedforward, backpropagation, and weight and bias updates (Li, 2024). The stages of backpropagation are as follows, and all equations presented in this stage refer to (Wulandari & Novita, 2024):

1. Feedforward
   a. Each input neuron $(X_i, i = 1, 2, , I)$ receives an input signal x_i moreover, sends it to the hidden layer.
   b. The weighted sum of signals for each hidden neuron $(Y_h, h = 1, 2, , H)$ is calculated as $y_{in_h} = v_{0h} + \sum_{i=1}^{I} x_i v_{ih}$.
      The output signal is then computed using the binary sigmoid activation function $y_h = f(y\_in_h) = \frac{1}{1+e^{-y\_in_h}}$.
   c. The weighted sum of signals for each output unit $(Z_r, r = 1, 2, , R)$ is calculated as $z_{in_r} = w_{or} + \sum_{h=1}^{H} y_h w_{hr}$.
      The activation function is applied to produce the output $z_r = f(z\_in_r) = \frac{1}{1+e^{-z\_in_r}}$.

2. Backpropagation
   a. Each output neuron $(Z_r, r = 1, 2, \dots, R)$ receives the target pattern corresponding to the learning input and computes the error $\delta_r = (k_r - \hat{z}_r) f'(z_{in_r})$. The weights w_{hr} and bias w_{0r} are then updated using the learning rate α: $\Delta w_{hr} = \alpha \delta_r y_h$ dan $\Delta w_{0r} = \alpha \delta_r$. The δ_r is propagated backward to the previous layer.
   b. Each hidden neuron $(Y_h, h = 1, 2, \dots, H)$ computes the sum of delta inputs from the upper layer: $\delta_{in_h} = \sum_{r=1}^{R} \delta_r w_{hr}$. To obtain the error information, this value is multiplied by the derivative of the activation function: $\delta_h = (\delta_{in_h}) f'(y_{in_h})$.
   c. The weights v_{ih} and bias v_{0h} are updated using $\Delta v_{ih} = \alpha \delta_h x_i$ dan $\Delta v_{0h} = \alpha \delta_h$.

3. Weight and bias update
   a. Each output neuron $(Z_r, r = 1, 2, , R)$ updates its weights and biases: $w_{hr}(\text{baru}) = w_{hr}(\text{lama}) + \Delta w_{hr}$.
   b. The weights and biases of each hidden neuron $(Y_h = 1, 2, , H)$ are updated: $v_{ih}(\text{baru}) = v_{ih}(\text{lama}) + \Delta v_{ih}$.
   c. The stopping condition is checked. The learning process can be terminated if the error $|k_r - z_r| \leq$ *threshold*). In the *neuralnet() package,* the stopping condition is met when the threshold is *reached threshold ≤ threshold.*

The relationship between the output (Z_t) and inputs $(Z_{t-1}, Z_{t-2}, , Z_{t-I})$ is represented by Equation 21 (Zhang, 2003):

$$Z_t = f\left(w_0 + \Sigma_{h=1}^{H} w_h \, f\left(v_{0h} + \Sigma_{i=1}^{I} v_{ih} Z_{t-i}\right)\right) + \varepsilon_t \quad (21)$$

Hybrid SARIMA-FFNN

The Hybrid SARIMA-FFNN model is a combination of linear and nonlinear models, designed to improve prediction accuracy. The working mechanism of the Hybrid SARIMA-FFNN model involves using the errors (nonlinear components) from the SARIMA model as input data, which the FFNN then processes to address nonlinear patterns. The output of the FFNN (nonlinear component) is subsequently

added to the SARIMA model output (linear component). This modeling approach is represented by Equation 22 (Zhang, 2003).

$$Z_t = Z_t^{(L)} + Z_t^{(NL)} + \varepsilon_t. \quad (22)$$

Selection of the Optimal Method

The optimal method was determined based on the calculation of Root Mean Square Error (RMSE) and Mean Absolute Percentage Error (MAPE) on the testing data predictions. The dataset was divided into 72 points for training and 12 points for testing to preserve the full annual cycle, ensuring that seasonal patterns in SST are captured while allowing reliable evaluation of predictive performance. The best-performing model is the one with the lowest RMSE value. The formulas for calculating RMSE and MAPE on the testing data are as follows (Chicco et al., 2021):

$$\mathrm{RMSE}_{test} = \sqrt{\frac{\sum_{t=n_{train}+1}^{n_{test}} \left(\hat{Z}_t - Z_t\right)^2}{n_{test} - n_{train}}} \quad (22)$$

$$\mathrm{MAPE}_{test} = \frac{1}{n_{test}-n_{train}} \sum_{t=n_{train}+1}^{n_{test}} \left|\frac{Z_t - \hat{Z}_t}{Z_t}\right| \times 100\%. \quad (23)$$

The evaluation of MAPE values can be classified based on the accuracy level of the predictions (Puteri, 2023). Table 2 presents the classification of the MAPE evaluation.

Table 2. Classification of MAPE values (Puteri, 2023).

MAPE Value	Prediction Accuracy Classification
< 10%	Very high
10 – 20%	High
20 - 50%	Moderate
> 50%	Poor

Results and Discussion

Data Cleaning

Based on the data collected across all locations, there were ten missing data points, with two occurring at the beginning of the dataset and eight occurring between two valid observations. One possible cause of the missing data is atmospheric obstructions, such as thick clouds, which prevent the satellite sensors from accurately measuring SST, resulting in data that are either unrecorded or deemed not to meet NASA's data quality standards. To ensure a complete dataset for modeling and avoid biases in the analysis, missing values were imputed using interpolation or extrapolation methods. The distribution of missing data and the results of data imputation are presented in Table 3.

Table 3. Distribution and imputation results of the data.

t	North	East	South	West
1	**26.516**	**26.832**	28.061	27.878
2	27.902	28.116	27.994	27.981
3	29.289	29.400	29.349	28.634
35	28.295	27.974	27.986	28.511
36	28.925	28.843	28.151	**26.931**
37	26.518	27.401	27.132	25.352
46	29.368	29.184	28.053	29.206
47	26.670	**28.439**	**28.072**	**28.712**
48	28.245	27.694	28.091	28.219
51	29.241	29.154	28.627	29.018
52	29.472	29.552	**29.007**	28.610
53	29.630	29.654	29.386	29.475
57	28.455	28.245	28.013	28.431
58	25.430	26.752	25.048	**28.148**
59	28.044	28.452	28.406	27.865
60	27.880	27.893	27.928	27.624
61	**27.862**	25.382	27.208	27.578
62	27.844	28.240	27.382	26.796
82	29.570	29.574	29.259	29.408
83	29.429	29.169	29.800	**29.269**
84	28.608	28.263	29.284	29.131

In Table 3, the bolded data represent the imputed values obtained through linear interpolation or extrapolation based on Equations 1 and 2. Once the missing data issue has been addressed, the dataset is ready for further analysis, including descriptive statistics, data exploration, and modeling using SARIMA, FFNN, and Hybrid SARIMA-FFNN.

Descriptive Statistics and Data Exploration

Table 4. Descriptive statistics.

Region	Min.	Max.	Mean	SD
North	25.061	30.355	28.517	1.239
East	24.956	30.241	28.448	1.237
South	24.942	30.200	28.438	1.231
West	24.941	30.231	28.469	1.180

Descriptive statistics were used to provide an overview of the characteristics of SST

data through the mean, minimum, maximum, and standard deviation values. Based on the results, it was observed that all values for each descriptive statistical measure across the regions were relatively similar. This indicates that the differences in SST among regions are not substantial. A complete descriptive statistical analysis for each location is presented in Table 4.

Based on Table 4, during the observation period on Enggano Island, the lowest recorded SST was in the western region at 24.941℃, while the highest SST was recorded in the northern region at 30.355℃. This indicates that SST on Enggano Island ranges from 24.941℃ to 30.355℃. Additionally, the average SST across all regions is approximately 28℃, with a standard deviation of 1℃. This suggests that the spatial variability of SST across the island is relatively low, indicating that SST in each region remained relatively stable throughout the observation period. The pattern of SST changes in each region over the observation period is visualized in Figure 3.

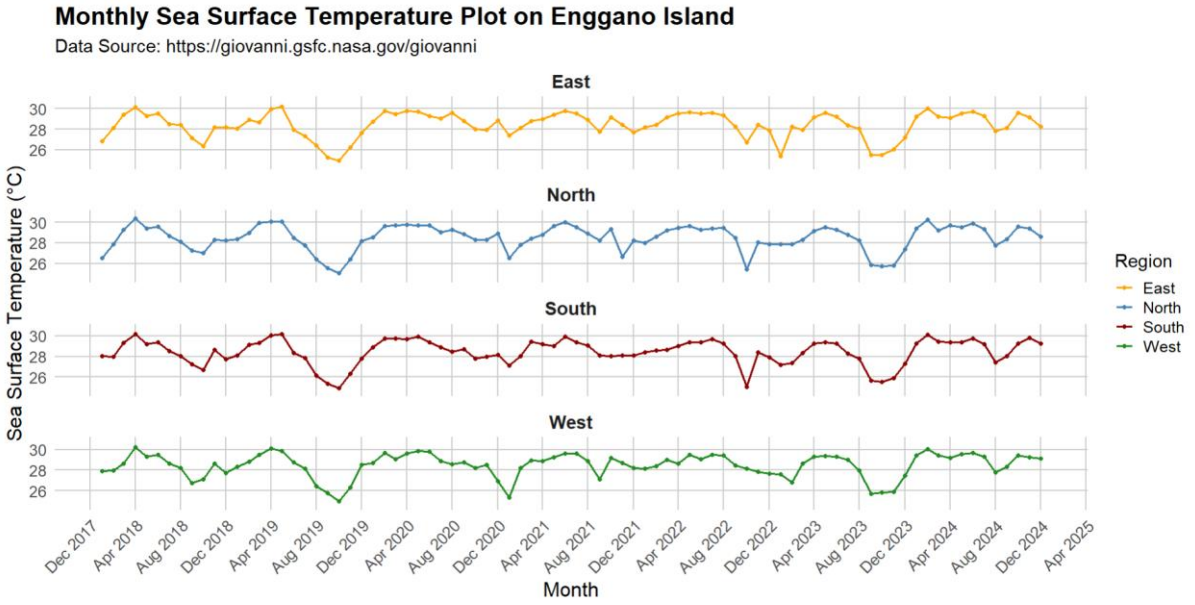

Figure 3. Plot of SST fluctuations on Enggano Island.

Based on Figure 3, it can be generally observed that SST across all regions of Enggano Island exhibits several periods of increase and decrease, with similar patterns of change. At a glance, recurring upward and downward fluctuations appear within certain time intervals. For instance, at the end of each year, SST in each region tends to show a noticeable decline. This provides an initial indication of the presence of seasonal patterns in SST across the regions of Enggano Island.

The seasonal pattern suggested by Figure 3 remains subjective, as it is based solely on visual observation. Therefore, seasonal pattern testing was conducted using spectral regression to identify the presence and strength of seasonal components statistically.

Seasonal Pattern Testing

For each region, testing was conducted under two data partitioning scenarios. First, assuming the presence of an annual seasonality, the data were divided into 72 training points and 12 testing points to preserve the full seasonal cycle. Second, to explore potential short-term seasonal patterns, such as quarterly or semiannual, a partitioning of 78 training points and 6 testing points was used. This partitioning aims to disrupt the annual cycle, allowing the identification of shorter seasonal

patterns, such as 3- or 6-month cycles. For example, Figure 4 presents a visualized periodogram plot for one of the regions. For other cases, periodogram plots can be visualized in the same manner.

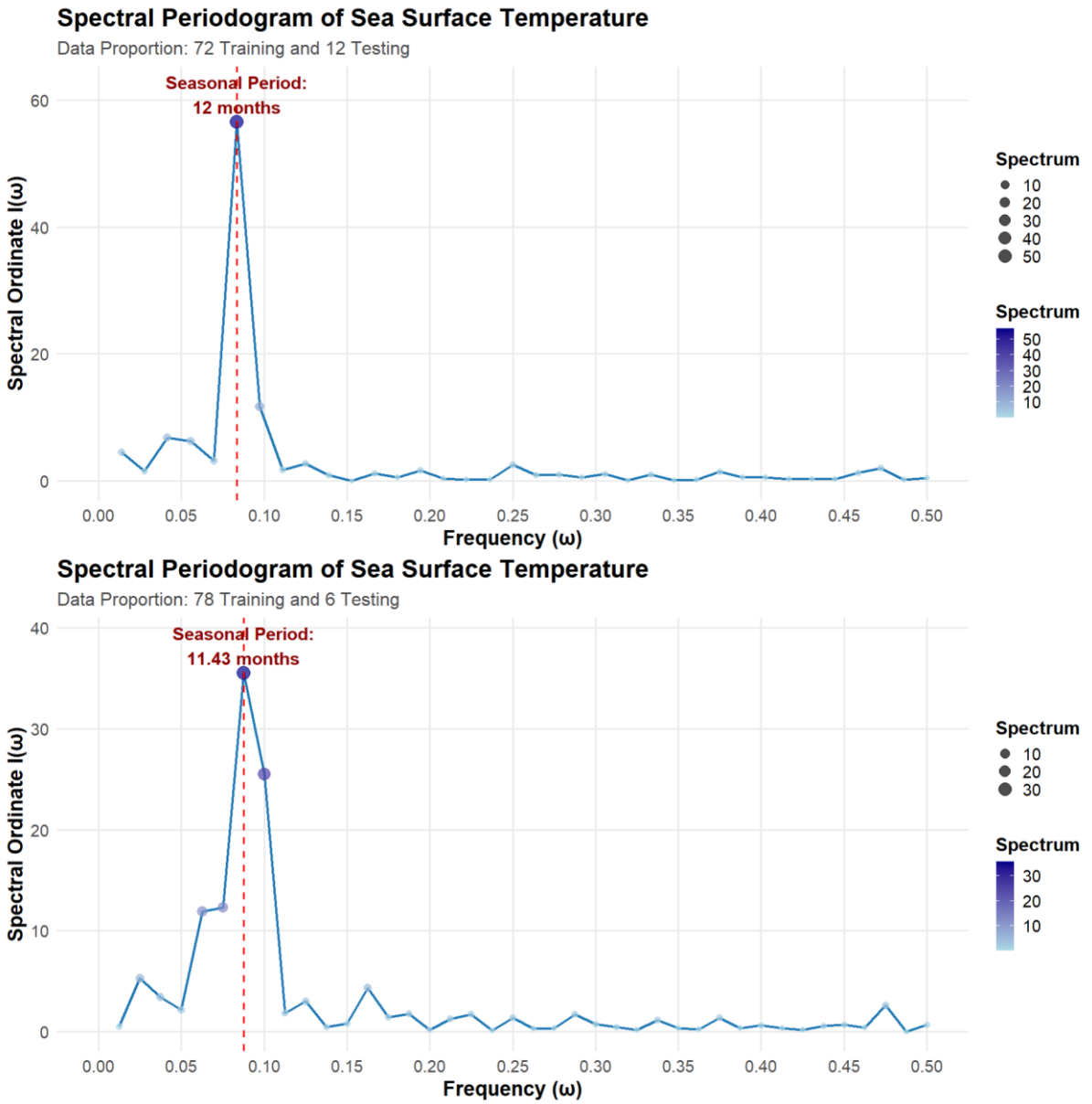

Figure 4. Periodogram plot of the Northern Region.

Table 5. Results of the seasonal component test.

Region	Period	$I(\omega_6)$	T	$g_{0.05}$
North	12	56.515	0.493	0.175
South	12	59.758	0.534	0.175
West	12	46.775	0.450	0.175
East	12	53.333	0.459	0.175

Based on the comparative test results of the two scenarios, it was observed that the training–testing data proportion of 72:12 consistently yielded higher ordinate values compared to the 78:6 proportion across all regions. For instance, as illustrated in Figure 4, the peak ordinate value obtained from the 72:12 proportion in the northern region was greater than that derived from the 78:6 proportion. This outcome suggests that employing a training period with an annual time interval is more effective in capturing the seasonal cycle, thereby facilitating a clearer identification of recurring patterns. Consequently, the seasonal

component identified under the 72:12 proportion was subjected to further analysis through spectral regression in order to statistically validate the existence, strength, and periodicity of the seasonal signal. The outcomes of this validation, including the statistical significance of the seasonal component, are summarized in Table 5. These findings provide a robust quantitative basis for characterizing the temporal structure of sea surface temperature variability around Enggano Island.

Based on Table 5, it can be observed that all regions have values $T > g_{0.05}$. This indicates that sea surface temperature across all regions of Enggano Island exhibits a annual seasonal pattern. Therefore, the sea surface temperature can be effectively modeled using the SARIMA approach.

Data Stationarity

Data stationarity is a prerequisite for SARIMA modeling and is tested through two assessments: stationarity with respect to variance and mean. The following presents the results of the stationarity check for variance.

Table 6. λ values in each region.

Trans.	λ			
	North	East	South	West
0	1.9999	1.9999	1.9999	1.9999
1	1.9999	1.9999	1.9999	1.9999
2	1.9999	1.9999	1.9999	1.9999
3	1.9999	1.9999	1.9999	1.9999
4	1.8404	1.7067	1.4163	1.5670
5	0.5321	1.2952	0.9086	0.8647
6	1.8766	1.0278	1.0518	1.0994

Based on the estimated λ parameters presented in Table 6, it can be observed that each region initially has a λ value of 1.9999. This indicates that the data are not yet variance-stationary. Therefore, a Box-Cox transformation in the form of $\frac{Z_t^{1.9999}-1}{1.9999}$ was applied. After applying the transformation up to three times, the λ value remained constant, suggesting that the Box-Cox transformation did not produce a significant change.

Considering that repeated transformations did not yield meaningful improvement and could potentially alter the data structure, increase model complexity, and complicate direct interpretation, the data were assumed to be variance-stationary, and subsequent analyses were conducted using the original data without Box-Cox transformation. This constitutes a limitation of the study.

Next, mean stationarity was assessed. The initial identification was conducted using ACF and PACF plots, which showed spikes in autocorrelation at certain lag multiples across all regions, indicating the presence of significant seasonal patterns. This aligns with the previous spectral regression analysis, which confirmed the existence of annual seasonal components. This pattern strongly suggests that the data do not satisfy the mean stationarity assumption, due to recurring seasonal fluctuations each year. Therefore, SST data in each region were addressed through seasonal differencing with a lag of 12. For example, Figure 5 presents the ACF and PACF plots of one region before and after the differencing process.

Based on Figure 5, it can be observed that after applying seasonal differencing, the previously dominant seasonal pattern appears weakened. This indicates that seasonal differencing successfully stabilized the seasonal mean. As a next step, the seasonally differenced data were tested for mean stationarity using the Augmented Dickey-Fuller (ADF) test. The results of the ADF test are presented in Table 7.

Table 7. Results of the ADF test.

Region	τ	$DF_{(0.05)}$	$P_{value}(\tau)$
North	-3.237	-1.95	0.002
East	-3.081	-1.95	0.003
South	-3.114	-1.95	0.003
West	-3.605	-1.95	0.001

Based on the results presented in Table 7, all regions have values $\tau < DF_{(0.05)}$ or

$P_{value}(\tau) < \alpha$. This indicates that the sea surface temperature data on Enggano Island satisfy the mean stationarity assumption. Once the stationarity test is confirmed, the analysis can proceed to SARIMA modeling.

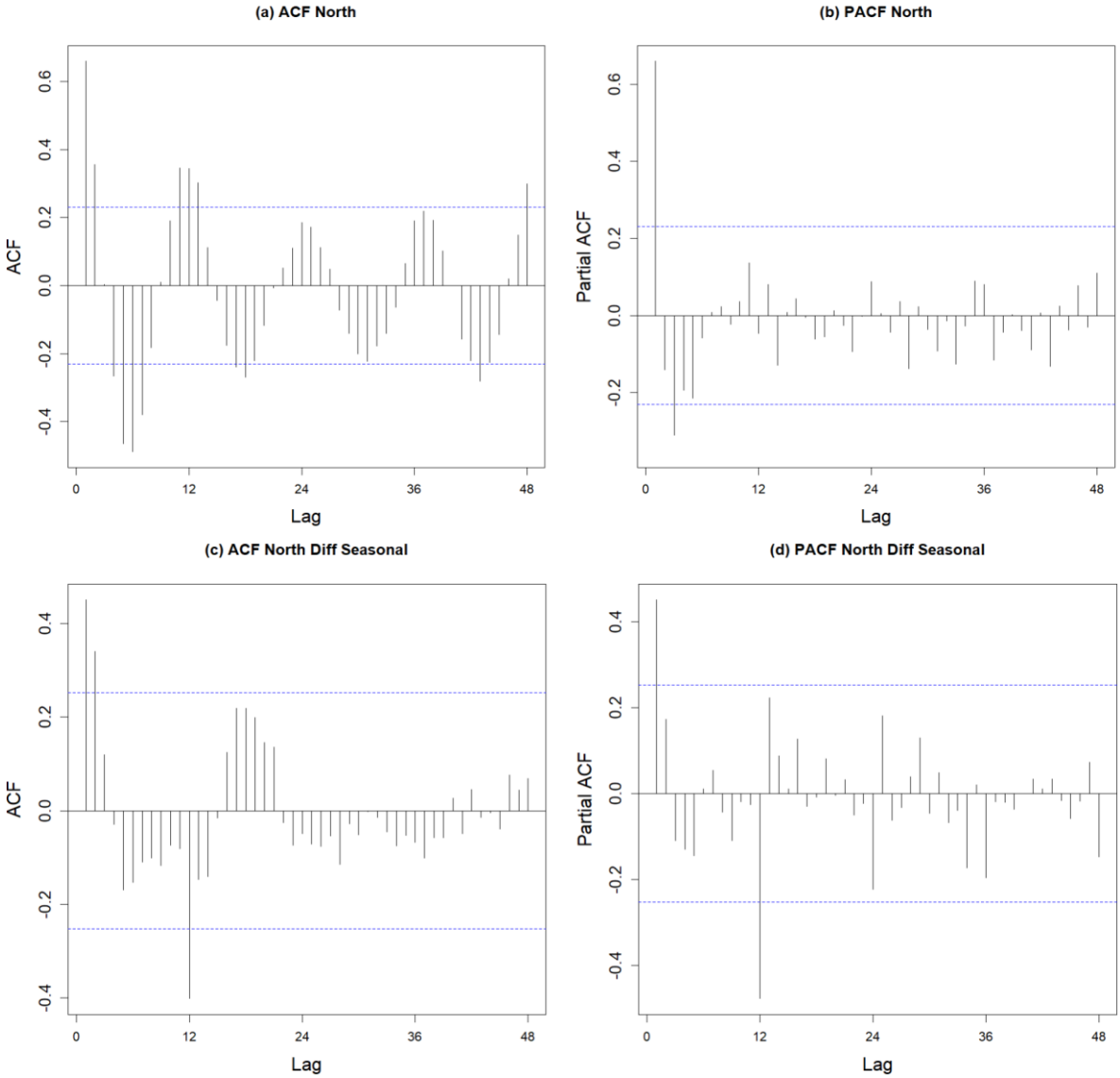

Figure 5. ACF and PACF plots of the Northern Region.

SARIMA Modeling

Table 8. Best SARIMA models.

Reg.	Model	Parameters	Estimates	Diagnostic Models					
				Ljung Box			KS		
				Q	$\chi^2_{\alpha;l}$	P_{value} (Q)	D_{KS}	$D_{\alpha;n}$	P_{value} (D_{KS})
North	SARIMA $(1,0,0)(0,1,1)^{12}$	AR(1) SMA(1)	0.547 -1	0.308	3.841	0.579	0.144	0.172	0.090
East	SARIMA $(1,0,0)(0,1,1)^{12}$	AR(1) SMA(1)	0.628 -1	0.012	3.841	0.912	0.144	0.172	0.091
South	SARIMA $(1,0,0)(0,1,1)^{12}$	AR(1) SMA(1)	0.587 -1	0.002	3.841	0.967	0.138	0.172	0.115
West	SARIMA $(1,0,0)(0,1,0)^{12}$	AR(1)	0.579	0.843	3.841	0.359	0.099	0.172	0.451

SARIMA modeling was conducted through a series of steps, including model identification using ACF and PACF plots, parameter estimation, parameter significance testing, model diagnostics, and selection of the best model. These steps produced the best SARIMA model for each region, as presented in Table 8, which lists the optimal model parameters alongside the results of diagnostic tests verifying model assumptions, such as residual autocorrelation and normality.

Based on Table 8, it can be seen that the best model for each region satisfies the model diagnostic assumptions, specifically regarding residual autocorrelation and normality. This is indicated by $P_{values}(Q \text{ and } D_{KS})$ greater than the chosen significance level (α). The fulfillment of these diagnostics suggests that the model adequately captures the underlying structure of the data, the residuals behave like white noise, and the parameter estimates are reliable for forecasting purposes.

The mathematical equations of the obtained models are as follows:

North

$$\hat{Z}_t = Z_{t-12} + 0.5472\, Z_{t-1} - 0.5472\, Z_{t-13} + e_t + e_{t-12}.$$

East

$$\hat{Z}_t = Z_{t-12} + 0.628 Z_{t-1} - 0.628 Z_{t-13} + e_{t-12} + e_t.$$

South

$$\hat{Z}_t = Z_{t-12} + 0.571 Z_{t-1} - 0.571 Z_{t-13} + e_{t-12} + e_t.$$

West

$$\hat{Z}_t = Z_{t-12} + 0.5792\, Z_{t-1} - 0.5792\, Z_{t-13} + e_t.$$

As an example, the following provides an interpretation of the SARIMA model for the western region of Enggano Island. Interpretations for other regions can be conducted in a similar manner.

The current sea surface temperature (SST) in the western region of Enggano Island is influenced by the SST of the previous month (lag 1), the SST of one year earlier (lag 12), and the SST of thirteen months earlier (lag 13).

1. An increase of 1℃ in the SST of the previous month (Z_{t-1}) increases the current SST by 0.5792℃, assuming other factors remain constant.
2. Conversely, an increase of 1℃ in the SST of thirteen months earlier (Z_{t-13}) decreases the current SST by 0.5792℃.
3. The SST of twelve months earlier (Z_{t-12}) directly contributes to the current SST with a coefficient of 1. This indicates that the SST of the same month in the previous year serves as the main baseline determining the current SST. In other words, the annual SST cycle in the western region is very strong and reflects a carry-over effect from the previous year.
4. In addition to these lagged effects, the current SST is also influenced by the error component (e_t), which represents random factors or external disturbances not captured by the model structure. This component reflects the inherent variability of SST that is unpredictable, such as short-term climatic events or weather anomalies.

Feed Forward Neural Network

Several steps were followed to model sea surface temperature using FFNN. The first step involved constructing the input data and normalizing it using min-max scaling. This study utilized monthly sea surface temperature data, resulting in 12 input neurons ($X_1, X_2, \ldots, X_{12}$) to fully represent the annual sequence of the time series, with each neuron reflecting the value from the preceding period.

Next, the FFNN architecture was designed, including the determination of the number of

neurons in the hidden layer, threshold values, and learning rate. In this study, the threshold was set at 0.1 to ensure that the training process would stop when the maximum weight gradient change was below 0.1. The learning rate was varied between 0.01 and 0.1, with increments of 0.01. The number of hidden neurons was then determined based on the configuration that produced the best evaluation metrics at the optimal learning rate. The resulting network architecture is presented in Table 9.

After obtaining the best network architecture for each region, the next step involved network training. This process included initializing weights and biases, followed by training using the backpropagation algorithm to obtain the optimal weights and biases. For illustration, Figure 6 presents one example of the resulting network architecture.

Table 9. Network architecture design.

Reg.	LR	Hidden Neurons	Network Architecture
North	0.01	2	FFNN (12-2-1)
East	0.07	9	FFNN (12-9-1)
South	0.01	2	FFNN (12-2-1)
West	0.03	2	FFNN (12-2-1)

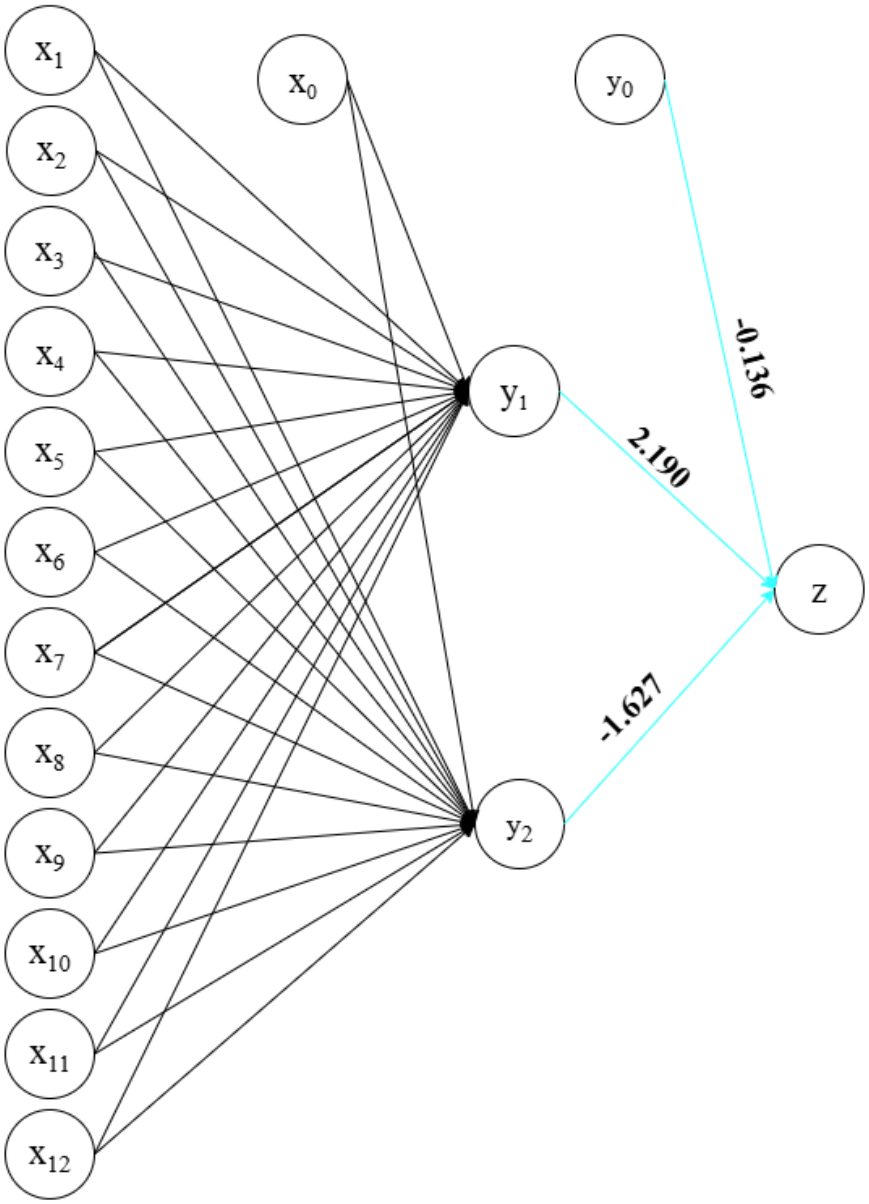

Figure 6. FFNN (12-2-1) Network architecture for the Northern Region of Enggano Island.

Based on Figure 6, the architecture of the FFNN network follows a (12-2-1) structure, consisting of 12 input neurons ($X_1, \dots, X_{12}$), 2 hidden neurons (y_1, y_2), and 1 output neuron (z_1). Each input neuron and bias is fully connected to all hidden neurons. The relationship between the input layer and the hidden layer is represented by the weights v_{ih}. Subsequently, each hidden neuron transmits its nonlinear activation to the output neuron through the weights w_{hr}.

The training results of the network for all regions can be expressed mathematically as follows:

North

$$\hat{Z}_t = f\Big((-0.136) + \big((y_1)(2.190)\big) + \big((y_2)(-1.627)\big)\Big).$$

East

$$\hat{Z}_t = f((-0.443) + \big((y_1)(0.209)\big) + \big((y_2)(-1.074)\big) + \big((y_3)(0.094)\big) + \big((y_4)(-1.157)\big) + \big((y_5)(-1.115)\big) + \big((y_6)(0.690)\big) + \big((y_7)(2.352)\big) + \big((y_8)(-0.364)\big) + \big((y_9)(0.274)\big).$$

South

$$\hat{Z}_t = f((0.007) + \big((y_1)(2.162)\big) + \big((y_2)(-1.774)\big)$$

West

$$\hat{Z}_t = f((0.609) + \big((y_1)(0.074)\big) + \big((y_2)(-1.147)\big).$$

As an example, the following provides an interpretation of the FFNN model for the northern region of Enggano Island. Interpretations for other regions can be conducted in a similar manner.

1. The current SST in the western region of Enggano Island is influenced by a nonlinear combination of two hidden neurons (y_1 and y_2) that are derived from transformations of the input variables (lagged SST values). The contribution of each hidden neuron to the current SST is represented by the output layer weights, with a value of 2.190 for neuron y_1 and –1.627 for neuron y_2. This indicates that the activation of neuron y_1 positively amplifies the current SST, while the activation of neuron y_2 contributes negatively, thereby reducing the current SST.
2. In addition, there is a bias of –0.136, which functions as a constant in the model to adjust the predictions and better align them with the observed data patterns.

Thus, the FFNN model captures more complex and nonlinear relationships among the lagged SST values compared to a linear model such as SARIMA. The hidden neurons y_1 and 2 serve as transformation functions that filter patterns from historical data, which are then combined in the output layer to predict the current SST.

Hybrid SARIMA-FFNN

Table 10. Network architecture design.

Reg.	LR	Network Architecture
North	0.1	*Hybrid* (SARIMA(1,0,0)(0,1,1)^{12}-FFNN (12-10-1))
East	0.01	*Hybrid* (SARIMA(1,0,0)(0,1,1)^{12}-FFNN (12-5-1))
South	0.01	*Hybrid* (SARIMA(1,0,0)(0,1,1)^{12}-FFNN (12-5-1))
West	0.02	*Hybrid* (SARIMA(1,0,0)(0,1,0)^{12}-FFNN (12-5-1))

In the Hybrid SARIMA-FFNN modeling, the input data consist of the errors from the best SARIMA model in each region. These errors are modeled using the FFNN mechanism to capture and learn the nonlinear patterns within them. The predicted errors are then added to the predictions from the SARIMA model to obtain improved overall forecasts. The resulting network architecture design for each region is presented in Table 10.

The results of network training across all regions can be mathematically represented as follows:

$$\hat{Z}_t = \hat{Z}_t^{(L)} + \hat{Z}_t^{(NL)}.$$

North

$$\hat{Z}_t^{(L)} = Z_{t-12} + 0.5472\, Z_{t-1} - 0.5472\, Z_{t-13} + e_t + e_{t-12}.$$

$$\hat{Z}_t^{(NL)} = f((5.435) + ((y_1)(5.031)) + ((y_2)(2.008)) + ((y_3)(-3.221)) + ((y_4)(-4.899)) + ((y_5)(-4.995)) + ((y_6)(-2.076)) + ((y_7)(-2.308)) + ((y_8)(3.754)) + ((y_9)(-4.888)) + ((y_{10})(4.394)).$$

East

$$\hat{Z}_t^{(L)} = Z_{t-12} + 0.628Z_{t-1} - 0.628Z_{t-13} + e_{t-12} + e_t.$$

$$\hat{Z}_t^{(NL)} = f((-0.276) + ((y_1)(0.047)) + ((y_2)(0.019)) + ((y_3)(0.376)) + ((y_4)(1.861)) + ((y_5)(-0.748)).$$

South

$$\hat{Z}_t^{(L)} = Z_{t-12} + 0.571Z_{t-1} - 0.571Z_{t-13} + e_{t-12} + e_t.$$

$$\hat{Z}_t^{(NL)} = f((-0.224) + ((y_1)(0.065)) + ((y_2)(0.028)) + ((y_3)(0.422)) + ((y_4)(1.871)) + ((y_5)(-0.731)).$$

West

$$\hat{Z}_t^{(L)} = Z_{t-12} + 0.5792\, Z_{t-1} - 0.5792\, Z_{t-13} + e_t.$$

$$\hat{Z}_t^{(NL)} = f((-0.216) + ((y_1)(0.063)) + ((y_2)(0.027)) + ((y_3)(0.426)) + ((y_4)(1.888)) + ((y_5)(-0.747)).$$

As an example, the following provides an interpretation of the Hybrid SARIMA-FFNN model for the eastern region of Enggano Island.

1. Interpretations of each model component separately (SARIMA and FFNN) can be conducted as previously described.
2. In general, the Hybrid model predicts SST by combining linear predictions from SARIMA with nonlinear predictions from FFNN. In the FFNN stage, the model processes the residuals or errors from the SARIMA model, allowing the FFNN to capture nonlinear patterns not explained by SARIMA. The final SST prediction is obtained by summing the SARIMA forecast and the FFNN output, enabling the Hybrid model to account for both linear seasonal patterns and more complex nonlinear dynamics.
3. The FFNN consists of one hidden layer with five neurons $(y_1, y_2, y_3, y_4, y_5)$. The output weights of these neurons are 0.047, 0.019, 0.376, 1.861, and –0.748, with a bias of –0.276. Each neuron processes the SARIMA residuals to extract nonlinear patterns:
   a. Neurons with positive weights (y_1, y_2, y_3, y_4) amplify the SST prediction,
   b. Neurons with negative weights (y_5) reduce the SST prediction.

Thus, the FFNN acts as a transformation function that filters the SARIMA residuals to capture nonlinear interactions among lagged SST values, before combining them in the output layer to produce the final SST forecast.

Selection of the Best Method for Each Region

The best method was determined by comparing the predictive performance of the three methods in each observation region. The following presents a visualization of the comparison between predicted results and actual testing data for each region.

Figures 7 to 10 present comparative plots between the actual data and the prediction results of the testing dataset across all methods in each region. In these plots, the red line represents the actual data, while the blue line represents the predicted values. As

shown in Figure 7, the SARIMA model in the northern region of Enggano demonstrates a relatively better predictive performance in capturing the actual data patterns compared to the FFNN and Hybrid SARIMA-FFNN models. Conversely, as illustrated in Figures 8 to 10, the FFNN model appears to follow the actual data patterns more closely than SARIMA and Hybrid SARIMA-FFNN in the eastern, southern, and western regions.

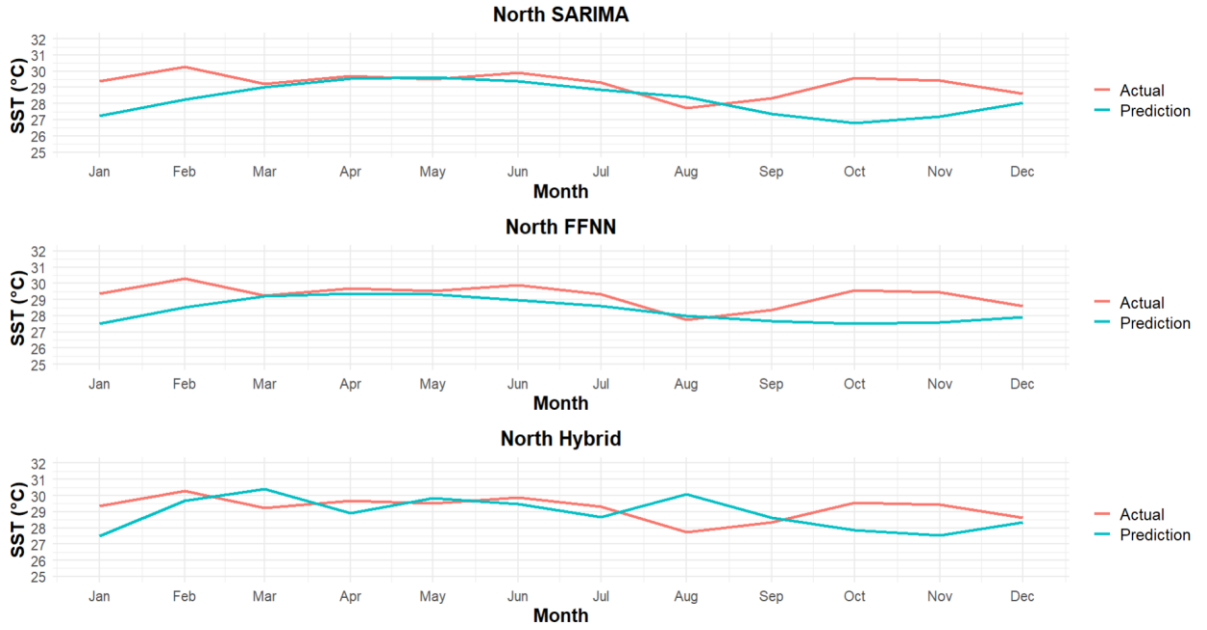

Figure 7. Plot of the model prediction results for Enggano's northern region.

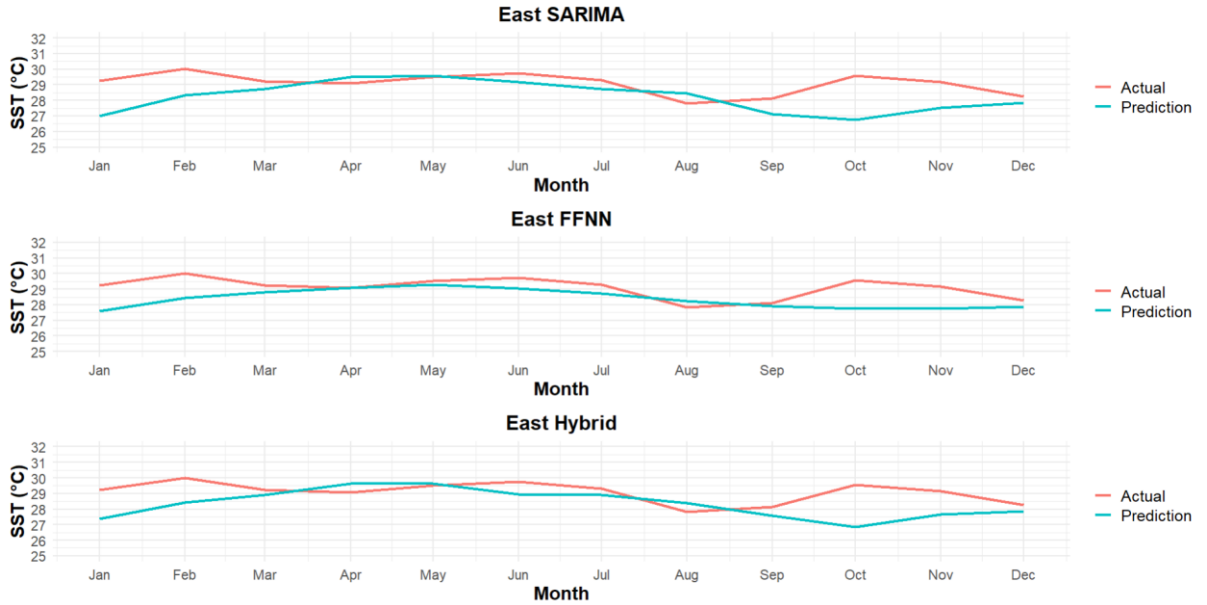

Figure 8. Plot of the model prediction results for Enggano's eastern region.

It should be noted that determining the best-performing method based solely on visual inspection of the comparative plots is inherently subjective and may not guarantee accuracy at each individual data point. Consequently, the selection of the optimal method in each region is more appropriately determined objectively using the lowest RMSE value derived from the prediction results on the testing dataset. The evaluation results are summarized in Table 11.

Table 11. Prediction evaluation results.

Model	North		East		South		West	
	RMSE	MAPE	RMSE	MAPE	RMSE	MAPE	RMSE	MAPE
SARIMA	1.409	3.652	1.330	3.597	1.404	3.778	2.040	5.270
FFNN	1.173	3.188	0.999	2.691	1.245	3.465	1.049	3.304
Hybrid SARIMA-FFNN	1.245	3.526	1.212	3.240	1.342	3.512	1.984	5.198

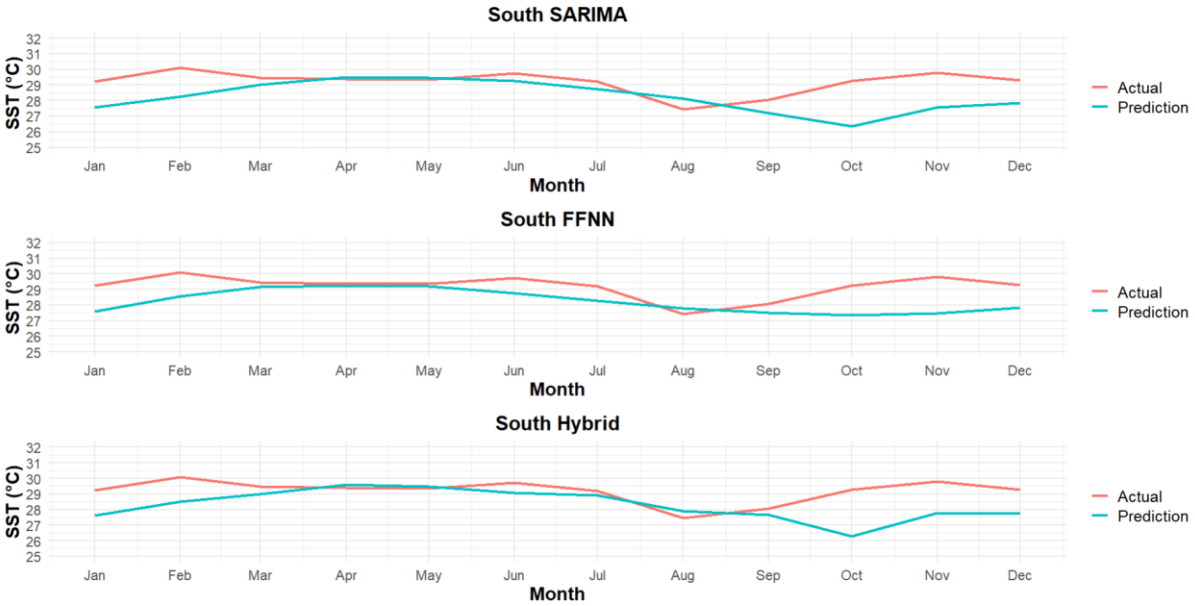

Figure 9. Plot of the model prediction results for Enggano's southern region.

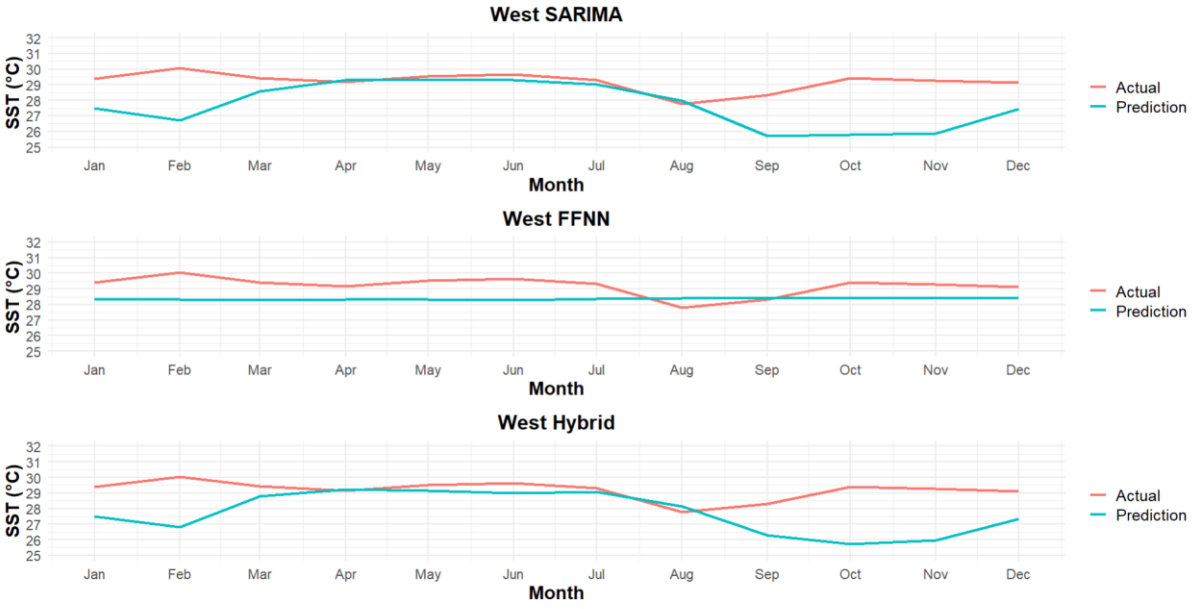

Figure 10. Plot of the model prediction results for Enggano's western region.

Based on Table 11, it can be seen that all models in the sea surface temperature modeling across Enggano Island demonstrate very high predictive performance. This is indicated by the MAPE values for each model in all regions being below 10%. Based on the RMSE values, it is evident that the Hybrid SARIMA-FFNN model consistently improves prediction accuracy compared to the standalone SARIMA model in all regions. However, the Hybrid SARIMA-FFNN model has not yet been able to surpass the performance of the FFNN model. This is reflected in the evaluation results, which show that FFNN is the best-performing model across all observation areas. This indicates that

the sea surface temperature data in Enggano Island is more suitably modeled using a nonlinear approach, specifically FFNN.

After it was determined that the FFNN model with each of its architectures is the best model across all regions, the model was then used to predict sea surface temperature. The prediction results are presented in Table 12.

Based on the prediction results presented in Table 12, it can be observed that the predicted values across the four regions for each month exhibit only minor differences. The predicted SST values fall within the range of 27.340℃ to 29.628℃. This temperature range is within the optimal conditions preferred by pelagic fish, which are between 26℃ and 29℃ (Esra et al., 2023). Meanwhile, other fish species may require adjustments according to their respective temperature preferences. The relatively similar SST predictions across regions provide greater flexibility for fishermen to conduct fishing activities without being constrained by regional differences. Nevertheless, adjustments must still be made based on the temperature preferences of the targeted fish species, as well as considering other factors that influence fish distribution.

Table 12. Prediction results of SST.

Month	North	East	South	West
January	27.528	27.610	27.611	28.341
February	28.509	28.419	28.574	28.300
March	29.191	28.807	29.157	28.272
April	29.368	29.099	29.265	28.314
May	29.327	29.278	29.202	28.328
June	28.971	29.033	28.752	28.282
July	28.596	28.728	28.293	28.355
August	27.979	28.243	27.779	28.382
September	27.692	27.896	27.522	28.397
October	27.522	27.754	27.340	28.404
November	27.607	27.754	27.451	28.391
December	27.905	27.882	27.830	28.386

Conclusion

The sea surface temperature (SST) in Enggano Island exhibits a relatively low spatial variability across the region, indicating that SST in each area remained relatively stable throughout the observed period. The optimal model for predicting sea surface temperature across all regions of Enggano Island for 2018–2024 was the FFNN. The details of the best network architecture are as follows: in the northern region, FFNN(12-2-1); in the eastern region, FFNN(12-9-1); in the southern region, FFNN(12-2-1); and in the western region, FFNN(12-2-1).

Based on the evaluation of model predictive performance using RMSE and MAPE values, all models for SST prediction in Enggano Island demonstrated very high predictive accuracy across all regions. This is indicated by MAPE values below 10% for each model in all areas. The most effective approach for modeling SST was the FFNN, with the best-performing architectures as follows: in the northern region, FFNN(12-2-1) with an RMSE of 1.173; in the eastern region, FFNN(12-9-1) with an RMSE of 0.999; in the southern region, FFNN(12-2-1) with an RMSE of 1.245; and in the western region, FFNN(12-2-1) with an RMSE of 1.049.

Based on the prediction results, the relatively consistent SST enables fishermen to carry out fishing activities more flexibly, without the need to consider regional differences. However, fishing practices should be adjusted according to the preferred temperature ranges of the target fish species, and other factors that influence fish distribution should be taken into account.

A limitation of this study is the violation of the variance stationarity assumption. Theoretically, this may result in biased SARIMA parameter estimates and inaccurate inferences (Ryan et al., 2025). Nevertheless, the study's findings indicate that, despite this violation, the model's predictions for the testing data across all regions still exhibited very high performance. This suggests that, in certain contexts, violating the variance stationarity

assumption does not necessarily hinder a model's ability to generate effective predictions. However, further research is recommended using alternative models that can address this issue, in order to achieve improved results and enhance the reliability of SST information to support fishing activities on Enggano Island.

Acknowledgements

The authors would like to express their gratitude to the NASA Goddard Earth Sciences Data and Information Services Center (GES DISC) through the Giovanni platform for facilitating the provision of sea surface temperature data, which served as the basis for this study's analysis.

The authors also extend their sincere appreciation to the editor, reviewers, and proofreader for their valuable contributions and suggestions that helped improve this manuscript. Special thanks are conveyed to the research team at the Department of Statistics, Faculty of Mathematics and Natural Sciences, University of Bengkulu, for their support in preparing equipment, data collection, and analysis throughout this study.

Author Contribution

Raditya Janaloka Natisharevi: Conceptualization, Methodology, Data Curation, Formal Analysis, Software, Writing – Original Draft. Conducted the research, collected SST data, implemented SARIMA, FFNN, and Hybrid SARIMA-FFNN modeling in R, and drafted the manuscript.

Jose Rizal: Supervision, Conceptualization, Writing – Review and Editing. Provided guidance on research design, methodology, and data analysis.

Firdaus: Validation, Formal Analysis, Writing – Review and Editing. Assisted in data analysis and validation, providing academic insights.

Pepi Novianti: Provided input during the data cleaning process to ensure the integrity of the processed data. Offered new perspectives in data interpretation and ensured the accuracy of the analysis in accordance with the research objectives.

Wina Ayu Lestari: Writing – Review and Editing, Supervision. Evaluated research findings, advised on FFNN training, and recommended improvements to the analysis.

Conflict of Interest

All authors have reviewed and approved this manuscript. The authors affirm that this article is an original work, is not under consideration by any other journal, and that there are no conflicts of interest. All stages of the research, analysis, and manuscript preparation were conducted independently and objectively, without influence from any external party.

References

Alrowais, R., Alwushayh, B., Bashir, M. T., Nasef, B. M., Ghazy, A., & Elkamhawy, E. (2023). Modeling and Analysis of Cutoff Wall Performance Beneath Water Structures by Feed-Forward Neural Network (FFNN). *Water*, 15(21), 3870. https://doi.org/10.3390/w15213870

Aminy, L. N., & Walid, W. (2022). Perbandingan Model Feed Forward Neural Network dan Arima untuk Meramalkan Perkembangan Covid-19 di Indonesia. *MATHunesa Jurnal Ilmiah Matematika*, 12(1), 1–10. https://doi.org/10.26740/mathunesa.v12n1.p1-10

Azmi, B. N., Hermawan, A., & Avianto, D. (2023). Analisis Pengaruh Komposisi Data Training dan Data Testing pada Penggunaan PCA dan Algoritma Decision Tree untuk Klasifikasi Penderita Penyakit Liver. *JTIM : Jurnal Teknologi Informasi dan Multimedia*, 4(4), 281–290. https://doi.org/10.35746/jtim.v4i4.298

Baharudin, A., Tangke, U., & Titaheluw, S. S. (2022). Distribusi Parameter Oseanografi Dengan Hasil Tangkapan

Ikan Pelagis Kecil Untuk Pemetaan Distribusi Daerah Potensial Penangkapan Di Perairan Teluk Weda. *Jurnal Biosainstek*, 4(1), 32–41. https://jurnal.ummu.ac.id/index.php/biosaintek/article/view/719

Chicco, D., Warrens, M. J., & Jurman, G. (2021). The Coefficient of Determination R-squared is More Informative than SMAPE, MAE, MAPE, MSE and RMSE in Regression Analysis Evaluation. *PeerJ Computer Science*, 7, e623. https://doi.org/10.7717/peerj-cs.623

Crayer, J. D. & Chan, K.-S. (2008). *Time Series Analysis with Applications in R*. Springer Science+Business Media. 2 ed. New York. https://doi.org/10.1007/978-0-387-75959-3

Esra, G., Herliany, N. E., & Adriani, A. (2023). Analisis Spasial Dna Temporal Hasil Tangkapan Ikan Pelagis Dan Thermal Front pada Musim Peralihan di Kabupaten Toli-Toli Sulawesi Tengah. *Prosiding Seminar Nasional Hasil Penelitian Kelautan Dan Perikanan*, 1(1), 147–152. https://semnas.bpfp-unib.com/index.php/semnaskel/article/view/115

Fadhlia, S., Hendri, E. P., & Cahyaningtyas A, D. D. (2024). Model Peramalan Nilai Tukar Rupiah Terhadap Dollar Singapura Menggunakan Metode Hybrid ARIMA-ANN. *Jurnal Ilmiah Pendidikan Matematika, Matematika Dan Statistika*, 5(3), 1513–1523. https://doi.org/10.46306/lb.v5i3.720

Glorot, X., & Bengio, Y. (2010). Understanding the Difficulty of Training Deep Feedforward Neural Networks. *Journal of Machine Learning Research*, 9, 249–256. https://proceedings.mlr.press/v9/glorot10a.html

Hastuti, R. P. W., Widianingsih, W., & Nuraini, R. A. T. (2024). Kondisi Meteorologi Laut Terhadap Suhu Permukaan Laut Di Perairan Kota Surabaya Tahun 2019 – 2021. *Journal of Marine Research*, 13(4), 701–712. https://doi.org/10.14710/jmr.v13i4.43227

Hisyam, M., Sumardi, S. R., Kainama, T. L. J., & Haryati, K. (2025). Prediksi Suhu Permukaan Laut di Perairan Kota Jayapura Tahun 2021-2025 Menggunakan Model SARIMA. *ACROPORA: Jurnal Ilmu Kelautan Dan Perikanan Papua*, 8(1), 37–43. https://doi.org/10.31957/acr.v8i1.4605

Ichwan, M., & Alfarisyi, S. F. (2024). Pemodelan Ritme Kalori Terbakar Setiap Waktu Selama Bersepeda dengan Feedforward Neural Network. *ELKOMIKA: Jurnal Teknik Energi Elektrik, Teknik Telekomunikasi, & Teknik Elektronika*, 12(1), 13–22. https://doi.org/10.26760/elkomika.v12i1.13

Izonin, I., Tkachenko, R., Shakhovska, N., Ilchyshyn, B., & Singh, K. K. (2022). A Two-Step Data Normalization Approach for Improving Classification Accuracy in the Medical Diagnosis Domain. *Mathematics*, 10(11), 1942. https://doi.org/10.3390/math10111942

Kambey, E. M., Jasin, M. I., & Mamoto, J. D. (2023). Studi Hidro Oseanografi Di Pantai Ranowulu. *Tekno*, 21(83), 319–326. https://ejournal.unsrat.ac.id/v3/index.php/tekno/article/view/47332

Kurniasari, D., Mahyunis, R. V., Warsono, W., & Nuryaman, A. (2023). Implementation of Artificial Neural Network (ANN) Using Backpropagation Algorithm By Comparing Four Activation Functions in Predicting Gold Prices. *Kumpulan Jurnal Ilmu Komputer (KLIK)*, 10(1), 93–105. https://klik.ulm.ac.id/index.php/klik/article/view/587

Li, M. (2024). Comprehensive Review of

Backpropagation Neural Networks. *Academic Journal of Science and Technology*, 9(1), 150–154. https://doi.org/10.54097/51y16r47

NASA Goddard Earth Sciences Data and Information Services Center (GES DISC). (2024). Giovanni Interactive Visualization and Analysis. *NASA GES DISC*. https://giovanni.gsfc.nasa.gov/giovanni

Pangruruk, F. A., & Barus, S. P. (2022). Predicting the Number of People Exposed to Covid 19 with the Newton Gregory Maju Polynomial Interpolation Method. *Formosa Journal of Science and Technology*, 1(8), 1275–1290. https://doi.org/10.55927/fjst.v1i8.2185

Permana, I., & Salisah, F. N. (2022). The Effect of Data Normalization on the Performance of the Classification Results of the Backpropagation Algorithm Pengaruh Normalisasi Data Terhadap Performa Hasil Klasifikasi Algoritma Backpropagation. *Indonesian Journal of Informatic Research and Software Engineering*, 2(1), 67–72. https://doi.org/10.57152/ijirse.v2i1.311

Puteri, D. I. (2023). Implementasi Long Short Term Memory (LSTM) dan Bidirectional Long Short Term Memory (BiLSTM) Dalam Prediksi Harga Saham Syariah. *Euler : Jurnal Ilmiah Matematika, Sains Dan Teknologi*, 11(1), 35–43. https://doi.org/10.34312/euler.v11i1.19791

Rifai, S. N. (2023). Analisis Oseanografi Lautan Menggunakan Model Jaringan Syaraf Tiruan. *Prosiding Seminar Nasional Pemanfaatan Sains Dan Teknologi Informasi*, 1(1), 1–10. https://epublikasi.digitallinnovation.com/index.php/sempatin/article/view/35

Ryan, O., Haslbeck, J. M. B., & Waldorp, L. J. (2025). Non-Stationarity in Time-Series Analysis : Modeling Stochastic and Deterministic Trends. *Multivariate Behavioral Research*, 60(3), 556–588. https://doi.org/10.1080/00273171.2024.2436413

Sari, I. P. (2020). Agama, Etnisitas dan Perdamaian di Pulau Enggano Provinsi Bengkulu. Hanifiya: Jurnal Studi Agama-Agama, 3(2), 77–86. https://doi.org/10.15575/hanifiya.v3i2.9987

Septiana, D., & Bangun, M. B. (2023). Perbandingan Antara Feed Forward Neural Network (FFNN) Dan Seasonal Autoregressive Integrated Moving Average (Sarima) Untuk Peramalan Data Runtun Waktu Terapan. *Jurnal Deli Sains Informatika*, 2(2). https://jurnal.unds.ac.id/index.php/dsi/article/view/218

Shabrina, N. N., Sunarto, S., & Hamdani, H. (2017). Penentuan Daerah Penangkapan Ikan Tongkol Berdasarkan Pendekatan Distribusi Suhu Permukaan Laut dan Hasil Tangkapan Ikan di Perairan Utara Indramayu Jawa Barat. *Jurnal Perikanan Dan Kelautan*, 8(1), 139–145. https://jurnal.unpad.ac.id/jpk/article/view/13901

Silsia, D., Yahya, R., & Lumbanbatu, U. M. (2019). Rendemen dan Karakteristik Minyak Bintangur dari Pulau Enggano Sebagai Bahan Baku Pembuatan Biodiesel. *Jurnal Agroindustri*, 9(1), 1–7. https://doi.org/10.25077/greentech.v1i1.10

Susila, M. R., Jamil, M., & Santoso, B. H. (2023). Akurasi Model Hybrid ARIMA-Artificial Neural Network dengan Model Non Hybrid pada Peramalan Peredaran Uang Elektronik di Indonesia. *Jambura Journal of Mathematics*, 5(1), 46–58. https://doi.org/10.34312/jjom.v5i1.14889

Syahrin, K. A., Disera, T. E., Youwea, A.

S. G. N., Merdeka, J., Saputra, A. H., Norman, Y., & Nugraheni, I. R. (2024). Prakiraan Perubahan Suhu Permukaan Laut dengan Neuralprophet di Taman Laut Bunaken. *Jurnal Laut Pulau*, 3(2), 42–50. https://doi.org/10.30598/jlpvol3iss2pp42-50

Wei, W. W. S. (2006). *Time Series Analysis Univariate and Multivariate Methods* (2nd ed.), Pearson. https://civil.colorado.edu/~balajir/CVEN6833/lectures/wwts-book.pdf

Wulandari, S., & Novita, D. (2024). Implementasi Feed Forward Neural Network (FFNN) dalam Memprediksi Penyakit Diabetes. *Jurnal MIPA Sains Terapan*, 3(1), 1–11. https://journal.unindra.ac.id/index.php/sainsmath/article/view/3048

Zhang, G. P. (2003). Time series forecasting using a hybrid ARIMA and neural network model. *Neurocomputing*, 50, 159–175. https://doi.org/10.1016/S0925-2312(01)00702-0

Zhang, Y., & Meng, G. (2023). Simulation of an Adaptive Model Based on AIC and BIC ARIMA Predictions. *Journal of Physics: Conference Series*, 2449(1), 012027. https://doi.org/10.1088/1742-6596/2449/1/012027

ISSN: 2579-5821 (Print)
ISSN: 2579-5546 (Online)
URL address: http://journal.unhas.ac.id/index.php/geocelebes
DOI: 10.70561/geocelebes.v9i2.47278

Jurnal Geocelebes Vol. 9 No. 2, October 2025, 213 – 225

Shear-Wave Velocity Structure in Southeast Asia from the 2025 Mw 8.8 Kamchatka Earthquake Using Hilbert–Huang Transform

Andri Kurniawan*, Ilham Dani, Sandri Erfani

Department of Geophysical Engineering, Universitas Lampung, Bandar Lampung 35145, Indonesia.

*Corresponding author. Email: andrikurniawan@eng.unila.ac.id

Manuscript received: 20 September 2025; Received in revised form: 6 October 2025; Accepted: 17 October 2025

Abstract

The 2025 Mw 8.8 Kamchatka earthquake generated long-period teleseismic surface waves recorded at stations in Australia (CTAO), Thailand (CHTO), and Indonesia (KAPI) at epicentral distances of ~6,400–8,200 km. These records provide a useful dataset to probe crust and upper-mantle structure across contrasting Southeast Asian tectonic domains. We apply the Hilbert–Huang Transform (HHT) to vertical seismograms to extract dispersion from non-stationary wave trains. Seismograms are decomposed by empirical mode decomposition, and dispersion ridges in the Hilbert spectrum are tracked to identify frequency-dependent group arrivals. Group-velocity curves are smoothed with a low-order polynomial, and dual-frequency anchors are used to enforce phase-velocity continuity. Group velocities increase from ~3.0 km/s at periods ≥150 s to ~5.5 km/s at 40–60 s, while phase velocities span 3.3–4.6 km/s. Phase-velocity curves initialized with CRUST1.0 are inverted for 1-D shear-wave velocity (Vs), indicating crustal thicknesses of ~30–40 km: thicker beneath CHTO, intermediate at CTAO, and thinner with a slower upper mantle beneath KAPI. These lithospheric variations are consistent with regional deformation inferred from GPS and InSAR. Overall, HHT yields stable dispersion measurements and reliable Vs models relative to global references, underscoring its utility in complex tectonic regions.

Keywords: crustal thickness; dispersion analysis; Hilbert–Huang Transform; Rayleigh waves; shear-wave velocity; Southeast Asia.

Citation: Kurniawan, A., Dani, I., & Erfani, S. (2025). Shear-Wave Velocity Structure in Southeast Asia from the 2025 Mw 8.8 Kamchatka Earthquake Using Hilbert–Huang Transform. *Jurnal Geocelebes*, 9(2): 213–225, doi: 10.70561/geocelebes.v9i2.47278

Introduction

The Magnitude Moment (Mw) 8.8 Kamchatka earthquake on 29 July 2025, a major tectonic event in the Pacific Ring of Fire, generated long-period teleseismic surface waves recorded at CTAO, CHTO, and KAPI (USGS, 2025; Patton, 2025). This event generated unique teleseismic surface waves that were detected at numerous seismic stations in Southeast Asia and Australia, such as CHTO (Thailand), KAPI (Indonesia), and CTAO (Australia) (Figure 1). Long-period surface waves predominantly characterized the recordings, with epicentral distances ranging from about 6,400 to 8,200 km. This information is particularly relevant for examining the structure of the crust and upper mantle via surface-wave dispersion analysis (Li et al., 2022; Giampiccolo et al., 2024).

Surface-wave dispersion analysis has historically served as a fundamental method in seismology for extracting shear-wave velocity (Vs) beneath the Earth's surface. Due to their dispersive characteristics, phase and group velocities vary with period, allowing for the investigation of different depth ranges by meticulous analysis of dispersion curves (Babikoff & Dalton, 2019; Magrini et al., 2023; Nishida et al., 2024; Moulik &

Ekström, 2025). Traditional methodologies, including Frequency–Time Analysis (FTAN) and Short-Time Fourier Transform (STFT), have been extensively utilized in global and regional tomography research (Yang et al., 2023; Dou et al., 2024).

However, intrinsic limits constrain Fourier-based methodologies. The Fourier transform presupposes linear and stationary signals, whereas teleseismic seismograms are non-stationary, exhibiting time-varying amplitudes and frequencies. Window-based techniques like STFT offer only a constant time-frequency resolution, which may obscure significant aspects of spectrum evolution (Eriksen & Rehman, 2023). These constraints frequently diminish the precision of group-velocity measurements at extended periods, which are essential for elucidating upper-mantle structures. Therefore, more flexible options are necessary.

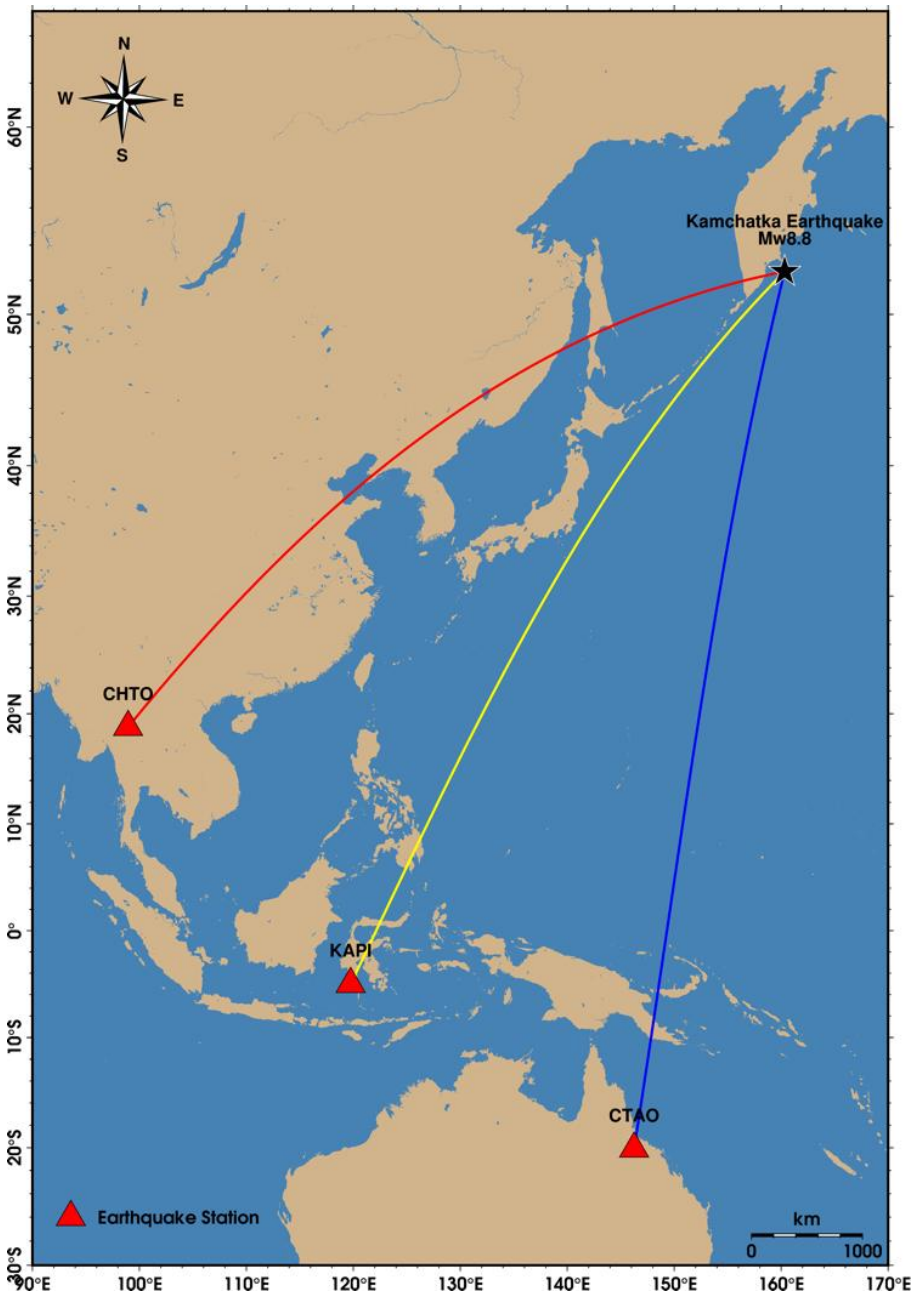

Figure 1. Map of the Mw 8.8 Kamchatka earthquake (29 July 2025) and the three GSN broadband stations analyzed: CTAO (Australia), CHTO (Thailand), and KAPI (Indonesia). Colored great-circle paths represent surface-wave propagation trajectories.

The HHT is an adaptive spectral technique that integrates Empirical Mode Decomposition (EMD) with Hilbert transform analysis to derive instantaneous frequency and amplitude from intrinsic signal components (Huang & Wu, 2008; de Souza et al., 2022; Eriksen & Rehman, 2023). Its primary advantage resides in its capacity to manage nonlinear and non-stationary data without dependence on predetermined basis functions (Harsuko et a., 2020). Chen et al. (2002) established that HHT is proficient at quantifying surface-wave group velocities and generating phase curves with considerable precision. Recent investigations, including Çakir & Kutlu (2023), emphasized that HHT can provide dependable dispersion curves even for intricate signals, hence serving as a complementing instrument to traditional FTAN-based methods.

Despite its potential, Southeast Asia still faces constraints in its implementation of HHT. Most research in Indonesia has focused on tomography utilizing ambient noise or global earthquake catalogs, whereas the systematic application of HHT to significant teleseismic events remains unaddressed. The CRUST1.0 global reference model (Laske et al., 2012) has traditionally functioned as a one-dimensional benchmark for crustal structure; yet regional evaluations and revisions of this model utilizing long-distance teleseismic data are limited in Indonesia. Due to the geological intricacies of the region, especially at the Indo-Australian and Eurasian plate boundary, discrepancies between CRUST1.0 and local conditions may be significant.

Fourier, or FTAN, methods are used in most studies of regional surface waves. These methods work best when the data is stationary, but they often have trouble with nonstationary teleseismic wave trains and single-event studies. Coverage in Southeast Asia is also spotty, and worldwide references like CRUST1.0 only give a rough idea of the structure.

We fill in these gaps by using the Hilbert–Huang Transform on vertical seismograms from the Mw 8.8 Kamchatka earthquake that happened on July 29, 2025, and was recorded at CTAO, CHTO, and KAPI. We use ridge tracking in the Hilbert spectrum to determine dispersion and the Chen et al. (2002) anchoring scheme to determine phase velocity, and we invert the curves for path-averaged 1-D Vs, starting with CRUST1.0 as a neutral global prior and using broad bounds and a stochastic global search to limit starting-model bias. We also include a simple FTAN baseline and compare it to global models. Our goal is to see if HHT gives us more steady dispersion and regionally accurate Vs than traditional Fourier-based methods.

Materials and Methods

Data

This investigation uses seismic recordings of the significant Kamchatka earthquake (Mw 8.8; July 29, 2025; 52.7°N, 160.2°E) from three broadband stations of the Global Seismographic Network (GSN): CTAO (Australia), CHTO (Thailand), and KAPI (Indonesia). The investigation centers on the vertical component (BHZ), given that fundamental-mode Rayleigh waves predominate in this channel, whereas horizontal channels are more significantly affected by Love waves and converted phases. Figure 1 illustrates the source location and ray paths, while Table 1 summarizes the station information. Waveforms and station metadata were retrieved from EarthScope Data Services (IRIS DMC) using Python (ObsPy) via FDSN web services (dataselect and station), using miniSEED and StationXML formats.

We selected CHTO, KAPI, and CTAO to sample three contrasting tectonic corridors while keeping comparable teleseismic distances and ensuring high-quality long-

period records. The criteria were clear fundamental-mode Rayleigh wave trains within the teleseismic window, adequate instrument and data quality, azimuthal diversity with respect to the source, and tectonic distinctiveness of the corridors (Büyük et al., 2020). For context, source-to-station azimuths are approximately 259° (CHTO), 225° (KAPI), and 194° (CTAO), and station elevations are ~420 m, ~300 m, and ~367 m, respectively. Paths and metadata are summarized in Figure 1 and Table 1.

Table 1. Seismic stations used in this study, including network codes, station names, geographic coordinates (°), and epicentral distances (km) from the 29 July 2025 Mw 8.8 Kamchatka earthquake.

Network Station	Latitude (°)	Longitude (°)	Epicentral Distance (km)
CTAO	-20.0883	146.255	8205
CHTO	18.8141	98.944	6430
KAPI	-5.0142	119.751	7456

Geology Regional

The seismic routes that were studied go via three different geodynamic domains: (i) the Southeast Asian margin (CHTO); (ii) the Sumatra–Sulawesi arc (KAPI), which is along the Indo-Australian subduction system; and (iii) the Australian continental margin (CTAO), which is a stable crustal lithosphere. This comparative evaluation of surface-wave velocities is made possible by the geological contrast, which emphasizes the heterogeneity of the crust and lithosphere along a transcontinental corridor. In this configuration, CHTO samples the Southeast Asian continental margin, KAPI traverses the Sunda arc and back-arc governed by Indo-Australian subduction, and CTAO lies on the stable Australian craton (Figure 1 and Table 1).

Regionally, the CHTO path crosses the Sunda land continental margin, a collage of continental blocks and volcanic arcs assembled since the Mesozoic; basin development and strike-slip belts reflect long-lived intraplate deformation within this continental core of SE Asia (Müller et al., 2019). In contrast, the KAPI path samples the Sunda arc/ back-arc, where the Indo-Australian plate subducts obliquely beneath the Sunda plate at ~50–80 mm/yr, and traverses the Sulawesi collage, where microcontinent collisions and back-arc extension produce highly heterogeneous crust and mantle structure (Hutchings & Mooney, 2021). The CTAO path lies on the Proterozoic basement of northeastern Australia (North Australian Craton) and represents stable cratonic lithosphere; regional reference models (AuSREM) indicate a comparatively smooth crust–upper-mantle structure typical of this margin.

Preprocessing

Waveforms were downloaded from the IRIS DMC at a sampling rate of 40 Hz and a recording length that exceeded 3 hours. Preprocessing procedures comprised the deconvolution of the instrument response, the removal of the mean and linear trend, and the application of a 1% taper to acquire ground displacement. To preserve Rayleigh energy from mid- to long-period, a band-pass filter was implemented at a frequency of 0.001–0.10 Hz. Subsequently, the data were downsampled to 2 Hz and trimmed to 6000 s around the primary surface-wave arrival using cascaded anti-alias filters (Figure 2). These choices preserve the target band 0.001–0.10 Hz while minimizing artifacts: detrend and demean remove offsets and drift, a 1% cosine taper reduces edge effects, and downsampling to 2 Hz after zero-phase anti-alias filtering keeps the 1 Hz Nyquist well above 0.10 Hz so no dispersion-band information is lost.

To improve data quality, short transients were removed using a median-absolute-deviation gate in the pre-event window, and we estimated signal-to-noise ratios from Hilbert amplitudes outside the Rayleigh window. Frequency choices preserve mid- to long-period Rayleigh energy while suppressing microseism and very-low-

frequency drift. Anti-alias filtering was applied before downsampling to 2 Hz.

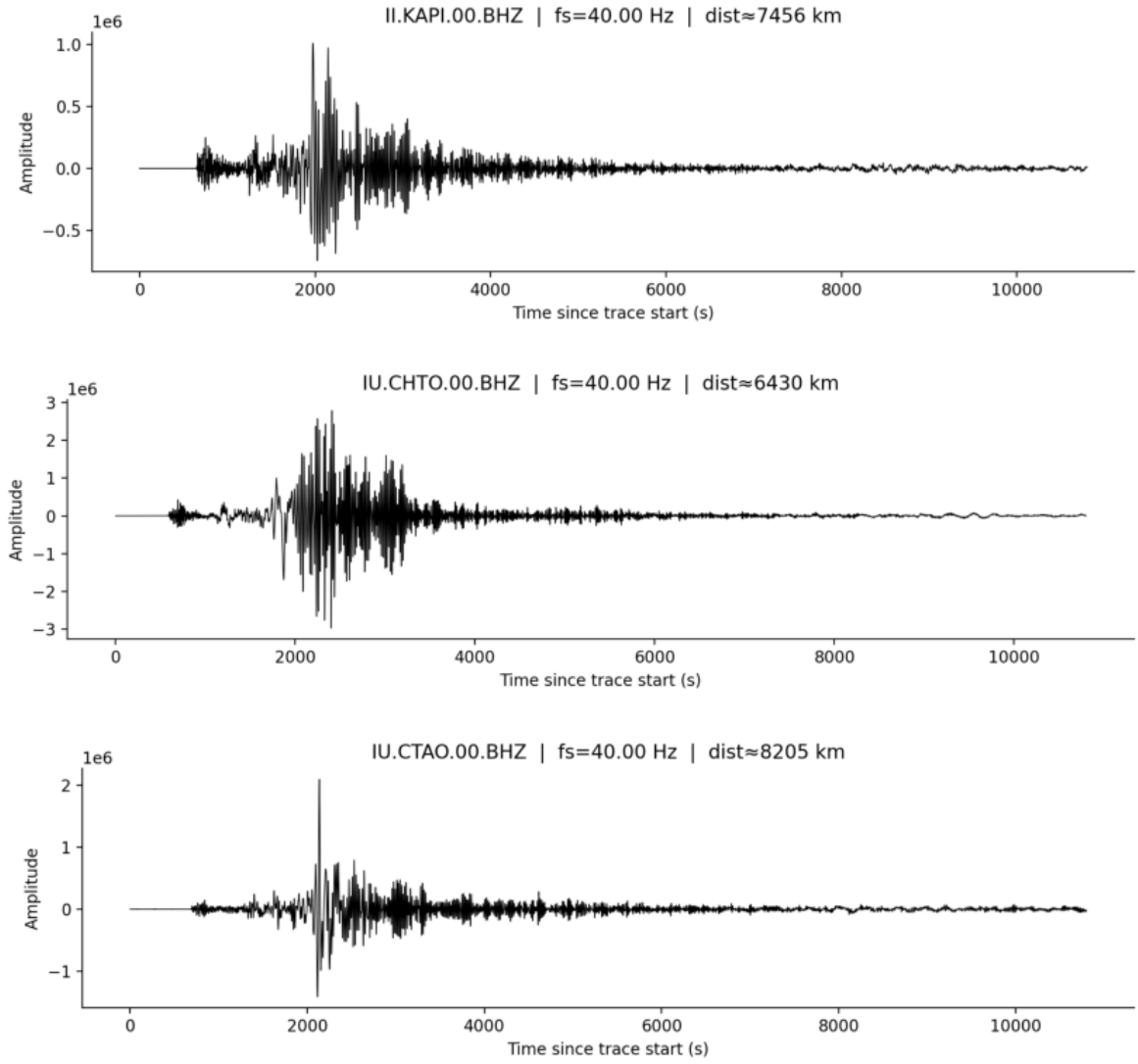

Figure 2. Vertical-component (BHZ) seismograms of the Mw 8.8 Kamchatka earthquake recorded at KAPI, CHTO, and CTAO stations after preprocessing. Distances from the epicenter range between 6,430 and 8,205 km.

Hilbert–Huang Transform

The HHT was used for adaptive spectral analysis (de Souza 2022; Eriksen & Rehman, 2023). Vertical seismograms were decomposed by EMD into intrinsic mode functions (IMFs). IMF4 typically captured sustained long-period oscillations (0.02–0.05 Hz) and was used for dispersion (Figures 3–4). We also tested adjacent modes (IMF3 and IMF5). In the 0.02–0.05 Hz band, their dispersion picks agree with IMF4 within the frequency-dependent picking uncertainty; IMF4 provides the highest SNR and the most continuous ridge, so we use it as the primary mode. Outside this band, IMF3 shows very-long-period drift and IMF5 exhibits higher-mode leakage, hence they are not used. The sifting stopped at a standard-deviation threshold of 0.2 or at ten sifts, and end effects were reduced by symmetric mirroring and spline envelopes. The analytic signal is (Huang & Wu, 2008):

$$z(t) = x(t) + i\,\hat{x}(t) \qquad (1)$$

where x(t) is the original signal and ẋ(t) is its Hilbert transform. The instantaneous frequency is (Huang & Wu, 2008):

$$f(t) = \frac{1}{2\pi}\frac{d\phi}{dt} \qquad (2)$$

The Hilbert spectrum was computed on overlapping windows to stabilize ridge continuity; windows that failed continuity or had Signal-to-Noise Ratio (SNR) > 3 were rejected. Let A(*t*,*f*) be the Hilbert amplitude. We restrict the search to a Rayleigh-wave window defined by the epicentral distance and a 2–5.5 km/s group-velocity bracket. For each frequency f, the group arrival time is (Chen et al., 2002),

$$t_{\text{peak}}(f) = \arg\max_{t \in W_R} A\,(t, f) \qquad (3)$$

The picked track is median-filtered (three bins) and spline-smoothed; samples that break window-to-window continuity or fail SNR > 3 are discarded. Choosing the amplitude maximum follows the modal ridge where Rayleigh energy concentrates and approximates the stationary-phase group delay, making it less sensitive than centroids to leakage, side lobes, or mode interference. The variance across overlapping windows is carried forward as frequency-dependent measurement weights for the inversion.

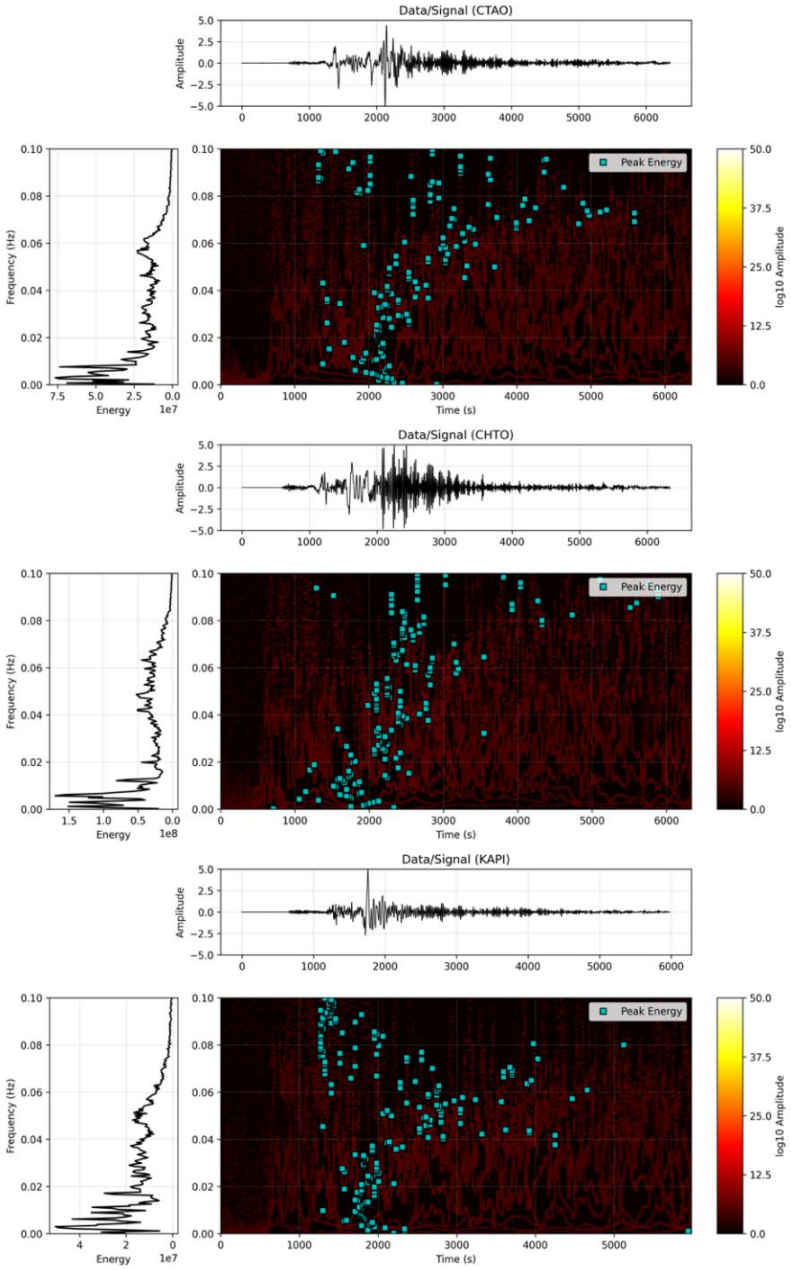

Figure 3. Hilbert spectra of vertical seismograms at CTAO, CHTO, and KAPI stations. Blue markers indicate ridge picks corresponding to the arrival of fundamental-mode Rayleigh energy.

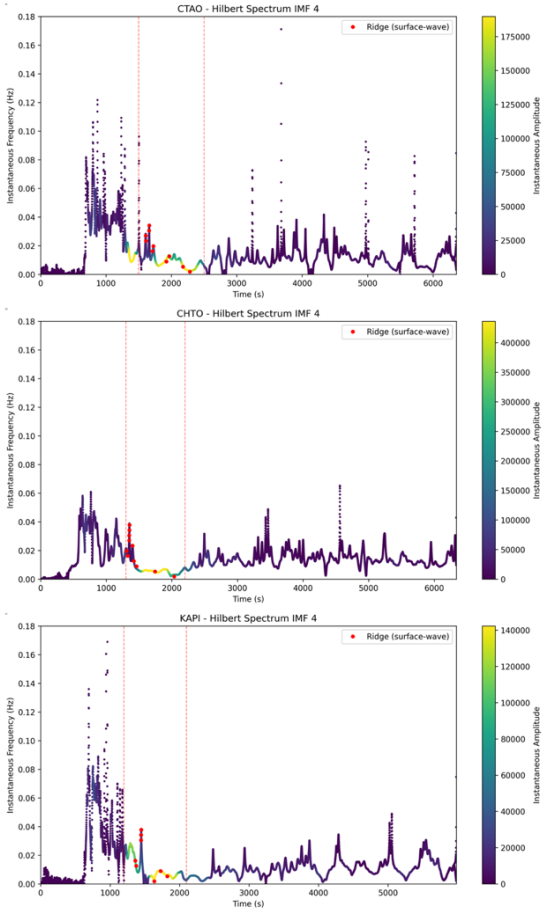

Figure 4. IMF4 Hilbert spectra at CTAO, CHTO, and KAPI stations. Red dots mark the extracted ridges used for group-delay measurements, while color shading denotes instantaneous amplitude.

Phase-Velocity Reconstruction and Vs Inversion

The group velocity was determined by the arrival timings of the ridges (Neukirch et al. 2021):

$$U(f) = \frac{X}{t_{peak}(f)} \quad (4)$$

where the epicentral distance is denoted by X (Table 1). A second-order (quadratic) polynomial is applied to $U(f)$ to suppress scatter while preserving long-period trends (Figures 5–6). Smoothing is needed to suppress high-frequency jitter from windowed picking and noise that would otherwise propagate into phase reconstruction and inversion. We choose a low-order polynomial because path-averaged dispersion varies smoothly with frequency; a low order preserves the broad trend and avoids spline-type wiggles. The order is kept minimal so residuals stay within the picking uncertainty, and features such as the Rayleigh minimum are not shifted.

The formulation of Chen et al. (2002) was followed for phase-velocity reconstruction:

$$\phi(f) = 2\pi \int_{f0}^{f} T_g(v)dv + \phi_0, \quad (5)$$

$$c(f) = \frac{\omega X}{\phi(f) - 2\pi N}, \quad \omega = 2\pi f \quad (6)$$

where N corrects for the 2π ambiguity and ϕ_0 is set by a dual-frequency anchor to ensure physical continuity. A low-order polynomial is used to remove small oscillations not resolvable by the data and to keep the group–phase pair mutually consistent (Figure 7).

For each path, the reconstructed $c(f)$ is inverted for a 1-D Vs profile. The initial model is taken from CRUST1.0 (Laske et al., 2012); forward modeling uses DISBA for the fundamental Rayleigh mode (Carchedi et al., 2025). The objective function combines a Huber misfit with smoothness and weak prior terms (Çakir & Kutlu, 2023),

$$J(m) = \sum_i \rho\delta\left(\frac{c_i^{obs} - c_i^{syn}(m)}{\sigma_i}\right) + \lambda\sum_j (V_{s,j+1} - V_{s,j})^2 + \beta\sum_{j\epsilon crust}(V_{s,j} - V_{s,j}^{(0)})^2 \quad (7)$$

where σ_i are frequency-dependent weights derived from the variance across overlapping windows, λ enforces profile smoothness, and β prevents unrealistic drift from the CRUST1.0 crust while not enforcing it. Long-period data (≳200 s) are emphasized to improve upper-mantle sensitivity; shorter periods provide secondary constraints (Figure 7).

We invert a path-averaged layered model with free Vs and layer thicknesses, including a free Moho depth; compressional velocity and density follow CRUST1.0 and are fixed. Parameter bounds are deliberately broad and guided

by period–depth sensitivity so the solution is driven by the dispersion data. The misfit uses the Huber loss with the frequency-dependent weights σ_i in Equation (7). Models are explored with a stochastic global search (Differential Evolution) with early stopping; small smoothness and prior terms stabilize the solution without enforcing CRUST1.0.

Results and Discussion

The Hilbert spectrum obtained from vertical-component decomposition indicates a distinct concentration of energy in the 20–200 s time region. Of the seven IMFs derived from EMD, IMF4 consistently demonstrated stable oscillations and the predominance of the fundamental-mode Rayleigh energy across all stations. The time-frequency maps (Figures 3–4) show continuous ridges, which were then taken out to identify arrival timings that depend on frequency. This method produces a clearer picture of dispersion than traditional Fourier-based methods that use fixed windowing (Huang et al., 1998; Huang & Wu, 2008; Khan et al., 2025) and its effectiveness is in line with recent Indonesian studies employing surface-wave dispersion techniques for Vs mapping (Putri et al., 2025).

Figures 5 and 6 show that group-velocity curves at CTAO and CHTO follow the same trend. At lengthy periods (>150 s), group velocities range from 3.0 to 3.5 km/s. At periods of 40–60 s, they rise to about 5.0–5.5 km/s. The dashed curves in Figure 5 denote second-order polynomial smoothing; trials with first- and third-order fits produced changes within the picking uncertainty. This pattern is due to the fact that fundamental-mode Rayleigh waves are more sensitive to depth than other types of waves (Babikoff & Dalton, 2019; Moulik & Ekström, 2025). Polynomial smoothing worked well to smooth out noise, especially at low frequencies.

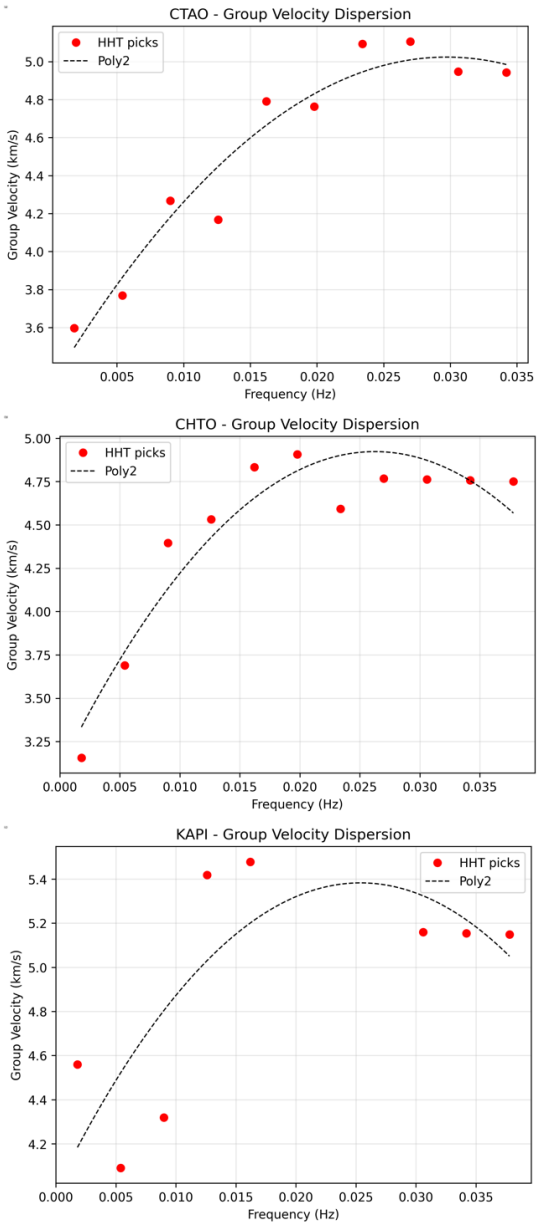

Figure 5. Group-velocity dispersion curves U(f) extracted from Hilbert–Huang ridges at CTAO, CHTO, and KAPI. Black dots represent observed ridge picks, and dashed lines show low-order polynomial smoothing.

Figure 6 shows the reconstructed phase-velocity curves using the Chen et al. (2002) formulation. They are stable in the frequency band of 0.004–0.04 Hz, with values between 3.3 and 4.6 km/s. CTAO and CHTO both show the U-shaped pattern of fundamental Rayleigh waves, with a velocity minimum between 0.005 and 0.01 Hz, which is in line with what has been seen around the world (Ritzwoller & Levshin, 1998; Yang et al., 2023). The data at KAPI, however, do not follow this trend. Instead,

they indicate an almost constant increase in speed with no clear minimum. Possible reasons for such variations include contamination from higher modes, incorrectly assigning the integer N in the Chen et al. (2002) formulation, or tectonic complexity along the Sumatra path that makes ridge extraction less stable. Such anomalies heighten inversion uncertainty and underscore the necessity for enhanced anchoring procedures and more rigorous data quality control (Xiao et al., 2022; Çakır & Kutlu, 2023).

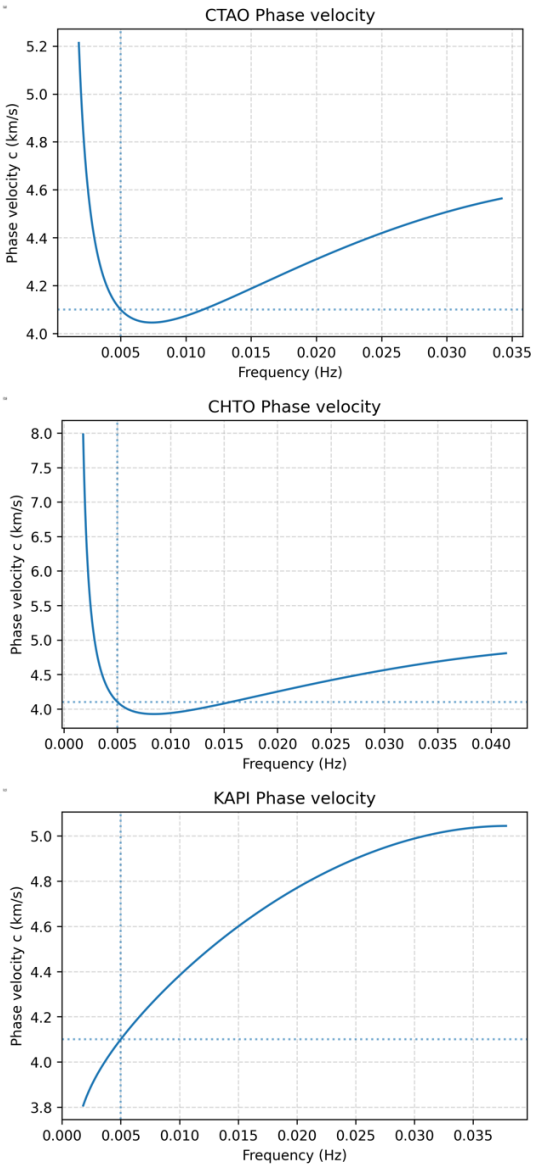

Figure 6. Phase-velocity curves c(f) reconstructed using the Chen et al. (2002) method for CTAO, CHTO, and KAPI. Gray dashed lines indicate uncertainty bounds.

The 1-D Vs inversion of the phase-velocity curves (Figure 7) indicates clear lateral differences among the three source–station paths. Here we define the crustal boundary (Moho) as the depth of the strongest positive Vs gradient that marks the transition from crustal to upper-mantle velocities in the inverted 1-D profile. The reported depth is read from the best-fitting model and is consistent with the period–depth sensitivity of the data.

At CTAO on the Australian continental margin, we infer ~35 km crust and relatively fast upper-mantle Vs (~4.6–4.7 km/s); together with smooth long-period dispersion and low inversion misfit, these observations are consistent with a cool, mechanically strong lithosphere at this margin. CHTO in mainland Southeast Asia shows a thicker crust (~40 km), in line with regional tomography (Dou et al., 2024). In contrast, KAPI in Indonesia indicates a thinner crust (~30–32 km) and a slower upper mantle, likely reflecting a weaker lithosphere associated with the ongoing Indo-Australian subduction. These patterns broadly agree with regional deformation from GPS and InSAR (Yang et al., 2023; Chen et al., 2025), while uncertainties remain larger at KAPI due to lower SNR and limited long-period constraints.

Overall, the data indicate significant variation in the lithosphere and crust across the transcontinental corridor. The tectonic difference between stable continental interiors and active subduction zones is shown by a thick crust in Southeast Asia, a rapid mantle under the Australian margin, and a weak lithosphere under Sumatra. The HHT and Chen-phase reconstruction method effectively generated stable dispersion curves from non-stationary waveforms. This technique led to Vs inversion findings that better reflect regional structure than the global CRUST1.0 reference (Laske et al., 2012). This method makes it possible to use dispersion analysis in areas with

complicated tectonics, and it lays the groundwork for future investigations in Southeast Asia on a regional scale. Similar approaches have also been successfully applied in Indonesian contexts for shallow crustal characterization using MASW (Putri et al., 2025), further underscoring the broader applicability of surface-wave dispersion methods.

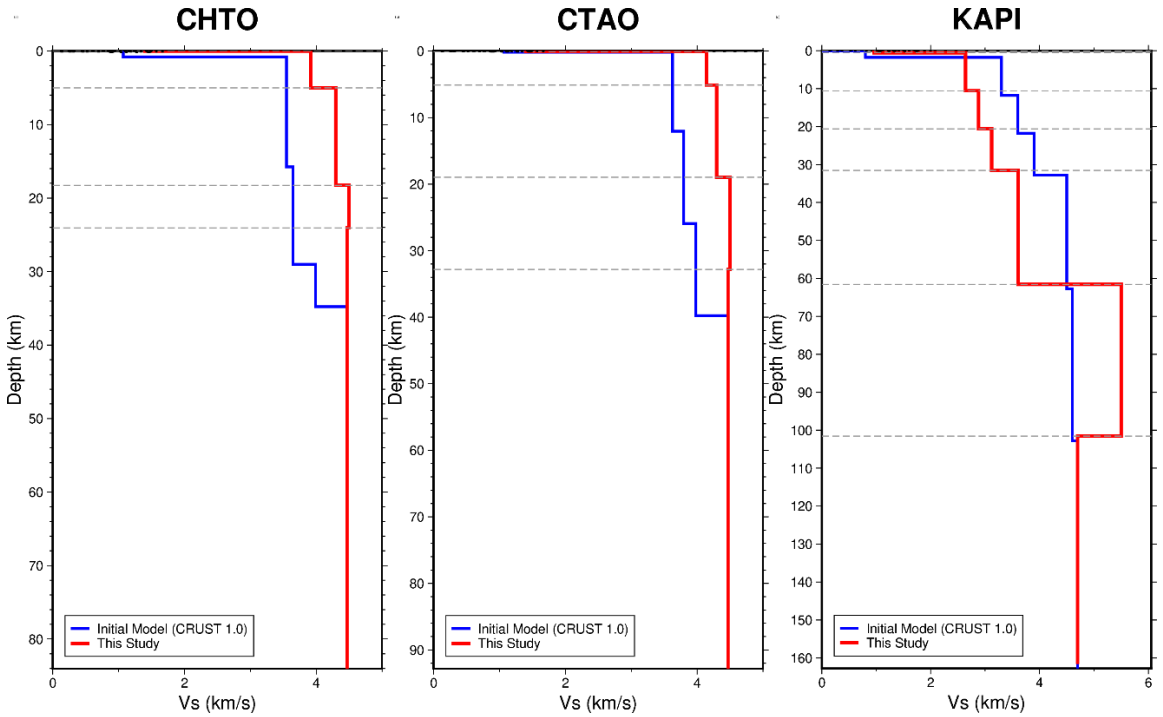

Figure 7. Inverted 1-D Vs models beneath CTAO, CHTO, and KAPI (red lines) compared with the CRUST1.0 reference model (blue lines). Moho discontinuities appear as velocity jumps at 30–40 km depth.

Conclusions

We tested the idea that an HHT workflow can extract stable dispersion from non-stationary teleseismic waves and produce Vs models that reflect regional geology. The results support this idea. Ridge tracking on the Hilbert spectrum presents continuous group and phase curves at CHTO in Thailand, KAPI in Indonesia, and CTAO in Australia. These three paths represent a continental margin, an arc and back-arc, and a craton.

We invert the dispersion using a neutral global prior and recover coherent lateral changes. The crust is thicker beneath the Southeast Asian margin, of intermediate thickness toward the Australian margin, and thinner with a slower upper mantle beneath Sulawesi. Accuracy and robustness follow from the inversion design. We use broad parameter bounds and a stochastic global search to limit dependence on the starting model. We also propagate dispersion-picking uncertainty with frequency-dependent weights and examine period–depth sensitivity to confirm that the data can resolve the reported features.

These findings are useful beyond method testing. The path-specific dispersion and Moho constraints can sharpen starting models and regularization in regional surface-wave tomography and can improve velocity structures and crustal corrections for seismic-hazard simulations in Southeast Asia. Future work will stack multiple events and add azimuthal analyses to examine anisotropy and to stabilize the longest periods.

Acknowledgements

This research did not receive any specific grant from funding agencies in the public,

commercial, or not-for-profit sectors. The authors gratefully acknowledge the IRIS Data Management Center (DMC) for providing open access to the seismic data used in this study. We also thank the journal editor and anonymous reviewers for their constructive comments, which helped improve the quality of this manuscript.

Author Contribution

Andri Kurniawan led the research, including conceptualization, methodology design, data collection and curation, software development, formal analysis, visualization, and preparation of the original draft. Ilham Dani contributed to validation and assisted with manuscript review and editing. Sandri Erfani provided supervision and contributed to manuscript review and editing.

Conflict of Interest

There were no funds or finances exchanged in this study, neither among the authors nor between the parties involved in the research. so that the author can explain it to the Journal of Geocelebes' rules.

References

Babikoff, J. C., & Dalton, C. A. (2019). Long-period Rayleigh wave phase velocity tomography using USArray. *Geochemistry, Geophysics, Geosystems*, 20(4), 1990–2006. https://doi.org/10.1029/2018GC008073

Büyük, E., Zor, E., & Karaman, A. (2020). Joint modeling of Rayleigh wave dispersion and H/V spectral ratio using Pareto-based multiobjective particle swarm optimization. *Turkish Journal of Earth Sciences*, 29, 684–695. https://doi.org/10.3906/yer-2001-15

Çakir, Ö., & Kutlu, Y. A. (2023). Forward modeling the group and phase velocities of Rayleigh and Love surface waves beneath Central Anatolia: Fifth parameter for transverse isotropy. *Malaysian Journal of Geosciences,* 7(2), 134–149. https://doi.org/10.26480/mjg.02.2023.134.149

Carchedi, C. J. W., Gaherty, J. B., Byrnes, J. S., Rondenay, S., Steckler, M. S., Ajala, R., Persaud, P., Sandvol, E. A., Alim, M. S., Singha, S., & Akhter, S. H. (2025). Evolving sediment structure and lithospheric architecture across the Indo-Burman forearc margin from the joint inversion of surface- and scattered-wave seismic constraints. *Journal of Geophysical Research: Solid Earth,* 130(6), e2024JB030050. https://doi.org/10.1029/2024JB030050

Chen, C.-H., Li, C.-P., & Teng, T.-L. (2002). Surface-wave dispersion measurements using Hilbert–Huang transform. *Terrestrial, Atmospheric and Oceanic Sciences,* 13(2), 171–184. https://doi.org/10.3319/TAO.2002.13.2.171(T)

Chen, Y., Li, J., Lu, K., & Hu, T. (2025). Coseismic slip model and early post-seismic deformation processes of the 2024 M7.5 Noto Peninsula, Japan earthquake revealed by InSAR and GPS observations. *Geophysical Journal International*, 240(2), 1048–1063. https://doi.org/10.1093/gji/ggae429

de Souza, U. B., Escola, J. P. L., & Brito, L. d. C. (2022). A survey on Hilbert–Huang transform: Evolution, challenges and solutions. *Digital Signal Processing*, 120, 103292. https://doi.org/10.1016/j.dsp.2021.103292

Dou, H., Xu, Y., Lebedev, S., Chagas de Melo, B., van der Hilst, R. D., Wang, B., & Wang, W. (2024). The upper mantle beneath Asia from seismic tomography, with inferences for the mechanisms of tectonics, seismicity, and magmatism. *Earth-Science Reviews*, 255, 104841.

https://doi.org/10.1016/j.earscirev.2024.104841

Eriksen, T., & Rehman, N. U. (2023). Data-driven nonstationary signal decomposition approaches: A comparative analysis. *Scientific Reports,* 13, 1798. https://doi.org/10.1038/s41598-023-28390-w

Giampiccolo, E., Tuvè, T., Bianco, F., & Del Pezzo, E. (2024). Depth and spatial variation of the shear-wave attenuation parameters in the shallow crust and lower crust/upper mantle of Mt. Etna (Italy). *Pure and Applied Geophysics*, 181, 171–187. https://doi.org/10.1007/s00024-023-03400-0

Harsuko, M. R. C., Zulfakriza, Z., Nugraha, A. D., Sarjan, A. F. N., Widiyantoro, S., Rosalia, S., Puspito, N. T., & Sahara, D. P. (2020). Investigation of Hilbert–Huang transform and Fourier transform for horizontal-to-vertical spectral ratio analysis: Understanding the shallow structure in Mataram City, Lombok, Indonesia. *Frontiers in Earth Science*, 8, 334. https://doi.org/10.3389/feart.2020.00334.

Huang, N. E., & Wu, Z. (2008). A review on Hilbert–Huang transform: Method and its applications to geophysical studies. *Reviews of Geophysics,* 46(2), RG2006. https://doi.org/10.1029/2007RG000228

Hutchings, S. J., & Mooney, W. D. (2021). The seismicity of Indonesia and tectonic implications. *Geochemistry, Geophysics, Geosystems*, 22(9), e2021GC009812. https://doi.org/10.1029/2021GC009812

Khan, S. B., Balajee, A., Shah, S. S. M., Mahesh, T. R., Alojail, M., & Gupta, I. (2025). A novel ensemble empirical decomposition and time–frequency analysis approach for vibroarthrographic signal processing. *Circuits, Systems, and Signal Processing*. https://doi.org/10.1007/s00034-025-03096-8

Laske, G., Masters, G., Ma, Z., & Pasyanos, M. E. (2012). CRUST1.0: An updated global model of Earth's crust. *Geophysical Research Abstracts,* 14, EGU2012-3743-1. https://meetingorganizer.copernicus.org/EGU2012/EGU2012-3743-1.pdf

Li, M., Song, X., Li, J., & Bao, X. (2022). Crust and upper mantle structure of East Asia from ambient noise and earthquake surface wave tomography. *Earthquake Science,* 35(2), 71–92. https://doi.org/10.1016/j.eqs.2022.05.004

Magrini, F., Kästle, E., Pilia, S., Rawlinson, N., & De Siena, L. (2023). A new shear-velocity model of continental Australia based on multi-scale surface-wave tomography. *Journal of Geophysical Research: Solid Earth,* 128(7), e2023JB026688. https://doi.org/10.1029/2023JB026688

Müller, R. D., Zahirovic, S., Williams, S. E., Cannon, J., Seton, M., Bower, D. J., Tetley, M. G., Heine, C., Le Breton, E., Liu, S., Russell, S. H. J., Yang, T., Leonard, J., & Gurnis, M. (2019). A global plate model including lithospheric deformation along major rifts and orogens since the Triassic. *Tectonics*, 38, 1841–2157. https://doi.org/10.1029%2F2018TC005462

Moulik, P., & Ekström, G. (2025). Radial structure of the Earth: (II) Model features and interpretations. *Physics of the Earth and Planetary Interiors*, 361, 107320. https://doi.org/10.1016/j.pepi.2025.107320

Neukirch, M., García-Jerez, A., Villaseñor, A., Luzón, F., Ruiz, M., & Molina, L. (2021). Horizontal-to-vertical spectral ratio of ambient vibration obtained by

Hilbert–Huang transform. *Sensors,* 21(9), 3292. https://doi.org/10.3390/s21093292

Nishida, K., Takagi, R., & Takeo, A. (2024). Ambient noise multimode surface wave tomography. *Progress in Earth and Planetary Science,* 11, 4. https://doi.org/10.1186/s40645-023-00605-8

Patton, J. R. (2025). *Earthquake report: M 8.8 Kamchatka*. EarthJay. https://earthjay.com/?p=12355

Putri, A. C. P., Refrizon, R., Hadi, A. I., & Al Ansory, A. R. (2025). Mapping of soil stability based on Vs30 using MASW on Kalimantan Highway, Bengkulu City. *Jurnal Geocelebes,* 9(1), 1–14. https://doi.org/10.70561/geocelebes.v9i1.34956

U.S. Geological Survey. (2025). *M 8.8—Kamchatka Peninsula, Russia earthquake*. USGS Earthquake Catalog. https://earthquake.usgs.gov/earthquakes/eventpage/us6000qw60

Xiao, X., Sun, L., Wang, X., & Wen, L. (2022). Simultaneous inversion for surface-wave phase velocity and earthquake centroid parameters: Methodology and application. *Journal of Geophysical Research: Solid Earth,* 127(9), e2022JB024018. https://doi.org/10.1029/2022JB024018

Yang, X., Luo, Y., Jiang, C., Yang, Y., Niu, F., & Li, G. (2023). Crustal and upper mantle velocity structure of SE Tibet from joint inversion of Rayleigh wave phase velocity and teleseismic body wave data. *Journal of Geophysical Research: Solid Earth,* 128(7), e2022JB026162. https://doi.org/10.1029/2022JB026162

ISSN: 2579-5821 (Print)
ISSN: 2579-5546 (Online)
URL address: http://journal.unhas.ac.id/index.php/geocelebes
DOI: 10.70561/geocelebes.v9i2.47083

Jurnal Geocelebes Vol. 9 No. 2, October 2025, 226 – 236

Subsurface Characterization using Electrical Resistivity Tomography (ERT) for Sponge City Planning in Nusantara Capital City (IKN), Indonesia

Wahidah[1*], Piter Lepong[1], Supriyanto[2], Djayus[2], Muhamad Akmal Firdaus[1], Dwi Azisyarlina[1]

[1]Geophysics, Mulawarman University, Samarinda 75123, Indonesia.
[2]Physics, Mulawarman University, Samarinda 75123, Indonesia.

*Corresponding author. Email: wahidah@fmipa.unmul.ac.id

Manuscript received: 10 September 2025; Received in revised form: 15 October 2025; Accepted: 22 October 2025

Abstract

Clay shale dominates the lithology along access roads in the IKN development area. Its impermeable nature poses challenges to implementing the Sponge City concept, which relies on enhanced rainwater absorption to reduce surface runoff. This study aims to map the spatial distribution of clay shale and assess its implications for Sponge City planning. The geoelectrical resistivity method was applied at three sites, each consisting of one long section and three cross sections. Resistivity contrasts were used to delineate subsurface lithology, producing two- and three-dimensional models. The results reveal three main lithological units: topsoil, clay shale, and sandy clay. Topsoil shows heterogeneous resistivity values with thicknesses ranging from <1 m to 5 m. Clay shale exhibits resistivity values below 50 Ωm and thicknesses of <5–30 m, while sandy clay exceeds 50 Ωm with variable thicknesses up to 30 m. The thick, low-resistivity clay shale indicates poor permeability, which limits infiltration and groundwater storage. These findings suggest that the IKN area is less suitable for a natural sponge system. Therefore, stormwater management should prioritize engineered solutions such as green roofs, retention ponds, and bioretention facilities to control runoff and support sustainable urban development.

Keywords: Clay Shale; Nusantara Capital City; Resistivity; Sponge City.

Citation: Wahidah, W., Lepong, P., Supriyanto, S., Djayus, D., Firdaus, M. A., & Azisyarlina, D. (2025). Subsurface Characterization using Electrical Resistivity Tomography (ERT) for Sponge City Planning in Nusantara Capital City (IKN), Indonesia. *Jurnal Geocelebes*, 9(2): 226–236, doi: 10.70561/geocelebes.v9i2.47083

Introduction

With the advancement of instrumentation and software technologies, geophysical methods have been extensively applied, particularly in developed countries, for geotechnical and environmental surveys. In Indonesia, research and applications of geophysics in the geotechnical field are relatively new but are expected to expand in line with the growing demand for subsurface characterization.

The planned development of a Sponge City in the prospective Nusantara Capital City (IKN) area of East Kalimantan is one of the projects requiring geophysical investigation. The dominant lithology in this region is clay shale. According to Bachtiar (2022), the geology of the study area consists of marine clay sediments belonging to the Pamaluan Formation of Late Oligocene age, deposited in a middle-shelf facies environment (Figure 1).

Alamsyah et al. (2024) reported that clay shale is not only exposed along the IKN access roads but also occurs in the subsurface, as confirmed by Seismic Refraction Tomography (SRT). In civil engineering, clay shale is classified as an intermediate rock containing

montmorillonite clay minerals, characterized by low durability due to weathering and high swelling potential, which pose significant challenges for construction (Ohlmacher, 2000; Wahidah et al., 2024). Higher clay content typically reduces both effective porosity and hydraulic conductivity (K) (Orozco et al., 2022). Furthermore, clay shale has inherently low permeability (Ningtyas et al., 2020), limiting its ability to transmit water. Low permeability reduces infiltration capacity, leading to soil saturation. Prolonged rainfall may cause waterlogged soils to swell and exert pressure on soil particles, potentially triggering mass movement (Bachtiar, 2022). These properties are unfavorable for the Sponge City concept, which aims to mitigate flooding by maximizing rainwater infiltration and minimizing surface runoff (Qiu, 2015; An et al., 2015; Liu et al., 2021; Li et al., 2022).

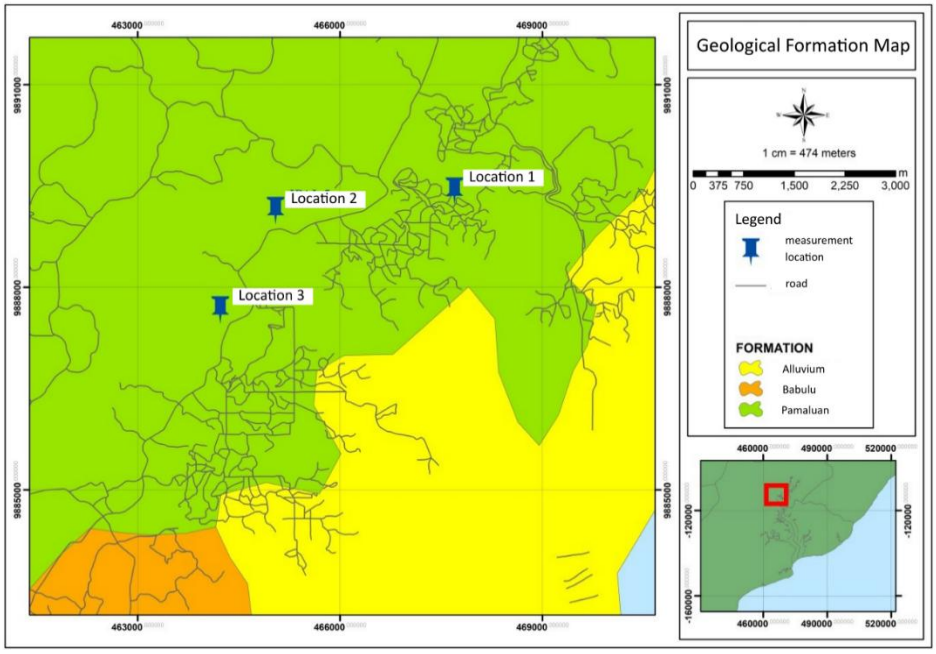

Figure 1. Geological formation map.

Since the 1980s, Chinese scholars have studied the Sponge City concept from various perspectives, including urban stormwater control, land use, and ecological construction. Several studies (Huang et al., 2018; Su et al., 2023; Liu et al., 2025) evaluated Sponge City suitability using Analytic Hierarchy Process (AHP) based on regional geology and hydrogeological conditions. Ye et al. (2018) provided recommendations for stormwater management facilities suited to different zones based on geological suitability assessments, while Wang et al. (2019) analyzed sponge characteristics such as vegetation cover, slope topography, vadose zone, and aquifers, and proposed a geological suitability evaluation framework for Sponge City planning.

Su et al. (2023) highlighted geology as a primary factor influencing Sponge City development, including lithology, vadose zone characteristics, aquifer thickness and composition, slope gradient, and groundwater abundance. Primary indicators include surface characteristics, vadose zone properties, and aquifer conditions, while secondary indicators consist of lithology, slope gradient, vadose zone thickness, and groundwater availability. Areas classified as suitable for Sponge City development typically support infiltration, vadose zone transport, and aquifer storage, enabling sustainable urban hydrological cycles when combined with

surface water storage and drainage infrastructure. Conversely, less suitable areas require emphasis on engineered stormwater management strategies, such as green roofs, retention ponds, and bioretention facilities, supported by geotechnical measures.

To evaluate the suitability of the Sponge City concept in IKN, comprehensive and multidisciplinary subsurface investigations are essential. The geoelectrical resistivity method represents a promising approach, as it exploits resistivity contrasts to delineate lithology and subsurface geological structures. This method offers a non-invasive and cost-effective alternative for mapping subsurface conditions (Bichet et al., 2016; Adeyemo et al., 2017; Feng et al., 2017; Hu et al., 2019; Tagoe et al., 2025), and it has been effectively applied to image clay-pan distributions (Jeřábek et al., 2017; Mathis et al., 2018) and to monitor seasonal water-content variations in clay (Genelle et al., 2012; Chrétien et al., 2014).

Therefore, this study aims to map clay shale distribution using the Electrical Resistivity Tomography (ERT) method, addressing the lack of previous research in the IKN area related to the Sponge City concept, and to assess its implications for the planned Sponge City. The results are expected to provide a clearer understanding of how clay shale affects groundwater infiltration and storage, offering valuable input for the Sponge City design in IKN.

Materials and Methods

The study area is located within the planned Nusantara Capital City (IKN), specifically in Sepaku District, Penajam Paser Utara Regency, East Kalimantan, as shown in Figure 1–4.

The geoelectrical survey was conducted in an area covered by the regional geological map of East Kalimantan (Figure 1). The three survey sites are situated within the Pamaluan Formation (Tomp), which is predominantly composed of claystone and shale with intercalations of marl, sandstone, and limestone.

The research workflow consisted of three main stages: (i) data acquisition using geoelectrical equipment, (ii) data processing to generate subsurface models, and (iii) data analysis and interpretation.

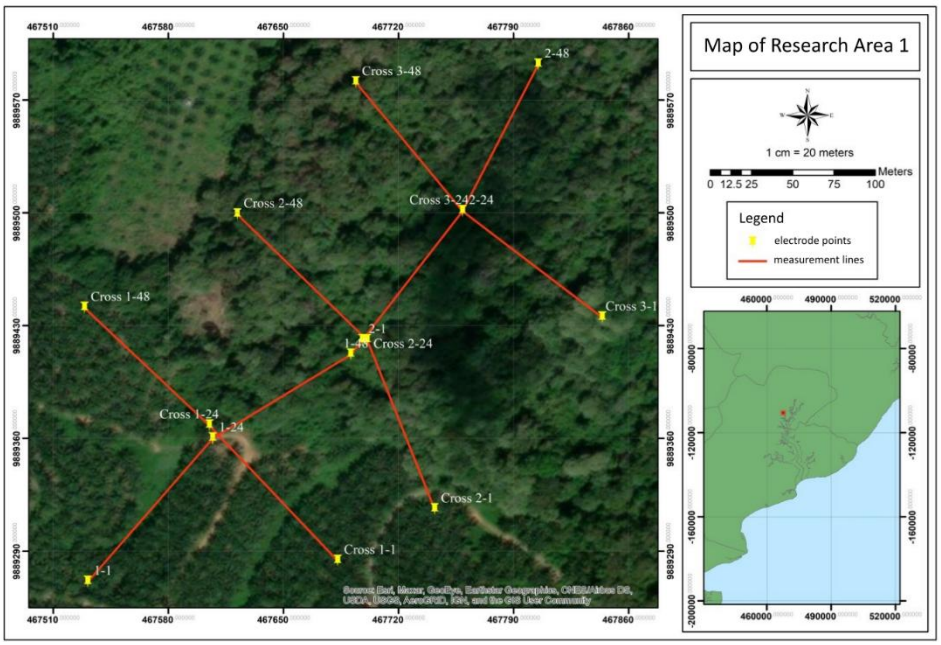

Figure 2. Research Area 1.

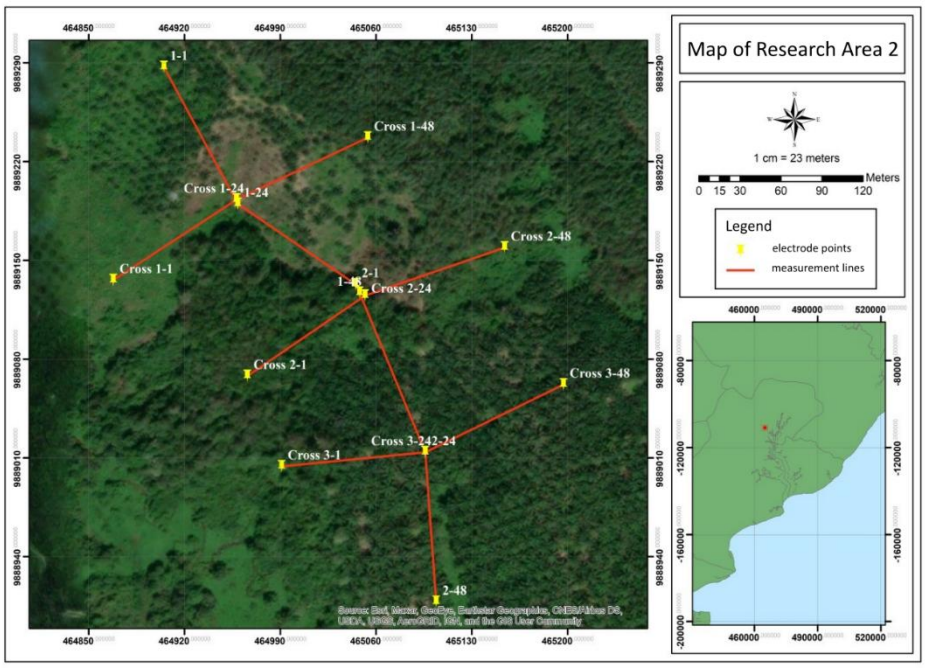

Figure 3. Research Area 2.

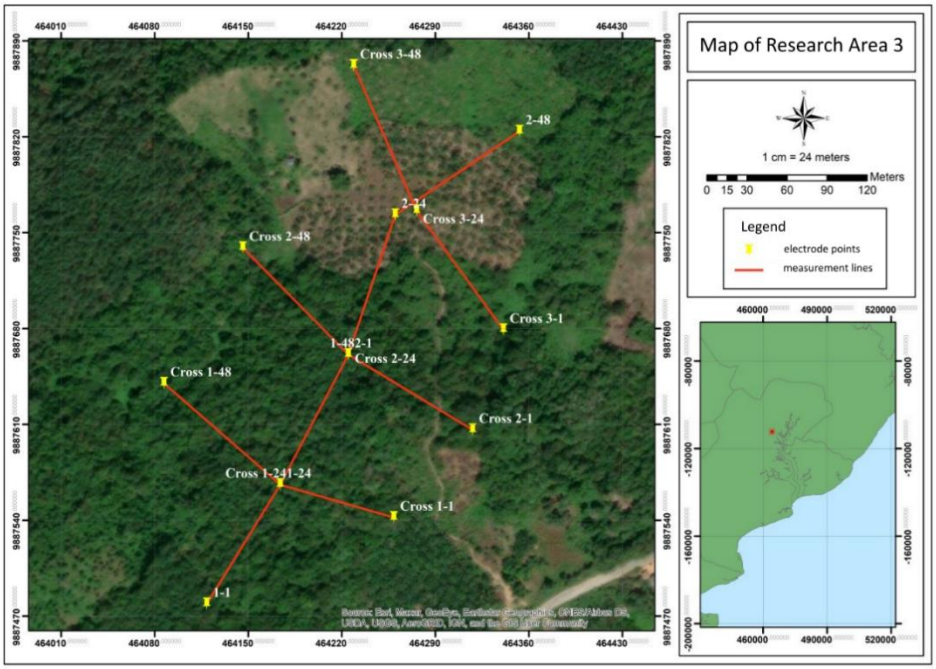

Figure 4. Research Area 3.

In the acquisition stage, measurements were performed at three survey sites (Figure 2–4) using a set of MAE Multi-Channel Resistivity and IP Meter equipment. The geoelectrical survey was conducted using the dipole-dipole configuration. Before data collection, survey configurations and field parameters, including electrode spacing, survey line length, and the number of profiles, were carefully determined. At each site, four survey lines were deployed: one main line and three cross-lines, resulting in a total of 12 profiles. Figure 2–4 illustrate the layout of the survey lines. The main survey line was 470 m long, whereas each cross-line measured 235 m.

After the data acquisition stage, the next step is data processing. In this phase, the recorded current values, potential measurements, and electrode spacing are entered and processed using geoelectrical software to generate a two-dimensional (2D) resistivity model. Subsequently, a three-dimensional (3D) modeling process is performed to visualize the spatial distribution of clay shale.

The resulting 2D resistivity sections and 3D clay shale models were subsequently analyzed and interpreted by comparing measured resistivity and chargeability values with published reference tables. Geological validation, which involved the regional geological map, was performed to ensure consistency between interpretation results and the actual subsurface conditions at the study site. As a working hypothesis, lithologies characterized by low resistivity values are interpreted as clay shale, which correlates with low permeability. Consequently, areas within IKN dominated by low-permeability lithology are considered less suitable for the implementation of the Sponge City concept.

Result and Discussion

The geoelectrical survey results are presented as resistivity sections. Each site comprises four survey lines (one long section and three cross-sections), yielding a total of twelve sections across the three investigated sites. For each site, the 2D long-section model was selected as the representative profile (Figure 5), as it most clearly illustrates the spatial distribution trend of clay shale. In contrast, the cross-section models are utilized in the 3D correlation to highlight the lateral continuity between sections.

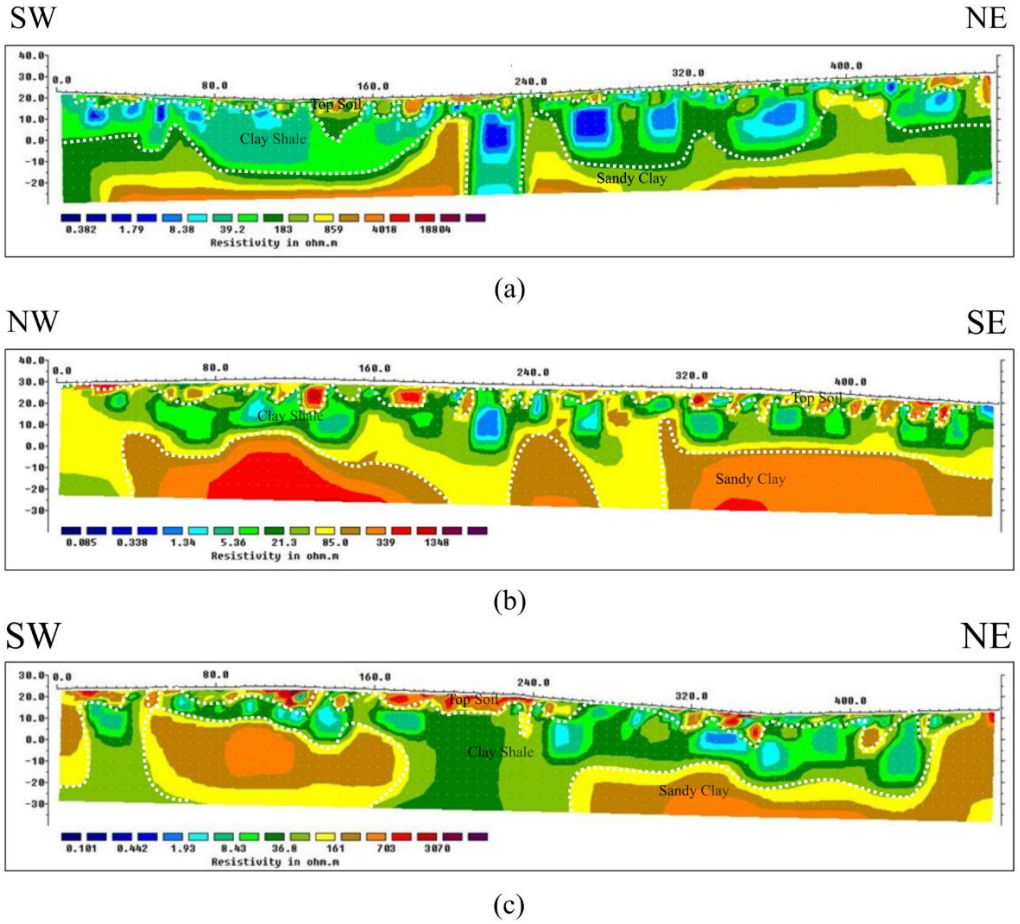

Figure 5. Geoelectrical Resistivity Longsection Profiles: (a) Location 1, (b) Location 2, (c) Location 3.

Figure 5 illustrates three main lithological units identified from the resistivity profiles: topsoil, clay shale, and sandy clay. The topsoil layer is relatively thin (<1 – 5 m), underlain by clay shale with resistivity values below 50 Ωm and thicknesses ranging from less than 5 m to over 30 m. The deepest unit is sandy clay, which shows resistivity values above 50 Ωm.

The profiles show clear spatial variations. At Location 1 (Figure 5a), the clay shale layer thickens toward the southwest, while the sandy clay unit becomes thinner in the same direction. Location 2 (Figure 5b), which trends northwest to southeast, exhibits a relatively thick sandy clay layer reaching up to 30 meters with a nearly horizontal stratification. At Location 3 (Figure 5c), oriented southwest to northeast, clay shale is the dominant lithology, with only a thin sandy clay layer observed at the base.

Overall, the presence of clay shale is significant, indicating high fluid saturation and low permeability. According to Fallah-safari et al. (2010), clay materials generally exhibit either higher water content or higher air-void ratios; in this study, the clay shale corresponds to the former, characterized by low resistivity (<50 Ωm) and high ionic fluid saturation.

The interpretation of the geoelectrical section indicates the presence of a hard soil layer, identified at the contact boundary between the topsoil and clay shale. Based on Figures 5 and 6, the hard layer occurs at a depth of approximately 2–4 meters, corresponding to the relatively thin topsoil observed in the section. From a hydrogeological perspective, the topsoil acts as an infiltration zone, where rainwater initially enters the ground through soil pores. This layer is also part of the vadose zone or the unsaturated zone, where pores contain both air and water, allowing downward water movement through gravity and capillary action. Beneath it lies an impermeable clay shale layer that serves as the lower boundary of the vadose zone, restricting vertical infiltration and impeding percolation into deeper layers. The underlying sandy clay layer exhibits higher permeability compared to the clay shale and potentially functions as a shallow confined aquifer, capable of storing infiltrated water from the upper layers.

Integration of the geoelectrical section and the 3D resistivity model (Figures 5 and 6) reveals that the clay shale forms a continuous low-resistivity layer (<50 Ωm) thickening toward the northeast. This thickening trend is consistent with the regional geological pattern, where the study area lies within the Pamaluan Formation (depicted in green on the geological map in Figure 1), composed predominantly of alternating claystone and shale. The clay shale distribution follows a southwest–northeast orientation, indicating agreement between the geoelectrical results and regional stratigraphic structures. In contrast, higher-resistivity zones in the southern and southwestern parts indicate the presence of sandy clay correlated with deposits of the Bebulu Formation and younger alluvium. Integration of the 3D resistivity model, geoelectrical cross-section, and regional geological map strengthens the interpretation that the clay shale of the Pamaluan Formation functions as an impermeable layer that controls infiltration processes and defines the position and thickness of the vadose zone, while the underlying sandy clay may serve as a limited shallow aquifer in the study area.

According to Filho et al. (2017), a decrease in resistivity values is generally caused by increased clay content and soil compaction. This finding aligns with Ningtyas et al. (2020), who reported that low resistivity correlates with low permeability. Therefore, clay shale with low resistivity values indicates poor water conductivity and impermeable characteristics. In relation

to porosity, lower permeability in a lithologic unit result in reduced water absorption, causing water to remain within the soil and increasing saturation levels. Saturated soils tend to expand during prolonged or intense rainfall, which may increase pore pressure and trigger slope instability, particularly in areas dominated by clay-rich materials.

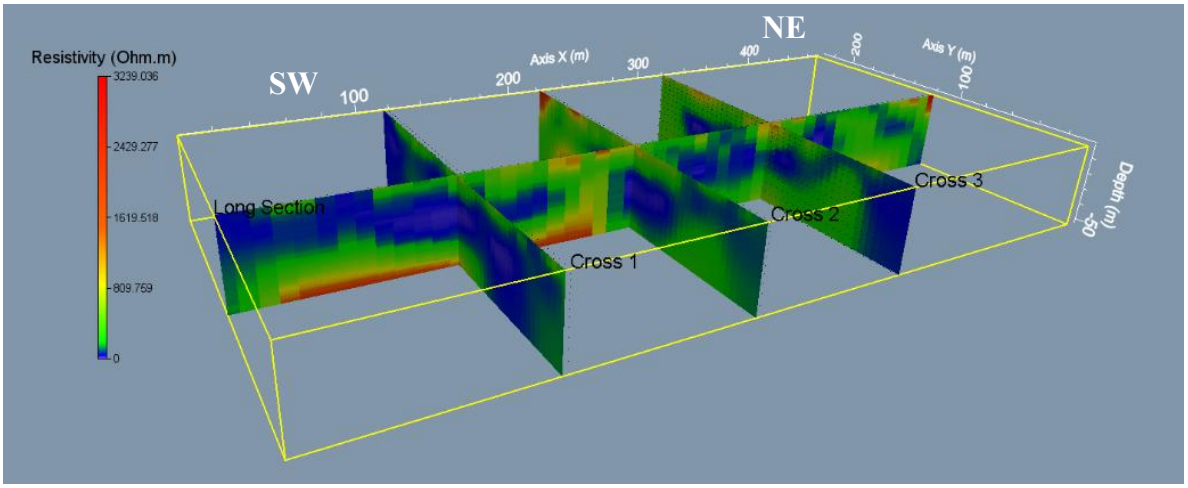

(a)

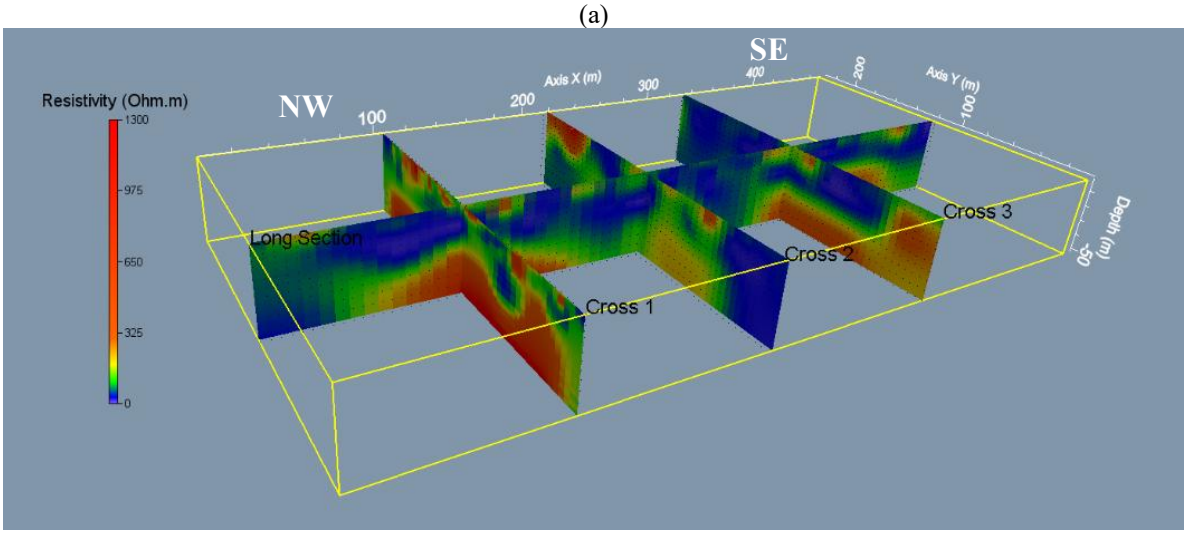

(b)

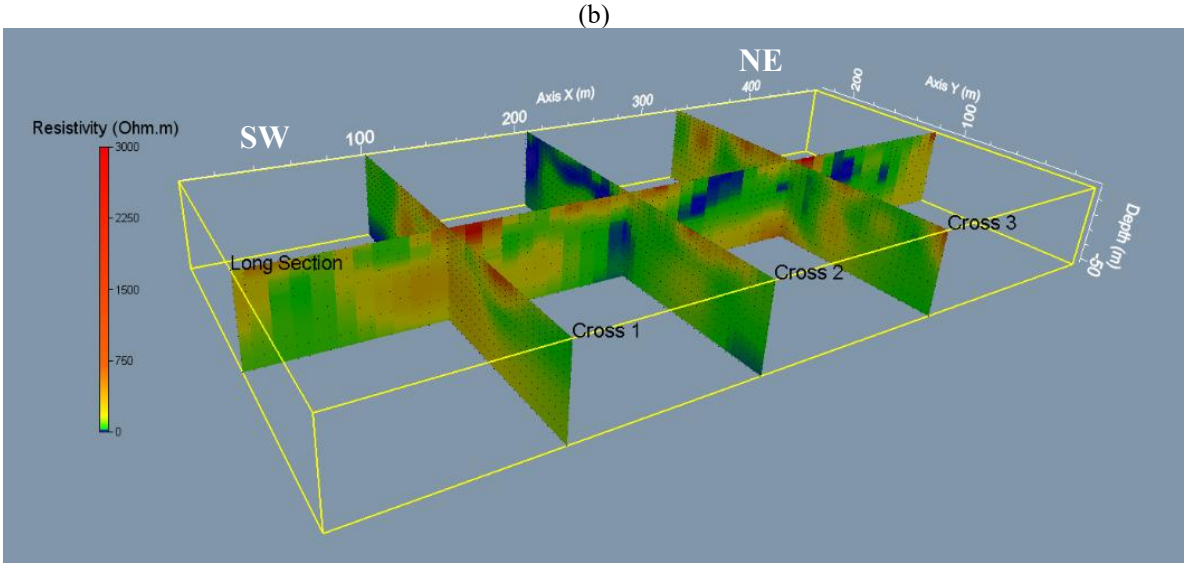

(c)

Figure 6. 3D Model of Geoelectrical Resistivity Sections at (a) Location 1, (b) Location 2, and (c) Location 3.

The geological conditions in the IKN region, dominated by thick, low-permeability clay shale, suggest that surface infiltration, water transport within the vadose zone, and natural aquifer storage are not well developed. Consequently, implementing the Sponge City concept that relies solely on natural recharge into deep aquifers would be ineffective in this region. The results of this study highlight the need for a hybrid approach that integrates natural and engineered systems. Water management strategies in IKN should emphasize surface retention and stormwater management, such as green roofs, retention ponds, and bioretention facilities, while also considering artificial recharge to replenish the deeper sandy clay aquifer. Further studies are recommended to determine the depth of the water table in order to delineate the lower limit of the vadose zone and evaluate the potential of the shallow aquifer.

In addition to its implications for Sponge City implementation, the presence of low-resistivity clay shale also has geotechnical and geotectonic consequences. The low resistivity of this layer likely reflects the presence of clay minerals such as illite or montmorillonite. Ohlmacher (2000) stated that clay shale containing illite and montmorillonite exhibits low shear strength and high swelling potential with increasing water content. Such lithologies are more prone to deformation and landslides than clay shale dominated by kaolinite or chlorite minerals. Therefore, the presence of clay shale should be considered a major factor in infrastructure design and slope stability mitigation across the IKN area.

Conclusion

The geoelectrical survey successfully mapped the distribution of clay shale in the IKN area, revealing a relatively thick layer (up to 30 meters) with low resistivity values (<50 Ωm), indicative of low permeability. This lithological characteristic restricts surface infiltration and groundwater recharge, suggesting that the natural implementation of the Sponge City concept would be less effective under such geological conditions. Therefore, the study concludes that a hybrid water management approach, integrating both natural and engineered systems, is essential to achieve sustainable stormwater control and effectively support the Sponge City framework in IKN.

Acknowledgements

The authors would like to express their sincere gratitude to the late Andi Alamsyah, who served as the Principal Investigator, for his invaluable contributions to this study. Special thanks are also extended to the Head of the Geophysics Laboratory for technical support with the Electrical Resistivity Tomography (ERT) equipment and to the Faculty of Mathematics and Natural Sciences, Mulawarman University (FMIPA UNMUL), for funding this research. The assistance of colleagues and students during the fieldwork is also gratefully acknowledged.

Author Contribution

Wahidah: Conceptualization, Writing - Review & Editing, Visualization, and Project administration. **Piter Lepong:** Writing – Original Draft, Supervision, Validation, and Investigation. **Supriyanto and Djayus:** Methodology and Formal Analysis. **Muhamad Akmal Firdaus dan Dwi Azisyarlina:** Data Curation and Software.

Conflict of Interest

The authors declare no conflict of interest.

References

Adeyemo, I., Omosuyi, G. O., & Adelusi, O. A. (2017). Geoelectric Soundings for Delineation of Saline Water Intrusion into Aquifers in Part of

Eastern Dahomey Basin, Nigeria. *Journal of Geoscience and Environment Protection*, 5, 213−232. http://doi.org/10.4236/gep.2017.53015

Alamsyah, A., Lepong, P., Wahidah, W., & Rahmiati, R. (2024). Application of seismic refraction tomography in determining the soil hardness level in IKN Nusantara Area. *Jurnal Geocelebes*, 8(1), 62−70. https://doi.org/10.20956/geocelebes.v8i1.32159

An, S. L., Huang, J. J., Zhang, L., Miao, S., & Ginger, S. (2015). The urban geological survey working direction and supporting role on sponge city construction—take Xuzhou city as an example (in Chinese). *Urban Geology*, 10(4), 6−10. http://doi.org/10.3969/j.issn.1007-1903.2015.04.002

Bachtiar, A. (2022). *Aspek geologi untuk mitigasi bencana ibukota nusantara (IKN)*. https://www.its.ac.id/tgeofisika/wp-content/uploads/sites/33/2022/11/Materi-Dr-Andang-Bachtiar.pdf

Bichet, V., Grisey, E., & Aleya, L. (2016). Spatial characterization of leachate plume using electrical resistivity tomography in a landfill composed of old and new cells (Belfort, France). *Engineering Geology*, 211, 61−73. https://doi.org/10.1016/j.enggeo.2016.06.026

Chrétien, M., Lataste, J. F., Fabre, R., & Denis, A. (2014). Electrical resistivity tomography to understand clay behavior during seasonal water content variations. *Engineering Geology*, 169, 112–123. http://doi.org/10.1016/j.enggeo.2013.11.019

Fallah-safari, M., Hafizi, M.-K., & Ghalandarzadeh, A. (2010). Correlation between electrical resistivity data and geotechnical data on a clay soil. *The 19th International Geophysical Congress and Exhibition of Turkey*. https://doi.org/10.13140/2.1.1050.3044

Feng, S.-J., Bai, Z.-B., Cao, B.-Y., Lu., S.-F., & Ai, S.-G. (2017). The use of electrical resistivity tomography and borehole to characterize leachate distribution in Laogang landfill, China. *Environmental Science and Pollution Research*, 24, 20811–20817. http://doi.org/10.1007/s11356-017-9853-0

Filho, A. M. S., Silva, C. L. B., Oliveira, M. A. A., Pires, T. G., Alves, A. J., Calixto, W. P., & Narciso, M. G. (2017). Geoelectric method applied in correlation between physical characteristics and electrical properties of the soil. *Transactions on Environment and Electrical Engineering*, 2(2), 37–44. http://dx.doi.org/10.22149/teee.v2i2.85

Genelle, F., Sirieix, C., Riss, J., & Naudet, V. (2012). Monitoring landfill cover by electrical resistivity tomography on an experimental site. *Engineering Geology*, 145–146, 18–29. http://doi.org/10.1016/j.enggeo.2012.06.002

Hu, J., Wu, X. W., Ke, H., Xu. X. B., Lan, J. W., & Zhan, L. T. (2019). Application of electrical resistivity tomography to monitor the dewatering of vertical and horizontal wells in municipal solid waste landfills. *Engineering Geology*, 254, 1–12. https://doi.org/10.1016/j.enggeo.2019.03.021

Huang, J. J., Wu, X., Jiang, S., Cui, L., Wei, Y., Zhang, L., & Lu, H. (2018). Geological impact and suitability evaluation of sponge city construction—a case study of Xuzhou. *Geological review*, 64(6), 1472−1480. https://doi.org/10.16509/j.georeview.2018.06.011

Jeřábek, J., Zumr, D., & Dostál, T. (2017). Identifying the plough pan position on cultivated soils by measurements of

electrical resistivity and penetration resistance. *Soil Tillage Res*, 174, 231–240. http://doi.org/10.1016/j.still.2017.07.008

Li, Y., Xu, L., Chen, J., Wang, Z., & Li, Z. (2022). Construction of hydrogeological structure model based on sponge city construction: A case study in the starting area of Changjiang New Town in Wuhan (in Chinese). *Resources Environment & Engineering*, 36(2), 198−203. http://doi.org/10.16536/j.cnki.issn.1671-1211.2022.02.010

Liu, M., Nie, Z.-L., Cao, L., Wang, L.-F., Lu, H.-X., & Wang, Z. (2021). Comprehensive evaluation on the ecological function of groundwater in the Shiyang river watershed. *Journal of Groundwater Science and Engineering*, 9(4), 326−340. http://doi.org/10.19637/j.cnki.2305-7068.2021.04.006

Liu, X., Chen, Y., Zhang, H., & Chang, J. (2025). An Evaluation of Sponge City Construction and a Zoning Construction Strategy from the Perspective of New Quality Productive Forces: A Case Study of Suzhou, China. *Land*, 14(4), 836. https://doi.org/10.3390/land14040836

Mathis, M. A. II., Tucker-Kulesza, S. E., & Sassenrath, G. F. (2018). Electrical Resistivity Tomography of Claypan Soils in Southeastern Kansas. *Kansas Agricultural Experiment Station Research Reports*, 4(3), 13. https://doi.org/10.4148/2378-5977.7574

Ningtyas, G. R., Priyantari, N., & Suprianto, A. (2020). Analisis data resistivitas dan uji permeabilitas tanah di daerah rawan longsor Desa Kemuning Lor Kecamatan Arjasa Kabupaten Jember. *Journal Online of Physics*, 6(1), 6−12. https://online-journal.unja.ac.id/jop/article/view/10181

Orozco, A. F., Steiner, M., Katona, T., Roser, N., Moser, C., Stumvoll, M. J., & Glade, T. (2022). Application of induced polarization imaging across different scales to understand surface and groundwater flow at the Hofermuehle landslide. *Catena*. 219, 106612. https://doi.org/10.1016/j.catena.2022.106612

Ohlmacher, G.C., (2000). The relationship between geology and landslide hazards of Atchison, Kansas, and Vicinity. *Current Research in Earth Science*, 244, 1–16. https://doi.org/10.17161/cres.v0i244.11833

Qiu, B. X. (2015). The connotation, way and prospect of Sponge City (LID). *Construction Science and Technology*, 41(3), 1−7. http://doi.org/10.16116/j.cnki.jskj.2015.01.003

Su, Y. J., Tang, H, Wu, A.-M., Dai, X.-P., Liu, S., Liu, H.-W., & Kuang, H. (2023). Geological suitability of natural sponge body for the construction of sponge city—a case study of Shuanghe Lake district in Zhengzhou airport zone. *Journal of Groundwater Science and Engineering*, 11(2), 146−157. https://doi.org/10.26599/JGSE.2023.9280013

Tagoe, R., Obiri-Nyarko, F., Okrah, C., Mainoo, P. A., Manu, E., Wemegah, D. D., Duah, A. A., Karikari, A. Y., & Agyekum, W. A. (2025). Investigating soil and groundwater contamination around the Kpone Engineered Landfill site, Ghana, using geoelectrical methods. *Acta Geophysica*, https://doi.org/10.1007/s11600-025-01668-5

Wahidah, W., Lepong, P., Alamsyah, A., Djayus, D., Supriyanto, S., Hermawan, Q. F., & Amir, A. (2024). Analysis and evaluation of stability for the reactivated road landslide using electrical resistivity and induced

polarization in Muara Badak district, East Kalimantan, Indonesia. *AIP Conference Proceedings*, 3095(1), 040002. https://doi.org/10.1063/5.0205097

Wang, S. W., Wang, X. Y., Sun, L., & Liu, C. (2019). A suitability evaluation system of sponge city construction based on environmental geological condition of urban sponge body and its application—a case study of Jiaozuo City (in Chinese). *Water Resources and Hydropower Engineering*, 50(2), 79−87. http://doi.org/10.13928/j.cnki.wrahe.2019.02.011

Ye, X. Y., Li, M. J., Du, X. Q., Fang, M., & Jia, S. (2018). Selection of suitable facility types of sponge city based on geological conditions. *Journal of Jilin University (Earth Science Edition)*, 48(3), 827−835. https://html.rhhz.net/JLDXXBDQKXB/html/2018-3-827.htm

ISSN: 2579-5821 (Print)
ISSN: 2579-5546 (Online)
URL address: http://journal.unhas.ac.id/index.php/geocelebes
DOI: 10.70561/geocelebes.v9i2.45784

Jurnal Geocelebes Vol. 9 No. 2, October 2025, 237 – 252

Facies Characteristics and Depositional Environment Reconstruction of the Minahaki Formation, "DM" Field, Banggai Basin

Ival Umar Sayaf[1]*, Vijaya Isnaniawardhani[1], Budi Muljana[1], Wingky Suganda[2]

[1]Geological Engineering, Universitas Padjadjaran, Sumedang 45363, Indonesia.
[2]Pertamina EP, Jakarta 12950, Indonesia.

*Corresponding author. Email: ival21001@mail.unpad.ac.id

Manuscript received: 22 July 2025; Received in revised form: 24 October 2025; Accepted: 30 October 2025

Abstract

The Miocene Minahaki Formation in the Banggai Basin represented a key hydrocarbon reservoir, but its pronounced heterogeneity posed a challenge for field development. This study aimed to characterize the formation's carbonate facies and reconstruct its depositional environment in the "DM" field to establish a predictive model for reservoir distribution. The research employed an integrated subsurface analysis of core, cuttings, and wireline log data from seven wells. Four principal lithofacies (Bioclastic Coralline Floatstone, Dolomitic Algae Bioclastic Packstone, Argillaceous Dolomitic Foraminifers Bioclastic Wackestone, and Bioclastic Wackestone) were identified and subsequently grouped into two distinct facies associations: a high-energy Reef Margin Complex (FA-1) and a lower-energy Fore-Reef Slope (FA-2). Spatial correlation of these associations revealed a clear proximal-to-distal environmental gradient from west to east. The depositional architecture of the Minahaki Formation in the study area was interpreted as a rimmed carbonate platform. This model accounts for the observed reservoir heterogeneity, concluding that higher-quality reservoir bodies, characterized by moldic, vuggy, and intercrystalline porosity, are concentrated within the single reefal buildup that defines the western margin of the field. This finding provides a direct, geology-based predictive tool for optimizing future drilling activities and serves as a useful analogue for similar carbonate systems elsewhere.

Keywords: Banggai-Sula; carbonate platform; depositional environment; facies analysis; Miocene carbonate reservoir.

Citation: Sayaf, I.U., Isnaniawardhani, V., Muljana, B., & Suganda, W. (2025). Facies Characteristics and Depositional Environment Reconstruction of the Minahaki Formation, "DM" Field, Banggai Basin. *Jurnal Geocelebes*, 9(2): 237–252, doi: 10.70561/geocelebes.v9i2.45784

Introduction

The Banggai Basin, located in the eastern arm of Sulawesi, is an established Indonesian hydrocarbon province hosting major gas and oil fields, such as the Senoro Field with estimated reserves of 362 MMBOE, within its Miocene carbonate successions (Satyana & Zaitun, 2016; Surjono et al., 2019). The primary reservoirs within the Salodik Group are characterized by high productivity but also significant heterogeneity, which presents a persistent challenge for exploration and field development (Haris et al., 2017; Hasanusi et al., 2012; Khairi et al., 2022; Ontosari et al., 2023). This reservoir variability, which manifests as rapid spatial changes in porosity and permeability, is fundamentally controlled by the distribution of primary depositional facies and their subsequent diagenetic alterations (Angkasa et al., 2024; Laya et al., 2022; Syah et al., 2019). Similar challenges in Miocene carbonate buildups across Southeast Asia, for instance in the Central Luconia province, offshore Malaysia, also highlight that the interplay between depositional facies and diagenesis represents a primary control on reservoir quality (Henglai et al., 2025). Therefore, a detailed understanding of depositional architecture is critical for predicting

reservoir quality and geometry, an objective best achieved through an integrated facies analysis that combines petrographic data from cores and cuttings with wireline log responses (Laya et al., 2022; Rahadian et al., 2018).

Extensive research has established a comprehensive regional framework for the Banggai Basin. The tectonic evolution, primarily controlled by the westward drift of the Banggai-Sula microcontinent and its subsequent Mio-Pliocene collision with the East Sulawesi Ophiolite Belt, is well-documented as the primary mechanism for basin formation and trap development (Nugraha & Hall, 2018; Serhalawan & Chen, 2024). Geochemical studies have identified the Early to Middle Miocene Tomori and Matindok formations as the primary source rocks for the basin's hydrocarbons (Satyana & Zaitun, 2016).

At the reservoir scale, numerous studies have characterized the Miocene carbonate plays. In the analogous Senoro Field, for instance, facies range from high-energy reefal buildups to lower-energy platform carbonates (Hasanusi et al., 2012; Rahadian et al., 2018). This distinction is highly analogous to the stratigraphy in the study area, where the high-energy reefal facies is typically developed as the distinct Mantawa Member, often overlying or interfingering with the generally finer-grained, muddier platform carbonates of the Minahaki Formation proper (Laya et al., 2022; Rahadian et al., 2018). Detailed facies analysis has distinguished specific environmental settings such as reef margins, fore-reefs, and back-reef lagoons (Muhammad et al., 2020; Pratama et al., 2020). This work, supported by sequence stratigraphy and detailed biostratigraphy, has led to varying interpretations of the overall platform geometry, including both rimmed platforms and, more recently, a carbonate ramp model for the fine-grained Minahaki Formation (Herdiansyah et al., 2022; Laya et al., 2022). The ramp interpretation is primarily supported by the widespread fine-grained nature of the formation and seismic geometries showing low-angle progradation without a distinct shelf-edge break (Laya et al., 2022). In contrast, rimmed platform models are argued based on lithofacies evidence for a distinct, high-energy reef margin creating a significant topographic break, a condition observed in analogous buildups within the basin (Rahadian et al., 2018).

Despite this comprehensive regional understanding, a detailed, facies-based depositional reconstruction specifically for the Minahaki Formation in the “DM” field remains a gap in the published literature. Regional models, while providing excellent context, often lack the granular resolution required for accurate field-scale prediction. This lack of resolution translates directly into higher exploration and development risk, as the precise location of high-quality reservoir bodies, such as porous reef margins, versus lower-quality, muddier facies remains unpredictable. What has escaped detailed attention is a well-calibrated, multi-well reconstruction that validates and refines these regional models at a local scale, particularly explaining the observed west-to-east facies transition within the "DM" field.

To address this gap, this study aims to characterize the lithofacies of the Minahaki Formation in the "DM" field and reconstruct their depositional environments through an integrated analysis of core, cuttings, and wireline log data. This integrated approach is essential because it allows the direct rock observations from limited core intervals to be used to calibrate the continuous wireline log data, enabling a reliable extrapolation of facies interpretations across all wells in the field. This approach allows for the creation of a spatially coherent geological narrative to explain observed reservoir heterogeneity. The goal is to develop a robust depositional reconstruction that serves as a predictive

framework for understanding reservoir distribution. Ultimately, this research provides not only a field-scale refinement to the regional depositional model of the Minahaki Formation but also delivers a direct, geology-based predictive tool for optimizing future hydrocarbon exploration and development in the Banggai Basin.

Materials and Methods

Geological Setting

The “DM” field is situated within the Banggai Basin, a foreland basin located on the eastern arm of Sulawesi, Indonesia (Figure 1). The basin's architecture and stratigraphy are direct products of a complex Cenozoic tectonic history dominated by the interaction between the Eurasian, Indo-Australian, and Pacific plates, which involves multiple subducting slabs (e.g., Sula Spur, Halmahera, and Celebes Sea Slabs) beneath the island (Greenfield et al., 2021; Hall, 2019; Kesumastuti et al., 2025; Serhalawan & Chen, 2024; Wibowo et al., 2025). The basin itself formed atop the Banggai-Sula microcontinent, a continental fragment that rifted from the northern margin of Gondwana (present-day Australia) during the Late Jurassic (Advokaat & van Hinsbergen, 2024; Garrard et al., 1988; Hall, 2012; Satyana & Zaitun, 2016). This microcontinent drifted westwards before its eventual collision with the East Sulawesi ophiolite belt, a major tectonic event that occurred from the Early Miocene to Early Pliocene (Nugraha & Hall, 2018; Patria et al., 2023).

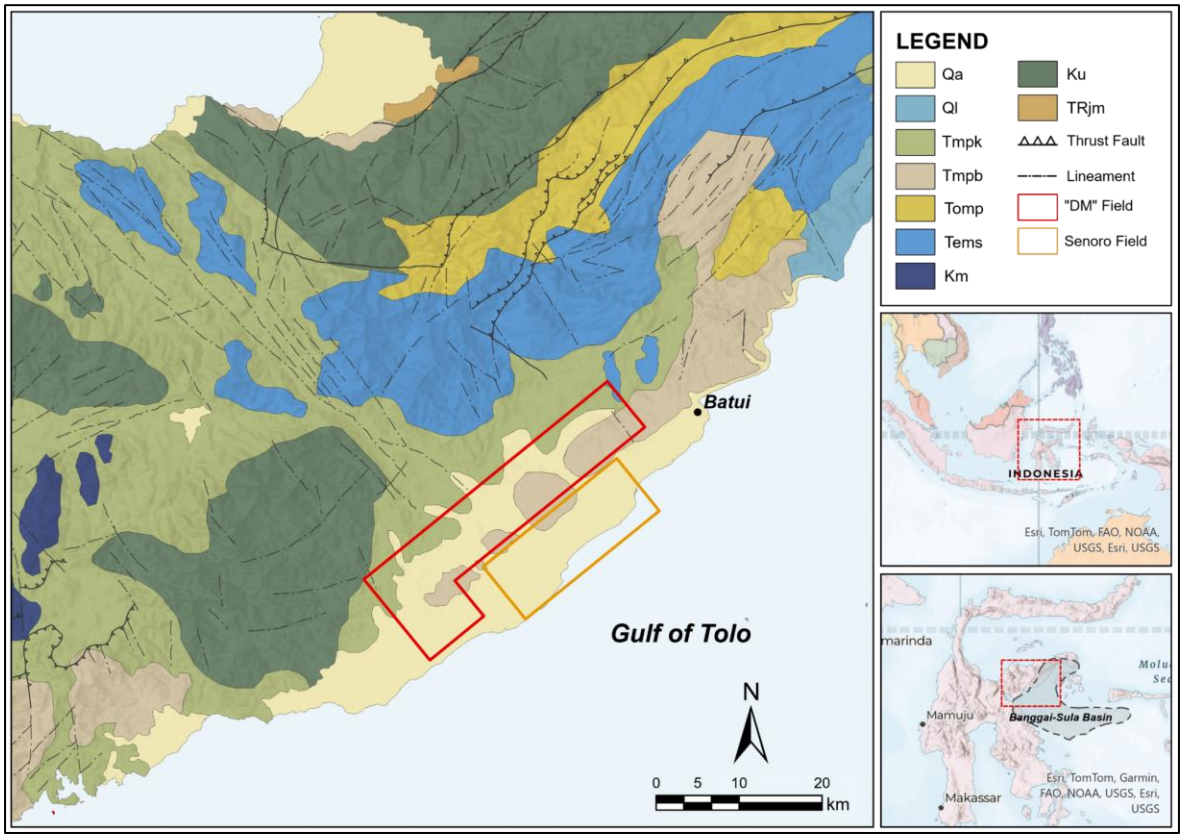

Figure 1. Regional geological map of the eastern arm of Sulawesi showing the location of the "DM" Field (this study) and the analogous Senoro Field. Inset maps illustrate the regional context and the outline of the Banggai Basin. (Geological map modified from the Geological Agency of Indonesia (Badan Geologi, ESDM); inset base maps from Esri and contributing partners).

This tectonic evolution resulted in a distinct tectonostratigraphy that governs the petroleum system of the region (Figure 2). Prior to the main collisional event, which

initiated in the Early Miocene, a period of relative tectonic quiescence during the Miocene allowed for the widespread development of a shallow-marine carbonate system known as the Salodik Group (Titu-Eki & Hall, 2020). This group comprises three main successions: the Lower Miocene Tomori Formation, the Middle Miocene Matindok Formation, and the Upper Miocene Minahaki Formation (Jambak et al., 2024). The Minahaki Formation, the focus of this study, is a key carbonate unit within this group, characterized by extensive platform development (Laya et al., 2022; Nugraha & Hall, 2022). Recent high-resolution biostratigraphic studies using nannoplankton have constrained the age of the Minahaki Formation to the Middle to Late Miocene (Nurhidayah et al., 2024). The subsequent collision terminated this carbonate production phase and initiated a compressional regime, creating complex fold-and-thrust structures that now serve as the primary hydrocarbon traps (Titu-Eki & Hall, 2020). This compression was followed by rapid subsidence and the deposition of thick Pliocene-Pleistocene syn-orogenic sediments of the Sulawesi Group, often referred to as the Celebes Molasse, which provide both the regional seal and the necessary overburden for the maturation of Miocene source rocks (Nugraha et al., 2022; Satyana & Zaitun, 2016).

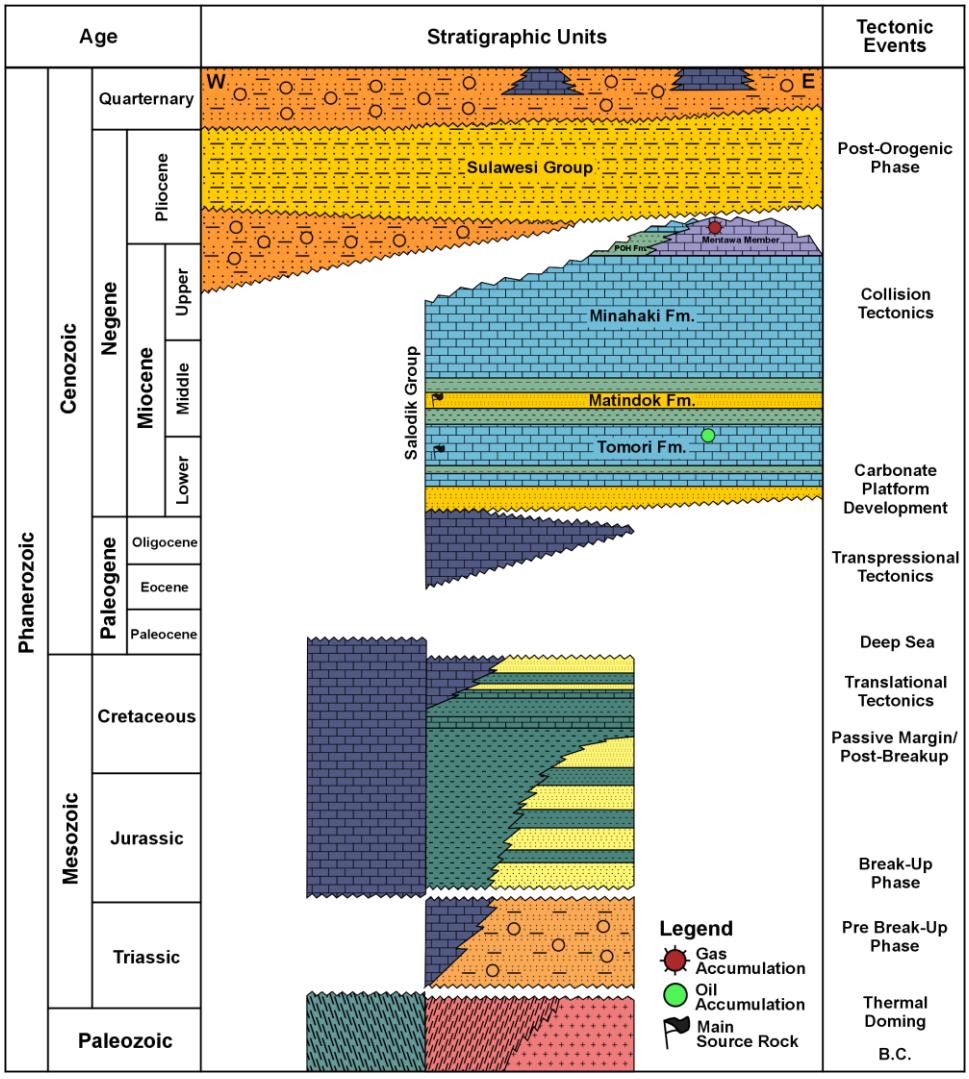

Figure 2. Generalized tectonostratigraphic column of the Banggai Basin, showing the Miocene Salodik Group as the primary carbonate succession (Compiled and modified from Advokaat & van Hinsbergen, 2024).

Data and Methods

The analytical workflow was conducted in three sequential stages using an integrated subsurface dataset from seven wells in the "DM" field (IUS-1 to IUS-7). The primary analysis was based on a 10-meter conventional core interval (2075.08–2084.20 m MD) from well IUS-1, which included visual core description, petrographic analysis of 11 thin sections, and supporting mineralogical and textural analysis using Scanning Electron Microscopy with Energy Dispersive X-ray Spectroscopy (SEM-EDX) and X-Ray Diffraction (XRD). Carbonate rock classification followed the depositional texture framework of Dunham (1962), as modified by Embry & Klovan (1971). This framework was specifically chosen because it classifies rocks based on depositional texture, which directly reflects the energy conditions of the depositional environment. The Embry & Klovan (1971) modification is essential for this study to accurately classify coarse-grained and framework-supported reefal carbonates (Flügel, 2010). Subsequently, the identified lithofacies were grouped into genetically related facies associations, which then formed the basis for a field-wide spatial framework constructed through well-to-well correlation using AspenTech Geolog™ 14.2 software. The primary correlation datum was picked at the top of the Fore-Reef Slope (FA-2), a key lithofacies surface consistently identified across all wells.

To extrapolate these findings, electrofacies were identified from Gamma Ray (GR) log patterns and calibrated against the core- and cuttings-derived lithofacies. This calibration is a proven method that enabled the robust interpretation and mapping of facies belts across the entire study area (Khazaie et al., 2022). Finally, the resulting spatial distribution of facies associations was used to reconstruct the paleo-depositional environments. Based on the initial identification of high-energy, reef-derived facies in the core data, the classic rimmed carbonate platform model of Wilson was chosen as the primary analog framework, as it accounts for a distinct, high-energy margin, which is a feature not present in alternative models such as a carbonate ramp (as modified and presented in Flügel, 2010).

Results and Discussion

Carbonate Lithofacies

Four distinct lithofacies were identified within the Minahaki Formation in the study area (Figure 3). These are distinguished by their texture, grain composition, and diagenetic features.

Bioclastic Coralline Floatstone (BCF)

Observed in 4 of the 11 thin sections analyzed, this facies is characterized by a mud-supported texture containing a significant volume of large, visibly abraded coral fragments (ranging from 8% to 18%). Fragment size, measured petrographically, ranges up to 7.5 cm. These fragments appeared to float within a fine-grained carbonate mud matrix (13–17%). Other bioclasts form a diverse accessory assemblage, including various types of foraminifera, red and green algae, echinoderms, and mollusks (Figure 3a). The total visual porosity for this facies is moderate, ranging from 10.5% to 14.0%, and is predominantly composed of fabric-selective moldic porosity (3–9%), including honeycomb textures from dissolved coral frameworks, and non-fabric selective vuggy porosity (3.5–4%), with minor contributions from microfracture, intercrystalline, and pint-point pores. The textural characteristics, particularly the poor sorting, the chaotic orientation of fragments, and the mixture of coarse skeletal debris in a fine matrix, were indicative of deposition by high-energy, short-duration events such as debris flows (Flügel, 2010). This lithofacies corresponds well with Standard Microfacies Type 5 (SMF 5), which represents allochthonous

bioclastic floatstones containing reef-derived biota deposited on slopes (Flügel, 2010). The occurrence of such deposits is consistent with observations in analogous Miocene buildups within the Banggai Basin, where facies comprising coral-algal fragments are developed adjacent to reefal buildups in the Senoro Field (Rahadian et al., 2018) and are considered part of the fore-reef slope system (Muhammad et al., 2020). This facies generally exhibits good reservoir quality, with routine core analysis measuring porosity values of 18–29% and horizontal permeabilities ranging from 4 to 63 mD.

Dolomitic Algae Bioclastic Packstone (DABP)

Observed in one of the 11 thin sections analyzed, this facies is characterized by a grain-supported texture with a low mud matrix content (approximately 10%). Its dominant allochems are reef-derived algal fragments (>10%), accompanied by coral debris and a diverse assemblage of other bioclasts (Figure 3b). The facies has undergone significant dolomitization, estimated at ~13% based on petrographic point counting, which imparted a sucrosic texture. The total visual porosity is approximately 13.5%, comprising a mix of vuggy (5%), moldic (4.5%), and intercrystalline (2%) pores. The grain-supported fabric, combined with the presence of coarse reef-derived bioclasts, is indicative of deposition from high-concentration sediment gravity flows originating from a nearby carbonate factory, likely on a proximal slope setting (Flügel, 2010; Hasanusi et al., 2012; Pratama et al., 2020). This lithofacies corresponds well with SMF 5, which represents allochthonous bioclastic packstones or grainstones deposited on a proximal slope setting (Flügel, 2010). This interpretation is consistent with the description of similar reef-associated facies in the analogous Senoro Field, where they are described as having excellent reservoir quality (Rahadian et al., 2018). This claim is substantiated by routine core analysis data from this facies, which measured a porosity of 24.5% and a permeability of 52 mD.

Argillaceous Dolomitic Foraminifers Bioclastic Wackestone (ADFW)

Observed in 2 of the 11 thin sections analyzed, this facies is characterized by a mud-supported wackestone texture with an abundant matrix (26%) that is notably argillaceous. The presence of detrital clay was identified petrographically and later quantified at 3–4% by XRD analysis. The grain assemblage is dominated by foraminifera (>10%), comprising a mix of planktonic, small benthic, and large benthic forms (Figure 3c). Notably, the abundance of planktonic forms is 1.5 to 3 times greater than that of large benthic foraminifera. This high ratio indicates a setting distal from the shallow-water environments where large benthic foraminifera typically thrive (Flügel, 2010; Pratama et al., 2020). The fine-grained, mud-dominated texture, combined with suspended clays and the significant presence of planktonic foraminifera, indicated deposition from suspension in a low-energy, open marine setting. This interpretation aligns with Standard Microfacies Type 3 (SMF 3), which represents a pelagic wackestone with planktonic microfossils characteristic of basinal and deep shelf environments below the storm wave base (Flügel, 2010). This finding is consistent with regional descriptions of the wider Minahaki Formation as a "foraminifera-rich wackestone with an argillaceous matrix" (Laya et al., 2022), however, this study further specifies that the high ratio of planktonic to large benthic foraminifera is a key indicator of a direct connection to the open sea. This facies exhibits moderate reservoir quality, with routine core analysis measuring porosity values of 18–22% and permeabilities ranging from 3 to 7 mD.

Bioclastic Wackestone (BW)

Observed in 4 of the 11 thin sections analyzed, this facies is characterized by a mud-supported wackestone texture with a variable matrix content (6–20%). Its constituent grains are composed of highly abraded, undifferentiated bioclasts, foraminifera, and fine coral debris (Figure 3d). The combination of highly abraded grains within a mud-supported fabric suggests deposition via textural inversion, a process involving the transport of reworked material from a higher-energy zone into a low-energy depositional setting, typically by storms or sediment gravity flows (Flügel, 2010). This lithofacies corresponds well with Standard Microfacies Type 10 (SMF 10), which describes bioclastic wackestones with worn skeletal grains characteristic of toe-of-slope or deeper shelf environments (Flügel, 2010). The occurrence of such reworked wackestones is consistent with the broader understanding of the Minahaki platform carbonates (Hasanusi et al., 2012; Rahadian et al., 2018). This facies exhibits variable reservoir quality, with routine core analysis measuring porosity values of 16–29% and permeabilities ranging from 5 to 27 mD.

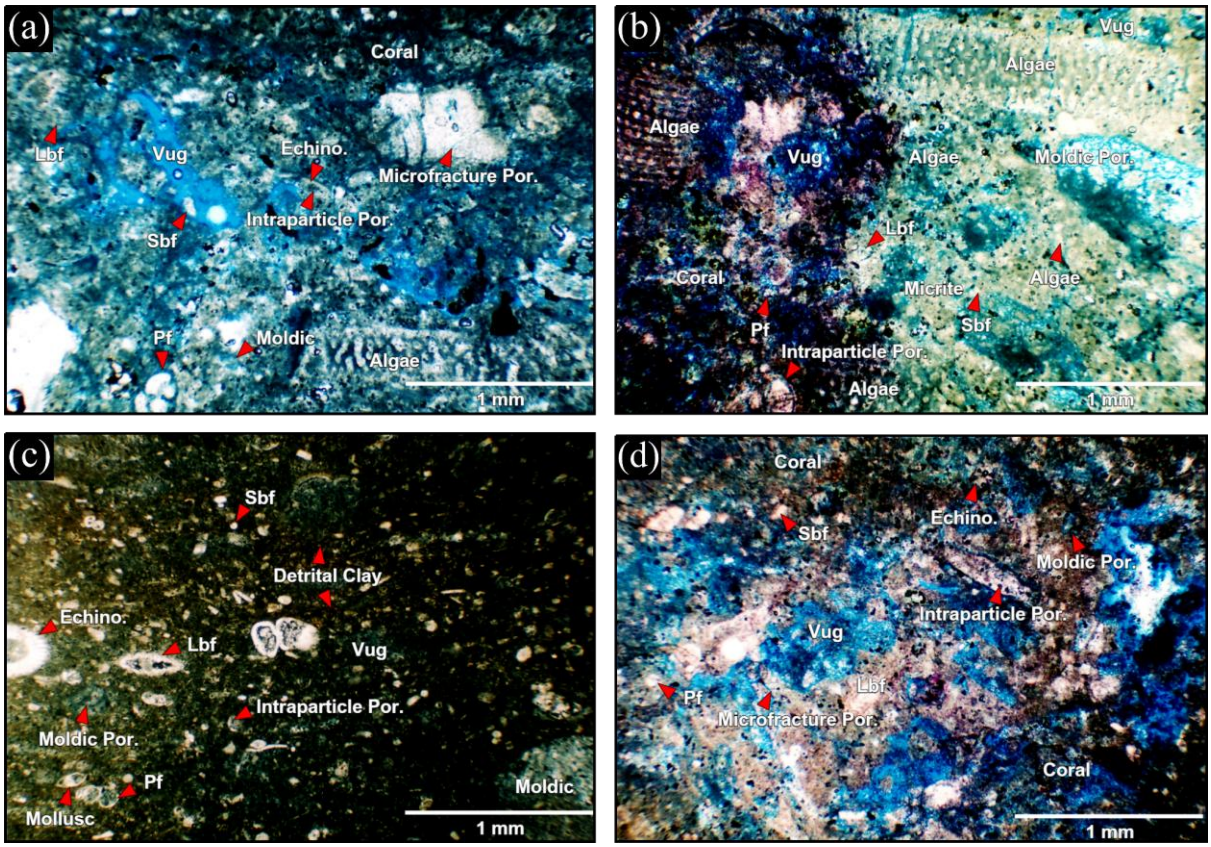

Figure 3. Photomicrographs of the four identified lithofacies from the Minahaki Formation in well IUS-1 (plane-polarized light). Samples were stained with Alizarin Red S to differentiate calcite and impregnated with blue-dyed epoxy to highlight porosity. (a) Bioclastic Coralline Floatstone (BCF). (b) Dolomitic Algae Bioclastic Packstone (DABP). (c) Argillaceous Dolomitic Foraminifers Bioclastic Wackestone (ADFW). (d) Bioclastic Wackestone (BW). Abbreviations are as follows: Lbf = Large Benthic Foraminifera; Sbf = Small Benthic Foraminifera; Pf = Planktonic Foraminifera; Echino = Echinoderm fragment; Vug = Vuggy Porosity.

Facies Associations and Depositional Environment

The four lithofacies are grouped into two associations (Figure 4), each representing a specific depositional environment within a carbonate platform system.

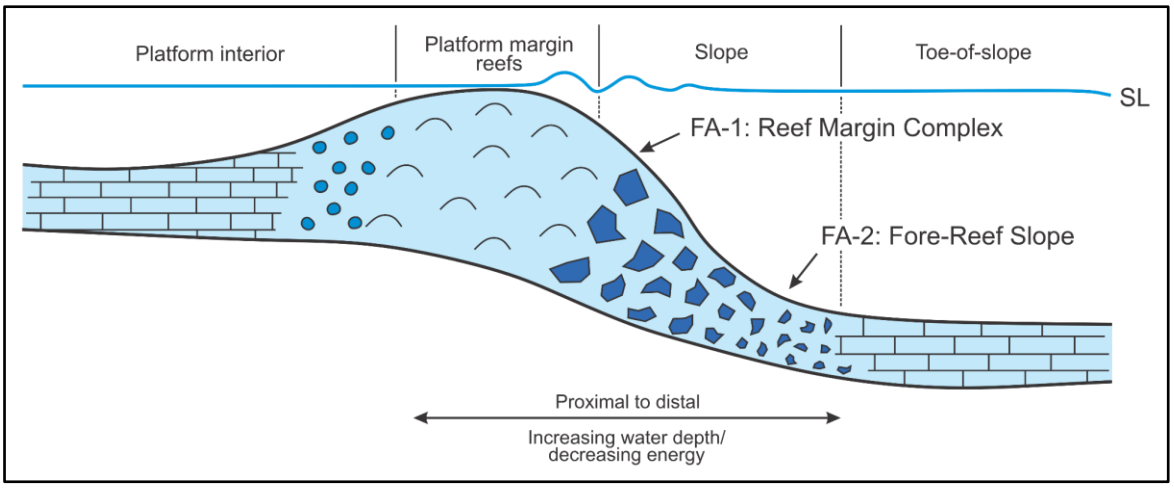

Figure 4. Schematic diagram showing the interpreted proximal position of Facies Association 1 (FA-1: Reef Margin Complex) near the platform margin (FZ 5) and upper slope, transitioning distally to Facies Association 2 (FA-2: Fore-Reef Slope) on the main slope (FZ 4) of a standard carbonate platform profile. (Model modified from the original of Wilson, as presented in Flügel, 2010).

- Facies Association 1 (FA-1): Reef Margin Complex

This association, comprising the Dolomitic Algae Bioclastic Packstone (DABP) and Bioclastic Coralline Floatstone (BCF) lithofacies, was interpreted as the high-energy reef margin complex that formed the pronounced outer edge of the platform. This interpretation is strongly supported by its characteristic low GR response, typically displaying a cylindrical (blocky) pattern with internal serrations (mean GR of ~39.4 ± 6.8 API, ranging from ~30 to 52 API based on 5-95 percentiles) (Figure 5). This low GR signature is consistent with the clean nature of carbonate debris accumulation, indicating minimal clay content. The DABP lithofacies and BCF lithofacies collectively represent the proximal fore-reef slope (talus) environment, with DABP likely forming coarser, more grain-supported accumulations closer to the reef crest. This environmental setting corresponds to the platform margin (FZ 5; Figure 8), typically found in shallow water depths of a few meters (e.g., 0-10 m), and the adjacent upper slope (FZ 4), which extends seaward below the margin (Flügel, 2010).

This interpretation of a distinct, high-energy reef margin complex is in strong agreement with several studies of the Miocene carbonates in the Banggai Basin. Rahadian et al. (2018) described a comparable "reefal build-up facies" in the Senoro field, characterized by grainstones and floatstones with abundant coral growth, which they distinguished from a separate, muddier platform facies. Similarly, Hasanusi et al. (2012) identified a "pinnacle reef build up type" as a key reservoir unit in the same area. The interpretation of the debris component (BCF) as a fore-reef talus deposit also aligns with the findings of Muhammad et al. (2020), who identified a distinct fore-reef system in their study of the Banggai Basin carbonates.

- Facies Association 2 (FA-2): Fore-Reef Slope

This association, consisting of the ADFW and BW lithofacies, was interpreted as the lower-energy, deeper-water fore-reef slope environment (corresponding to FZ 4), situated seaward of the reef margin complex (Figure 4). This association is characterized by a higher and more variable GR response compared to FA-1, typically exhibiting a bell-shaped log pattern (mean GR of ~49.8 ± 10.6 API, ranging from ~35 to 69 API based on 5-95 percentiles) (Figure 5). This higher GR signature reflects the greater proportion of carbonate

mud and argillaceous material consistent with a lower-energy, more distal setting. The combination of these two mud-supported lithofacies represents a transition within the slope: the BW lithofacies, with its highly abraded bioclasts, suggests deposition on a middle slope environment receiving reworked skeletal debris, while the ADFW lithofacies indicates a more distal, lower-slope setting influenced by open-marine conditions. This distinction is supported by foraminiferal assemblages: the ADFW facies shows a significantly higher ratio of planktonic to large benthic foraminifera (1.5:1 to 3:1) compared to the BW facies (0.5:1 to 1.5:1), indicating increasing open-marine influence downslope. According to Flügel (2010), the slope environment (FZ 4) typically extends below the platform margin (FZ 5) and is characteristically composed of reworked platform material mixed with fine-grained pelagic components, consistent with the lithologies observed in this association.

The interpretation of this association as a fore-reef slope environment is also well-supported by regional analogues. Pratama et al. (2020) specifically documented a slope environment in the Senoro Field that included "planktonic foraminifera wackestone and packstone", providing a direct lithological match for the ADFW facies. Furthermore, the overall muddy character of this association is consistent with the lower energy "platform facies" described by Rahadian et al. (2018) as being distinct from the high-energy reefal buildup in the Senoro Field.

- Depositional Model Synthesis

The spatial distribution of the previously defined facies associations was mapped through well-to-well correlation, integrating the petrographic data with calibrated electrofacies patterns from GR logs. The analysis revealed a predictable relationship between the facies associations and their log responses. Facies Association 1 (Reef Margin Complex) consistently showed a low GR response with a cylindrical (blocky) to serrated log pattern, characteristic of relatively clean, thick-bedded carbonate debris. In contrast, Facies Association 2 (Fore-Reef Slope) exhibited a higher and more variable GR response with a bell-shaped pattern, reflecting its greater content of carbonate mud and argillaceous material (Tiab & Donaldson, 2024).

The well-correlation cross-sections revealed a distinct and predictable depositional gradient across the “DM” field (Figure 5). The dip-oriented section (Figure 5a) illustrates a clear west-to-east transition: thick packages of the Reef Margin Complex (FA-1) with minor intercalations of FA-2 dominate the western wells, thinning eastward where they increasingly interfinger with and are ultimately replaced by the Fore-Reef Slope (FA-2) as the predominant facies association. The strike-oriented sections (Figure 5b; Figure 5c) confirm the lateral continuity of these depositional belts along the platform margin. The field's overall structure is presented in Figure 6. The interpreted spatial distribution of these facies associations across the structure is summarized in Figure 7, illustrating FA-1 forming the core of the structural high, transitioning eastward into FA-2.

This documented spatial relationship provides strong evidence for a rimmed carbonate platform architecture (Figure 8), consistent with the classic depositional model originally proposed by Wilson (as described in Flügel, 2010). Based on regional context and previous studies suggesting isolated platform growth in the area (e.g., Muhammad et al., 2020), this rimmed platform is interpreted as an unattached (isolated) build-up. This interpretation differs from the carbonate ramp model that has been proposed for the Minahaki Formation in other parts of the Banggai Basin (e.g., Laya et al., 2022). A ramp model is defined by a gently sloping

profile lacking a distinct high-energy shelf-edge barrier. However, the data from the "DM" field, specifically the presence of a well-defined, high-energy Reef Margin Complex (FA-1) and its associated coarse talus deposits (BCF lithofacies), clearly indicates a significant topographic break, or shelf-margin break. This feature is the primary diagnostic criterion for a rimmed platform and is not characteristic of a ramp profile (Flügel, 2010). Therefore, while a ramp architecture may exist elsewhere, the depositional system in the "DM" field is more accurately represented by a rimmed platform model.

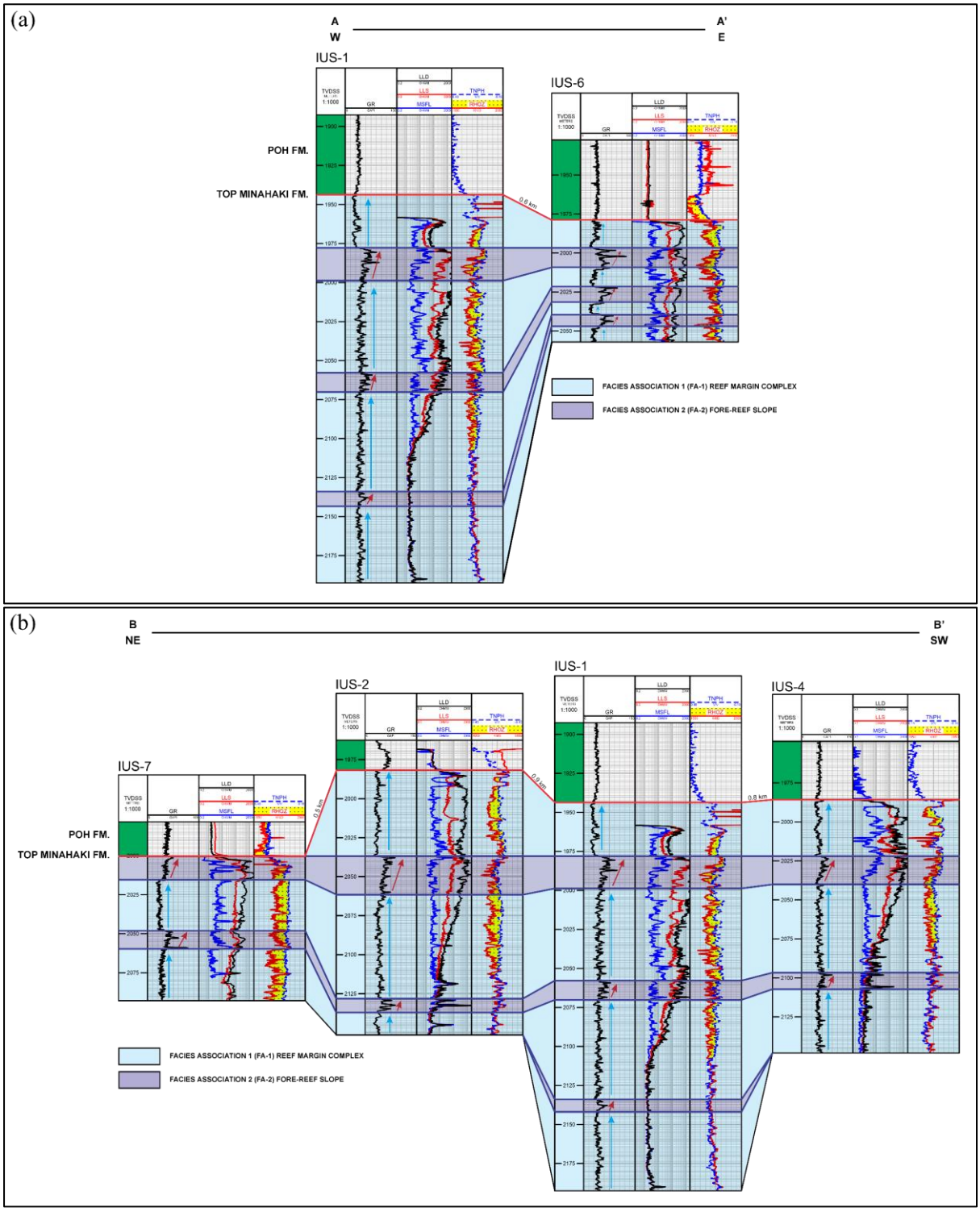

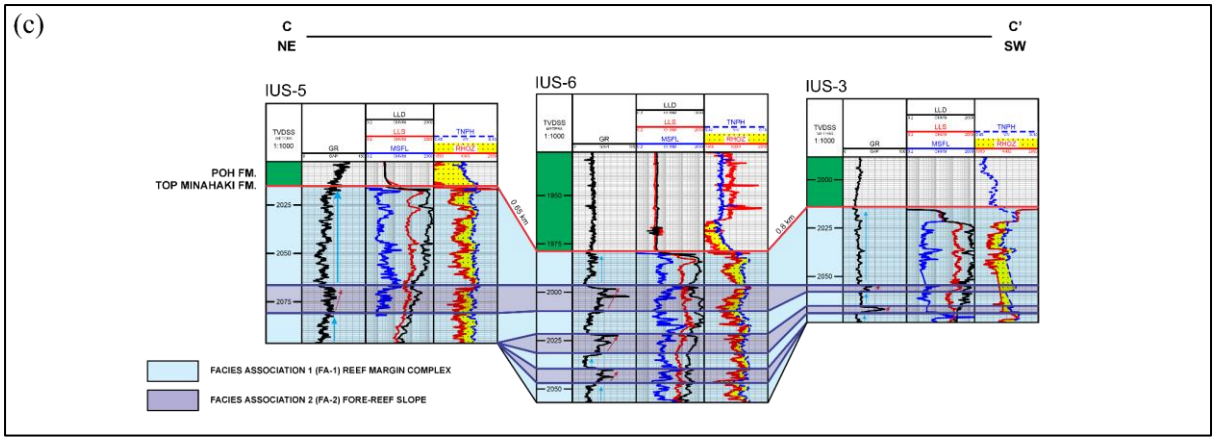

Figure 5. Well-to-Well Correlation Cross-Sections of the Minahaki Formation. The panels illustrate the spatial distribution of the primary facies associations across the "DM" field. The primary correlation datum corresponds to the top of the Fore-Reef Slope (FA-2) to visually emphasize the depositional relief of the reefal buildup. The legend defines the Reef Margin Complex (FA-1) and the Fore-Reef Slope (FA-2). Log trends are indicated by arrows on the Gamma Ray (GR) track. See Figure 6 for section locations. Vertical scale is indicated on well logs; horizontal distances between wells are shown numerically.

(a) Dip-oriented Section A-A' (W-E) illustrating the eastward transition from thick FA-1 successions with minor FA-2 intercalations in the west to thinner, interfingering FA-1 layers within the increasingly predominant FA-2 toward the east.
(b) Strike-oriented Section B-B' (NE-SW) illustrating the lateral continuity and correlation of both FA-1 and FA-2 in the western part of the field.
(c) Strike-oriented Section C-C' (NE-SW) illustrating the lateral continuity and correlation of both FA-1 and FA-2 in the eastern part of the field.

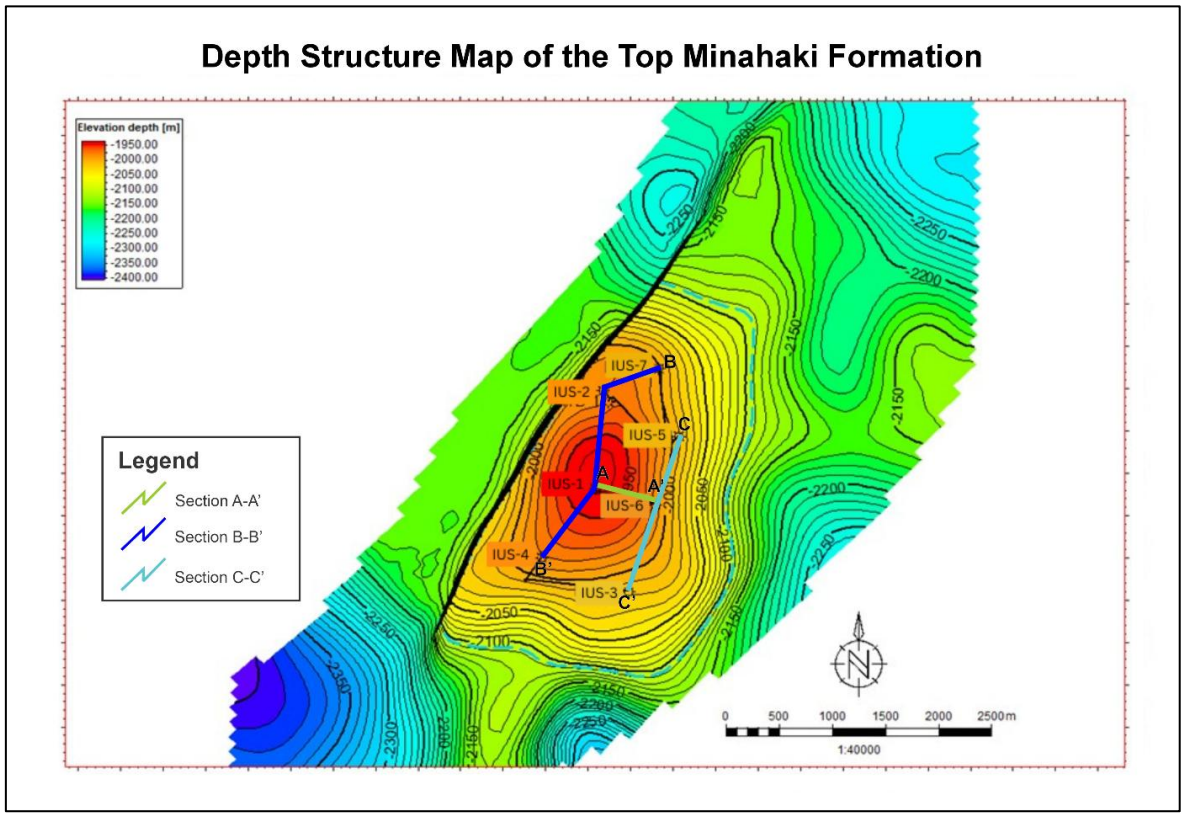

Figure 6. Depth Structure Map of the Top Minahaki Formation in the "DM" field showing well locations (IUS-1 to IUS-7) and structural contours (in meters subsea). This map serves as the base for the facies distribution interpretation in Figure 7.

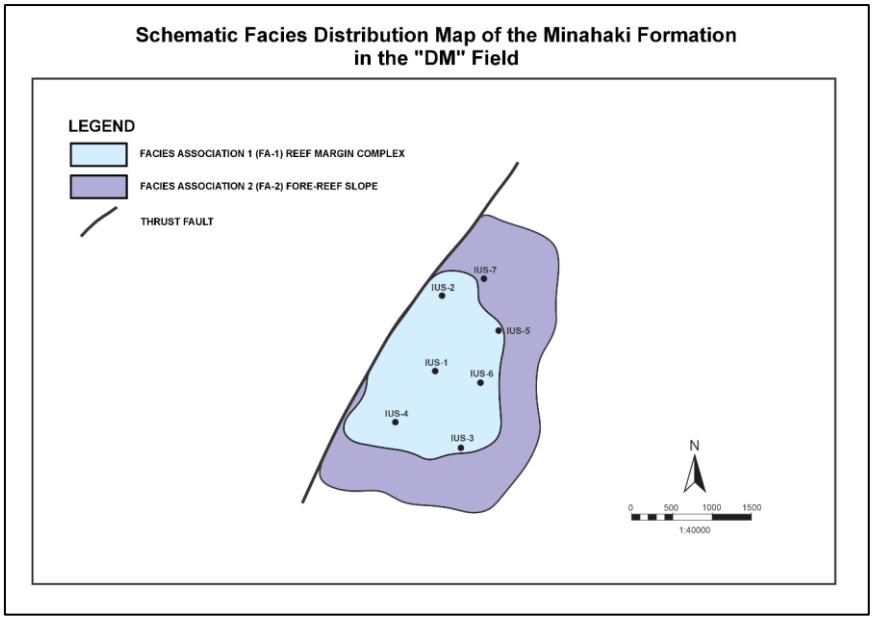

Figure 7. Schematic Facies Distribution Map of the Minahaki Formation in the "DM" Field, overlaid on the Top Minahaki depth-structure contours (from Figure 6). The map illustrates the interpreted distribution of Facies Association 1 (FA-1: Reef Margin Complex, blue) predominantly on the structural crest, transitioning to Facies Association 2 (FA-2: Fore-Reef Slope, purple) on the flanks and distal areas.

Despite the robust interpretation of a rimmed carbonate platform, it is important to acknowledge the inherent limitations of the well-based dataset in constraining the full extent of the depositional system. The stratigraphic penetrations in the "DM" field are predominantly concentrated within the platform margin (FA-1) and fore-reef slope (FA-2) environments. As a result, facies associated with the shallower platform interior (e.g., lagoonal or back-reef settings) were not intersected in the studied wells. This restricts direct observations of the depositional system to its outermost portions, thereby limiting a comprehensive characterization of the platform's areal extent and internal proximal facies variability.

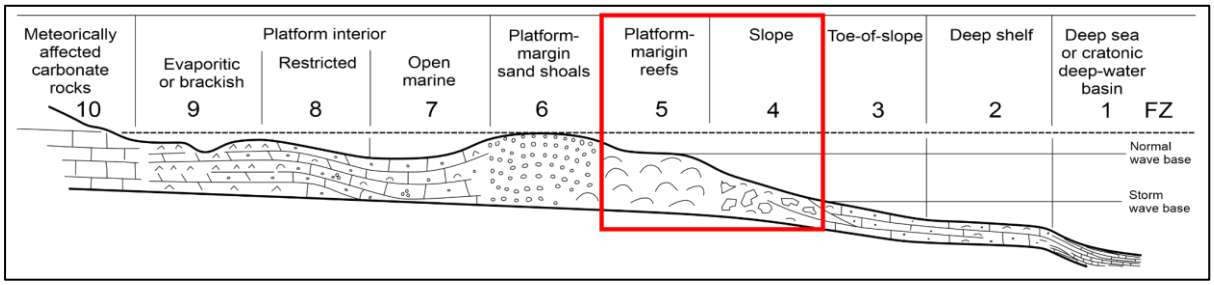

Figure 8. Conceptual depositional model of a rimmed carbonate platform, illustrating the distribution of standard facies zones (FZ). The model shows the typical environmental belts from the shallow platform interior to the deep basin. The facies associations identified in this study correspond directly to this profile: the Reef Margin Complex (FA-1) represents the platform margin (FZ 5), while the Fore-Reef Slope (FA-2) represents the adjacent slope environment (FZ 4). The red box highlights these key environments that define the depositional system in the "DM" field. (Model modified from the original of Wilson, as presented in Flügel, 2010).

This depositional model directly explains the observed reservoir heterogeneity across the field. The highest-quality reservoir properties are predicted to be concentrated within the Reef Margin Complex (FA-1) in the western part of the field (average porosity ≈ 24%, average permeability ≈ 33 mD). In contrast, the muddier, fine-grained lithologies of the Fore-Reef Slope (FA-2) exhibit lower overall permeability (average porosity ≈ 20%, average permeability ≈ 11 mD).

Conclusion

This study characterized the carbonate facies of the Miocene Minahaki Formation in the "DM" field and reconstructed its depositional architecture. Four main lithofacies were identified (DABP, BCF, ADFW, BW) and grouped into two distinct associations: a high-energy Reef Margin Complex (FA-1) and a lower-energy, deeper-water Fore-Reef Slope (FA-2). The spatial correlation of these associations revealed a clear proximal-to-distal environmental gradient from west to east. The depositional architecture of the Minahaki Formation in the study area was interpreted as a rimmed carbonate platform, supported by the observed high-energy, blocky GR responses of FA-1 at the structural high, transitioning to bell-shaped GR responses of FA-2 on the flanks. This model explained the observed reservoir heterogeneity, concluding that higher-quality reservoir bodies are concentrated within the single reefal buildup in the western part of the field, which is composed of the coarse-grained Reef Margin Complex (FA-1) (average porosity ≈ 24%, average permeability ≈ 33 mD). In contrast, the muddier, fine-grained Fore-Reef Slope (FA-2) exhibits lower reservoir quality (average porosity ≈ 20%, average permeability ≈ 11 mD). This finding provides a direct, geology-based predictive tool for optimizing future drilling activities within the "DM" field and offers valuable insights for exploration and development of similar carbonate plays in the Banggai Basin and broader Southeast Asian region. This research highlights the value of integrated facies analysis in building predictive depositional models for complex carbonate reservoirs and provides a specific, field-scale refinement to the regional understanding of the Banggai Basin.

Acknowledgements

The authors would like to thank Pertamina EP Cepu for providing the data and permission to publish this research, which was conducted as part of a final-year project internship. Gratitude is also extended to the faculty and staff at the Department of Geological Engineering, Universitas Padjadjaran, for their guidance and support.

Author Contribution

Ival Umar Sayaf was responsible for the study's conceptualization, methodology, formal analysis, and investigation. He also carried out data curation, prepared the visualizations, and wrote the original draft of the manuscript. Vijaya Isnaniawardhani and Budi Muljana provided supervision, validated the results, and contributed to the review and editing of the manuscript. Wingky Suganda supplied essential resources for the project and assisted with supervision and validation.

Conflict of Interest

The authors declare that they have no conflicts of interest relevant to the content of this publication.

References

Advokaat, E. L., & van Hinsbergen, D. J. J. (2024). Finding Argoland: Reconstructing a microcontinental archipelago from the SE Asian accretionary orogen. *Gondwana Research*, 128, 161–263. https://doi.org/10.1016/J.GR.2023.10.005

Angkasa, S. S., Nugraha, H. D., Fatimah, D. Y., & Pratama, A. B. K. (2024). Diagenetic features recorded in sedimentary rocks within a gas chimney: A case study from the Makassar Strait, offshore Indonesia. *Journal of Natural Gas Geoscience*, 9(5), 361–371.

https://doi.org/10.1016/J.JNGGS.2024.07.003

Dunham, R. J. (1962). Classification of Carbonate Rocks According to Depositional Texture. In W. E. Ham (Ed.), *Classification of Carbonate Rocks – A Symposium* (pp. 108–121). American Association of Petroleum Geologists (AAPG). https://pubs.geoscienceworld.org/aapg/books/edited-volume/1475/chapter/107178011/Classification-of-Carbonate-Rocks-According-to

Embry, A. F., & Klovan, J. E. (1971). A Late Devonian Reef Tract on Northeastern Banks Island, N.W.T. *Bulletin of Canadian Petroleum Geology*, 19(4), 730–781. https://pubs.geoscienceworld.org/cspg/bcpg/article-abstract/19/4/730/57032/A-LATE-DEVONIAN-REEF-TRACT-ON-NORTHEASTERN-BANKS?redirectedFrom=fulltext

Flügel, E. (2010). *Microfacies of Carbonate Rocks: Analysis, Interpretation and Application* (2nd ed.). Springer Berlin Heidelberg. https://doi.org/10.1007/978-3-642-03796-2

Garrard, R. A., Supandjono, J. B., & Surono, S. (1988). The Geology of the Banggai-Sula Microcontinent, Eastern Indonesia. *Proceedings of the 17th Annual Convention Indonesian Petroleum Association*, 1, 23–52. https://www.ipa.or.id/id/publications/the-geology-of-the-banggai-sula-microcontinent-eastern-indonesia

Greenfield, T., Copley, A. C., Caplan, C., Supendi, P., Widiyantoro, S., & Rawlinson, N. (2021). Crustal Deformation and Fault Strength of the Sulawesi Subduction Zone. *Tectonics*, 40(3), e2020TC006573. https://doi.org/10.1029/2020TC006573

Hall, R. (2012). Late Jurassic–Cenozoic reconstructions of the Indonesian region and the Indian Ocean. *Tectonophysics*, 570–571, 1–41. https://doi.org/10.1016/J.TECTO.2012.04.021

Hall, R. (2019). The subduction initiation stage of the Wilson cycle. *Geological Society Special Publication*, 470(1), 415–437. https://doi.org/10.1144/SP470.3

Haris, A., Siburian, I. B., & Riyanto, A. (2017). Facies Modeling of Kais Formation Limestone: A Case Study of Kafor Field, West Papua, Indonesia. *International Journal of GEOMATE*, 13(40), 160–166. https://doi.org/10.21660/2017.40.69647

Hasanusi, D., Kwartono, K., & Wijaya, R. (2012). Carbonate Reservoir Characterization and its Use on Reservoir Modeling: A Case Study of Senoro Field. *Proceedings of the SPWLA 18th Formation Evaluation Symposium of Japan*, SPWLA-JFES-2012-I. https://onepetro.org/SPWLAJFES/proceedings-pdf/JFES12/JFES12/SPWLA-JFES-2012-I/1610047/spwla-jfes-2012-i.pdf

Henglai, P., Fongngern, R., Saller, A., Laochamroonvorapongse, R., Thamniyom, P., & Lendam, S. (2025). Diagenetic and depositional controls on reservoir quality in a Middle Miocene carbonate buildup, Central Luconia, offshore Malaysia. *Marine and Petroleum Geology*, 181, 107528. https://doi.org/10.1016/J.MARPETGEO.2025.107528

Herdiansyah, F., Burhannudinnur, M., Prakoso, S., Putra, I. H., Kurnianto, D., Irano, T., & Harnest, B. (2022). Sequence Stratigraphy of Miocene Mixed Carbonate-Siliciclastic in Fold and Thrust Belt System, Banggai Basin. *IOP Conference Series: Earth and Environmental Science*, 1104(1), 012045. https://doi.org/10.1088/1755-1315/1104/1/012045

Jambak, M. A., Ibrahim, I., Harnest, B., Irano, T., Prabawa, G., Luthfi, R., & Prasetyo, A. B. (2024). Reinterpretation of Salodik Group Performance Based on Facies and Diagenesis Approaches to Classify Reservoir Quality. *Indonesian Journal on Geoscience*, 11(1), 91–109. https://doi.org/10.17014/ijog.11.1.91-109

Kesumastuti, L., Pilia, S., Rawlinson, N., Whattam, S. A., & Supendi, P. (2025). Evidence of Multiple Subducting Slabs Beneath Sulawesi From Teleseismic P-Wave Tomography. *Geophysical Research Letters*, 52(11), e2025GL115393. https://doi.org/10.1029/2025GL115393

Khairi, H., Burhannudinnur, M., & Herdiansyah, F. (2022). Carbonate Reservoir Characterization Based on Rock Type Analysis in Minahaki Formation and Tomori Formation, "HK" Field, Banggai Basin. *IOP Conference Series: Earth and Environmental Science*, 1104(1), 012037. https://doi.org/10.1088/1755-1315/1104/1/012037

Khazaie, E., Noorian, Y., Moussavi-Harami, R., Mahboubi, A., Kadkhodaie, A., & Omidpour, A. (2022). Electrofacies modeling as a powerful tool for evaluation of heterogeneities in carbonate reservoirs: A case from the Oligo-Miocene Asmari Formation (Dezful Embayment, southwest of Iran). *Journal of African Earth Sciences*, 195, 104676. https://doi.org/10.1016/J.JAFREARSCI.2022.104676

Laya, K. P., Adhiperdana, B. G., Pratama, P. Y., Helbet, R., Yumansa, A., Khawarizmy, A., Rendy, O. T., Wibowo, S., & Syafrie, I. (2022). Integrated Microfacies and Sedimentology Analysis of Minahaki Fm: Analogue for Carbonate Ramp Depositional Model and Microporosity-dominated Reservoir Performance. *Proceedings of the PIT 51st IAGI Convention*. https://www.iagi.or.id/web/digital/71/PITIAGI-22-P-Abs-166.pdf

Muhammad, F., Benyamin, B., & Herdiansyah, F. (2020). Analisis Litofasies dan Sistem Terumbu Batuan Karbonat Berdasarkan Data Log dan Core, Cekungan Banggai, Sulawesi Tengah. *Journal of Geoscience Engineering and Energy*, I(1), 33–39. https://e-journal.trisakti.ac.id/index.php/jogee/article/view/6694

Nugraha, A. M. S., & Hall, R. (2018). Late Cenozoic palaeogeography of Sulawesi, Indonesia. *Palaeogeography, Palaeoclimatology, Palaeoecology*, 490, 191–209. https://doi.org/10.1016/J.PALAEO.2017.10.033

Nugraha, A. M. S., & Hall, R. (2022). Neogene sediment provenance and paleogeography of SE Sulawesi, Indonesia. *Basin Research*, 34(5), 1714–1730. https://doi.org/10.1111/bre.12682

Nugraha, A. M. S., Hall, R., & BouDagher-Fadel, M. (2022). The Celebes Molasse: A revised Neogene stratigraphy for Sulawesi, Indonesia. *Journal of Asian Earth Sciences*, 228, 105140. https://doi.org/10.1016/J.JSEAES.2022.105140

Nurhidayah, E. M., Akmaluddin, A., Barianto, D. H., Husein, S., & Saripudin, A. (2024). Nannoplankton Biostratigraphy from Banggai-Sula Basin, Central Sulawesi. *Journal of Tropical Biodiversity and Biotechnology*, 9(1), 85308. https://doi.org/10.22146/JTBB.85308

Ontosari, D., Hafeez, A., & Setyadi, A. L. (2023). Carbonate shoal microfacies characterization using the interdependent of depositional systems and diagenesis of Kais

Formation in the Matoa Field, Salawati Basin. *Berita Sedimentologi*, 49(2), 56–74. https://doi.org/10.51835/bsed.2023.49.2.438

Patria, A., Natawidjaja, D. H., Daryono, M. R., Hanif, M., Puji, A. R., & Tsutsumi, H. (2023). Tectonic landform and paleoseismic events of the easternmost Matano fault in Sulawesi, Indonesia. *Tectonophysics*, 852, 229762. https://doi.org/10.1016/J.TECTO.2023.229762

Pratama, P. Y., Dzaki, D. F., Luqman, Rahardian, R., Helbet, R., Anastasia, S., Raharjo, W. B., Junaedi, Wibowo, R., & Haryanto, S. (2020). Facies Analysis Using Biostratigraphy Data and Also Development and Controlling Factors of Miocene Carbonate Buildups, Central Sulawesi. *Society of Petroleum Engineers - SPE/IATMI Asia Pacific Oil and Gas Conference and Exhibition 2019, APOG 2019*. https://doi.org/10.2118/196348-MS

Rahadian, R., Dzakirin, D. F., Pratama, P. Y., Luqman, L., Anastasia, S., Raharjo, W. B., Wibowo, R., & Zaidy, A. (2018). Facies Characterization and Depositional Environment Relationship of Miocene Carbonates Reservoir in S Field, Central Sulawesi. *Proceedings of the IATMI Symposium 2018,* 551–557. https://www.iatmi.or.id/download/3695/?tmstv=1761289465

Satyana, A. H., & Zaitun, S. (2016). Origins of Oils and Gases at Banggai – Sula Microcontinent, Eastern Sulawesi – North Moluccas: Constraints from Biomarkers and Isotope Geochemistry – Implications for Further Exploration of Cenozoic and Pre-Cenozoic Objectives. *Proc. Indonesian Petrol. Assoc., 40th Ann. Conv.* https://doi.org/10.29118/IPA.0.16.575.G

Serhalawan, Y., & Chen, P.-F. (2024). Seismotectonics of Sulawesi, Indonesia. *Tectonophysics*, 883, 230366. https://doi.org/10.1016/J.TECTO.2024.230366

Surjono, S. S., Asy'ari, M. R., & Gunawan, A. (2019). Application of Seabed Core Geochemistry for Further Exploration in Banggai-Sula Area. *CAJG 2018*, *Advances in Science, Technology and Innovation*, 171–173. https://doi.org/10.1007/978-3-030-01455-1_36

Syah, M. H. F., Kano, A., Iizuka, T., & Kakizaki, Y. (2019). Depositional and diagenetic history of limestones and dolostones of the Oligo-Miocene Kujung Formation in the Northeast Java Basin, Indonesia. *Island Arc*, 28(6), e12326. https://doi.org/https://doi.org/10.1111/iar.12326

Tiab, D., & Donaldson, E. C. (2024). *Petrophysics: Theory and Practice of Measuring Reservoir Rock and Fluid Transport Properties* (5th ed.). Elsevier. https://doi.org/10.1016/C2023-0-01203-1

Titu-Eki, A., & Hall, R. (2020). The Significance of the Banda Sea: Tectonic Deformation Review in Eastern Sulawesi. *Indonesian Journal on Geoscience*, 7(3), 291–303. https://doi.org/10.17014/IJOG.7.3.291-303

Wibowo, B. A., Bai, L., Rohadi, S., Sahara, D. P., Chen, Z., Karyono, K., Setiawan, Y., Widyadharma, P. H., Arimuko, A., Rahayu, A. N., Adi, S. P., & Karnawati, D. (2025). Slab morphology and associated seismic and volcanic activities beneath Sulawesi Island, Indonesia. *Journal of Volcanology and Geothermal Research*, 465, 108352. https://doi.org/10.1016/j.jvolgeores.2025.108352

Indexing and Abstracting

GEOFISIKA
UNIVERSITAS HASANUDDIN

ISSN 2579-5546